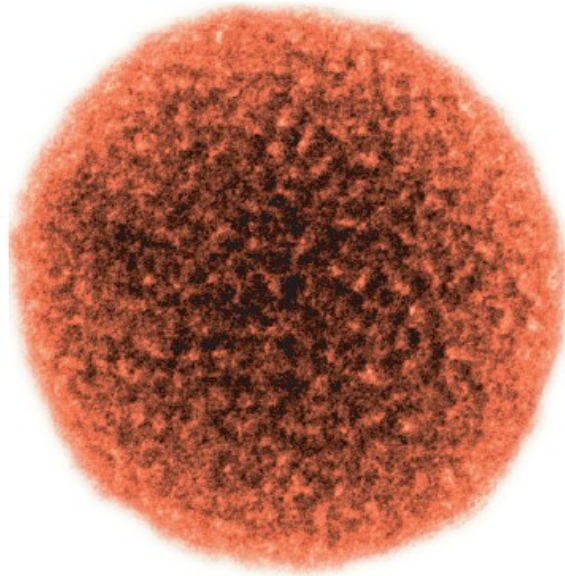


Steffen Waglöhner

Oxidation of soot on iron oxide catalysts





WiKu-Wissenschaftsverlag Dr. Stein

www.wiku-verlag.de

www.stonespublishingcologne.eu

“Oxidation of soot on iron oxide catalysts”

zur Erlangung des akademischen Grades eines
DOKTORS DER INGENIEURWISSENSCHAFTEN (Dr.-Ing.)

der Fakultät für Chemieingenieurwesen und Verfahrenstechnik des
Karlsruher Institut für Technologie (KIT)

genehmigte
DISSERTATION

von
Dipl.-Ing. Steffen Waglöhner
aus Heilbronn

Referent: Prof. Dr.-Ing. Henning Bockhorn

Korreferent: Prof. Dr.-Ing. Rainer Reimert

Korreferent: Prof. Dr. rer. nat. Sven Kureti

Tag der mündlichen Prüfung: 17.02.2012

Bibliografische Informationen

Die Deutsche Bibliothek verzeichnet diese Publikation in der Deutschen Nationalbibliografie; detaillierte bibliografische Daten sind im Internet über <http://dnb.ddb.de> abrufbar.
Kurzsigel des Verlages: WiKu

ISBN 978-3-86553-405-7

© 2012 **WiKu-Wissenschaftsverlag Dr. Stein, Köln & Duisburg**
Wissenschaftsverlag und Kulturedition

Der Inhalt wurde sorgfältig recherchiert, bleibt aber ohne Gewähr für Richtigkeit und Vollständigkeit. Alle Rechte, insbesondere das Recht der Vervielfältigung und Verbreitung sowie der Übersetzung, vorbehalten. Die Copyrightbestimmungen beziehen sich ebenfalls auf das WiKu-Logo. Kein Teil des Werkes darf in irgendeiner Form (durch Fotokopie, Mikrofilm oder ein anderes Verfahren) ohne schriftliche Genehmigung des Verlages reproduziert oder unter Verwendung elektronischer Systeme verarbeitet, vervielfältigt oder verbreitet werden.

Das WiKu-Logo ist ein beim Deutschen Marken- und Patentamt eingetragenes Warenzeichen und gesetzlich geschützt (Akz.: 303 53 255.6/16). Sofern in diesem Werk eingetragene Marken ohne die Bezeichnung ® erwähnt werden, kann daraus nicht geschlossen werden, dass diese zur Verwendung frei sind.

Printed in the EU

„So eine Arbeit wird eigentlich nie fertig, man muss sie für fertig erklären, wenn man nach Zeit und Umständen das Möglichste getan hat.“

Johann Wolfgang von Goethe

Danksagung

Die vorliegende Arbeit entstand im Zeitraum von Juli 2008 bis April 2011 am Institut für Technische Chemie und Polymerchemie des Karlsruher Instituts für Technologie sowie am Institut für Energieverfahrenstechnik und Chemieingenieurwesen der TU Bergakademie Freiberg.

Mein ganz besonderer Dank gilt Herrn Professor Dr. S. Kureti für das entgegengebrachte Vertrauen, die mir gewährten Freiheiten sowie seinem großen Interesse und der steten Diskussionsbereitschaft. Vielen Dank!

Weiterhin bedanke ich mich bei Herrn Professor Dr.-Ing. H. Bockhorn für sein Vertrauen, seine Unterstützung sowie für die Aufgabenstellung.

Großer Dank gilt der Firma Umicore für die finanzielle Unterstützung dieser Arbeit, sowie den Doktoren G. Jeske, B. Southward und L. Jongen, die in zahlreichen Projektbesprechungen wertvolle Anstöße geliefert haben, welche maßgeblich zum Gelingen dieser Arbeit beigetragen haben.

Ich möchte mich auch bei meinen Kollegen für die angenehme und gemeinsame Zeit bedanken, welche neben fachlichen auch viele außer-fachlichen Aktivitäten umfasste. Insbesondere richtet sich dieser Dank an die Doktoren D. Reichert, F. Schott, P. Balle und S. Zürcher sowie die Herren B. Geiger, A. Pacher, W. Boll und T. Kaltschmitt.

Besonderer Dank geht an Herrn H. Herberger für seine tatkräftige Unterstützung und seine niemals versiegenden Lösungsvorschläge beim Anlagenaufbau sowie für die kulinarische Verkürzung zahlreicher Mittagspausen.

Des Weiteren danke ich den Herren A. Wagner, A. Jaks sowie J. Finsterle für die stete Hilfsbereitschaft bei Auf- und Umbauarbeiten.

Für ihre Unterstützung danke ich Frau Dr. M. Kurkova, Frau S. Starke, Frau K. Schäfer, Frau C. Notar und Herrn J. Pesek; danke auch an Frau A. Beilmann und Frau J. Heck, die während ihrer Ausbildung einen Beitrag zu dieser Arbeit geleistet haben.

Ferner gebührt den Studenten, die mich während meiner Arbeit begleitet haben, herzlicher Dank; an dieser Stelle auch Dankeschön an Herrn F. Mück, Frau E. Ogel, Herrn M. Staehr, Frau K. Roppertz, Herrn J. Bär und Frau G. Cevasoglu!

Schließlich möchte ich mich bei meiner Familie, die mir immer mit Rat und Tat zur Seite stand, für ihre Unterstützung und ihren Rückhalt bedanken.

Abstract

In the present work, a highly active Fe₂O₃-based catalyst for soot oxidation in diesel exhaust has been engineered through the combination of results from three different research methods. These methods are mechanistic and kinetic experiments, kinetic and fluid dynamic modelling, and structure-activity relation of different types of iron oxides.

The elucidation of the reaction mechanism included a systematic sequence of experiments on a well-defined Fe₂O₃ model catalyst, i.e. α -Fe₂O₃, in which the reaction conditions and gas composition were varied. In addition, mechanistic studies using ¹⁸O₂ were conducted. The results showed oxygen transfer to proceed from the catalyst surface to the soot. Resulting surface defect sites are refilled from both, bulk and migrating surface oxygen atoms. This demonstrated that crystalline domains of the catalyst provide bulk oxygen transport whereas amorphous domains advance migration of surface oxygen atoms by promoting oxygen uptake from the gas phase. These findings suggest a highly active iron oxide catalyst to be composed of crystalline as well as amorphous domains.

The modelling part of this work covered kinetic and fluid-dynamic simulations of the catalytic soot conversion. Unknown kinetic parameters were determined on the basis of a global kinetic approach by fitting experimental results. Thus estimated kinetic parameters were implemented in a 2-dimensional CFD (computational fluid dynamics) model revealing the local heat production to have large effect on the kinetics of catalytic soot oxidation. Experimentally hard to determine parameters like local O₂ and CO₂ concentration as well as temperature gradients were simulated. The CFD model including kinetics of the catalytic soot oxidation could be validated by experimental concentration-time-results with very high accordance.

Finally, different types of iron oxides were tested for their catalytic soot oxidation activity. Comparison of physical-chemical properties and catalytic activity showed that a balance between crystalline and amorphous domains as well as a high number of Lewis acid sites on the catalyst surface is highly beneficial for the activity. This coincides with the results of the mechanistic investigations and supports the presented mechanism of catalytic soot oxidation on α -Fe₂O₃.

Based on these findings an advanced nano-sized Fe₂O₃ catalyst has been developed featuring a crystallinity of ca. 50 wt.% and a high number of Lewis acid sites on the surface. This material was synthesised on a tens-of-grams scale with a self-

engineered flame-spray pyrolysis set-up. The catalyst synthesis and the catalytic coating of diesel particulate filter (CDPF) were completed in one step. Testing of the CDPF under real exhaust conditions showed that an optimum between catalyst loading and filter backpressure was achieved at a catalyst loading of 50 g/l.

Zusammenfassung

Die vorliegende Arbeit behandelt die wissensbasierte Entwicklung eines Fe_2O_3 -basierten Katalysators zur Oxidation von Ruß in Dieselabgas. Die Grundlage dieses Entwicklungsprozesses umfasst drei wesentliche Schwerpunkte, nämlich Studien zur Aufklärung des Reaktionsmechanismus, kinetische und fluiddynamische Modellierung, sowie Untersuchungen zur Aktivitäts-Struktur-Relation von Eisenoxiden.

Zur Evaluierung des Reaktionsmechanismus wurde eine systematische Reihe an Experimenten an einem definierten Modellkatalysator ($\alpha\text{-Fe}_2\text{O}_3$) durchgeführt, in denen Reaktionsbedingungen und Gaszusammensetzung variiert wurden. Zudem erfolgten Untersuchungen unter Verwendung von isotopenmarkiertem Sauerstoff. Es konnte nachgewiesen werden, dass der Sauerstofftransport während der katalysierten Rußoxidation an Fe_2O_3 von der Katalysatoroberfläche zum Rußpartikel verläuft. Die resultierenden Sauerstoff Fehlstellen an der Oberfläche werden sowohl durch Gitter-, als auch durch Oberflächensauerstoff aufgefüllt. In diesem Zusammenhang konnte gezeigt werden, dass der Transport von Gittersauerstoff hauptsächlich in kristallinen Bereichen des Katalysators stattfindet, wohingegen der Sauerstoffaustausch zwischen Fe_2O_3 -Oberfläche und Gasphase vor allem an amorphen Bereichen erfolgt. Für einen leistungsfähigen Katalysator impliziert dies das Vorhandensein beider Bereiche. Weiterhin wurde verdeutlicht, dass die Anzahl an Kontaktpunkten sowie das Stoffmengenverhältnis von Katalysator und Ruß großen Einfluss auf die Rußoxidation hat.

Die Modellierungen umfassten die chemische Kinetik und Fluiddynamik der katalysierten Rußumsetzung. Auf Grundlage eines globalkinetischen Modells wurden die relevanten kinetischen Parameter erhalten. Dieses Modell wurde anschließend in das 2-dimensionale CFD (computational fluid dynamics) Modell implementiert, wobei nachgewiesen wurde, dass insbesondere die lokale Wärmefreisetzung signifikante Auswirkung auf die Kinetik der katalysierten Rußoxidation hat. Außerdem ermöglichte das 2-dimensionale Modell die zeitliche und örtliche Auflösung von

experimentell schwer zugänglichen Parametern wie beispielsweise O_2 und CO_2 Konzentration während der Reaktion. Zur Validierung des Modells wurden Simulationen vorgenommen, die den experimentellen Daten gegenübergestellt wurden und dabei sehr gute Übereinstimmung zeigten.

Die physikalisch-chemische Charakterisierung von verschiedenen Eisenoxiden lieferte detaillierte Informationen über die Beschaffenheit der Materialien. Eine Struktur-Aktivitäts Korrelation ergab, dass eine Ausgewogenheit an kristallinen und amorphen Bereichen, sowie eine große Anzahl an Lewis-sauren Oberflächenzentren die katalytische Aktivität erhöhen. Dies ist im Einklang mit den mechanistischen Untersuchungen und bekräftigt den vorgestellten Mechanismus der katalysierten Rußoxidation. Auf Grundlage dieser Erkenntnisse wurde schließlich ein hoch aktiver Katalysator entwickelt, der eine Kristallinität von ca. 50 % sowie eine große Anzahl an aktiven Lewis Oberflächenplätzen aufweist. Die Herstellung dieses Materials erfolgte in einer eigens konstruierten Apparatur mittels Flammenpyrolyse. Das Konzept dieser Anlage ermöglicht die simultane Katalysatorsynthese und Deposition auf einem Partikelfilter. Der letzte Schritt des Entwicklungsprozesses beinhaltete schließlich die Beschichtung und Evaluierung von Partikelfiltern unter realen Bedingungen. Dabei wurde für eine Filterbeladung von 50 g/l Katalysator ein Optimum bezüglich Beladung und Gegendruck des Partikelfilters gefunden.

Contents

1	Introduction	1
1.1	General aspects of polluting emissions	1
1.2	Exhaust aftertreatment in diesel cars	3
1.2.1	DeNO _x processes	4
1.2.2	Removal of soot	4
1.3	Aim and outline	5
2	Methods for the characterisation of solids and the analysis of catalytic soot oxidation	8
2.1	Electron microscopy	8
2.2	Nitrogen physisorption	9
2.3	Thermogravimetry and difference thermal analysis	9
2.4	Temperature programmed techniques	10
2.4.1	Temperature programmed oxidation	11
2.4.2	Temperature programmed desorption	11
2.4.3	Temperature programmed reduction	14
2.4.4	Isotopic oxidation studies with ¹⁸ O ₂	14
2.5	X-ray diffraction	15
2.6	Techniques for gas phase analysis	15
2.6.1	Infrared spectroscopy	15
2.6.2	Chemical ionisation mass spectrometry	16
3	Mechanistic and kinetic studies of catalytic soot oxidation	17
3.1	Theoretical background of the oxidation of soot	17
3.1.1	Non-catalytic soot oxidation	17
3.1.2	Catalytic soot oxidation	18
3.1.3	Kinetics of the soot oxidation on Fe ₂ O ₃ catalysts	19
3.2	Experimental results from the mechanistic studies	22

3.2.1	Variation of the reaction conditions	22
3.2.2	Temperature distribution in the catalyst/soot mixture	29
3.2.3	Variation of the composition of the gas feed	31
3.2.4	Temperature programmed reduction of α -Fe ₂ O ₃ by soot	38
3.2.5	Isotopic studies with ¹⁸ O ₂	41
3.3	Discussion	52
3.3.1	Variation of the reaction conditions	52
3.3.2	Temperature distribution in the catalyst/soot mixture	58
3.3.3	The effect of varying the gas feed	58
3.3.4	Temperature programmed reduction of α -Fe ₂ O ₃ with soot	61
3.3.5	Isotopic studies with ¹⁸ O ₂	63
3.4	Summary and conclusion of the mechanistic studies	71
4	Kinetic and fluid dynamic modelling of catalytic soot oxidation on Fe₂O₃ catalyst	73
4.1	Development of a reactor model	73
4.2	Modelling of the chemical kinetics	77
4.2.1	Determination of unknown parameters	80
4.2.2	Validation of the kinetic model	83
4.2.3	Description of the effect of different contact modes on the kinetics of the catalytic soot oxidation	85
4.3	Modelling of the fluid dynamics	90
4.3.1	Setting-up of conservation equation	90
4.3.2	Implementation of chemical kinetics	97
4.4	Discussion	101
5	Evaluation of different iron oxide catalysts for soot oxidation	107
5.1	Requirements of an advanced catalyst for soot oxidation	107
5.2	Physical-chemical characterisation of different Fe ₂ O ₃ catalysts	108
5.2.1	Preparation of Flame-spray Fe ₂ O ₃	109
5.2.2	Experimental results	112
5.3	Kinetic modelling of the NH ₃ adsorption and desorption	130

5.3.1	Fundamentals of the adsorption and desorption of NH ₃	131
5.3.2	Results of the kinetic modelling	133
5.4	Coupling of physical-chemical properties and the catalytic performance of different Fe ₂ O ₃ materials	139
6	Coating and testing of laboratory diesel particulate filters	143
6.1	Modification of the flame-spray pyrolysis bench	143
6.2	TPO studies of the coated laboratory filters	144
6.2.1	DPF coated by Fe ₂ O ₃	145
6.3	Characterisation of the coated laboratory filters	147
6.3.1	Backpressure vs. loading	147
6.3.2	Axial coating thickness	148
6.4	Discussion	150
7	Conclusions and outlook	152
8	Literature	153
9	Appendix	159
A	Accuracies of measurements	159
B	Calculation of mass transfer limitations	160
B.1	Film diffusion	160
B.2	Pore diffusion	160
C	Numerical values for CFD	161
D	Physical Parameters for CFD	162
E	TPD studies of different types of soot	164
F	Thermogravimetric analysis of different types of soot	167
G	Properties of the atomisation nozzle of the FSP bench	169
H	Glossary of abbreviations and symbols	169

1 Introduction

1.1 General aspects of polluting emissions

Increasing industrialisation and the continuously growing demand for faster and cheaper mobility options has resulted in a greater need for energy. The majority of our energy is provided by the combustion of fossil fuel sources like coal, natural gas and oil. While carbon dioxide (CO_2) and water (H_2O) represent the major combustion products of fossil fuels, pollutants such as nitrogen oxides (NO_x), carbon monoxide (CO), hydrocarbons (HC) and particulate matter (PM) are formed as well. These toxic emissions are a serious threat to the ecosystem and in previous decades have forced governments of industrialised countries to introduce legal restrictions on these emissions [1].

When specifically considering the combustion of motor fuel, the proportion of pollutants originating from traffic play a major role in the overall emissions. This is shown in Figure 1-1 for Germany in the year 2008 [2]. Carbon monoxide and nitrogen oxides reveal a relatively high proportion ($> 30\%$) of the total emissions, whereas particulate matter make up less than $10\ \mu\text{m}$ (PM_{10}) and less than $2.5\ \mu\text{m}$ ($\text{PM}_{2.5}$) in diameter contributes to 16 and 22 %, respectively.

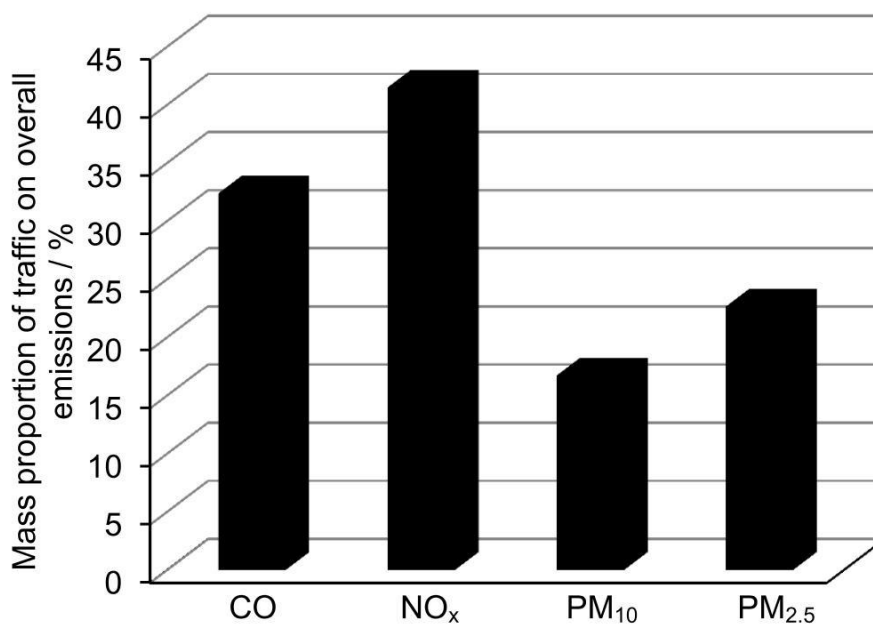


Figure 1-1: Proportion of pollutants originating from the traffic sector on overall emissions [2].

Emission regulations for the automotive sector were implemented in the 1970s and led to the introduction of three way catalysts (TWC) for the abatement of pollutants;

Germany first introduced regulations in 1974 (Technische Anleitung zur Reinhaltung von Luft). Europe-wide limitations, for traffic emissions alone, were established in 1992 by the so-called Euro-Normen (Euro-I) [3]. These regulations were steadily intensified culminating in the Euro-VI-Norm which will come into effect in 2014 (Figure 1-2).

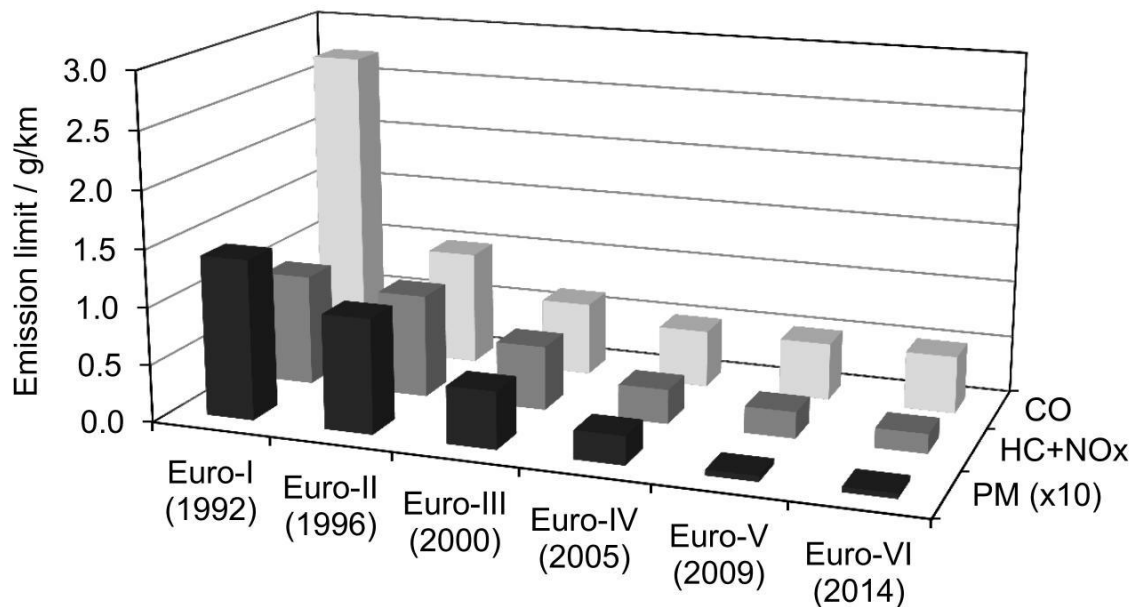


Figure 1-2: Development of the emission regulations for diesel passenger cars in the European union [4].

The exhaust aftertreatment of passenger cars can be differentiated into gasoline and diesel engines. Gasoline engines operate at an air ratio of 1 as a consequence of the TWC performance. This enables the simultaneous conversion of NO_x , CO and HC. Emissions of PM are below current regulations due to complete combustion as a result of premixing fuel and air [4]. The general composition of such a TWC includes a ceramic monolith structure ($d_{\text{channel}} \leq 1 \text{ mm}$). The active catalyst is coated on the walls of the monolithic channels and consists of a porous washcoat ($\gamma\text{-Al}_2\text{O}_3$) to increase the surface, CeO_2 components for oxygen storage and noble metal components (Pd, PdO) which constitute the catalytic active sites. For optimum catalytic performance the air ratio is controlled by the lambda sensor in a window between 0.97 and 1.03 [5]. In contrast, diesel engines have an excess of oxygen in the exhaust, which makes NO_x abatement difficult due to insufficient raw emissions of reducing agents. HC and CO are oxidised on the diesel oxidation catalyst (DOC), which consists of a ceramic monolith and contains Pd or Pt/Pd components.

Alternative aftertreatment techniques are necessary for NO_x removal. Moreover, incomplete mixing of air and fuel in the cylinder leads to the formation and emission of soot. Nevertheless, diesel engines exhibit the highest efficiency for automotive applications. For this reason their low fuel consumption leads to reduced production of the greenhouse gas CO_2 and also requires smaller amounts of fossil resources. This, in turn, causes rising demand for diesel cars, as it is shown by the increasing number of registrations in Germany within recent years (25 % in 1998 vs. 50 % in 2005) [6].

The following paragraph gives more detailed explanation of state-of-the-art techniques in diesel exhaust, aftertreatment processes. These techniques cover the abatement of NO_x , HC, CO and PM, with particular focus on the removal of soot.

1.2 Exhaust aftertreatment in diesel cars

Up until the introduction of the Euro-V-Norm (valid since 2009), legal restrictions on the emissions of diesel vehicles were met by applying a diesel oxidation catalyst (DOC) and via engine modifications. However, with the introduction of the Euro-V regulations, emission standards of NO_x and PM have to be reduced to an extent that engine modifications on their own are no longer sufficient. This derives from the trade-off in combustion for NO_x and soot, as illustrated in Figure 1-3. The minimisation of soot leads to an increase of NO_x and vice versa. Therefore, additional processes for the removal of NO_x or soot must be applied.

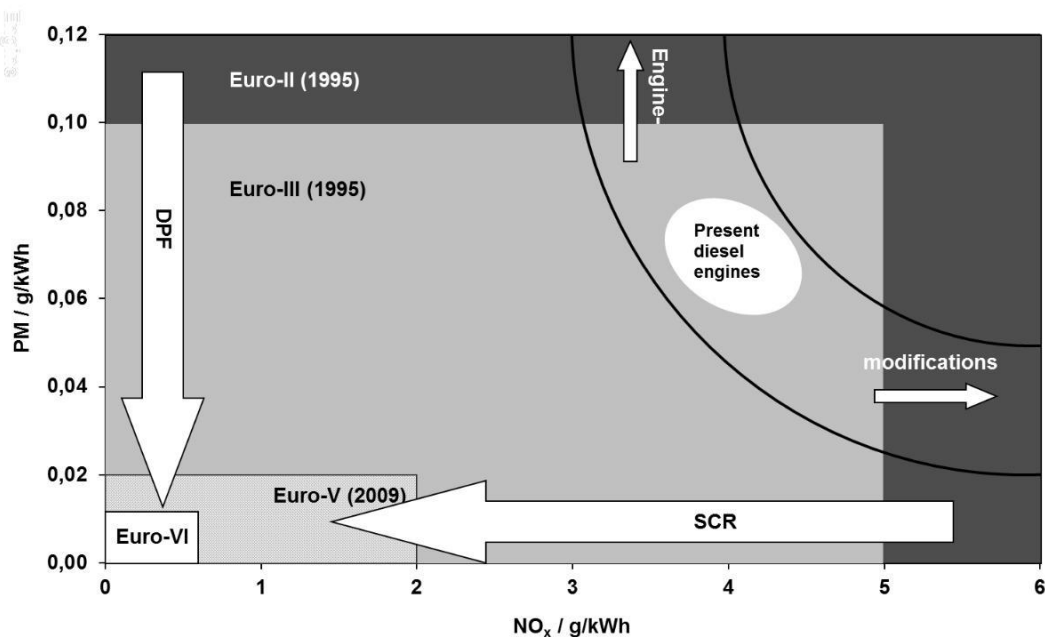


Figure 1-3: Trade-off for NO_x and soot. Strategies to meet Euro regulations in passenger cars [7].

1.2.1 DeNO_x processes

At present, two processes for the abatement of NO_x in diesel exhaust are in use; the selective catalytic reduction (SCR) and the NO_x storage reduction catalyst (NSR). In the SCR process, which originates from stationary applications i.e. flue gas cleaning in power plants, NO_x is continuously reduced by NH₃, which is provided via the thermolysis and hydrolysis of urea [8]. The NO_x species are converted selectively to nitrogen and water on vanadium containing catalysts (V₂O₅/WO₃/TiO₂) [9] and on Fe containing zeolites [10]. In contrast, the NSR technology offers a discontinuous NO_x elimination and was originally developed for lean spark-ignition engines. Nitrogen dioxide species are adsorbed on basic components of the catalyst (Al₂O₃, BaCO₃) in the form of nitrates during lean phases of the engine. When the storage capacity of the catalyst is reached, rich engine conditions are regulated resulting in desorption of NO_x and subsequent reduction of these species by present H₂, CO and HC on noble metal contacts of the catalyst. However, this technique has two disadvantages: (i) Even small SO₂ concentrations in the exhaust, which are present to a higher degree with the combustion of diesel fuel, cause sulphur poisoning of the catalyst by formation of Ba(SO₄). A catalyst regeneration step, to decompose the Ba(SO₄) species is necessary which requires exhaust temperatures above 650°C [5]. (ii) The cyclic change between lean and rich phases necessitates sophisticated engine management.

1.2.2 Removal of soot

In order to remove soot from the exhaust gas diesel particulate filters (DPF) have been developed. These have already been introduced in several countries [11]. While the trapping of soot works efficiently through the use of wall-flow monoliths [12,13], the resulting soot accumulation causes backpressure and remains a considerable problem. A regeneration technique that does not require a separate step, is provided by the continuous regenerating trap (CRT) in which soot is oxidised by NO₂ to form CO and NO [14] in an operation window of about 200 to 450°C. However, this process requires a sufficient soot/NO_x ratio, which is only available in heavy duty engines. For this reason, diesel passenger cars need additional processes for filter regeneration. One currently applied technique is non-catalytic filter regeneration which heats the DPF to 750°C, thus accelerating soot oxidation. These exhaust temperatures are obtained by post injection of fuel, which is oxidised on a diesel oxidation catalyst (DOC) located upstream to the DPF. Another possible

regeneration technique is catalytic soot oxidation, achieved either by adding catalytic components to the fuel [15] or by catalytic coating of the DPF (CDPF). Both techniques are currently being intensively researched, but are not yet in an advanced state. The so-called fuel borne catalysts (FBC) refer to metal organic compounds (mostly Ce and Fe). These are added directly to the fuel. The soot is already oxidised in the combustion chamber of the engine due to close contact between catalyst and soot. However, residue of the catalyst in the form of ash remains on the DPF and causes backpressure effects. In the case of CDPF, suitable catalytic materials like CeO_2 and Fe_2O_3 are coated on the filter. However, one problem with this technique is the insufficient contact between soot and catalyst. A real benefit, when compared to non-catalytic regeneration, is only observed in so-called tight contact mode [16].

Figure 1-4 illustrates a possible design for the combination of SCR and DPF technology to meet Euro-V emission limits. In the first section of the exhaust aftertreatment system CO, HC and NO are oxidised on a DOC. The second section represents a DPF for removal of PM and the third part shows the SCR unit including the urea dosing system, followed by the SCR catalyst and the NH_3 oxidation catalyst to avoid the slip of NH_3 .

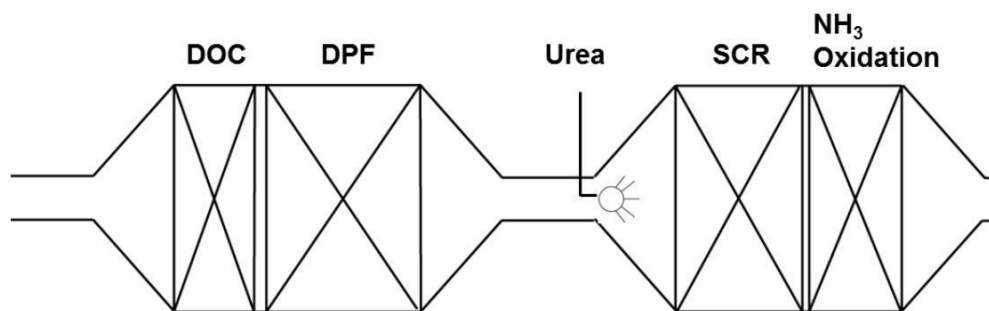


Figure 1-4: Possible design of an exhaust aftertreatment system for diesel passenger cars to meet Euro-V emission limits [4].

1.3 Aim and outline

Of the techniques for the regeneration of diesel particulate filters mentioned above, the CDPF seems to be most promising and efficient. Non-catalytic soot oxidation requires high energy consumption, while the CRT effect is insufficient due to an inadequate amount of NO_x in the exhaust of diesel passenger cars. A combination of the CRT technique and the catalytic soot oxidation was shown to cause significant problems with the contact between catalyst and soot [17]. Moreover, the use of FBCs leads to backpressure problems due to resultant ash deposits on the filter.

The CDPF is currently a focus of research for which two major challenges can be identified: (i) A passive filter regeneration requires an operation range from ca. 200-400°C and (ii) an improvement of the filter coating to provide closer contact between soot and catalyst. The aim of this work is to develop highly active catalysts for soot oxidation. Iron oxide was selected as a catalytic component as it shows encouraging potential [18], is non-toxic [19] and circumvents the use of rare earths (i.e. La, Ce and Pr). Furthermore, the development process is knowledge-based and requires fundamental understanding of the catalytic soot oxidation on Fe₂O₃. Therefore, rational and targeted catalyst design is based on three research fundamentals: (1) Elucidation of the reaction mechanism, (2) kinetic and fluid dynamic modelling and (3) physical-chemical screening of different Fe₂O₃ modifications. Examinations of the reaction mechanism contribute to the development process by elucidation of reaction pathways of soot conversion and parameters which affect the reaction rate. Modelling activities cover kinetic and fluid dynamic simulations and provide information about chemical kinetics and insights into fluid dynamics i.e. evolution of reaction heat, oxygen consumption etc. Physical-chemical screening accounts for a knowledge-based catalyst development by correlating physical-chemical properties of several iron oxide materials with their catalytic performance to identify properties beneficial for the activity in soot oxidation. Finally, the insights from these three research methods are combined and taken as a basis for the development of an advanced catalyst based on iron oxide. This advanced catalyst can be transferred to a real DPF system and evaluated under real conditions.

This thesis includes six chapters as well as a list of literature and an appendix (Figure 1-5). Each chapter contains a theoretical section and a results and discussion section. After the introduction, methods for characterisation of solids and the analysis of the catalytic soot oxidation are described. Chapters 3, 4 and 5 cover the three fundamental research fields of the thesis: Mechanistic and kinetic studies for the elucidation of the reaction mechanism, kinetic and fluid dynamic modelling as well as physical-chemical screening of different Fe₂O₃ modifications and their catalytic performance. The latter also includes findings of the best material designed. Chapter 6 deals with the transfer and testing of the developed material to a real DPF system. The conclusion and outlook are presented in chapter 7.

1. Introduction		
<ul style="list-style-type: none"> • Motivation and objectives. • Layout of the thesis. 		
2. Methods for characterisation		
<ul style="list-style-type: none"> • Image guided techniques. • Spectroscopic techniques. • Temperature programmed techniques. • X-ray techniques. 		
3. Mechanistic and kinetic studies	4. Kinetic and fluid dynamic modelling	5. Fe₂O₃ catalysts for soot oxidation
<ul style="list-style-type: none"> • Variation of reaction conditions. • Variation of the gas feed composition. • Isotopic studies. 	<ul style="list-style-type: none"> • Kinetic modelling. • Fluid dynamic modelling. 	<ul style="list-style-type: none"> • Physical-chemical characterisation • Coupling of physical-chemical properties and activity.
6. Transfer to a real DPF system		
<ul style="list-style-type: none"> • Coating of DPF in laboratory scale. • Testing and evaluation of the coating. 		
7. Conclusion and outlook		
Literature and Appendix		

Figure 1-5: Outline of the thesis.

2 Methods for the characterisation of solids and the analysis of catalytic soot oxidation

This chapter addresses the methods and techniques used for the characterisation required for this study. More specifically, characterisation refers to the physical-chemical properties of the catalysts and soot, the gas phase analysis, and the elucidation of the catalyst-soot interaction. An overview of these methods and their respective functions is given in Figure 2-1. The overview in this chapter provides only basic principles. For more detailed descriptions, please see the references to further literature.

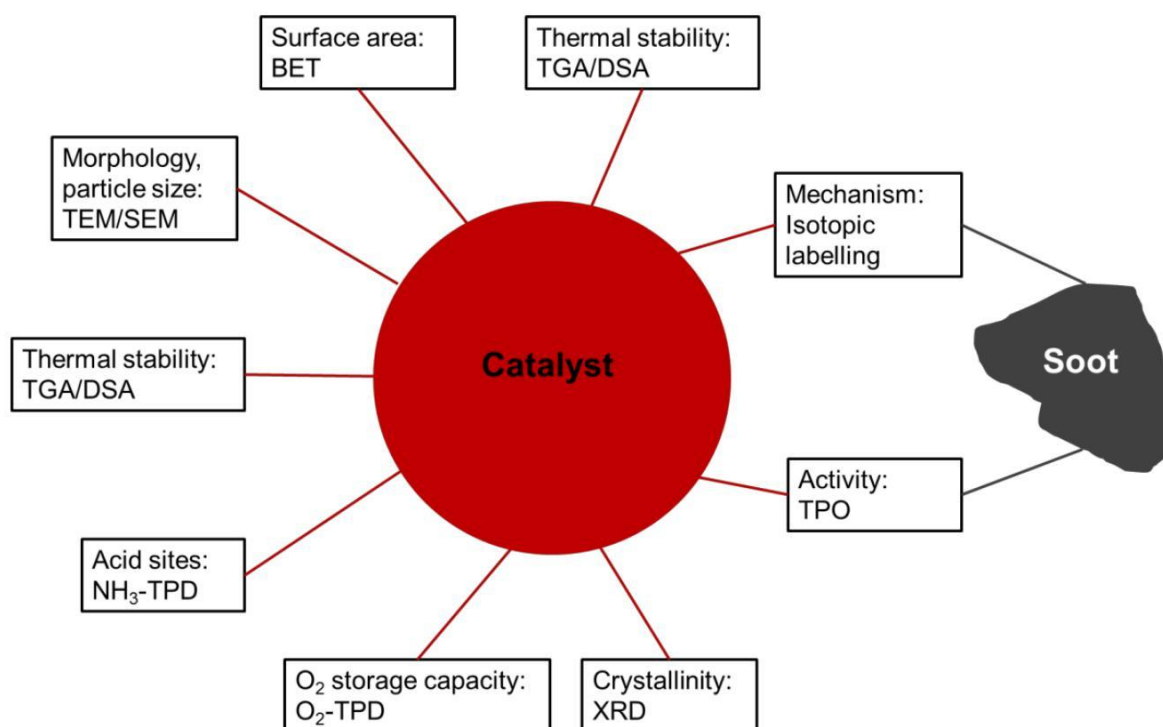


Figure 2-1: Analytical tools for investigation of physical-chemical properties of the catalyst and soot as well as for elucidation of catalyst-soot interaction.

2.1 Electron microscopy

Electron microscopy is a technique for the determination of the morphology and size of particles [20]. Electrons, which interact with matter, can provide information about the composition and internal structure of solids. In this work, the transmission electron microscope (TEM) is used.

TEM is a technique similar to the design of an optical microscope, but instead of light electrons are used. A primary electron beam of high energy passes through a condenser to parallelise the beam, which impacts on the sample. The transmitted

electrons form a two-dimensional projection of the sample, as the weakening of the beam is dependent on the thickness and mass of the material. In this study, a TEM EM912 from Omega/Carl-Zeiss Oberkochen was used and provided a resolution of ca. 0.4 nm. The sample is prepared by breaking-up agglomerates under ultrasonic treatment in isopropanol.

To estimate the range of the particle diameters, 10 images of each sample were taken.

2.2 Nitrogen physisorption

Nitrogen physisorption is an analysis technique which provides information about the specific surface area of porous solids. For routine analyses, the method according to Brunauer, Emmet and Teller (BET) [21] is often used with N₂ as probe molecule. The nitrogen adsorption isotherm of a sample is recorded at the nitrogen boiling point (77K). The specific amount of nitrogen, which is required for the formation of a monolayer on the sample surface is calculated on the basis of the BET equation [22]. The adsorption and desorption isotherm of the sample was recorded on a Sorptomatic 1990 from Porotec (Frankfurt). For the removal of adsorbed species, such as water, the sample was thermally pre-treated. Due to agglomeration effects of the nano-scaled materials the temperature was limited to 250°C. This was maintained for 15 min at 3·10⁻⁴ mbar. Possible errors in the BET results may occur from imprecise probe weighing or from condensation of nitrogen in micro pores of the sample.

2.3 Thermogravimetry and difference thermal analysis

In this work, thermogravimetry (TG) is used for the examination of the thermal stability of materials. The weight loss of a sample is measured in dependency of time or temperature during a defined heating ramp. The sample is placed in a cup located in a corundum tube, which is flushed with gases such as nitrogen or synthetic air. In parallel to the mass change, the temperature of the cup, which contains the sample and a reference, can be measured. This measurement provides information on endothermal and exothermal processes like phase changes, crystallisation and chemical reactions [22]. For the TG/DTA studies performed on a STA 409 from Netzsch (Selb), a sample mass between 20 mg and 50 mg was taken and heated from 100°C to 650°C with a ramp of 3.3 K/min under a flow of 500 mL/min of synthetic air (Air liquid), dosed by a flow controller (Brooks Instruments, Hatfield).

Errors may occur from buoyancy of the gas flow, an imprecise weighted probe and from impurities of the sample introduced into the sample during its synthesis.

2.4 Temperature programmed techniques

Temperature programmed techniques elucidate the kinetics of gas/solid or catalytic reactions during linear temperature changes in time. This study uses temperature programmed oxidation (TPO), temperature programmed desorption (TPD) and temperature programmed reduction (TPR). The basic set-up of these experiments is always the same and is presented in Figure 2-2.

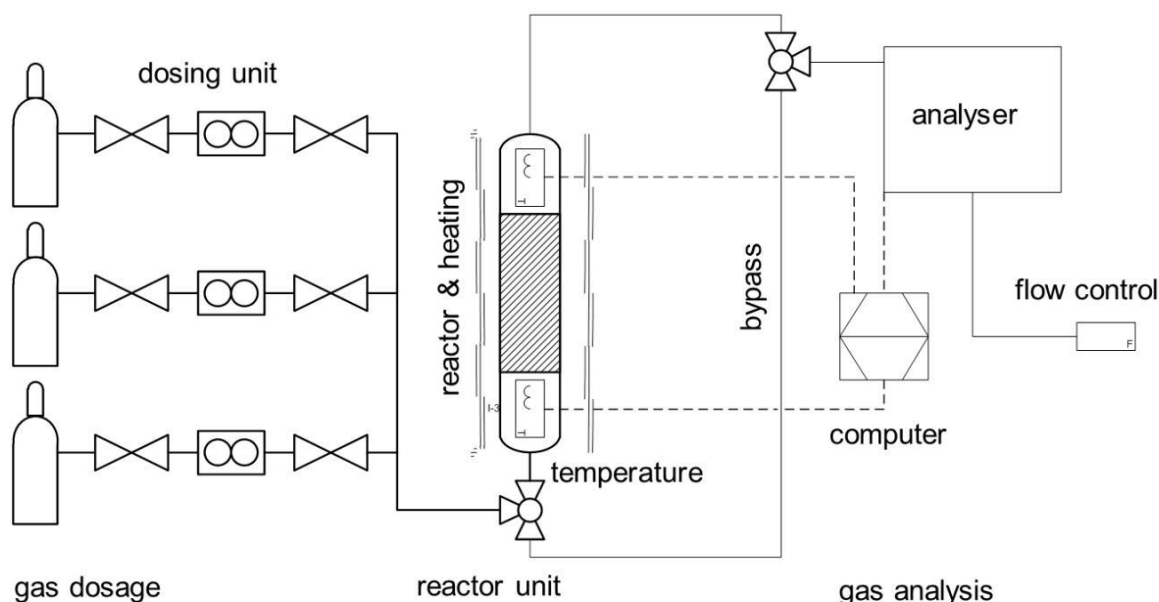


Figure 2-2: Basic experimental set-up of the temperature programmed techniques.

This bench consists of three main components; the gas dosage, reactor unit and gas analysis. The respective gas mixture was a blend of the pure components (Air Liquide) and was dosed from independent flow controllers (MKS Instruments, Munich). The reactor unit was a tubular plug flow reactor (PFR) made of quartz glass with a length of 800 mm. For TPO the inner diameter was 10 mm, for TPD 12 mm and for TPR 8 mm. The powder sample was pressed for 2 min at 40 MPa and sieved (125 μm to 250 μm) to avoid discharge. Subsequently, the sample was fixed as a packed bed in the middle of the reactor by quartz wool. The temperature was monitored by two K-type thermocouples located directly in front of and behind the sample. While the temperature was increased by a constant heating ramp, the effluent species were detected by suitable gas analysers. The following paragraphs

describe the purpose and detailed experimental parameters of the respective methods.

2.4.1 Temperature programmed oxidation

The TPO experiments were performed to evaluate the catalytic activity of solid catalysts in soot oxidation. In TPO, the total gas flow was kept at 500 mL/min (STP), while the feed consisted of 10 vol.% O₂ and N₂ as balance. The temperature was linearly increased from room temperature to 750 °C with a heating rate of 3.3 K/min and the effluent CO and CO₂ were analysed with a BINOS non-dispersive infrared spectrometer (Leybold-Heraeus, Köln). The experiments were performed with a catalyst/soot mixture in a molar ratio of 10 mmol catalyst/5 mmol soot ($m_{\text{total}}=1.66\text{g}$). The mixing of both solids can be done by two different approaches: First, a so called loose-contact mixture was established by shaking the catalyst powder and soot in a glass vial. Second, a so called tight-contact mixture was prepared by ball milling. Catalyst and soot were milled for 15 min in a Pulverisette 0 from Fritsch (Idar-Oberstein) on medium stage with a hardened steel ball ($m=940\text{ g}$). After mixing, the sample was prepared as described in the previous section. Former investigations demonstrated that pressing and granulating does not affect the activity of the mixture, whereas the initial grinding procedure was found to be the crucial step upon the preparation [23].

For kinetic studies under more realistic conditions, special diesel particulate filters were examined at laboratory scale (for details see chapter 6). These cylindrical cordierite filters (DHC-611 300/12) from NGK (Kronberg im Taunus) show a length of 2" and a diameter of 1" with a cell density of 300 cpsi. The TPO was performed in a quartz glass tube (i.d. 1") with a total flow of 6500 mL/min containing 10 % O₂ and 2 % H₂O; N₂ was used as balance. Water was dosed by oxidising the respective amount of H₂ and O₂ on a platinum catalyst (250°C) prior to the reactor. The effluent gases were detected by FTIR spectroscopy (see Table 2-3), while the temperature was increased from 150°C to 650°C with a heating ramp of 3.3 K/min.

2.4.2 Temperature programmed desorption

TPD studies were made to investigate the interaction between gaseous molecules and the surface of the solid catalysts. The TPD provides information about the number and bond strength of the species which are chemisorbed on active sites of the sample. The basic experimental approach requires 4 steps. The first step is the

elimination of impurities through heating the sample under flowing inert gas. The second step is the adsorption phase, in which the sample is exposed to the respective gaseous species until saturation equilibrium is reached. In the third step, the sample is flushed with inert gas to remove physisorbed species. The final step is initiated by linearly heating the flow of inert gas inducing desorption of the chemisorbed species. The desorption spectra give information about the examined sample. The area of the TPD curve corresponds to the amount of adsorbed species, whereas the temperature of the desorption maximum is associated with the activation energy for desorption. Furthermore, the possible appearance of multiple desorption maxima indicates different adsorption sites or different bond strengths. Figure 2-3 provides a schematic overview of the experimental steps and the information which can be obtained from a TPD.

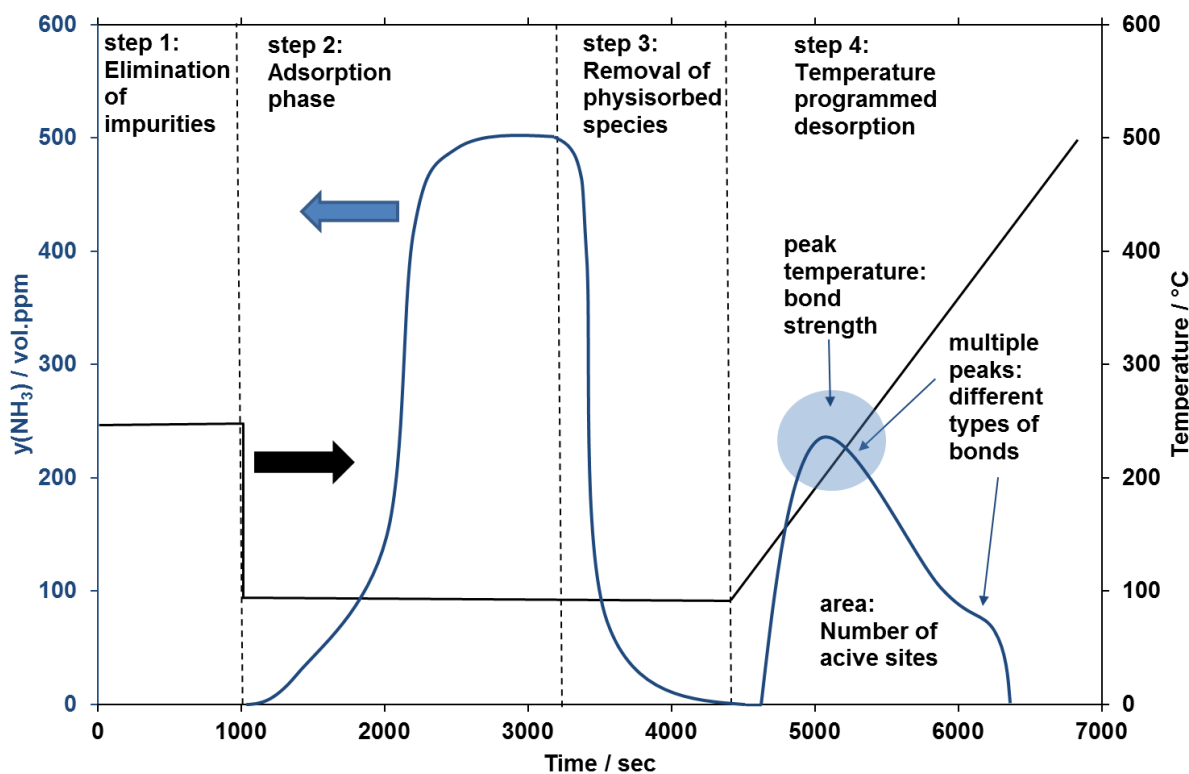


Figure 2-3: Schematic overview of the experimental procedure and the information which can be obtained from a TPD experiment.

In this work, NH₃ and O₂ were used as probe molecules. In the case of NH₃, the TPD spectra provide information about the number of acidic sites on the catalyst surface. Additionally, spectral deconvolution leads to the differentiation of Lewis and Brønsted acid sites, which elucidate the surface structure of the catalyst [24]. The deconvolution is conducted by Origin software using Gaussian peak analysis which is only a formal act and is not based on a model:

$$f_{\text{Gaussian}}(x) = y_0 + \frac{A \cdot \exp\left[-4 \cdot \ln 2 \cdot \left(\frac{x - x_c}{w}\right)^2\right]}{w \cdot \sqrt{\frac{\pi}{4 \cdot \ln 2}}} \quad (2-1)$$

y_0 : Height of baseline.

A : Area of the peak.

x_c : Centre of the peak.

w : Width of the peak.

To obtain fits with sufficient accuracy, the coefficient of determination (Eq. (4-16)) is kept above 0.98. Furthermore, recently performed DRIFTS studies [25] identified the low temperature NH_3 desorption peak to be a Brønsted bond NH_3 species and the high temperature desorption to be a Lewis bond NH_3 . The experimental conditions are listed in Table 2-1. The NH_3 volume fraction was recorded with a BINOS non-dispersive infrared spectrometer (Leybold-Heraeus, Köln).

Table 2-1: Experimental conditions for NH_3 -TPD. Total flow is always 500 ml/min (STP).

Step	Gas composition	Temperature	Time
Eliminating of impurities	N_2	250°C	15 min
Adsorption	$\text{N}_2 + 500 \text{ ppm } \text{NH}_3$	50°C	until equilibrium
Removal of physisorbed species	N_2	50°C	until $c(\text{NH}_3) \approx 0$
Desorption	N_2	50°C-500°C	$\beta = 10 \text{ K/min}$

As the oxygen transport from the catalyst surface to the soot particle is considered to be the rate determining step in the catalytic soot oxidation [18], oxygen TPD studies were also performed. These experiments potentially offer the possibility to determine the activation energy of oxygen desorption and to specify the amount of surface and bulk oxygen. Furthermore, integration of the desorption signal reveals the amount of oxygen stored on the catalyst surface. The conditions used are presented in Table 2-2. Oxygen was monitored with an Airsense 500 chemical ionisation mass spectrometer (MS4, Rockenberg).

Table 2-2: Experimental conditions for O₂-TPD. Total flow is always 500 ml/min (STP).

Step	Gas composition	Temperature	Time
Elimination of impurities	N ₂	250°C	15 min
Adsorption	N ₂ +500 ppm O ₂	200°C	30 min
Removal of physisorbed species	N ₂	200°C	until c(O ₂)≈0
Desorption	N ₂	200°C-900°C	β=10 K/min

2.4.3 Temperature programmed reduction

Temperature programmed reduction can provide information about the oxidation state of oxidic catalysts under reducing conditions. The temperature programmed reduction by H₂ (HTPR) required linearly heating (β=15 K/min) from 25°C to 900°C under a flow of 200 mL/min consisting of 95 vol.% Ar and 5 vol.% H₂. For iron oxide based catalysts, the TPR profile is expected to reveal three H₂ consumption maxima associated with the reduction sequence Fe₂O₃ → Fe₃O₄ → FeO → Fe [26,27], whereas the area ratio of the first peak to the sum of the other peaks is expected to be 8 for pure Fe₂O₃ materials. Further information about oxidative composition can be derived by comparing the molar amount of Fe used to the consumed quantity of H₂ resulting in a ratio of 1.5 for pure Fe₂O₃ according to the sequence



The conversion of H₂ was recorded by Cirrus mass spectrometer (MKS, Munich).

2.4.4 Isotopic oxidation studies with ¹⁸O₂

In isotopic TPO, ¹⁸O₂ labelled oxygen (Campro, Berlin) was used to investigate the oxygen transfer from the catalyst to soot [23]. To minimise the amount of ¹⁸O₂ used, modified reaction conditions according to literature [28] were employed requiring a constant mass of soot (m=3.7 mg). Depending on the catalyst:soot ratio, the respective amount of catalyst was mixed with the soot either by ball milling for 15 min (tight contact) or by shaking in a glass vial (loose contact, dimensions of the vial: 24x52 mm). This mixture was fixed in a quartz glass tube reactor (i.d.=8 mm, length=800 mm). Then, the feed consisting of 2270 ppm ¹⁸O₂ in 500 mL/min N₂ was dosed, while the temperature was increased with 20 K/min from 200°C to 1000°C. The gas phase analysis was done with CI mass spectrometer Airsense 500 from

MS4 (Rockenberg). Subsequent to the TPO run, a HTPR experiment was performed to determine the $^{18}\text{O}_2$ amount transferred to the catalyst. This was done by monitoring H_2^{16}O and H_2^{18}O . For HTPR, the sample was quenched to 200°C immediately after the TPO experiment by stopping the reactor heating and $^{18}\text{O}_2$ dosage (below 500°C). Then, the reactor was heated up (heating rate: 20 K/min) to 1000°C in a gas flow of 500 ml/min composed of $10\text{ vol.}\%$ H_2 and $90\text{ vol.}\%$ N_2 .

2.5 X-ray diffraction

X-ray diffraction (XRD) was used to check the structure of a crystalline solid. This technique is based on the diffraction of X-rays by crystalline layers according to the Bragg equation [20].

The diffractograms were recorded on a D8 Advance diffractometer from Bruker (Karlsruhe) with $\text{Co-K}\alpha$ -radiation ($35\text{ kV}/45\text{ mA}$) and Goebel mirror in $2-\Theta$ mode from 10° to 80° with a step width of 0.0164° and an angle speed of 0.05 s per step. A phase analysis of the diffractograms was done with TOPAS software (Bruker-AXS) by an implemented standard fitting procedure corresponding to the Rietveld refinement [29]. The Co anode was chosen due to fluorescence of the iron oxide samples upon exposure to a standard $\text{Cu-K}\alpha$ radiation. However, the use of the Goebel mirror broadened the reflexes, which prevented accurate discrimination between the $\gamma\text{-Fe}_2\text{O}_3$ and Fe_3O_4 phase in the phase analysis. Therefore, this differentiation was made on the basis of the HTPR experiments.

2.6 Techniques for gas phase analysis

2.6.1 Infrared spectroscopy

Infrared (IR) spectroscopy is used to detect gaseous molecules, which possess a static or dynamic dipole moment under in-situ conditions. In this study, non-dispersive infrared (NDIR) spectroscopy and Fourier transformed infrared (FTIR) spectroscopy were used. NDIR spectroscopy operates with one discrete IR wavelength and measures the volume fraction of the respective gaseous species according to the Lambert-Beer law. In contrast, FTIR works under a broad IR spectrum, which depends on the infrared source and is based on the principle of the Michelson interferometer. The interferogram is converted by Fourier transformation into the full absorption spectrum, thus enabling the detection of numerous species at

the same time. Table 2-3 gives an overview of the IR analysers used and also provides information about the measurement principle and operating range.

Table 2-3: Deployed IR analysers.

Manufacturer	Type	Principle	Gas	Range
Leybold-Heraeus	Binos	NDIR	CO CO ₂	0-600 ppm 1-15 vol. %
Leybold-Heraeus	Binos	NDIR	CO	0-1 vol. %
Leybold-Heraeus	Binos	NDIR	NH ₃	0-500 ppm
MKS	MultiGas 2030	FTIR	multiple	

2.6.2 Chemical ionisation mass spectrometry

For detection of non IR active gaseous species (i.e. ¹⁸O₂, ¹⁶O₂, H₂), chemical ionisation mass spectrometry was used. In accordance to a conventional mass spectrometer, the relative molecular mass is measured. But, in contrast, CIMS does not ionise the respective species by electron impact ionisation, the ionisation is done gently by primary gas ions, which suppresses fragmentation of the molecules. This is achieved by a charge transfer from pre-ionised primary gases (Xe⁺, Kr⁺ and Hg⁺) to the sample molecules [30]. By selecting the primary ion, a separation of molecules with the same mass/charge ratio is possible because the ionisation energy of the respective primary gases is in the same range as the ionising potentials of the species to be detected. For calibration of the isotopic species the ionisation potential of the respective molecules (e.g. ¹⁸O₂ vs. ¹⁶O₂) was assumed to be the same.

3 Mechanistic and kinetic studies of catalytic soot oxidation

This chapter outlines the understanding of the reaction mechanism of the catalytic soot oxidation on Fe₂O₃. The studies presented contribute to the rational design of an advanced Fe₂O₃ catalyst through the elucidation of the mechanism, kinetics and the possible relationship between catalyst structure and catalytic activity. Therefore, this chapter covers theoretical aspects, which provide possible reaction mechanisms and kinetic models of the catalytic soot oxidation. The experimental section involves studies, which analyse the effect of different reaction parameters on the kinetics of catalytic soot oxidation, measure the temperature distribution in the catalyst/soot mixture, and draw on isotopic examinations using ¹⁸O₂.

3.1 Theoretical background of the oxidation of soot

The theoretical reflections of this chapter are related to the mechanism of non-catalytic and catalytic soot oxidation. In the case of catalytic soot oxidation, a kinetic expression is derived, allowing the description of the reaction rate for CO_x formation using a global rate law. This rate expression is the basis for the kinetic model described in the present thesis.

3.1.1 Non-catalytic soot oxidation

The gasification of carbon includes two general steps [31]: The first step is oxygen transfer from the gas phase to the solid under formation of surface complexes. The second step is the loss of a surface carbon atom due to decomposition of these complexes. Several authors have reviewed possible reaction steps for non-catalytic soot oxidation [32,33] and a rough scheme of such a mechanism can be summarised as follows [23]:

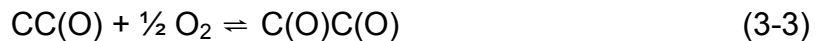
The first step is the reaction of a free and reactive carbon site (C_f). This free and reactive carbon site has a neighbouring non-reactive carbon site (C) and is oxidised to the surface complex CC(O).



This CC(O) complex is present in the form of an ether or carbonyl species and desorbs only if the bond to the neighbouring C atoms is broken.



A further reaction with O₂ oxidises the neighbouring C atom and results in an activation of the CC(O) complex:



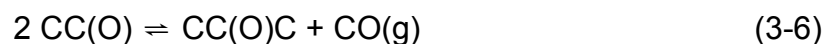
This oxygen rich C(O)C(O) complex is able to release CO₂ thermally:



Moreover, the C(O)C(O) complex may also be considered together with neighbouring surface C atoms in form of (OC)CC(O) or 2 C(CO). Such compounds are thermally instable and break under the formation of CO(g):



These surface complexes may form stable species on CO(g) release:



In addition, the soot does not only consist of carbon atoms and oxygen surface complexes. In fact, hydrocarbons (HC) and molecular O₂ and H₂O are also present.

3.1.2 Catalytic soot oxidation

The presence of a catalyst decreases the activation energy for soot oxidation by offering alternative reaction pathways. This results in a lower ignition temperature for the reaction. The role of the catalyst is to act as oxygen transmitter [23]. In the literature three major mechanism are reported [23,34,35]: (1) In the Mars-van-Krevelen mechanism surface O atoms react at the catalyst/soot interface and are replaced by bulk O atoms. Simultaneously, O₂ molecules from gas phase adsorb dissociatively on the catalyst and are incorporated in the surface layer. (2) The spill-over mechanism implies dissociative adsorption of molecular oxygen on the catalyst surface and is followed by a transfer of molecular oxygen to the soot, at which the O₂ molecule dissociates. (3) The redox mechanism reveals oxygen transfer from the oxidic catalyst to the soot under local reduction of the catalyst. The catalyst is re-oxidised by gas phase oxygen. Additionally, Gross et al. describe a mechanism on K/CeO₂ involving the formation of superoxides [36]. The kind of mechanism is strongly depending on the catalyst. Mul [34] reported a Mars-van-Krevelen mechanism for Co₃O₄ and Fe₂O₃ catalysts, a spill-over mechanism for Cr₂O₃ and a redox mechanism for MoO₃, V₂O₅ and K₂MoO₄. A further classification of catalysts and their corresponding mechanism can be given according to their mobility, i.e.

mobile and non-mobile catalysts. Mobile catalysts comprise alkaline, earth alkaline and several transition metals with low melting points [23,33,37]. Such catalysts are able to migrate on the surface of the soot, thus being able to consistently build up new contact points. Non-mobile catalysts comprise temperature resistant oxidic materials like CeO_2 , ZrO_2 and Fe_2O_3 [28,37,38] implying that contact between catalyst and soot is crucial. The effect of contact is demonstrated by van Setten and Neeft [16,39], who show a drastic decrease in catalytic activity for so called loose contact between catalyst and soot. There is also an intimate mixing of both solids which leads to so called tight contact mode resulting in an increase of catalytic activity.

In addition to the Mars-van-Krevelen mechanism for soot oxidation on Fe_2O_3 [34] already described, Reichert and Zhang describe a “push-pull” redox mechanism [18,40] which indicates only surface and subsurface layers of the iron oxides participate in oxygen transfer. A kinetic description of such a mechanism is presented in the following chapter.

3.1.3 Kinetics of the soot oxidation on Fe_2O_3 catalysts

The setting-up of a preferably detailed kinetic expression, which is able to cover variable reaction conditions for catalytic soot oxidation, is rather difficult. The high heterogeneity of the soot surface, the variety of surface compounds and the change of the soot morphology during the reaction results in a complex network of elementary reactions. In the literature mainly global expressions are found [36,41-44]. Specifically, Hurt [45] reviewed a number of different kinetic expressions and gives a reliable description of the reaction kinetics using a power-law over a wide range of oxygen partial pressure. This is applicable when the breadth of the activation energy distribution for adsorption and/or desorption is large due to surface heterogeneity [45]. In this thesis, the basis for a kinetic expression is taken from a global approach for catalytic soot oxidation on Fe_2O_3 presented by Reichert et al. [18]. The rate equation (Eq. (3-7) to (3-12)) depends on the number of active carbon sites and the gas phase concentration of oxygen and represents the most detailed global approach which can be found yet.

$$r_{\text{CO}_2} = k_{\text{CO}_2} \cdot n(\text{C}_f) \cdot c(\text{O}_2)^n \quad (3-7)$$

Furthermore, formation of CO can be neglected, since the Fe_2O_3 catalyst used is reported to be highly active for CO oxidation [27]. This is also in accordance with our

own experimental findings (chapter 3.2.3.2). The rate constant k_{CO_2} is Arrhenius based and is expressed in dependency on the pre-exponential factor A_∞ , the activation energy E_A and the temperature.

$$k_{\text{CO}_2} = A_\infty \exp\left(\frac{-E_A}{RT}\right) \quad (3-8)$$

The number of active carbon sites $n(\text{C}_f)$ depends on the soot morphology, which changes with soot conversion and is dependent on surface concentration λ of C_f sites and development of surface area $S(X)$.

$$n(\text{C}_f) = \lambda \cdot S(X) \quad (3-9)$$

λ : Surface concentration of active sites [mol/m²]

The evolution of the surface area is expressed in accordance with the random pore model of Bhatia [46,47].

$$S = S_0 \cdot \sqrt{1 + f \cdot X} \quad (3-10)$$

X : Soot conversion []

S_0 : Initial BET surface area ($X=0$), $X \leq 1$ [m²/g]

f : Semi-empiric factor []

This approach is shown in Figure 3-1. Fitting of Eq. (3-10) on the normalised surface area at different conversion levels of self-made soot from C_3H_6 reveals the factor f being 60 [23].

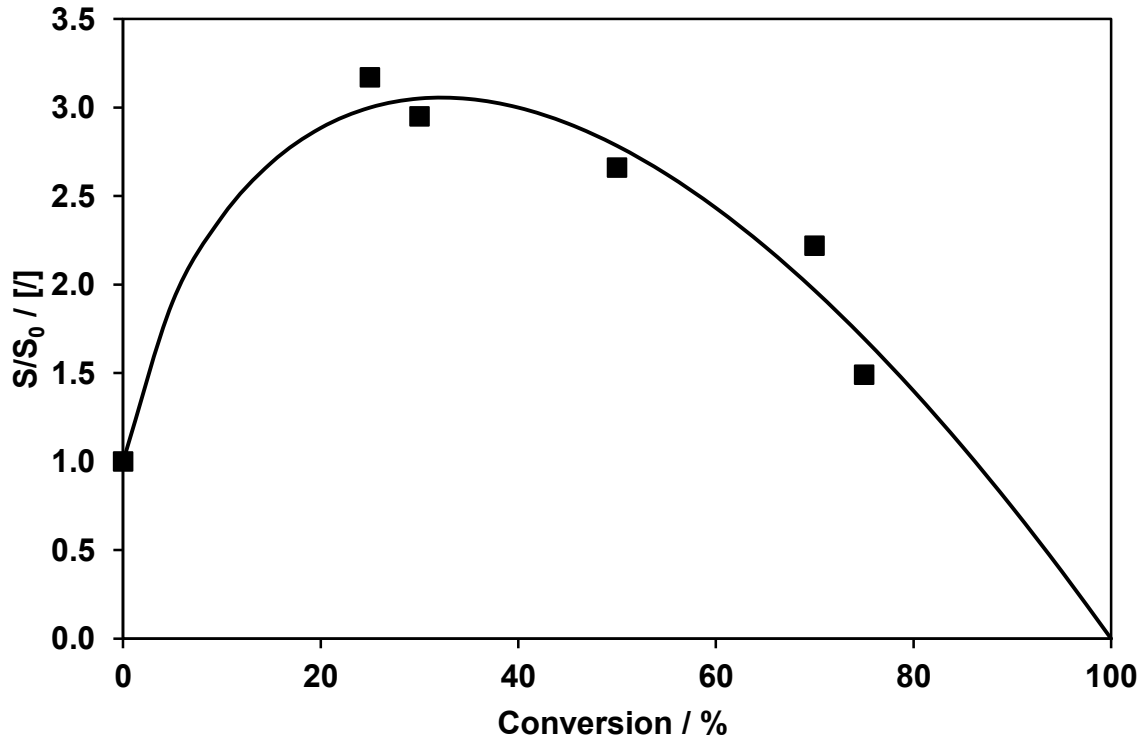


Figure 3-1: Evolution of S/S_0 dependent on soot conversion for home-made C_3H_6 soot; experimental data (■) are compared with the random pore model from Eq (3-10). $R^2=0.995$.

The absolute surface area $S(X)$ is simply calculated on the basis of the expression for the evolution of surface area and the mass of soot $m(X)$ remaining in oxidation:

$$S(X) = S \cdot m(X) = S \cdot m_0 \cdot (1 - X) = S_0 \cdot \sqrt{1 + f \cdot X} \cdot m_0 \cdot (1 - X) \quad (3-11)$$

The surface concentration of C_f sites is estimated on the basis of TPD studies by comparing the amount of CO_x released to the mass of soot, and then coupling it with the BET surface area [48]. In doing so, Reichert determined λ to be $8.7 \cdot 10^{-6}$ mol/m² which is very close to the literature data [23].

Lastly, a kinetic expression for the catalytic soot oxidation is set-up by coupling the presented equations. An important pre-condition for this expression is that BET development is the same for catalytic and non-catalytic soot oxidation.

$$r_{CO_2}(T, X) = A_\infty \cdot \exp\left(\frac{-E_A}{RT}\right) \cdot m_0 \cdot (1 - X(T)) \cdot \lambda \cdot S_0 \cdot \sqrt{1 + f \cdot X} \cdot c(O_2)^n \quad (3-12)$$

A_∞	: Pre-exponential factor	[m ³ /(mol·s)]
E_A	: Activation energy	[J/mol]
λ	: Surface concentration of active sites	[mol/m ²]
$m(X)$: Mass after soot conversion X	[g]

$c(\text{O}_2)$: Oxygen concentration	[mol/m ³]
n_{O_2}	: Apparent reaction order of O ₂	[/]
X	: Soot conversion	[/]
S_0	: Initial BET surface area (X=0), $X \leq 1$	[m ² /g]
f	: Semi-empiric factor	[/]

3.2 Experimental results from the mechanistic studies

The experimental work from the mechanistic and kinetic studies comprises the variation of reaction conditions, isotopic studies with ¹⁸O₂ and temperature measurements in a packed bed with an infrared (IR) camera. The variation of reaction conditions considers (1) contact mode, (2) type of soot, (3) catalyst:soot ratio, (4) composition of the gas feed (i.e. O₂, CO, CO₂ and H₂O) and (5) variation of the heating rate. To assure clear and reproducible results, these examinations were based on a model catalyst represented by a well-defined α -Fe₂O₃ catalyst; for its preparation and characterisation see chapter 5.2.2.1. The figures presented exclusively display CO₂ profiles, since formation of CO was not detected due to the high oxidation activity of the Fe₂O₃ catalyst [27].

3.2.1 Variation of the reaction conditions

3.2.1.1 Variation of the type of soot

To study the effect of the type of soot upon catalytic soot oxidation, four different samples were tested in a tight contact mixture with bulk α -Fe₂O₃ (see also chapter 3.2.1.2). Three of these samples are commercially sourced: (a) Spezial Schwarz 6 (Degussa), (b) PrintexU (Evonik) and (c) PrintexL (Evonik). The fourth sample was a soot from C₃H₆ which was produced in a diffusion burner by a propen/oxygen flame with a production rate of 3 mg/min. A description of the manufacturing process and the set-up of the bench is given in literature [49,50]. Former physical-chemical studies on this soot [23] revealed a mean diameter of the primary particles of 50 nm, a BET surface area of 91 m²/g and a low hydrogen content (0.5 wt.%) which agrees with our own studies (Table 3-1 and Table 3-2). The CO₂ traces upon catalytic TPO of these four types of soot exhibit clear differences (Figure 3-2) thus leading to the activity sequence Spezial Schwarz 6>PrintexU>C₃H₆ soot>PrintexL. The catalytic oxidation of the Spezial Schwarz 6 sample was initiated at 330°C and had a maximum CO₂ volume fraction at 366°C. This was the lowest value of the

temperature of maximum $y(\text{CO}_2)$, i.e. $T_{\text{CO}_2, \text{max}}$, among all the soot materials. The peak CO_2 volume fraction was 3.3 vol.%, while formation of CO_2 was detectable up to 440°C , suggesting that this is the broadest temperature range among all the samples. The CO_2 traces of PrintexU, C_3H_6 soot and PrintexL possess similar profiles with peak CO_2 volume fraction between 7.4 vol.% and 8.9 vol.%. $T_{\text{CO}_2, \text{max}}$ appeared at 380°C , 408°C and 424°C , respectively. Additionally, the elementary analysis performed on a vario MACRO cube (Elementar Analysensysteme, Hanau) of the soot materials is given in Table 3-1. This shows a correlation between mass fraction of carbon and oxygen with the sequence presented above. The Spezial Schwarz 6 soot offers the lowest proportion of carbon (89.5 wt.%) and the highest amount of oxygen (9.0 wt.%), whereas PrintexL features the highest carbon fraction (99.2 wt.%) and no detectable oxygen content. In addition, the same trend is obvious by comparing the respective BET surface areas, the amount of adsorbed species, derived from TG in N_2 (see Appendix F) and the heating value (Table 3-2).

In the following studies, the soot from C_3H_6 was taken as standard material due to the possibility of direct filter loading at the burner in the later development process. Results derived from powder experiments can be up-scaled to real filter systems without changing the characteristics of the soot.

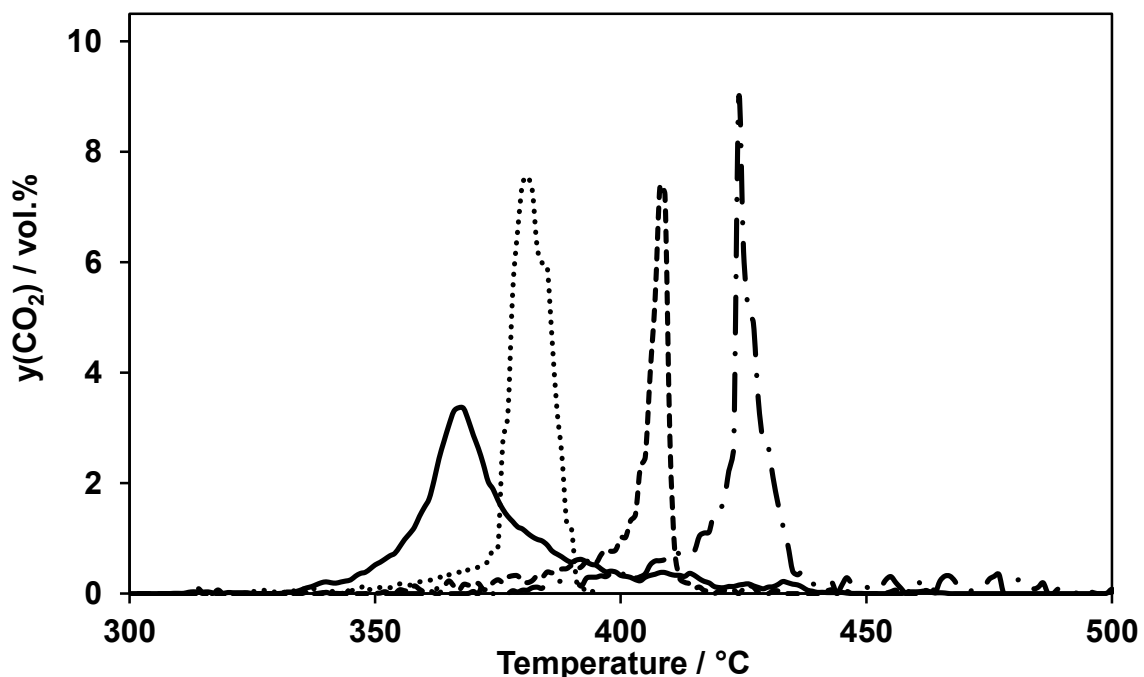


Figure 3-2: CO_2 profile of catalytic soot oxidation on $\alpha\text{-Fe}_2\text{O}_3$ using different types of soot. Spezial Schwarz 6 (—), PrintexU (···), soot from C_3H_6 (- -) and PrintexL (-·-·). Conditions: $F=500$ ml/min (STP), $y(\text{O}_2)=10$ vol.%, N_2 balance, $\beta=3.3$ K/min, catalyst:soot ratio=10 mmol:5 mmol, tight contact mode.

Table 3-1: Elementary composition of the four different types of soot ^{*)}.

Sample	Carbon (wt.%)	Hydrogen (wt.%)	Nitrogen (wt.%)	Oxygen (wt.%)
Spezial Schwarz 6	89.5	0.4	0.6	9.0
PrintexU	96.7	0.7	0.3	2.0
Soot from C ₃ H ₆	97.5	0.6	0.2	1.5
PrintexL	99.2	0.1	0.3	0

^{*)} Determined by high temperature combustion and sequentially analysis of the combustion gases on a vario MACRO cube (Elementar Analysensysteme, Hanau).

Table 3-2: Specific surface areas, amount of adsorbed species and heating value of the four different types of soot.

Sample	S _{BET} (m ² /g)	Adsorbed species (wt.%) ^{*)}	Heating value ^{**)} [kJ/kg]
Spezial Schwarz 6	300	22	29857
PrintexU	152	9.8	33365
Soot from C ₃ H ₆	92	4	33348
PrintexL	95	4.3	33474

^{*)} The corresponding TG profiles are depicted in the appendix (Figure F-1 to Figure F-4).

^{**)} Determined by combustion calorimetry on a C5000 (IKA, Staufen).

3.2.1.2 Variation of the contact mode

The effect of the contact mode is depicted in Figure 3-3, which shows explicit differences in the CO₂ profile on TPO. CO₂ formation for the experiment using a tight contact Fe₂O₃/soot mixture (for preparation procedure see chapter 2.4.1) exhibits a sharp CO₂ trace with a maximum volume fraction of 7.5 vol.% CO₂ at 408°C. The TPO made in the loose contact mode shows CO₂ production between 400°C and 650°C with a broad shoulder at 500°C and a weak peak volume fraction of 0.6 vol.% at 590°C. Additionally, the CO₂ signal of non-catalytic soot oxidation is illustrated in Figure 3-3 suggesting correlation with the high-temperature traces of the experiment established with Fe₂O₃ in loose contact mode. To avoid exothermal effects due to heat production, the soot was diluted with quartz wool for the run in absence of iron oxide.

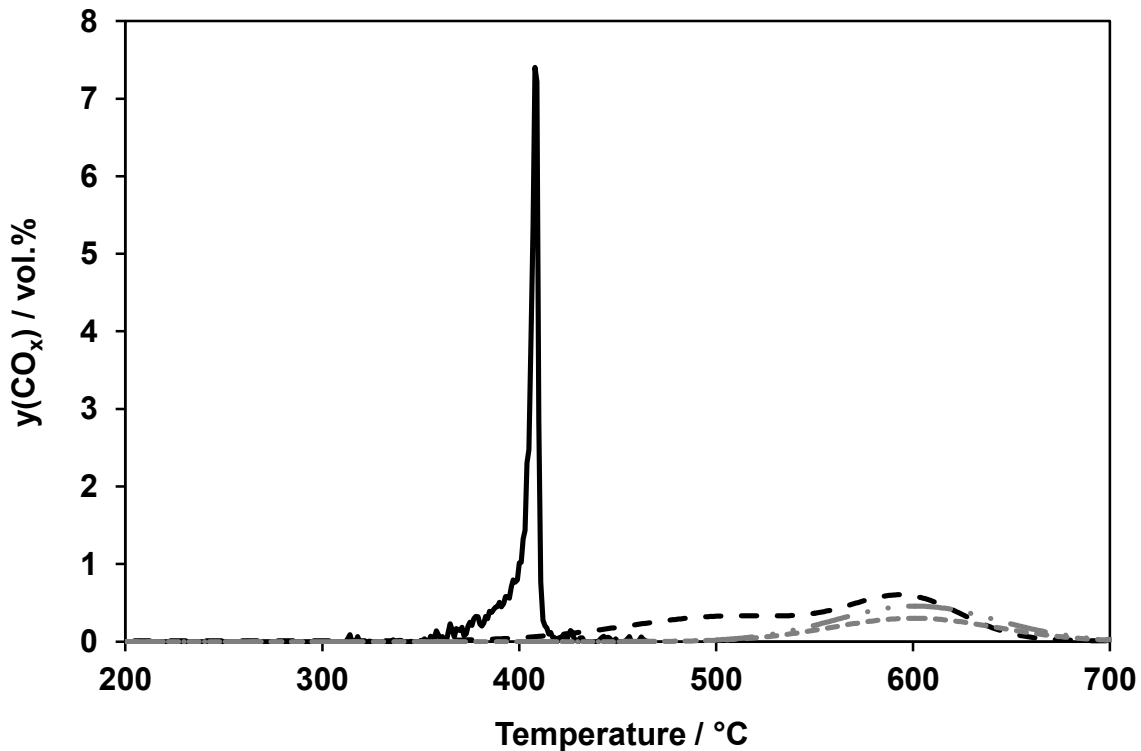


Figure 3-3: CO₂ profile of tight contact (—) and loose contact (--) mode in catalytic soot oxidation on α -Fe₂O₃. Additionally, CO₂ (-·-·-) and CO (···) profiles of non-catalytic soot oxidation are depicted. Conditions: F=500 ml/min (STP), y(O₂)=10 vol.%, N₂ balance, β =3.3 K/min, catalyst:soot ratio=10 mmol:5 mmol.

3.2.1.3 Variation of the catalyst:soot ratio

The following series of experiments shows the effect of different catalyst soot ratios in tight contact mode. The studies performed comprise TPO runs with an amount of Fe₂O₃ ranging from 20 mmol to 0.375 mmol. The initial amount of soot was kept at 5 mmol. The results of the TPO investigations using a molar catalyst amount of 1.25, 2.5, 5, 10 and 20 mmol are depicted in Figure 3-4. This shows that the proportion of Fe₂O₃ has a significant impact on the CO₂ profile. The experiment using maximum amount of Fe₂O₃ (20 mmol) reveals a broad CO₂ trace and a $T_{CO_2,max}$ at ca. 430°C. A reduction of the amount of catalyst leads to a sharp CO₂ profile and a decrease in $T_{CO_2,max}$. The TPO run with a quantity of 1.25 mmol catalyst shows the lowest temperature of the maximum CO₂ volume fraction being 375°C only. To check the influence of a further reduction of the amount of catalyst, TPO studies were performed using 0.625 and 0.375 mmol Fe₂O₃ (Figure 3-5). A comparison with the experiment using 1.25 mmol catalyst reveals an increase in $T_{CO_2,max}$ (395°C for 0.625 mmol and 400°C for 0.375 mmol vs. 375°C for 1.25 mmol) and a broadening of the CO₂ profile. Although, formation of CO could be neglected for catalyst quantities of

more than 1.25 mmol, the TPO studies using smaller amounts of Fe_2O_3 showed an increase in the CO volume fraction (Figure 3-6). The TPO using 1.25 mmol Fe_2O_3 gave a total quantity of 0.14 mmol CO, while a Fe_2O_3 proportion of 0.675 mmol produced 0.24 mmol CO. The experiment with 0.375 mmol catalyst yielded an overall amount of 1 mmol CO.

For a further examination of the effect of the catalyst:soot ratio, temperature measurements in the packed bed of selected experiments were made. A K type micro-thermocouple with a diameter of 0.2 mm (length $L=1$ m) was placed in the centre of the packed bed, i.e. the catalyst/soot mixture, monitoring the temperature development in the mixture during the soot oxidation. Figure 3-7 and Figure 3-8 show that an increase in the amount of catalyst results in a decrease in the temperature in the packed bed. The TPO using 2.5 mmol Fe_2O_3 reveals a difference between inlet and peak temperature of ca. 160 K, while the experiment with an amount of 10 mmol catalyst shows a temperature difference of ca. 60 K. The TPO with a quantity of 20 mmol features a temperature difference of 35 K only.

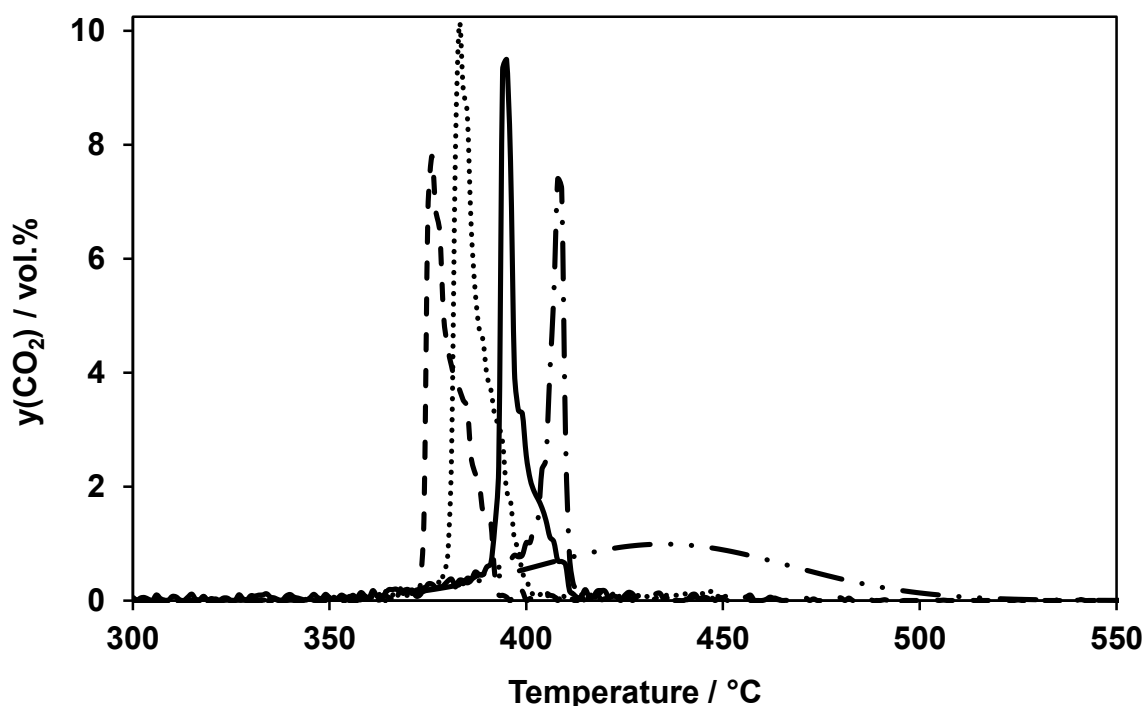


Figure 3-4: CO_2 profile of different molar catalyst:soot ratios in catalytic soot oxidation on $\alpha\text{-Fe}_2\text{O}_3$ in dependence of the inlet temperature. 1.25:5 (- -), 2.5:5 (···), 5:5 (—), 10:5 (—·—) and 20:5 (— · —). Conditions: $F=500$ ml/min (STP), $y(\text{O}_2)=10$ vol.%, N_2 balance, $\beta=3.3$ K/min, tight contact mode.

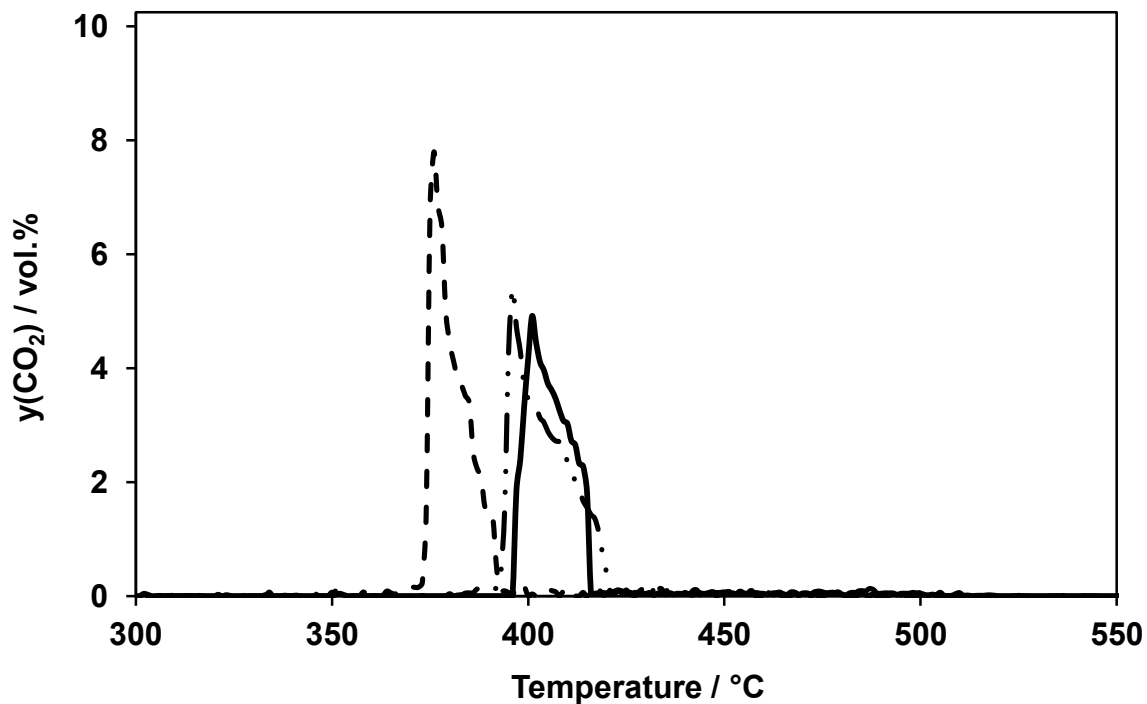


Figure 3-5: CO₂ profile of different molar catalyst:soot ratios in catalytic soot oxidation on α -Fe₂O₃. 1.25:5 (- -), 0.625:5 (- · - ·) and 0.375:5 (—). Conditions: F=500 ml/min (STP), $y(\text{O}_2)$ =10 vol.%, N₂ balance, β =3.3 K/min, tight contact mode.

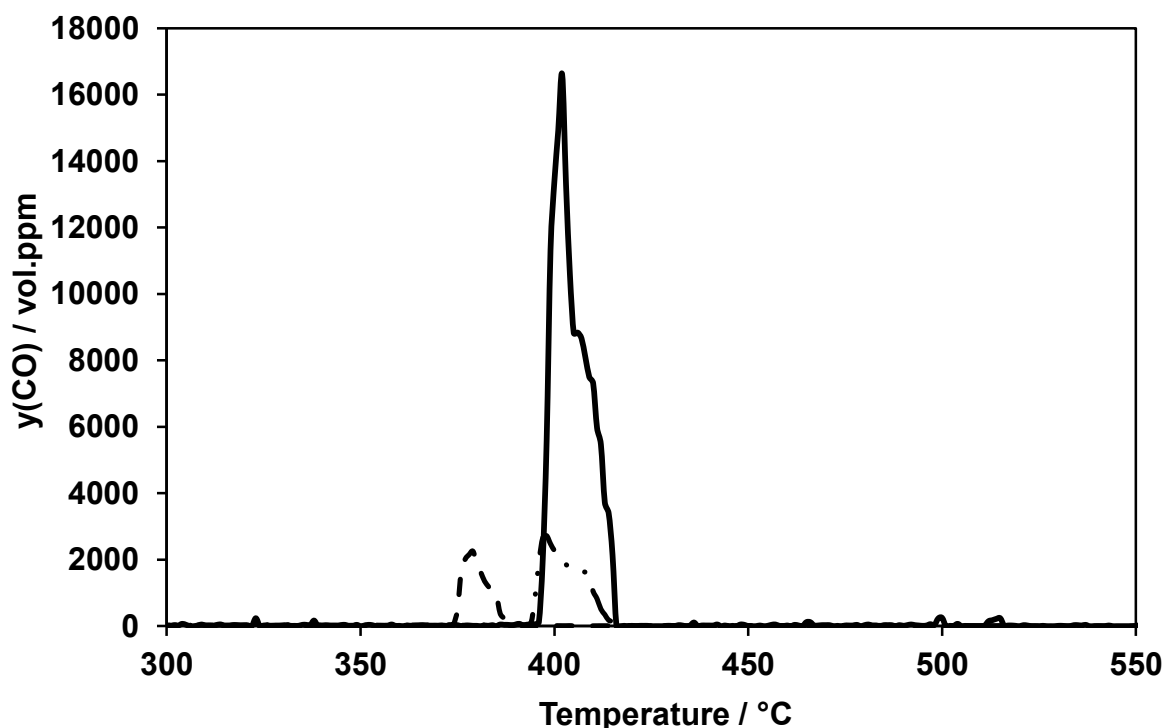


Figure 3-6: CO profile of different molar catalyst:soot ratios in catalytic soot oxidation on α -Fe₂O₃. 1.25:5 (- -), 0.625:5 (- · - ·) and 0.375:5 (—). Conditions: F=500 ml/min (STP), $y(\text{O}_2)$ =10 vol.%, N₂ balance, β =3.3 K/min, tight contact mode.

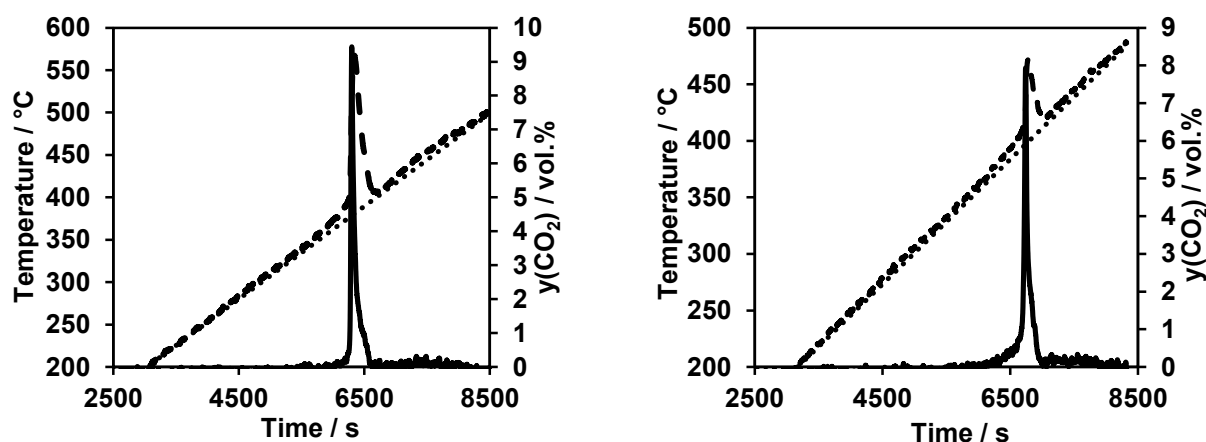


Figure 3-7: Temperature profile in the centre of the packed bed (- -) and at the inlet of the reactor (···) upon a TPO using a Fe_2O_3 /soot mixture. (—) represents $y(\text{CO}_2)$. Used ratios: Left: 2.5 mmol:5 mmol. Right: 10 mmol:5 mmol. Conditions: $F=500$ ml/min (STP), $y(\text{O}_2)=10$ vol.%, N_2 balance, $\beta=3.3$ K/min, tight contact mixture.

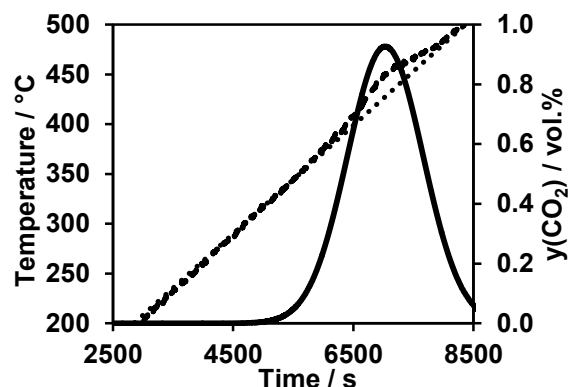


Figure 3-8: Temperature profile in the centre of the packed bed (- -) and at the inlet of the reactor (···) upon a TPO using a Fe_2O_3 /soot mixture. (—) represents $y(\text{CO}_2)$ of an experiment using a ratio of 20 mmol: 5 mmol. Conditions: $F=500$ ml/min (STP), $y(\text{O}_2)=10$ vol.%, N_2 balance, $\beta=3.3$ K/min, tight contact mixture.

3.2.1.4 Variation of the heating rate

To extend the findings related to the impact of heat production on the CO_2 profile, as presented in section 3.2.1.3 (variation of the catalyst:soot ratio), the heating ramp was varied in TPO using rates of 1.8, 3.3, 5 and 10 K/min. Figure 3-9 illustrates a broad CO_2 profile for a heating rate of 1.8 K/min. The CO_2 evolution with a rate of 1.8 K/min and higher shows sharp profiles and no differences in $T_{\text{CO}_2, \text{max}}$ (all 408°C). Again, temperature measurements in the packed bed were taken (Figure 3-10) indicating a temperature increase of ca. 25 K for a heating rate of 1.8 K/min compared to $\Delta T=60$ K for the TPO using a temperature rise of 3.3 K/min. In addition, the area below all the curves in Figure 3-9 corresponds to an amount of 5 mmol CO_2 formed.

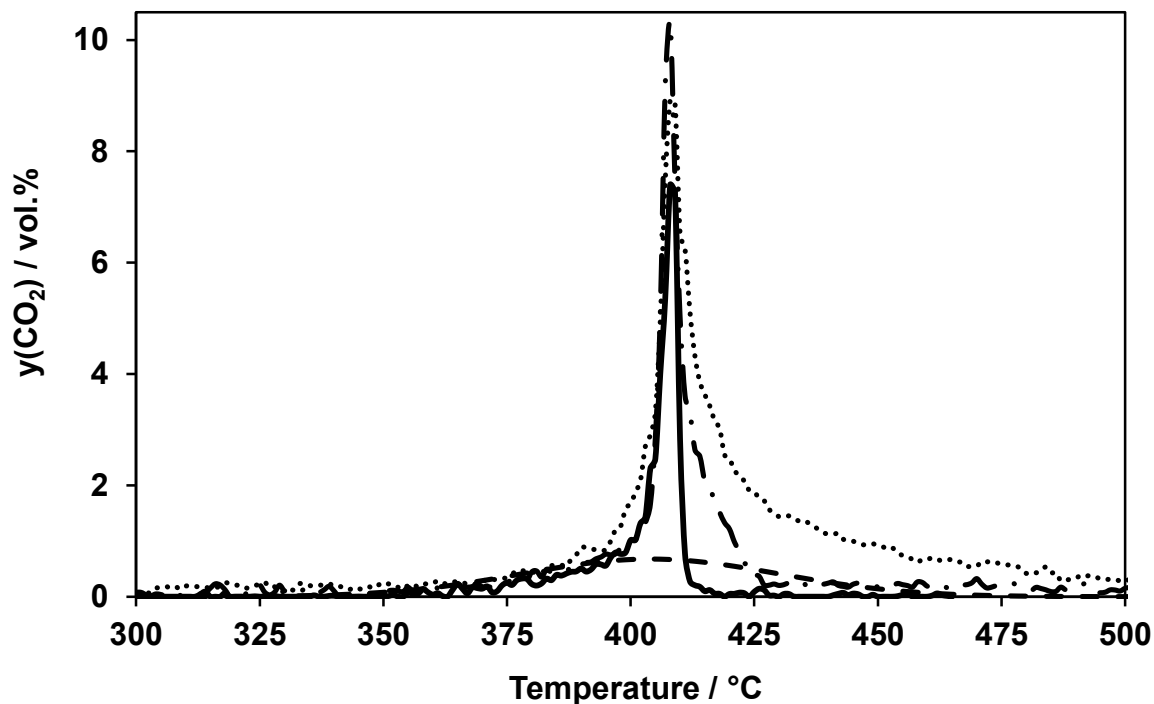


Figure 3-9: CO₂ profiles for different heating rates in catalytic soot oxidation on α -Fe₂O₃. 1.8 K/min (---), 3.3 K/min (—), 5 K/min (— — —) and 10 K/min (···). Conditions: F=500 ml/min (STP), $y(\text{O}_2)$ =10 vol.%, N₂ balance, catalyst:soot ratio=10 mmol:5 mmol, tight contact mixture.

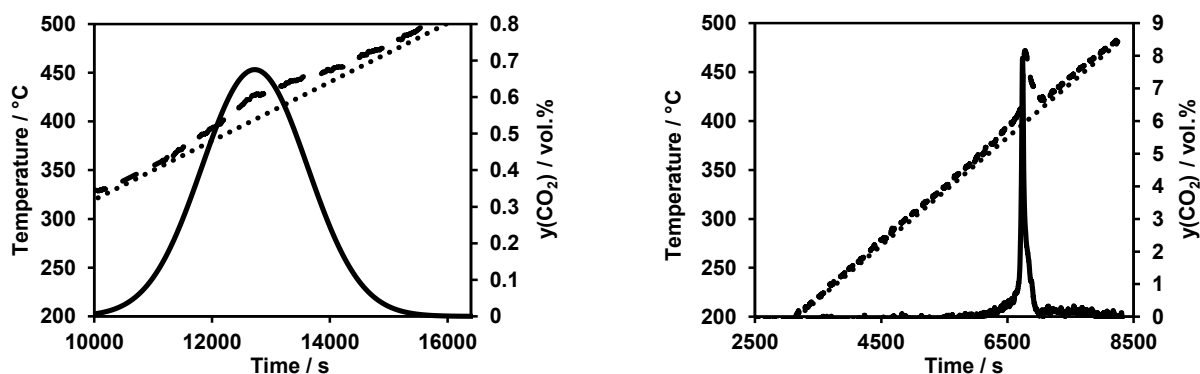


Figure 3-10: Temperature profile in the centre of the packed bed (---) and at the inlet of the reactor (···) upon a TPO using a Fe₂O₃/soot mixture. (—) represents the respective CO₂ profile. Left: 1.8 K/min. Right: 10 K/min. Conditions: F=500 ml/min (STP), $y(\text{O}_2)$ =10 vol.%, N₂ balance, catalyst:soot ratio=10 mmol:5 mmol, tight contact mixture.

3.2.2 Temperature distribution in the catalyst/soot mixture

To obtain further insights into the exothermic processes during the catalytic soot oxidation, measurements with an IR camera were made. These measurements analysed the heat distribution at the surface of the packed bed of the catalyst/soot mixture. This approach required the engineering of a special reactor due to the spectral range (i.e. 3-5 μm wavelength) of the Pyroview 380M IR camera used (DIAS, Dresden). The stainless steel reactor designed has a sapphire window which offers IR transmission in the appropriate spectral range. This is illustrated in Figure

3-11. Figure 3-12 depicts 6 images taken by the IR camera during a TPO with soot and $\alpha\text{-Fe}_2\text{O}_3$ catalyst. A typical mixture of 10:5 mmol in tight contact mode was used. The pictures correspond to the CO_2 profile shown in Figure 3-13 revealing a peak temperature of 510°C at an inlet temperature of 430°C according to the maximum CO_2 volume fraction (3.7 vol.%). Moreover, the heat evolution suggests initiation of the reaction in the centre of the packed bed and a displacement in direction of the reactor outlet.

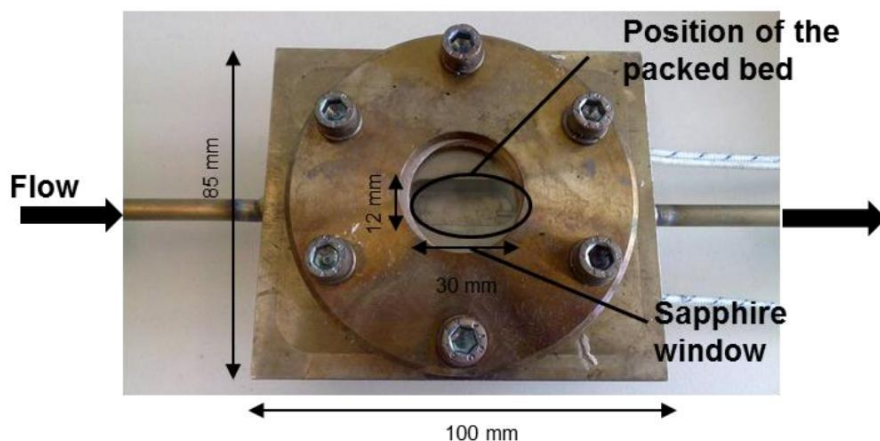


Figure 3-11: Reactor design for IR camera measurements.

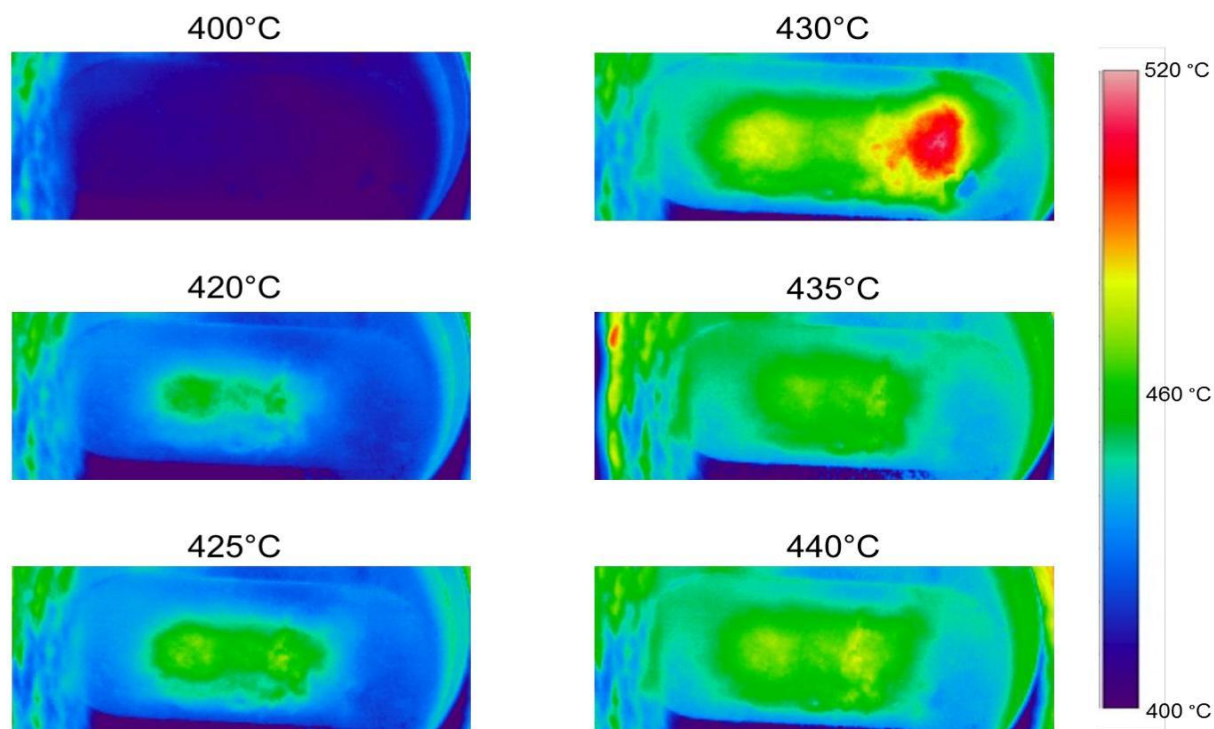


Figure 3-12: Surface temperature distribution of the packed bed upon catalytic soot oxidation at different reactor inlet temperatures. Conditions: $F=500$ ml/min (STP), $y(\text{O}_2)=10$ vol.%, N_2 balance, $\beta=8.6$ K/min, catalyst:soot ratio=10 mmol:5 mmol, tight contact mixture.

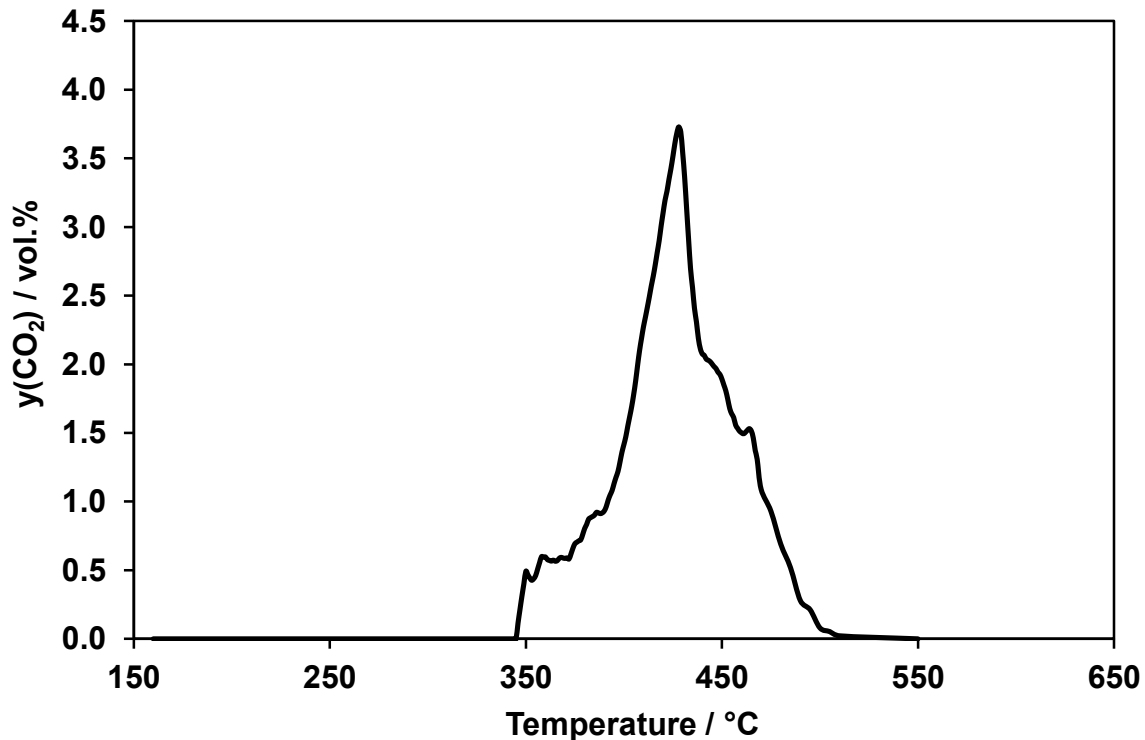


Figure 3-13: CO₂ production in the TPO of the α -Fe₂O₃/soot mixture performed in the special IR reactor. Conditions: F=500 ml/min (STP), $y(\text{O}_2)$ =10 vol.%, N₂ balance, β =8.6 K/min, catalyst:soot ratio=10 mmol:5 mmol, tight contact mixture.

3.2.3 Variation of the composition of the gas feed

3.2.3.1 O₂ variation

The variation of the O₂ volume fraction of the gas feed is shown to have great impact on $T_{\text{CO}_2, \text{max}}$ and the peak volume fraction of CO₂ in the catalytic TPO of soot (Figure 3-14). An O₂ volume fraction of 20 vol.% corresponds to a $T_{\text{CO}_2, \text{max}}$ of 380°C and a maximum volume fraction of ca. 16 vol.%. A volume fraction of 1 % O₂ induces a strong broadening of the CO₂ trace, ranging from 400°C until complete soot conversion at 575°C, and a decrease in peak volume fraction to ca. 0.5 vol.% only. O₂ contents of 7.5 vol.% and 5 vol.% follow this trend; i.e. reduction of O₂ volume fraction increases $T_{\text{CO}_2, \text{max}}$ and decreases the maximum volume fraction of CO₂.

Since the results presented in Figure 3-7 exhibit strong heat production for high CO₂ volume fractions, the chosen reaction conditions (Figure 3-14) are expected to amplify the effect of O₂ variation. For this reason, moderate reaction conditions in respect to the heating rate were chosen for further examinations. These further examinations attempt to elucidate the reaction order of oxygen at a rate of 2 K/min (Figure 3-15). This change in the reaction conditions results in an increase of $T_{\text{CO}_2, \text{max}}$, while the maximum CO₂ volume fraction is between 0.75 and 0.8 vol.% for

all the experiments as compared to the studies using a heating rate of 3.3 K/min. These findings enable an analytical determination of the reaction order of oxygen. For this, the reaction rate presented in section 3.1.3 represents the basis for this analysis:

$$r_{\text{CO}_2}(T, X) = A_{\infty} \cdot \exp\left(\frac{-E_A}{RT}\right) \cdot m_0 \cdot (1 - X(T)) \cdot \lambda \cdot S_0 \cdot \sqrt{1 + f \cdot X} \cdot c(\text{O}_2)^n \quad (3-13)$$

At low temperatures the soot conversion X is very small making it possible to neglect X . This leads to the following expression:

$$r_{\text{CO}_2}(T, X) = \frac{dc(\text{CO}_2)}{dt} = K \cdot c(\text{O}_2)^n \quad (3-14)$$

With K being constant for $T = \text{const.}$

$$K = A_{\infty} \cdot \exp\left(\frac{-E_A}{RT}\right) \cdot m_0 \cdot S_0 \cdot \lambda \quad (3-15)$$

A double-logarithmic illustration of Eq. (3-14) allows us to determine the reaction order of oxygen by calculating the slope of the resulting curve:

$$\log\left(\frac{dc(\text{CO}_2)}{dt}\right) = \log(K) + n \cdot \log(c(\text{O}_2)) \quad (3-16)$$

Figure 3-16 depicts this approach at a temperature of 365°C which offers a compromise between measurable reaction rate and soot conversion ($X \sim 0$). The rate of CO_2 formation is derived from Figure 3-15. The reaction order of oxygen was calculated to be $n = 1.0$. A discussion of this approach is presented in section 3.3.3.

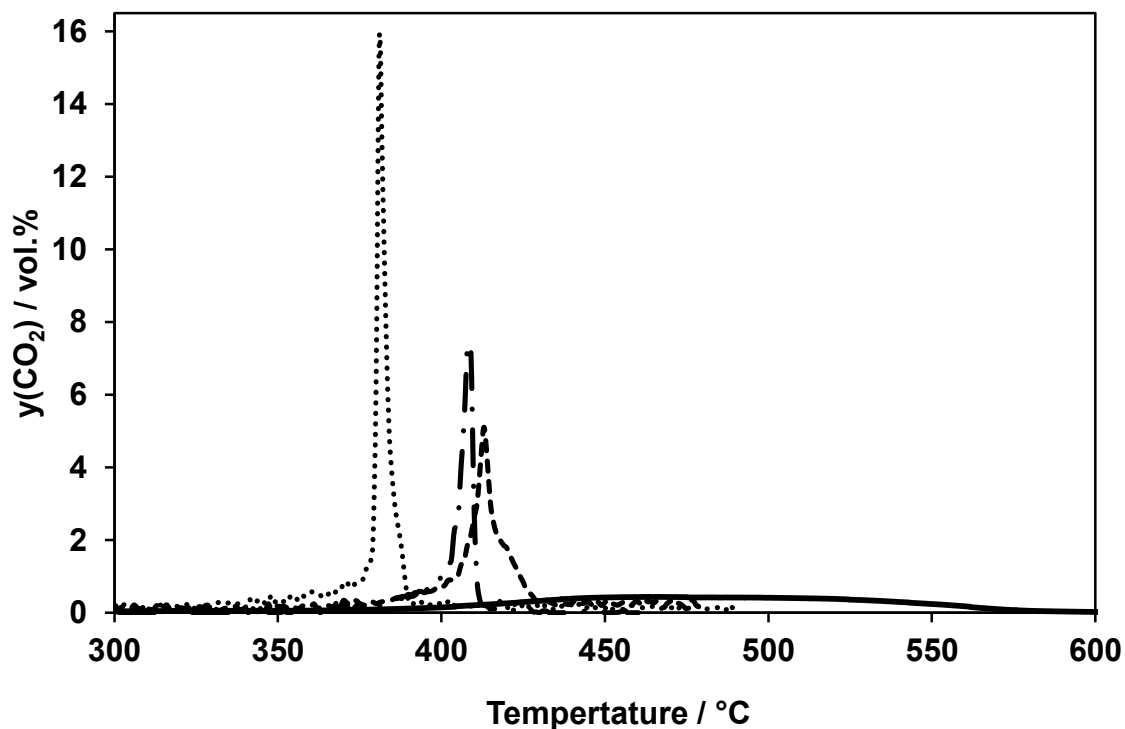


Figure 3-14: CO₂ profile of catalytic soot oxidation on α -Fe₂O₃ for different O₂ inlet volume fractions. 20 vol.% O₂ (···), 10 vol.% O₂ (— · —), 5 vol.% O₂ (---) and 1 vol.% O₂ (—). Conditions: F=500 ml/min (STP), N₂ balance, β =3.3 K/min, catalyst:soot ratio=10 mmol:5 mmol, tight contact mixture.

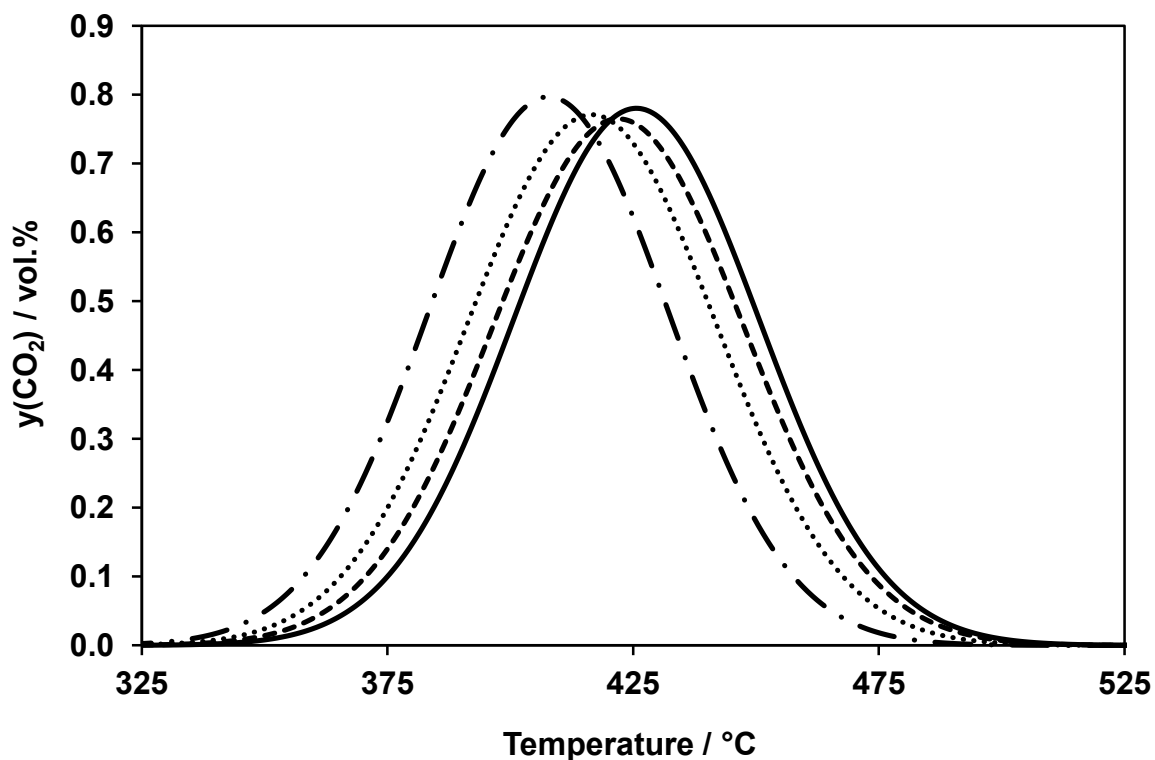


Figure 3-15: CO₂ profile of catalytic soot oxidation on α -Fe₂O₃ for different O₂ inlet volume fractions. 20 vol.% O₂ (— · —), 10 vol.% O₂ (···), 7.5 vol.% O₂ (---) and 5 vol.% O₂ (—). Conditions: F=500 ml/min (STP), N₂ balance, β =2 K/min, catalyst:soot ratio=10 mmol:5 mmol, tight contact mixture.

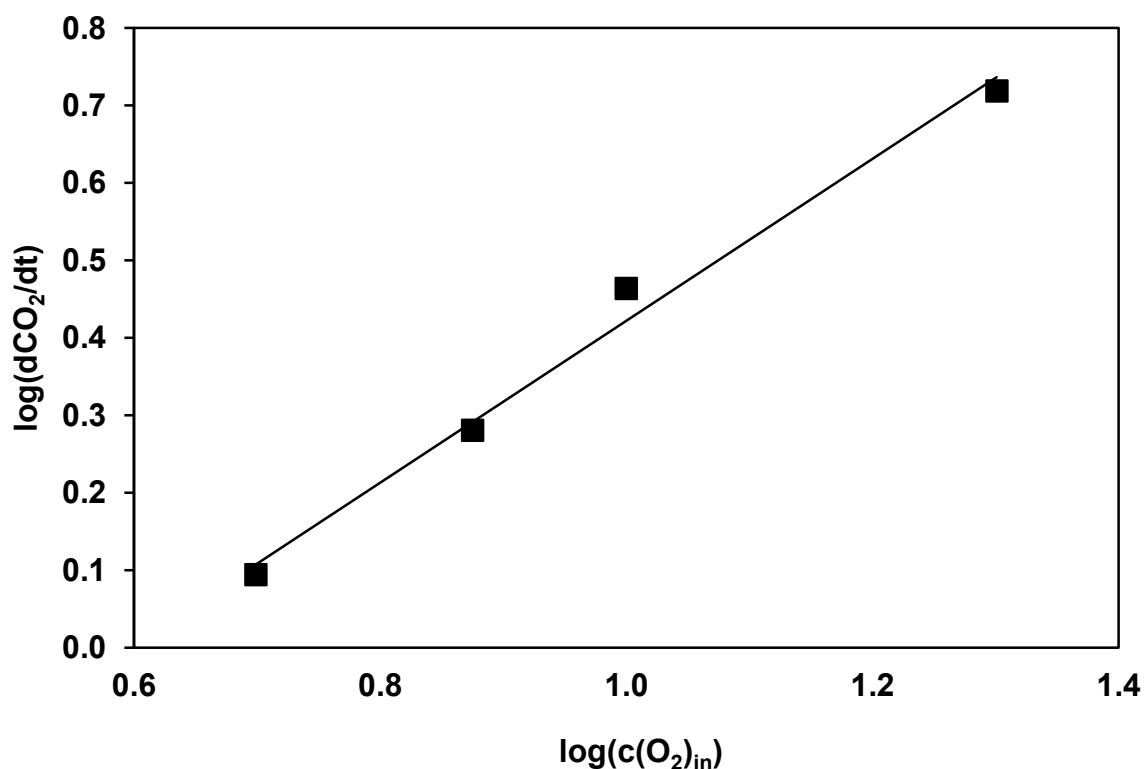


Figure 3-16: Double-logarithmic illustration of the time rate of change in CO_2 volume fraction versus the oxygen volume fraction of the gas feed. $T=365^\circ\text{C}$, $R^2=0.89$. Conditions: $F=500$ ml/min (STP), N_2 balance, $\beta=2$ K/min, catalyst:soot ratio=10 mmol:5 mmol, tight contact mixture.

3.2.3.2 CO variation

For the examination of the influence of CO proportion in the feed gas on catalytic soot oxidation, three different inlet CO volume fractions (1, 2 and 5 vol.%) were used. By comparing the results (Figure 3-17) with the TPO without dosage of carbon monoxide it is clear that raising CO inlet volume fraction causes a lowering of $T_{\text{CO}_2,\text{max}}$ in the sequence 0 % CO ($T_{\text{CO}_2,\text{max}}=408^\circ\text{C}$) \rightarrow 1 % CO ($T_{\text{CO}_2,\text{max}}=368^\circ\text{C}$) \rightarrow 2 % CO ($T_{\text{CO}_2,\text{max}}=335^\circ\text{C}$) \rightarrow 5 % CO ($T_{\text{CO}_2,\text{max}}=240^\circ\text{C}$). Moreover, the CO_2 volume fraction on the TPO using 5 vol.% CO shows a maximum CO_2 volume fraction of ca. 13 vol.% thus exceeding the O_2 inlet fraction of 10 vol.% and indicating temporary reduction of the Fe_2O_3 catalyst. In addition, the temperature profile in the packed bed (Figure 3-18) was measured by a micro-thermocouple ($d=0.2$ mm) located in the centre of the packed bed. This shows a peak temperature of 500°C at the highest CO_2 volume fraction (13 vol.%) which corresponds to an inlet temperature of 240°C . Complete soot conversion was observed for all the experiments.

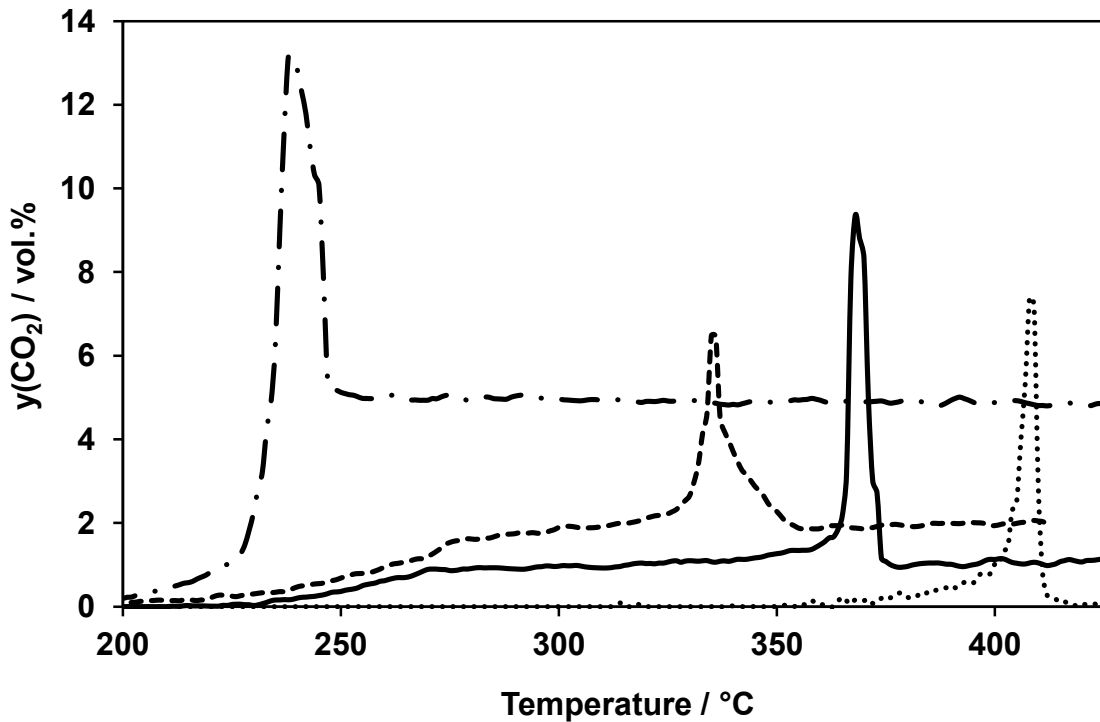


Figure 3-17: CO₂ profile of catalytic soot oxidation on α -Fe₂O₃ for different CO inlet volume fractions. 5 vol.% CO (— · —), 2 vol.% CO (---), 1 vol.% CO (—) and 0 vol.% CO (···). Conditions: $F=500$ ml/min (STP), $y(\text{O}_2)=10$ vol.%, N₂ balance, $\beta=3.3$ K/min, catalyst:soot ratio=10 mmol:5 mmol, tight contact mixture.

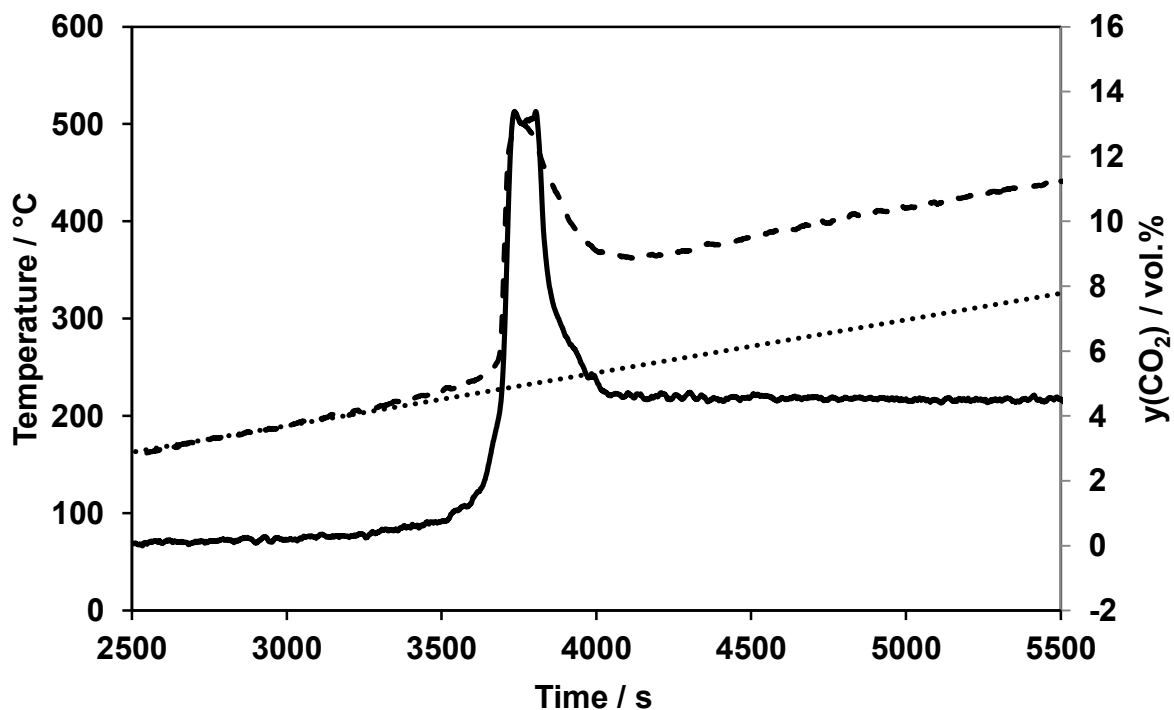


Figure 3-18: Temperature profile in the centre of the packed bed (---) and at the inlet of the reactor (···) upon catalytic soot oxidation on α -Fe₂O₃. (—) represents the respective CO₂ profile of the experiment using a CO inlet volume fraction of 5%. Conditions: $F=500$ ml/min (STP), $c(\text{O}_2)=10$ vol.%, N₂ balance, $\beta=3.3$ K/min, catalyst:soot ratio=10 mmol:5 mmol, tight contact mixture.

3.2.3.3 CO₂ variation

For the analysis of the influences of different CO₂ proportions in the gas matrix upon catalytic soot oxidation on α -Fe₂O₃, three volume fractions (1.5 vol.%, 4 vol.% and 10 vol.%) were adjusted. The results were then compared to a TPO without additional supply of CO₂. Figure 3-19 shows no significant impact of CO₂ variation on the soot conversion. $T_{\text{CO}_2, \text{max}}$ ranges from 403°C (1.5 vol.%) to 415°C (10 vol.%) while the reference experiment without carbon dioxide in the feed gas exhibits a $T_{\text{CO}_2, \text{max}}$ of 408°C. This seems to be a trend, but it is in the range of the reproducibility (section Appendix A) and therefore it is important not to over-interpret the results. Also the profile without additional CO₂ is in between these TPO profiles.

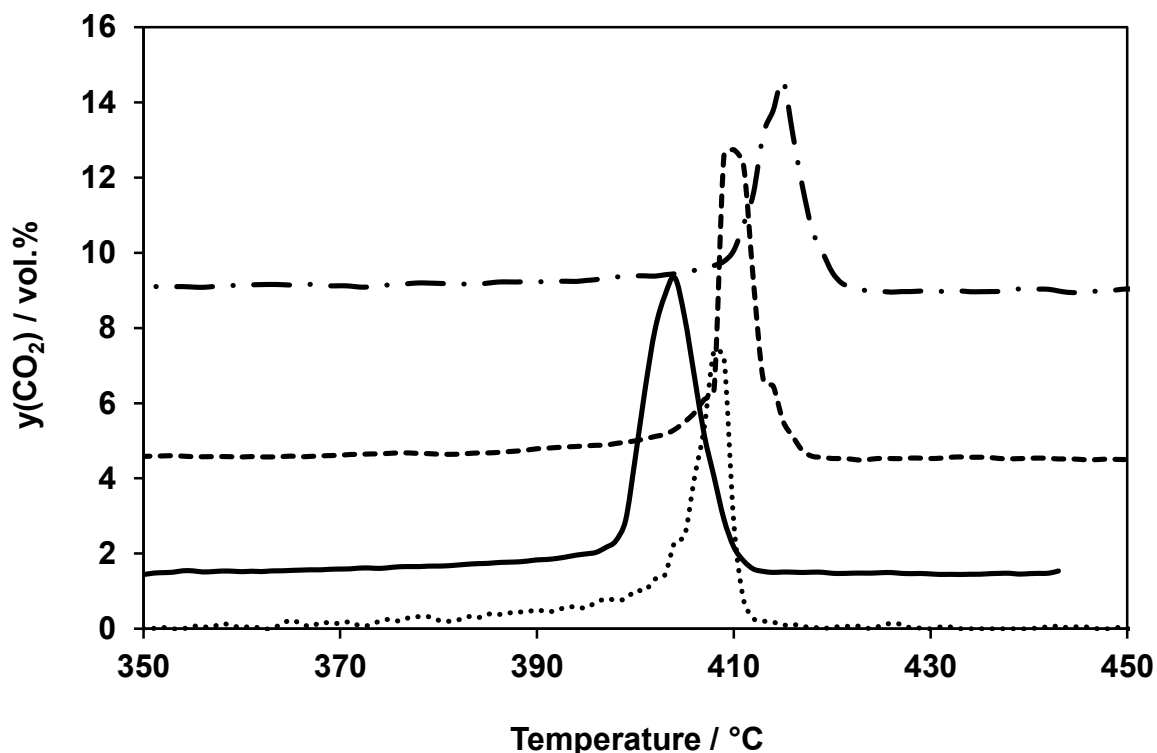


Figure 3-19: CO₂ profile of catalytic soot oxidation on α -Fe₂O₃ for different CO₂ inlet volume fractions. 1.5 vol.% CO₂ (—), 4 vol.% CO₂ (---), 10 vol.% CO₂ (— · —) and 0 vol.% CO₂ (···). Conditions: $F=500$ ml/min (STP), $y(\text{O}_2)=10$ vol.%, N₂ balance, $\beta=3.3$ K/min, catalyst:soot ratio=10 mmol:5 mmol, tight contact mixture.

3.2.3.4 H₂O variation

For inspection of the effect of water on catalytic soot oxidation, two different H₂O contents in the gas feed (2 vol.% and 8.5 vol.%) were examined (Figure 3-20). In comparison to the blank experiment excluding H₂O ($T_{\text{CO}_2, \text{max}}=408^\circ\text{C}$), water has a beneficial effect on the catalytic soot oxidation. This is shown by the shift of $T_{\text{CO}_2, \text{max}}$ being 384°C (8.5 % H₂O) and 385°C (2 % H₂O) as well as by the increasing CO₂ volume fraction, which is ca. 10 vol.% for both experiments using water supply in the

gas feed. Moreover, this enhancing effect is also observable in a TPO performed in the absence of the Fe_2O_3 catalyst (Figure 3-21). The temperatures of maximum CO and CO_2 volume fraction feature a shift from 570°C to 530°C when supplying 2 vol.% H_2O in the gas matrix indicating the positive implication of water on soot oxidation.

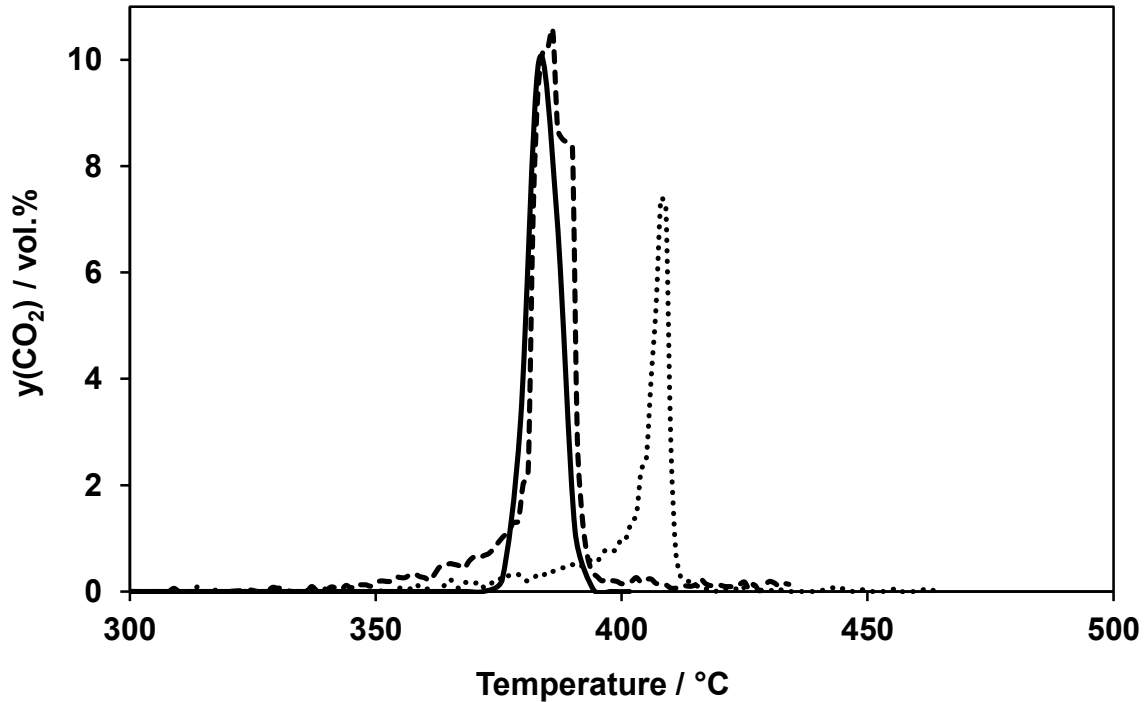


Figure 3-20: CO_2 profile of catalytic soot oxidation on $\alpha\text{-Fe}_2\text{O}_3$ for different H_2O inlet volume fractions. (—)=8.5 vol.% H_2O , (--) =2 vol.% H_2O , (···)=0 vol.% H_2O . Conditions: $F=500$ ml/min (STP), $y(\text{O}_2)=10$ vol.%, N_2 balance, $\beta=3.3$ K/min, catalyst:soot ratio=10 mmol:5 mmol, tight contact mixture.

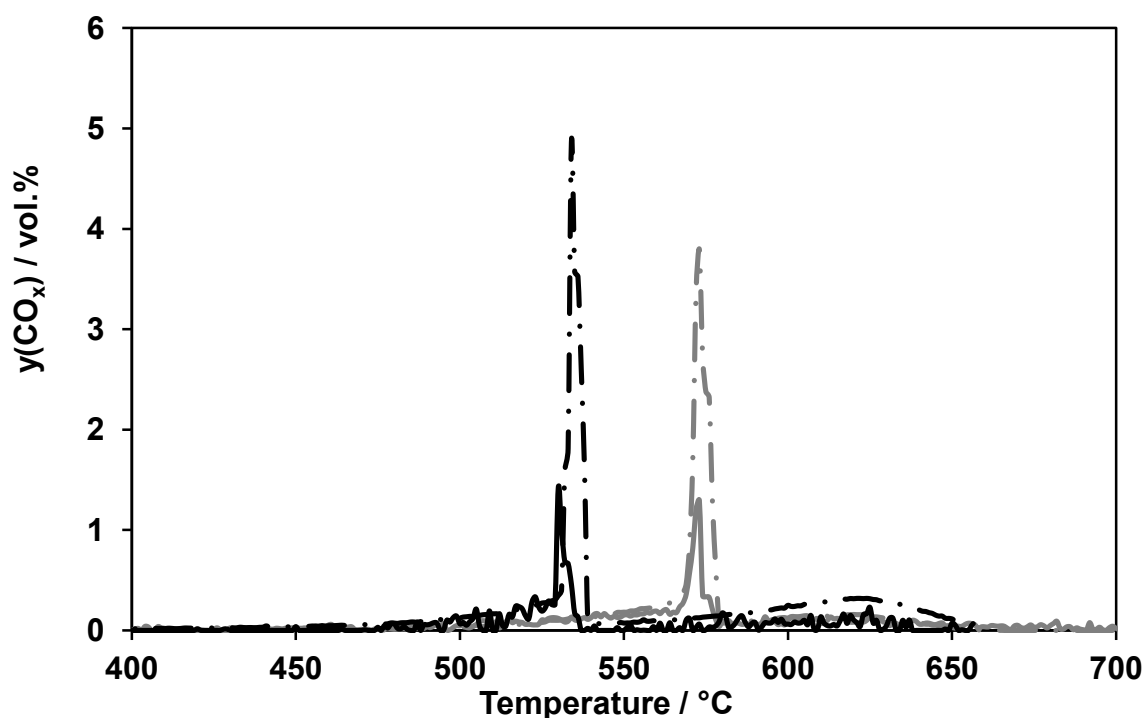


Figure 3-21: CO (— · —) and CO₂ (—) profiles of non-catalytic soot oxidation with 2 vol.% H₂O (— · —) and without (—) H₂O in the gas feed. Conditions: F=500 ml/min (STP), y(O₂)=10 vol.%, N₂ balance, β=3.3 K/min, 5 mmol C₃H₆ soot.

3.2.4 Temperature programmed reduction of α-Fe₂O₃ by soot

In the temperature programmed reduction of Fe₂O₃ by soot the contact between both solids as well as the transfer from bulk oxygen of Fe₂O₃ to soot has been investigated [23]. The experimental procedure requires the linear heating of the Fe₂O₃/soot mixture (3.3 K/min) under flowing N₂. Figure 3-22 show results from the experiment using a tight contact catalyst/soot mixture. The figures present two major peaks (650°C and 880°C) as well as a shoulder at 510°C. CO₂ formation starts above 200°C (see inlet), while CO production begins above 720°C, with maximum volume fraction at 870°C. The total amount of CO and CO₂ is ca. 4.9 mmol, indicating complete conversion (initial amount: 5 mmol). A diffractogram, recorded subsequently to the experiment (Figure 3-24), reveals wuestite (Fe_{1-x}O) to be the exclusive crystalline phase. In contrast, Figure 3-23 reveals CO₂ evolution upon the experiment using a loose contact Fe₂O₃/mixture. A first shoulder is detected at 500°C, whereas the CO₂ trace above 500°C exhibits increasing volume fraction and several shoulders up to 1000°C. CO formation starts at 840°C and continuously rises until the end of the experiment at 1000°C. From the CO and CO₂ evolution the overall conversion of soot is determined to be 2.3 mmol referring to a conversion level of ca.

46 %. The subsequently recorded XRD pattern (Figure 3-25) reveals magnetite (Fe_3O_4) as crystalline phase.

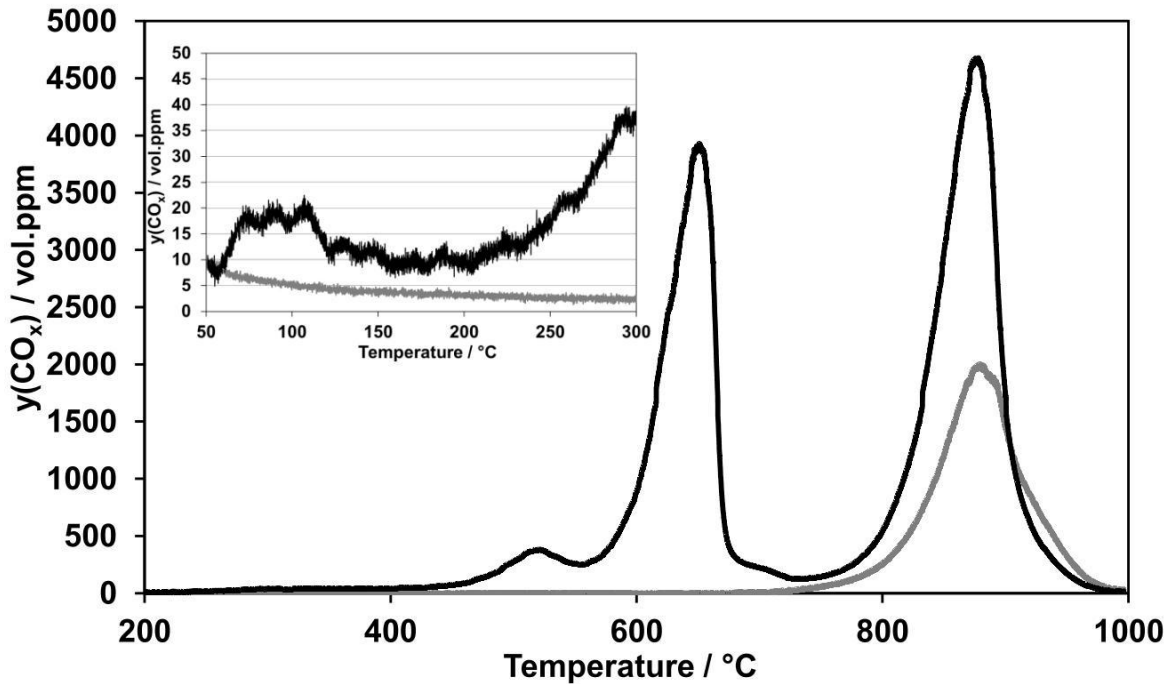


Figure 3-22: CO_2 (—) and CO (---) profile of temperature programmed reduction of $\alpha\text{-Fe}_2\text{O}_3$ with soot in tight contact mixture. Conditions: 10 mmol Fe_2O_3 , 5 mmol soot. $F=500$ mL/min N_2 . $\beta=3.3$ K/min. The inlay presents the CO_2 formation in the low temperature range.

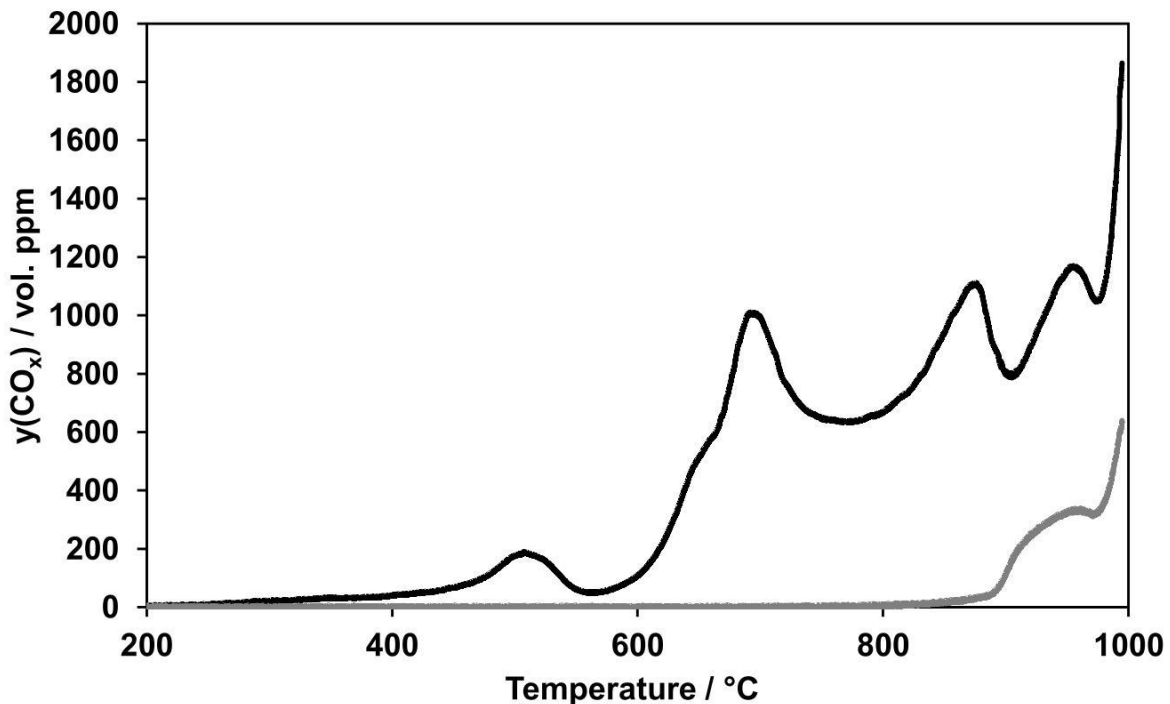


Figure 3-23: CO_2 (—) and CO (---) profile of temperature programmed reduction of $\alpha\text{-Fe}_2\text{O}_3$ with soot in loose contact mixture. Conditions: 10 mmol Fe_2O_3 , 5 mmol soot. $F=500$ mL/min N_2 . $\beta=3.3$ K/min. The inset presents the CO_2 formation in low temperature range.

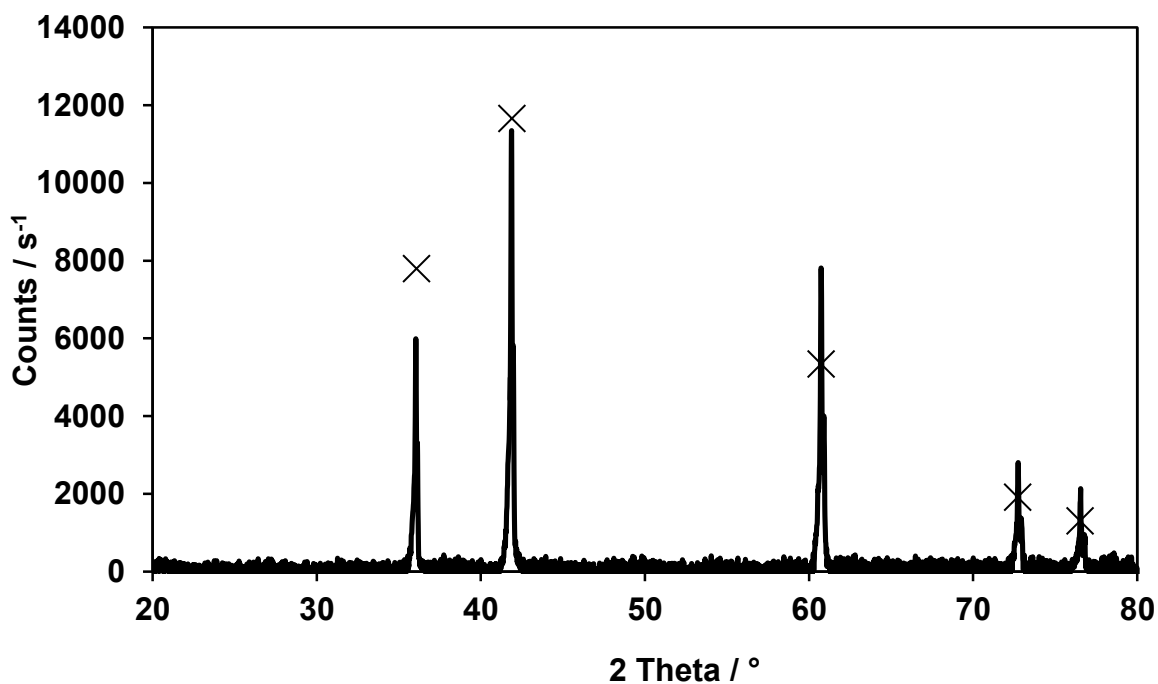


Figure 3-24: XRD pattern of Fe₂O₃ after temperature programmed reduction with soot in tight contact mode. (X) corresponds to ideal wustite phase (Fe_{1-x}O).

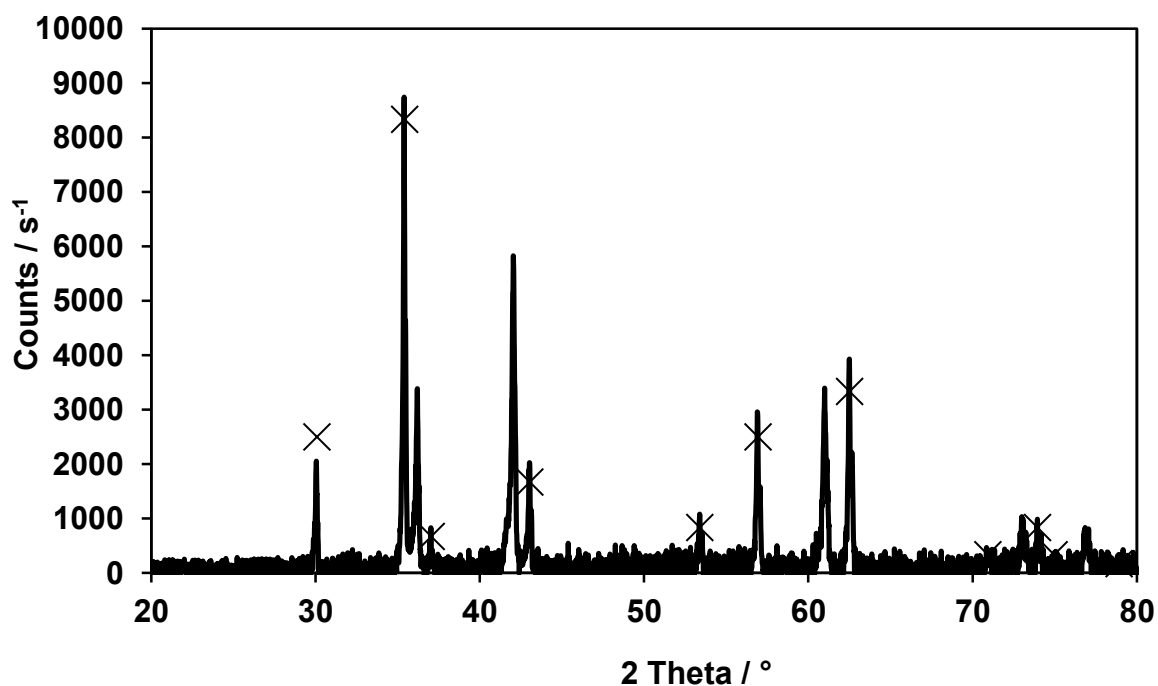


Figure 3-25: XRD pattern of Fe₂O₃ after temperature programmed reduction with soot in loose contact mode. (X) corresponds to ideal magnetite phase (Fe₃O₄).

3.2.5 Isotopic studies with $^{18}\text{O}_2$

The isotopic studies address the role of the catalyst in soot oxidation. The use of $^{18}\text{O}_2$ gas phase oxygen provides insights into the interaction of catalyst and soot by following the oxygen transfer from catalyst to soot. This is done by analysing all the formed C^{16}O_y and C^{18}O_y species within a TPO run thus providing the quantity of oxygen originating from the catalyst and gas phase, respectively. Detailed information can be derived from variation of the reaction parameters by using (a) loose and tight contact mixtures, (b) different catalyst/soot ratios and (c) different morphology of the catalyst.

Moreover, to minimise the required amount of $^{18}\text{O}_2$, the reaction conditions were modified as compared to the standard TPO approach (see Chapter 2.4.1) according to previous experiments of Reichert [23]. The isotopic studies were performed for two Fe_2O_3 materials (bulk $\alpha\text{-Fe}_2\text{O}_3$ and nano- Fe_2O_3 (C10-20)). The bulk $\alpha\text{-Fe}_2\text{O}_3$ was chosen for reference purpose, as it has a clearly defined crystalline composition (100 % $\alpha\text{-Fe}_2\text{O}_3$ phase) and high thermal stability. Additionally, a commercial nano-sized Fe_2O_3 sample (Chempur 10-20 nm) has been examined, since it reveals advanced catalytic activity (see chapter 5.2.2.2).

3.2.5.1 Bulk $\alpha\text{-Fe}_2\text{O}_3$ in tight contact mixture (ratio: 2:1)

Figure 3-26 presents the results of the $^{18}\text{O}_2$ TPO study of bulk $\alpha\text{-Fe}_2\text{O}_3$ in tight contact mixture at a molar ratio of Fe_2O_3 :soot of 2:1. It is obvious that the TPO pattern shows different CO_x profile as compared to the standard TPO conditions due to the modified experimental conditions [23]. CO_2 formation starts at 200°C and is completed at 950°C , whereas all C^xO_2 profiles reveal several shoulders. The main product is $\text{C}^{16}\text{O}^{18}\text{O}$ with a peak temperature of ca. 565°C indicating a total quantity of $137\ \mu\text{mol}\ \text{C}^{16}\text{O}^{18}\text{O}$ corresponding to 45 % of the total amount of carbon. The C^{16}O_2 profile exhibits a maximum at 670°C and a number of $101\ \mu\text{mol}\ \text{C}^{16}\text{O}_2$ (33 % of used carbon). Moreover, C^{18}O_2 shows a maximum at 564°C and reveals an amount of $69\ \mu\text{mol}\ \text{C}^{18}\text{O}_2$, which is 23 % of the used carbon. Additionally, the formation of H_2^{16}O , H_2^{18}O , C^{16}O and C^{18}O was not observed. In the initial phase of the soot oxidation (200°C - 300°C) C^xO_2 formation, C^{16}O_2 starts setting in followed by $\text{C}^{16}\text{O}^{18}\text{O}$ and C^{18}O_2 . With increasing temperature, the volume fraction of $\text{C}^{16}\text{O}^{18}\text{O}$ exceeds that of C^{16}O_2 , while C^{16}O_2 is exceeded by C^{18}O_2 at 350°C . However, above 500°C the volume fraction of C^{16}O_2 significantly increases, finally resulting in the highest volume

fraction of C^xO_2 species located at 669°C. Furthermore, above 350°C oxygen exchange between gas phase and catalyst is observed. This is indicated by formation of $^{16}O^{18}O$ volume fraction which exceeds the $^{18}O_2$ signal at 820°C. The integral amount of $^{16}O^{18}O$ is quantified to be 330 μmol . No $^{16}O_2$ was formed. In addition, it must be stated that the natural distribution of $^{18}O_2$, which is 0.2 %, is neglected.

The HTPR (Figure 3-27), performed subsequent to the TPO run, leads to 704 μmol $H_2^{16}O$ and 796 μmol $H_2^{18}O$, respectively. From these data the oxygen exchange degree is derived to be 53 % representing the fraction of ^{16}O substituted by ^{18}O in the catalyst. Table 3-3 quantifies the ^{16}O and ^{18}O containing reactants referring to both, oxygen atoms and ions. From this balance it is evident that the catalyst provides 1500 μmol ^{16}O , while 3568 μmol ^{18}O are from gas phase oxygen. In connection to this, the amount of ^{16}O is derived from the total amount of formed H_2^xO during the TPR run. The amount of ^{16}O originating from soot is neglected. The used C_3H_6 soot includes 3.5 μmol O (referred to 3.7 mg soot) only [23]. Finally, the variance of incoming and effusing species of less than 10 % indicates acceptable quality for the balance of the oxygen.

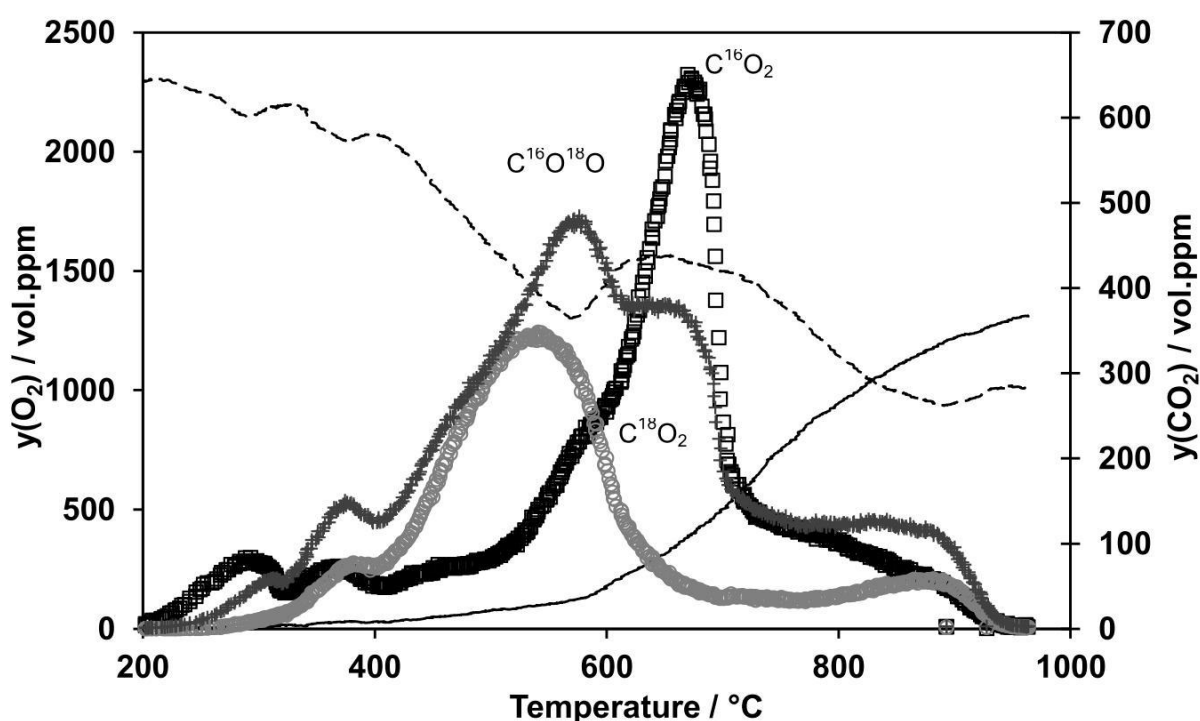


Figure 3-26: Volume fraction of $C^{18}O_2$ (\circ), $C^{16}O^{18}O$ (+), $C^{16}O_2$ (\square), $^{18}O_2$ (- -) and $^{16}O^{18}O$ (—) in the catalytic soot/ O_2 reaction. Experimental conditions: Bulk $\alpha\text{-Fe}_2O_3$ in tight contact mixture, molar ratio of Fe_2O_3 :soot is 2:1, $m(\text{mixture})=100$ mg, $y(^{18}O_2)_{in}=2270$ ppm, $F=500$ mL/min, $\beta=20$ K/min, balance N_2 .

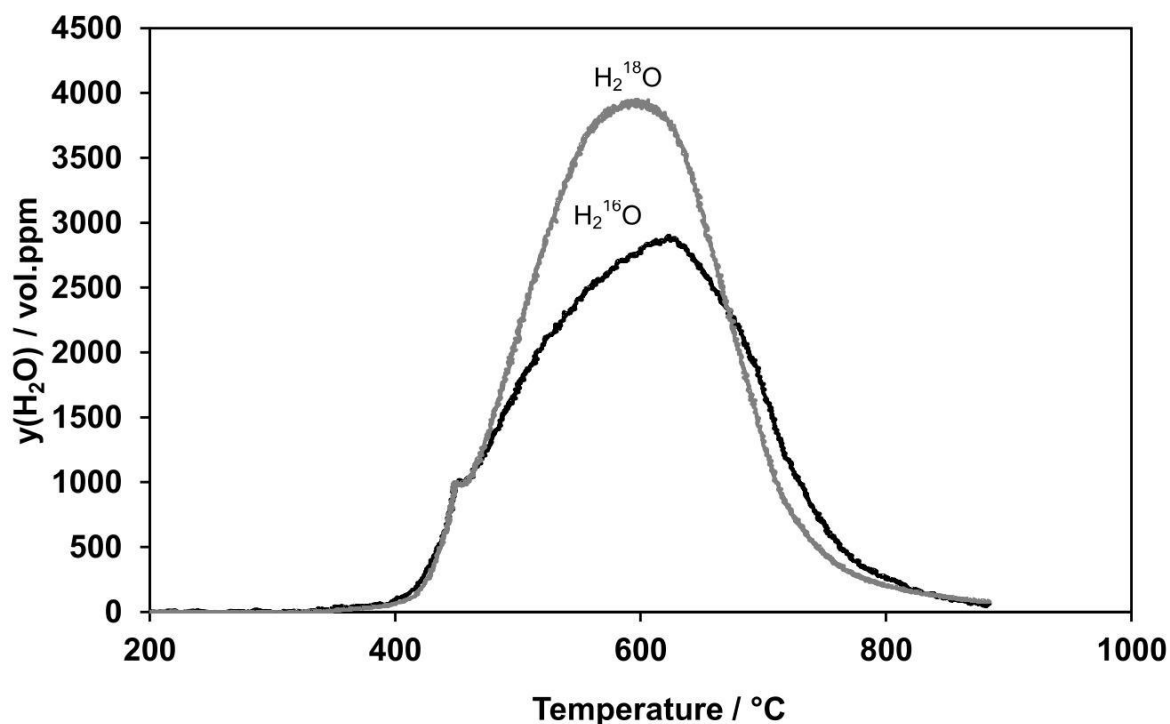


Figure 3-27: Volume fraction of (—) H_2^{16}O and (---) H_2^{18}O in the HTPR of $\alpha\text{-Fe}_2\text{O}_3$, performed after the isotopic TPO with bulk $\alpha\text{-Fe}_2\text{O}_3$ in tight contact mixture and a molar ratio of Fe_2O_3 :soot of 2:1. $y(\text{H}_2)=10$ vol.%, N_2 balance, $F=500$ mL/min, $\beta=20$ K/min.

Table 3-3: Molar amounts of oxygen containing species in isotopic TPO of the bulk $\alpha\text{-Fe}_2\text{O}_3$ /soot mixture (2:1) in tight contact and subsequent HTPR.^{a)}

¹⁸ O	In		Out	
	Amount (μmol)	Source	Amount (μmol)	Source
TPO	3568	¹⁸ O ₂	137	C ¹⁶ O ¹⁸ O
			138	C ¹⁸ O ₂
			2456	¹⁸ O ₂
			330	¹⁶ O ¹⁸ O
HTPR	0		796	H ₂ ¹⁸ O
Total	3568		3857	

¹⁶ O		In			Out	
	Amount (μmol)	Source	Amount (μmol)	Source		
TPO	1500	Fe ₂ O ₃	137	C ¹⁶ O ¹⁸ O		
			202	C ¹⁶ O ₂		
			330	¹⁶ O ¹⁸ O		
HTPR	0		704	H ₂ ¹⁶ O		
Total	1500		1373			

a) Reaction conditions are demonstrated in Figure 3-26 and Figure 3-27.

3.2.5.2 Bulk α-Fe₂O₃ in loose contact mixture (ratio 2:1)

The isotopic soot oxidation, with a loose contact mixture of α-Fe₂O₃ and soot in the molar ratio of 2 (Figure 3-28), shows initial CO₂ production at 250°C. However, the soot consumption extends to a broad temperature range up to 1000°C as indicated by the C^xO₂ traces. As for tight contact, the main product upon TPO is C¹⁶O¹⁸O. This shows an integral quantity of 144 μmol corresponding to 47 % of the mass of carbon initially used, which is similar to the tight contact experiment using a molar ratio of 2:1. The maximum of the C¹⁶O¹⁸ signal is found at 660°C and shoulders are located at 380°C and at 606°C. The C¹⁶O₂ curve shows the peak volume fraction at 733°C as well as shoulders at 280°C and 550°C. This curve exhibits an integral proportion of 86 μmol (28 % of total amount of carbon). Moreover, the C¹⁸O₂ signal reveals a maximum at 600°C and a total amount of 80 μmol formed during the experiment corresponding to 26 % of the initial mass of carbon. As already described in section 4.2.1, the formation of H₂^xO and C^xO was not observed. In the temperature range from 250°C to 430°C C¹⁶O₂ forms in substantial abundance. At temperatures above 485°C the C¹⁶O¹⁸O and C¹⁸O₂ traces extend the C¹⁶O₂ volume fraction, indicated by a steep increase of both species. The C¹⁶O¹⁸O and the C¹⁸O₂ signals exhibit up to 600°C by almost congruent progression, whereas C¹⁶O¹⁸O increases further until 660°C remaining the predominant species then. The formation of C¹⁸O₂ decreases above 600°C. Like in the previous experiment, oxygen exchange between gas phase and catalyst is observed above 430°C indicated by a rise of ¹⁶O¹⁸O volume fraction totally amounting to 422 μmol. Again, no ¹⁶O₂ was detected. The following HTPR investigation (Figure 3-29) led to formation of 669 μmol H₂¹⁸O and 934 μmol H₂¹⁶O evidencing the level of oxygen exchange to be 42 %. Table 3-4 summarises the

quantities of all the ^{16}O and ^{18}O containing reactants. This list provides evidence that the mass is balanced for ^{16}O as well as ^{18}O within the limits of the CIMS analyser used.

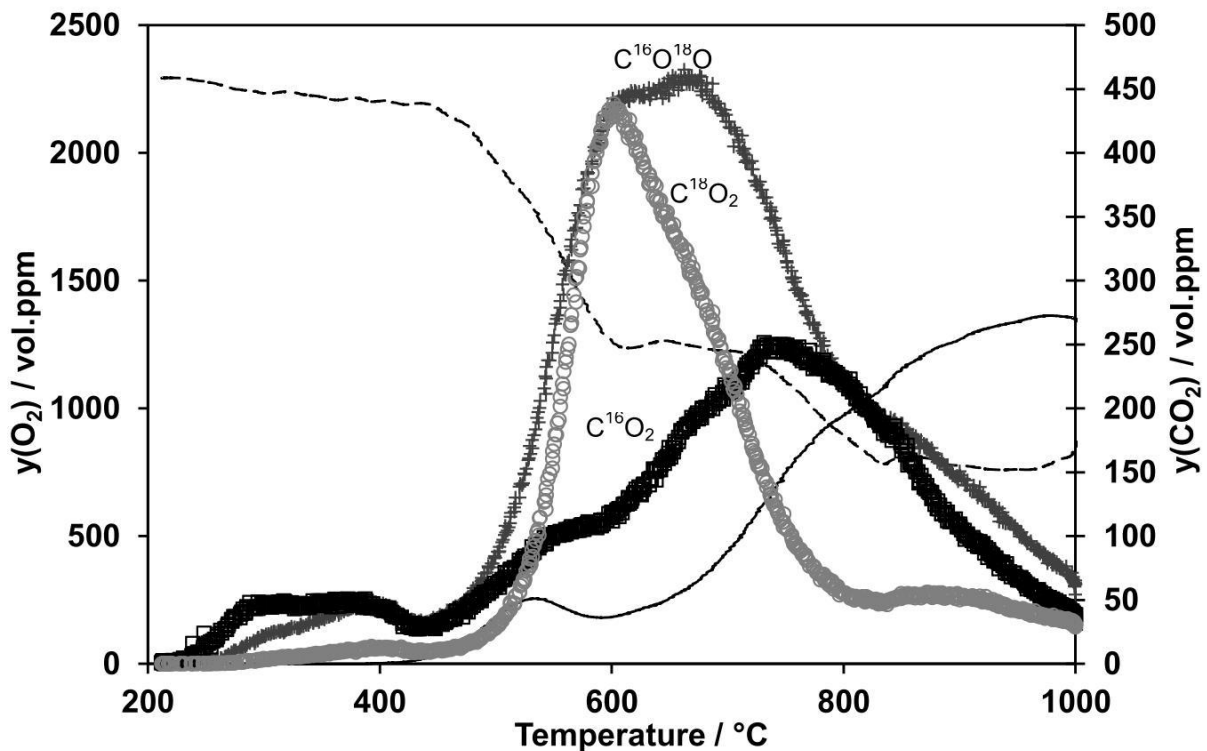


Figure 3-28: Volume fraction of C^{18}O_2 (\circ), $\text{C}^{16}\text{O}^{18}\text{O}$ ($+$), C^{16}O_2 (\square), $^{18}\text{O}_2$ ($- -$) and $^{16}\text{O}^{18}\text{O}$ ($-$) in the catalytic soot/ O_2 reaction. Experimental conditions: Bulk $\alpha\text{-Fe}_2\text{O}_3$ in loose contact mixture, molar ratio of Fe_2O_3 :soot is 2:1, $m(\text{mixture})=100$ mg, $y(^{18}\text{O}_2)_{\text{in}}=2270$ ppm, $F=500$ mL/min, $\beta=20$ K/min, balance N_2 .

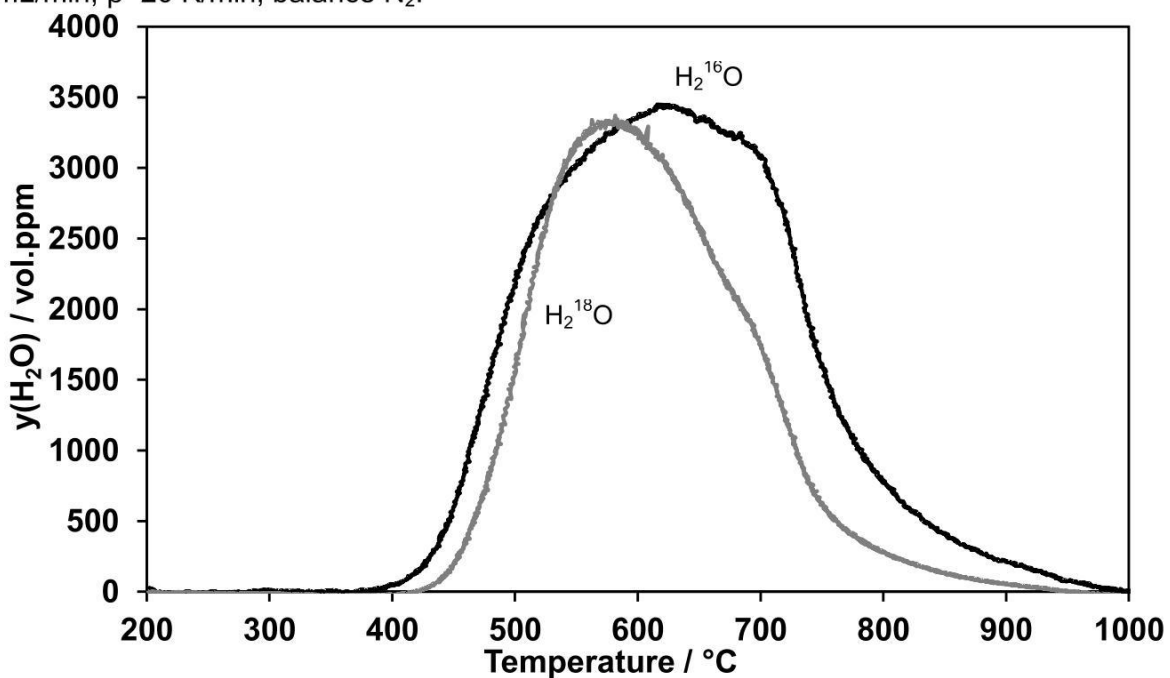


Figure 3-29: Volume fraction of ($-$) H_2^{16}O and ($- -$) H_2^{18}O in the HTPR of $\alpha\text{-Fe}_2\text{O}_3$, performed after the isotopic TPO with bulk $\alpha\text{-Fe}_2\text{O}_3$ in loose contact mixture and a molar ratio of Fe_2O_3 :soot of 2:1. $y(\text{H}_2)=10$ vol.%, N_2 balance, $F=500$ mL/min, $\beta=20$ K/min.

Table 3-4: Molar amounts of oxygen containing species in isotopic TPO of the bulk α -Fe₂O₃/soot mixture (2:1) in loose contact with ¹⁸O₂ and subsequent HTPR.^{b)}

¹⁸ O				
In			Out	
	Amount (μmol)	Source	Amount (μmol)	Source
TPO	3826	¹⁸ O ₂	144	C ¹⁶ O ¹⁸ O
			160	C ¹⁸ O ₂
			2476	¹⁸ O ₂
			422	¹⁶ O ¹⁸ O
HTPR	0		669	H ₂ ¹⁸ O
Total	3826		3871	
¹⁶ O				
In			Out	
	Amount (μmol)	Source	Amount (μmol)	Source
TPO	1603	Fe ₂ O ₃	144	C ¹⁶ O ¹⁸ O
			172	C ¹⁶ O ₂
			422	¹⁶ O ¹⁸ O
HTPR	0		934	H ₂ ¹⁶ O
Total	1603		1672	

^{b)} Reaction conditions are demonstrated in Figure 3-28 and Figure 3-29.

3.2.5.3 Bulk α -Fe₂O₃ in tight contact mixture (ratio 1:2)

Figure 3-30 illustrates the results of the isotopic TPO study of α -Fe₂O₃ and soot in a tight contact mixture with a reduced molar ratio of Fe₂O₃:soot of 1:2. This experiment shows CO₂ formation in a temperature range from 250°C to 850°C. The major product is C¹⁸O₂, which shows peak volume fraction at 543°C and an integral quantity of 150 μmol (49 % of initial mass of carbon). C¹⁶O¹⁸O reveals a peak at 590°C and amounts to a total of 127 μmol corresponding to 41 % of the initial mass of carbon used. Furthermore, C¹⁶O forms only in rather small quantities as indicated by an integral proportion of 30 μmol (10 % of the initially amount of carbon); its maximum volume fraction appears at 611°C. C¹⁶O₂ and C¹⁶O¹⁸O volume fractions are similar between 250°C to 280°C, but formation of C¹⁶O₂ decreases above 280°C followed by a maximum at 610°C. In contrast to this, formation of C¹⁶O¹⁸O starts at 280°C and rises continuously up to the peak temperature of 590°C. Additionally,

oxygen exchange between gas phase and catalyst sets in at about 450°C; the total amount of $^{16}\text{O}^{18}\text{O}$ is quantified to 178 μmol . Again, $^{16}\text{O}_2$ was not found.

The HTPR study immediately performed after the TPO results in 415 μmol H_2^{18}O and 234 μmol H_2^{16}O providing a degree of exchange equal to 64 %.

To summarise, Table 3-5 lists the amounts of all ^{16}O and ^{18}O containing species showing balanced mass within the accuracy of the detector for both O species.

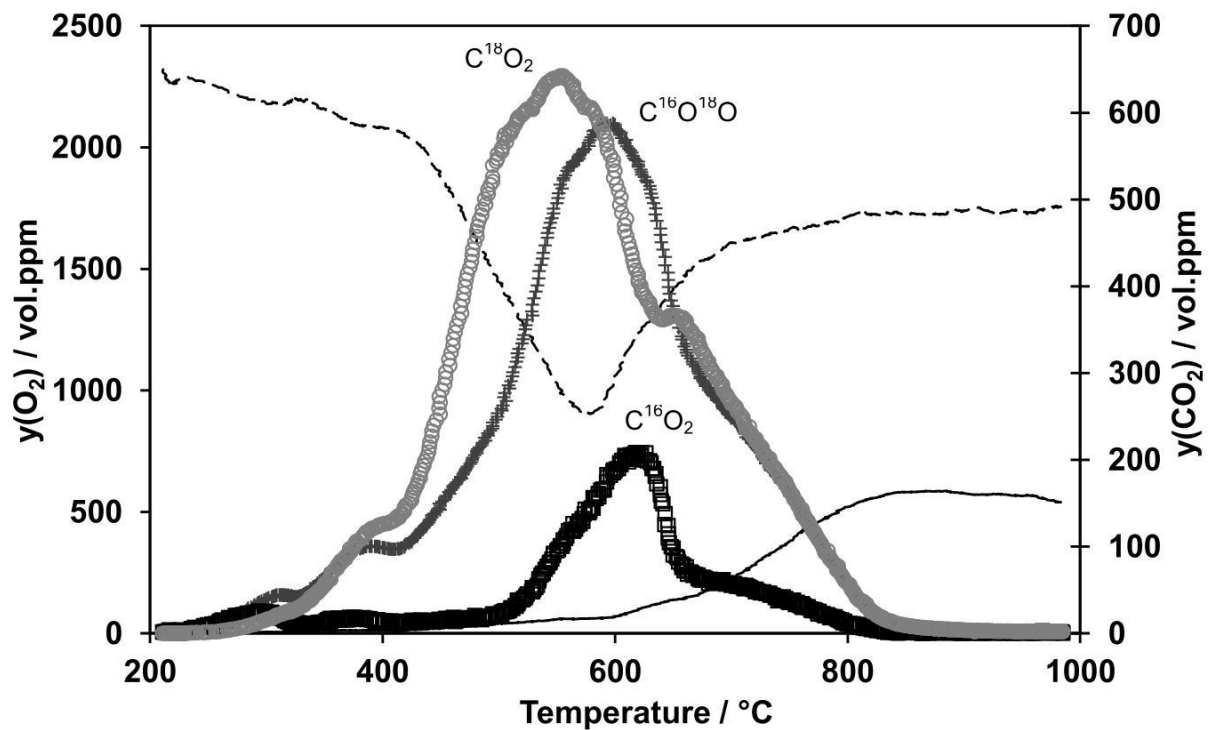


Figure 3-30: Volume fraction of C^{18}O_2 (\circ), $\text{C}^{16}\text{O}^{18}\text{O}$ ($+$), C^{16}O_2 (\square), $^{18}\text{O}_2$ ($- -$) and $^{16}\text{O}^{18}\text{O}$ ($-$) in the catalytic soot/ O_2 reaction. Experimental conditions: Bulk $\alpha\text{-Fe}_2\text{O}_3$ in tight contact mixture, molar ratio of Fe_2O_3 :soot is 1:2, $m(\text{mixture})=27$ mg, $y(^{18}\text{O}_2)_{\text{in}}=2270$ ppm, $F=500\text{mL}/\text{min}$, $\beta=20\text{K}/\text{min}$, balance N_2 .

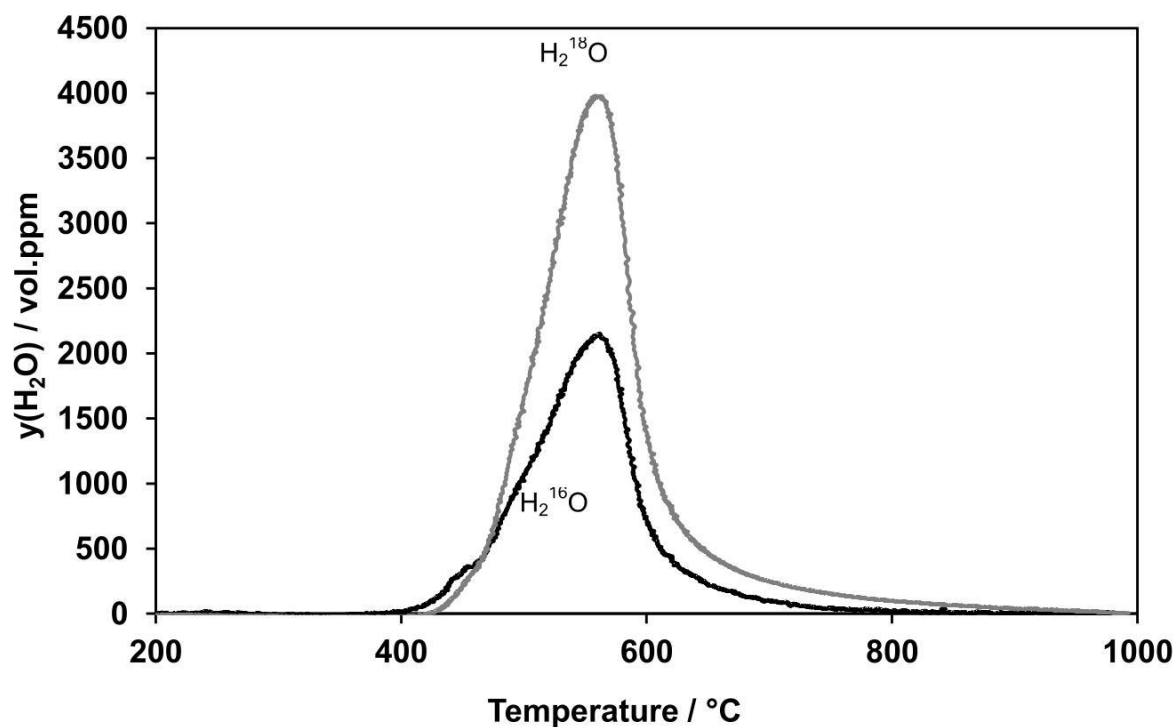


Figure 3-31: Volume fraction of (—) H_2^{16}O and (---) H_2^{18}O in the HTPR of $\alpha\text{-Fe}_2\text{O}_3$, performed after the isotopic TPO with bulk $\alpha\text{-Fe}_2\text{O}_3$ in tight contact mixture and a molar ratio of Fe_2O_3 :soot of 1:2. $y(\text{H}_2)=10$ vol.%, N_2 balance, $F=500$ mL/min, $\beta=20$ K/min.

Table 3-5: Molar amounts of oxygen containing species in isotopic TPO of the bulk $\alpha\text{-Fe}_2\text{O}_3$ /soot mixture (1:2) in tight contact with $^{18}\text{O}_2$ and subsequent HTPR.^{c)}

^{18}O	In		Out	
	Amount (μmol)	Source	Amount (μmol)	Source
TPO	3684	$^{18}\text{O}_2$	127	$\text{C}^{16}\text{O}^{18}\text{O}$
			300	C^{18}O_2
			2742	$^{18}\text{O}_2$
			178	$^{16}\text{O}^{18}\text{O}$
HTPR	0		415	H_2^{18}O
Total	3684		3762	

¹⁶ O				
In			Out	
	Amount (μmol)	Source	Amount (μmol)	Source
TPO	649	Fe_2O_3	127	$\text{C}^{16}\text{O}^{18}\text{O}$
			60	C^{16}O_2
			178	$^{16}\text{O}^{18}\text{O}$
HTPR	0		234	H_2^{16}O
Total	649		599	

^{c)} Reaction conditions are demonstrated in Figure 3-30 and Figure 3-31.

3.2.5.4 Nano-sized Fe_2O_3 in tight contact (ratio 2:1)

The isotopic TPO (Figure 3-32) with the nano-sized Fe_2O_3 , which showed in previous experiments higher activity compared to the bulk $\alpha\text{-Fe}_2\text{O}_3$, was carried out in tight contact mode at a molar of Fe_2O_3 :soot of 2:1. In this study, the CO_2 formation ranges from 215°C to 815°C with $\text{C}^{16}\text{O}^{18}\text{O}$ being the main product. The maximum of $\text{C}^{16}\text{O}^{18}\text{O}$ appears at 507°C, while a shoulder is located at 365°C. The quantity of $\text{C}^{16}\text{O}^{18}\text{O}$ amounts to 133 μmol referring to 43 % of the initially taken mass of carbon. The C^{16}O_2 profile shows two maxima (530°C and at 594°C), whereas the latter peak is ascribed to structural changes of the catalyst. The O_2 -TPD and TG/DTA studies of the nano-sized Fe_2O_3 (Figure 5-9 and Figure 5-10) suggest oxygen release and a phase change at about 580°C. Thus, the 594°C peak of C^{16}O_2 is rather associated with the reaction of oxygen removed from the catalyst by structural changes and not with any catalytic processes. The total amount of detected C^{16}O_2 is 130 μmol (42 % of the initial quantity of carbon). Furthermore, the C^{18}O_2 trace shows peak production at 506°C; the overall amount is quantified to 44 μmol C^{18}O_2 , which corresponds to 14 % of the amount of carbon established. In the temperature regime from 200°C to 280°C, $\text{C}^{16}\text{O}^{18}\text{O}$ and C^{16}O_2 exhibit almost identical volume fractions, while above 300°C the $\text{C}^{16}\text{O}^{18}\text{O}$ signal shows a steep rise, whereas C^{18}O_2 shows small volume fractions in the whole temperature range. Furthermore, oxygen exchange between gas phase and catalyst is again indicated by the evolution of $^{16}\text{O}^{18}\text{O}$ above 350°C. The $^{16}\text{O}^{18}\text{O}$ signal features unsteadiness (580°C-650°C, 780°C-985°C) attributed to the above-mentioned structural changes of the sample at high temperatures (>800°C), which is also substantiated by the TG/DTA study (Figure 5-10). In contrast to the previous experiments, appearance of $^{16}\text{O}_2$, H_2^{16}O and H_2^{18}O is detected, which

is also attributed to morphological changes and loss of water due to desorption of surface OH groups. As shown in Figure 3-33, H_2^{16}O is monitored between 230°C and 430°C as well as above 800°C, indicating an integral amount of 114 μmol . Additionally, only little amount of H_2^{18}O is recorded with an overall quantity of 13 μmol . Moreover, $^{16}\text{O}_2$ formation starts at 800°C and reveals an integral amount of 34 μmol .

The final HTPR experiment (Figure 3-34) exhibits 927 μmol H_2^{18}O and 641 μmol H_2^{16}O suggesting an oxygen exchange degree of 59 %. Table 3-6 lists the overall amounts of the ^{16}O and ^{18}O containing species. These data show a total quantity of 1352 μmol ^{16}O containing species, predominately originating from the catalyst, and 3732 μmol ^{18}O , in the form of gas phase oxygen, are provided. The divergence of the balance is below 3 % indicating the reliability of the measurements.

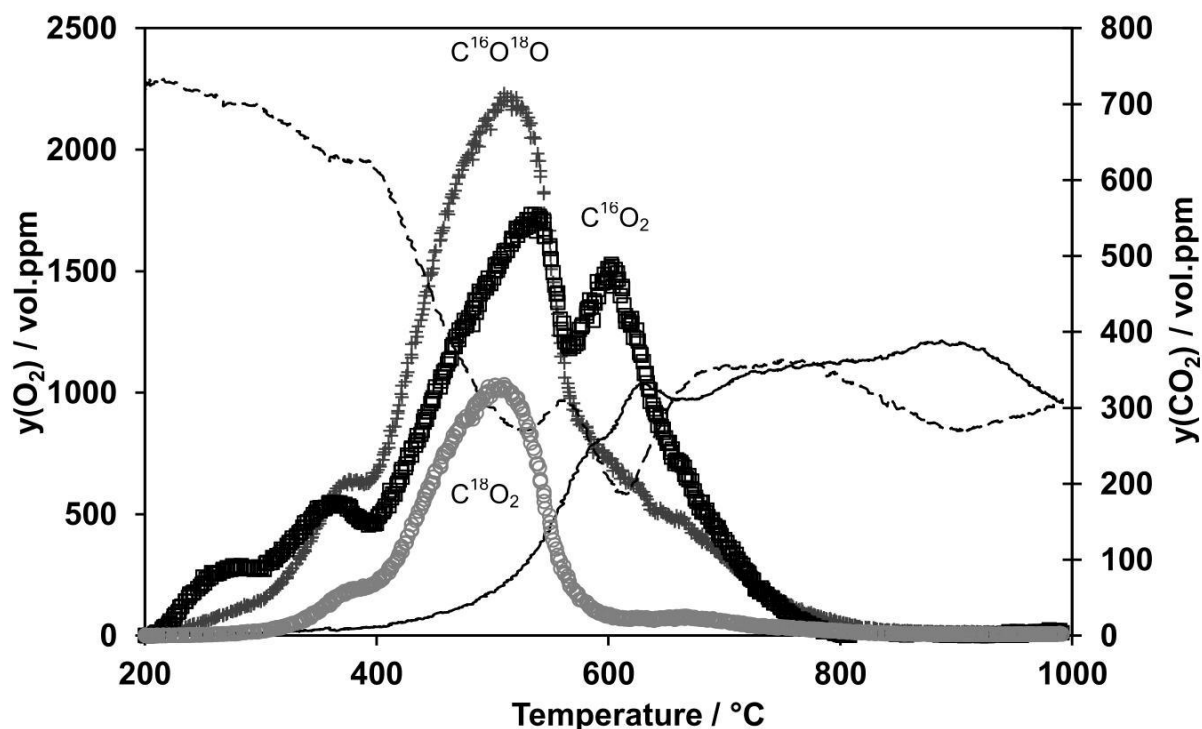


Figure 3-32: Volume fraction of C^{18}O_2 (\circ), $\text{C}^{16}\text{O}^{18}\text{O}$ ($+$), C^{16}O_2 (\square), $^{18}\text{O}_2$ ($- -$) and $^{16}\text{O}^{18}\text{O}$ ($-$) in the catalytic soot/ O_2 reaction. Experimental conditions: Nano-sized Fe_2O_3 in tight contact mixture, molar ratio of Fe_2O_3 :soot is 2:1, $m(\text{mixture})=100$ mg, $y(^{18}\text{O}_2)_{\text{in}}=2270$ ppm, $F=500$ mL/min, $\beta=20$ K/min, balance N_2 .

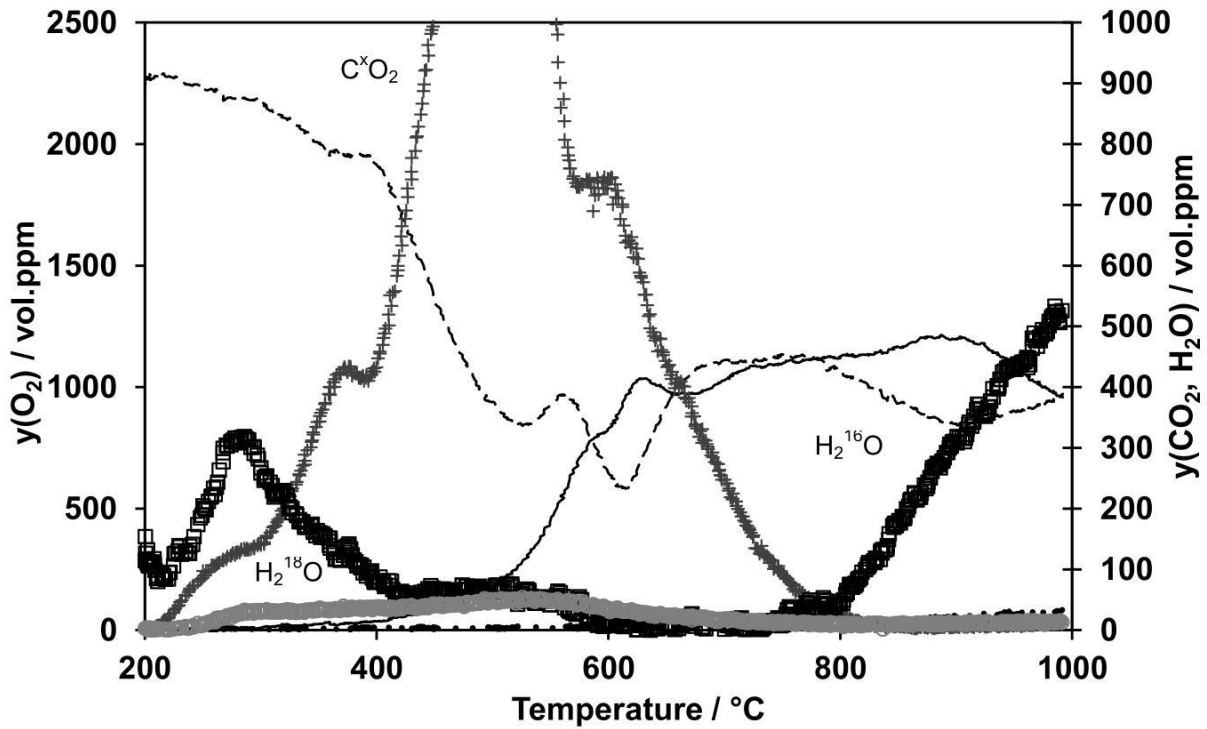


Figure 3-33: Volume fraction of C^xO_2 (+), H_2^{16}O (□), H_2^{18}O (○), $^{16}\text{O}_2$ (- · - · -), $^{18}\text{O}_2$ (- -) and $^{16}\text{O}^{18}\text{O}$ (—) in the catalytic soot/ O_2 reaction. Experimental conditions: Nano-sized Fe_2O_3 in tight contact mixture, molar ratio of Fe_2O_3 :soot of 2:1, $m(\text{mixture})=100$ mg, $y(^{18}\text{O}_2)_{\text{in}}=2270$ ppm, $F=500$ mL/min, $\beta=20$ K/min, balance N_2 .

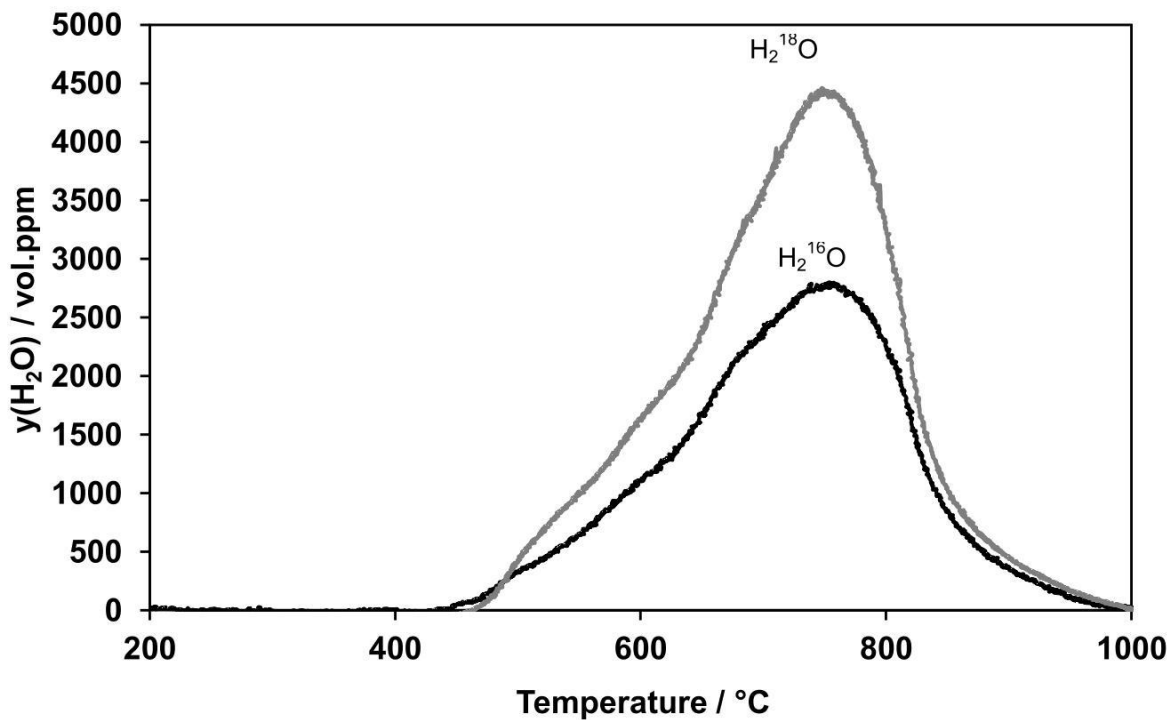


Figure 3-34: Volume fraction of (—) H_2^{16}O and (---) H_2^{18}O in the HTPR of nano-sized Fe_2O_3 , performed after the isotopic TPO with bulk $\alpha\text{-Fe}_2\text{O}_3$ in tight contact mixture and a molar ratio of Fe_2O_3 :soot of 2:1. $y(\text{H}_2)=10$ vol.%, N_2 balance, $F=500$ mL/min, $\beta=20$ K/min.

Table 3-6: Molar amounts of oxygen containing species in isotopic TPO of the nano-sized Fe₂O₃/soot mixture (2:1) in tight contact with ¹⁸O₂ and subsequent HTPR.^{d)}

¹⁸ O				
In			Out	
	Amount (μmol)	Source	Amount (μmol)	Source
TPO	3732	¹⁸ O ₂	133	C ¹⁶ O ¹⁸ O
			86	C ¹⁸ O ₂
			2096	¹⁸ O ₂
			513	¹⁶ O ¹⁸ O
			13	H ₂ ¹⁸ O
HTPR	0		927	H ₂ ¹⁸ O
Total	3732		3768	
¹⁶ O				
In			Out	
	Amount (μmol)	Source	Amount (μmol)	Source
TPO	1568	Fe ₂ O ₃	133	C ¹⁶ O ¹⁸ O
			260	C ¹⁶ O ₂
			513	¹⁶ O ¹⁸ O
			34	¹⁶ O ₂
			114	H ₂ ¹⁶ O
HTPR	0		641	H ₂ ¹⁶ O
Total	1568		1606	

^{d)} Reaction conditions are demonstrated in Figure 3-32 and Figure 3-34.

3.3 Discussion

3.3.1 Variation of the reaction conditions

3.3.1.1 The effect of varying the type of soot

The experimental series performed (Figure 3-2) exhibited major differences in the reactivity of different types of soot upon catalytic oxidation on the Fe₂O₃ catalyst. In order to understand the reasons for these differences thorough physical-chemical characterisation of the soot was done. On the basis of N₂ thermogravimetry and BET analysis a correlation (Figure 3-35) between the amount of adsorbed species, the active surface area and the reactivity of the soot samples, which is quantified by the

temperature of maximum CO₂ volume fraction ($T_{\text{CO}_2, \text{max}}$), can be derived; the sample with the highest amount of adsorbed species and highest surface area (Spezial Schwarz 6 with 22 w.t.% adsorbed species and $S_{\text{BET}}=300 \text{ m}^2/\text{g}$) shows the best reactivity ($T_{\text{CO}_2, \text{max}}=366^\circ\text{C}$) while the PrintexL sample (4.3 w.t.% adsorbed species and $S_{\text{BET}}=95 \text{ m}^2/\text{g}$) shows the worst activity ($T_{\text{CO}_2, \text{max}}=424^\circ\text{C}$). This correlation is explained by a large number of reactive species. These are present in the form of oxygen surface complexes and adsorbed hydrocarbons on the soot surface for the samples showing superior reactivity. The reactivity of such oxygen surface species was shown by Sendt [51], while Neeft et al. attributed differences in the activity between real diesel soot and industrial carbon black (PrintexU) [32] to adsorbed hydrocarbons. A further reason for the different reactivity among the different types of soot is found by comparing their elementary composition (Table 3-1). A high oxygen content, i.e. 9 w.t.% for the most active Spezial Schwarz 6 soot, is accompanied by a high activity ($T_{\text{CO}_2, \text{max}}=366^\circ\text{C}$). An explanation for this is given by Nejar who related a high oxygen content of soot to the presence of reactive surface complexes, which increase carbon reactivity [52]. Moreover, TPD studies performed with the different types of soot (see Appendix E) suggest the highest amount of desorbed CO_x for the Spezial Schwarz 6 sample substantiating its high reactivity.

Table 3-1 shows a correlation between composition of the soot and its heating value. The Spezial Schwarz 6 sample offers a carbon fraction of 89.5 wt.% and a heating value of 29857 kJ/kg, whereas the PrintexL has a proportion of 99.2 wt.% carbon and a heating value of 33474 kJ/kg indicating that a high proportion of carbon increases the heating value. This is based on the fact that elementary carbon contributes with a formation enthalpy of $-393 \text{ kJ/mol}_{\text{carbon}}$ ($\text{C} + \text{O}_2 \rightarrow \text{CO}_2$, for $T=298 \text{ K}$ and $p=1 \text{ bar}$) to the heating value, while CO ($\text{CO} + 0.5 \text{ O}_2 \rightarrow \text{CO}_2$, $\Delta H_f^0 = -110.5 \text{ kJ/mol}_{\text{carbon}}$) and HC (e.g. $\text{CH}_4 + 2 \text{ O}_2 \rightarrow \text{CO}_2 + 2 \text{ H}_2\text{O}$, $\Delta H_f^0 = -75 \text{ kJ/mol}_{\text{carbon}}$) contribute to the heating value to a smaller extent.

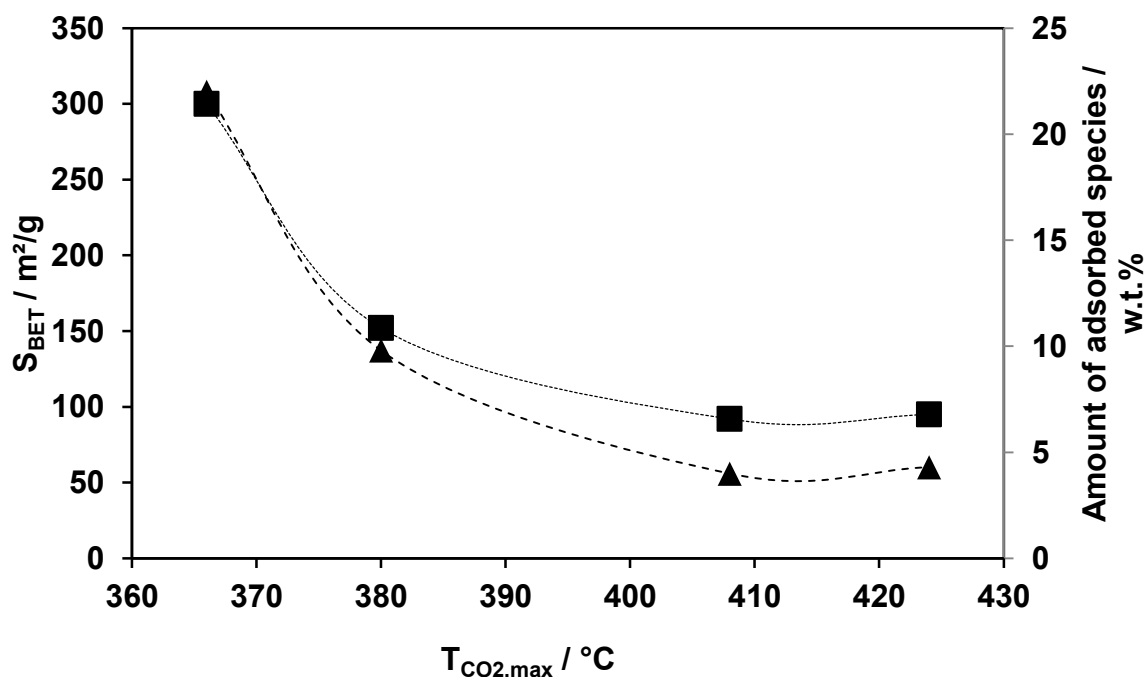


Figure 3-35: Dependency of the soot reactivity on the active surface area (■) and the amount of adsorbed species (▲) upon oxidation on Fe_2O_3 catalyst.

3.3.1.2 The effect of varying the contact mode

The results presented in Figure 3-3, which were obtained to study the effect of the type of soot on catalytic soot oxidation, indicated the need of a sufficient amount of contact points. The CO_2 profile of the loose contact experiment shows two maxima. The low-temperature shoulder of the curve is attributed to catalytic and the high-temperature (HT) peak to non-catalytic soot oxidation since this HT peak shows similar curve progression as compared to the non-catalytic TPO using bare soot. These findings are in accordance with literature [16,53]. However, a drastic decrease in catalytic performance is reported for non-mobile catalysts (e.g. Fe_2O_3 and Co_3O_4) by comparing the combustion temperature for tight and loose contact mixtures between catalyst and soot. A possible reason for this might be the distance between soot and catalyst that has to be overcome. Simonsen [54] showed by in-situ TEM studies under oxygen atmosphere the possibility of soot migration to non-mobile catalysts at catalytic soot oxidation. For tight contact catalyst/soot mixtures the distance between catalyst and soot is small, but for loose contact mixtures the bridging of this gap requires energy thus becoming more and more rate determining for increasing distance. This issue is deepened and further discussed in the chapter dealing with the kinetic modelling of the catalytic soot oxidation (Chapter 4.2.3). The established tight contact mode does not reflect the exact contact between catalyst

and soot on a real DPF system. Nevertheless, this mixing procedure was chosen due to its high reproducibility and it demonstrates the differences in the catalytic activity for different reaction conditions and catalysts [55]. In addition, the mechanical mixing of soot and catalyst in air may result in an increased activity due to structural modifications of the particulates. This was shown by Barthe [56].

3.3.1.3 The effect of varying the catalyst:soot ratio

A variation of the catalyst:soot ratio was shown to have strong effects on the reaction rate on catalytic soot oxidation. An increase of the amount of catalyst results in a decrease of the activity of the catalyst/soot mixture indicated by increasing $T_{\text{CO}_2, \text{max}}$ (Figure 3-4). Nevertheless, an insufficient amount of the Fe_2O_3 catalyst (molar catalyst:soot ratio < 1.25:5) leads to considerable formation of carbon monoxide and a decrease in activity (Figure 3-5 and Figure 3-6).

The temperature measurements taken (Figure 3-7 and Figure 3-8) clearly indicate a decline in the temperature of the packed bed (i.e. the catalyst/soot mixture in the tube reactor) with increasing amount of catalyst. The temperature difference between the reactor inlet and the middle of the packed bed is 160 K for a mixture ($n_{\text{soot}}=5$ mmol) using 2.5 mmol Fe_2O_3 , while it is 35 K for a mixture ($n_{\text{soot}}=5$ mmol) with 20 mmol catalyst. This temperature rise in the packed bed is ascribed to the heat evolution due to the exothermic soot oxidation. Since the amount of soot is kept constant, the temperature rise depends on the heat capacity of the packed bed corresponding to the amount of catalyst used. The quantity of Fe_2O_3 affects the heat evolution in the catalyst/soot mixture, which partly influences the temperature dependent reaction rate of the catalytic soot oxidation (see chapter 3.1.3). Similar findings were presented by TG analysis of Neeft et al. [57] emphasizing the dependency of the mass of catalyst. The appearance of considerable amounts of CO and the decrease in catalytic soot oxidation for molar catalyst:soot ratios using very small amounts of Fe_2O_3 (< 1.25:5) is attributed to an insufficient amount of active Fe sites and contact points, respectively. This leads to non-catalytic soot oxidation and to formation of CO (also see Figure 3-3). A certain proportion of the detected CO may also be attached to the feature of catalytic CO oxidation on Fe_2O_3 . Carbon monoxide, which is always formed upon catalytic soot oxidation via desorption of oxygen containing surface complexes, is oxidised by the iron oxide catalyst. But, for a low Fe_2O_3 proportion the catalytic performance is insufficient for complete CO oxidation. These findings emphasise the importance of finding an optimum between the amount of catalyst, i.e.

to assure sufficient contact points, and high heat evolution, which must additionally be weighed in terms of thermal stability of the catalyst. In a real filter system used in exhaust aftertreatment, the issue of finding an optimum heat capacity (i.e. amount of catalyst) is problematic due to the use of the catalytically coated wall flow filters which possess a huge mass and heat capacity, respectively.

3.3.1.4 The effect of varying the heating rate

The results of the experiments performed with different heating rates (Figure 3-9) show that a low heating rate (1.8 K/min) gives moderate CO₂ formation and a broad TPO curve ($y(\text{CO}_2)_{\text{max}}=0.7$ vol.%, ranging from 360°C to 460°C), whereas a heating rate greater than 3.3 K/min causes a steep rise in the CO₂ volume fraction and a sharp TPO profile ($y(\text{CO}_2)_{\text{max}}=7.5$ vol.%, ranging from 360°C to 420°C). The studies reveal that the CO₂ traces are not affected by varying the heating rate between 3.3 K/min and 10 K/min. These findings can be explained by the energy flow in the packed bed. A low heating rate leads to a slow temperature increase of the catalyst/soot mixture, which results in the above described moderate CO₂ formation. In contrast, a high heating rate, which indicates more energy input in the packed bed within the same time unit, causes higher CO₂ production in this time period, i.e. 0.04 W for a heating rate of 1.8 K/min and 0.08 W for $\beta=3.3$ K/min referring to a heat capacity of 0.4 J/K for 10 mmol Fe₂O₃ (see Table 4-1). Due to the exothermal reaction the heat production in the packed bed is intensified by high heating rates. This results in an acceleration of the soot oxidation.

The CO₂ traces for heating rates of 3.3, 5 and 10 K/min feature a similar curve progression, which may be an indication for a limitation of the reaction rate. Below 3.3 K/min the heating rate is faster than the reaction rate, since increasing β shifts the reaction to higher temperature as the heating rate is faster than the reaction rate; above 3.3 K/min the reaction rate exceeds the heating rate, since a further rise of β does not affect the CO₂ formation. These unchanging CO₂ profiles may be attributed to oxygen deficiency in the gas phase. Comparing the CO₂ traces of the TPO using heating rates of 3.3 K/min, 5 K/min and 10 K/min shows the peak CO₂ volume fraction being close to 10 vol.%, which corresponds to the O₂ volume fraction in the inlet gas feed (10 vol.%). The soot oxidation, which was shown to be first order in O₂ concentration (see chapter 3.2.3.1), runs into oxygen limitation and the reaction cannot be accelerated, despite higher heating rates. Limitations in the mass and heat transfer can be excluded. A rough estimation of the heat transfer from gas phase to

the particles in the packed bed can be done by setting-up a balance describing this transfer (Eq. ((3-17)). It can be assumed that the Fe_2O_3 /soot pellets have a diameter of 250 μm (referring to the preparation procedure in chapter 2.4) and a porosity of $\varepsilon=0.5$ (Table C-1). The mass of one pellet is calculated by taking the density of Fe_2O_3 (5.24 g/cm^3) only.

$$V_p \cdot \rho_{\text{Fe}_2\text{O}_3} \cdot \varepsilon \cdot c_p \cdot \frac{dT}{dt} = \pi \cdot d^2 \cdot k_s \cdot \Delta T \quad (3-17)$$

V_p	: Volume of a particle	$[\text{m}^3]$
$\rho_{\text{Fe}_2\text{O}_3}$: Density of iron oxide	$[\text{g}/\text{m}^3]$
ε	: Porosity (Table C-1)	$[\text{—}]$
c_p	: Heat capacity of iron oxide (see Table 4-1)	$[\text{J}/(\text{g}\cdot\text{K})]$
k_s	: Heat transfer coefficient	$[\text{W}/(\text{m}^2\cdot\text{K})]$
d	: Particle diameter	$[\text{m}^2]$
ΔT	: Temperature gradient gas phase/particle	$[\text{K}]$

The heat transfer coefficient is determined according:

$$k_s = \frac{1}{\frac{1}{\alpha} + \frac{d}{2k_{\text{pellet}}}} \quad (3-18)$$

α	: Heat transmission coefficient air/spherical particle	$[\text{W}]$
k_{pellet}	: Thermal conductivity of a Fe_2O_3 /soot mixture [57]	$[\text{W}/(\text{m}\cdot\text{K})]$
k_s	: Heat transfer coefficient	$[\text{W}/(\text{m}^2\cdot\text{K})]$

The heat transmission coefficient of air is determined on the basis of the Nu-number considering the marginal case of minimal Nu_{min} (for $\text{Re}\approx 0$) number being 2 for a overflowed spherical particle [58]:

$$\text{Nu}_{\text{min}} = 2 = \frac{\alpha \cdot d}{k} \quad (3-19)$$

k	: Thermal conductivity of air (Table C-1)	$[\text{W}/(\text{m}\cdot\text{K})]$
-----	---	--------------------------------------

Taking a temperature difference of $\Delta T=10$ K as a basis, the differential equation (Eq. (3-17) results in a time of $\Delta t < 1$ sec for compensation of this temperature difference. A comparison with the heating rate of 10 K/min shows that the heat transfer is more than one order in magnitude smaller. This suggests that a resistance in heat transfer is unlikely.

A calculation of the Mears criterion [59] and the Weisz-Prater module [60] (see Appendix) excludes film and pore diffusion which means that there are no limitations in mass transfer.

3.3.2 Temperature distribution in the catalyst/soot mixture

The measurements using an IR camera revealed heat evolution to start in the middle of the catalyst/soot mixture (Figure 3-12). The reasons for this can be attributed to the boundary stream due to the packed bed. For further discussion of this, reference is made to the fluid dynamic modelling presented in chapter 4.4.1.3. The setting-up of the conservation equations for mass, heat and momentum transport as well as the formulation of the boundary conditions contributes to the understanding of the heat distribution in the packed bed. The location of the maximum temperature is displaced into the outlet direction of the packed bed, which is attributed to convective heat transport.

Furthermore, the recorded surface heat distribution clarifies the problem of reproducible measurements by the micro thermocouples (e.g. Figure 3-7 and Figure 3-8). An even smaller variation in the location of the thermocouple causes differences in the measured temperature. A comparison between Figure 3-12 and Figure 3-7 shows that the IR measurement reveals a maximum differential temperature of 80 K whereas the measurement taken by the micro thermocouple suggests a difference of 60 K for identical reaction conditions.

3.3.3 The effect of varying the gas feed

3.3.3.1 O₂ variation

The variation of O₂ content of the gas feed strongly affects the reaction rate of the catalytic soot oxidation. The sharp TPO profiles using a heating rate of 3.3 K/min (Figure 3-14) are attributed to a strong heat evolution (see chapter 3.3.1.4). An oxygen content of 20 vol.% in the gas feed causes an acceleration of the reaction rate (see Eq. (3-12)), which leads to a temperature of maximum CO₂ volume fraction of 380°C, compared to 408°C for the TPO using 10 vol.% O₂. Moreover, the CO₂ traces of this experiment show oxygen supply to be a key step in catalytic soot oxidation. A doubling in the oxygen content from 10 vol.% to 20 vol.% of the feed results in a shift of ca. 28 K in $T_{\text{CO}_2, \text{max}}$ and a rise in peak CO₂ volume fraction from ca. 7.5 vol.% to ca. 16 vol.%. A decrease of the heating rate from 3.3 k/min to 2 K/min leads to moderate CO₂ evolution (Figure 3-15, $y(\text{CO}_2)_{\text{max}}=0.8$ vol.%, ranging

from 300°C to 500°C). This enables the determination of the reaction order of oxygen by a double-logarithmic evaluation of the recorded data for low levels of conversion. The determined value ($n_{O_2}=1$) is in fair agreement with literature. Reichert assumed n_{O_2} being 1 [23], whereas Neeft et al. [32] found n_{O_2} to range between 0.85 and 0.94 depending on the conversion level of the used PrintexU soot.

In addition, the area of validity for the presented approach is very small. As noted in section 3.2.3.1, the temperature of 365°C offers an optimum compromise between measurable reaction rate and soot conversion ($X \sim 0$). At lower temperatures ($T < 360^\circ\text{C}$) the reaction rate is too small to do any reliable analysis; the measurement error would exceed the coefficient of determination upon the linear regression. At higher temperatures ($T > 380^\circ\text{C}$), the assumption of negligible soot conversion ($X \sim 0$) cannot be met. Moreover, the reaction order of oxygen changes with increasing temperature. At 370°C n_{O_2} is 0.96 while at 375°C n_{O_2} is 0.86 substantiating the findings of Neeft. For both cases the assumption of insignificant soot conversion is still satisfied ($X=0.5\%$ vs. $X=0.7\%$ for the experiment using 20 vol.% O_2).

3.3.3.2 CO variation

The illustrated series of CO variation in the gas feed (Figure 3-17) reveals a strong promotional effect on the soot oxidation on Fe_2O_3 catalyst. The shift of $T_{CO_2,max}$ to lower temperatures is attributed to the exothermic CO oxidation on the Fe_2O_3 catalyst, which is reported to start above 200°C [27]. The temperature of the catalyst/soot mixture rises and accelerates the reaction rate of the catalytic soot oxidation. This is supported by calculating the caloric combustion temperature [61] related to oxidation of 5 vol.% CO in 10 vol.% O_2 and 85 vol.% N_2 ($F=500$ ml/min, $T=T^0$) resulting in a combustion temperature of 750 °C. The experimental measurement of this temperature rise is illustrated in Figure 3-18 and is 260 K higher than the inlet temperature. For reference purpose, the temperature increase ($\Delta T=60$ K) in the experiment done with the same reaction conditions but without CO in the feed is shown in Figure 3-7. Moreover, this temperature rise seems to be so great that even local reduction of the Fe_2O_3 catalyst is possible under these reaction conditions, since the peak CO_2 volume fraction (13 vol.%) is considerably higher compared to the 10 vol.% O_2 inlet volume fraction. Randall [62] showed that reduction of Fe_2O_3 is possible in the presence of CO even at temperatures of only 300°C. Based on these assumptions an additional proportion of $1.6 \cdot 10^{-3}$ mol O_2 (i.e. 7 vol.% referring to 10 mmol Fe_2O_3 and $F=500$ ml/min) is theoretically available thus

leading to a total content of 17 vol.% O₂ in the gas feed. Nevertheless, in-situ XRD studies showed no reduced Fe₂O₃, indicating local reduction only, as well as a fast re-oxidation of reduced iron oxide structures.

For consideration in a real exhaust aftertreatment system these findings suggest the combination of DOC and DPF into one unit to utilise the reaction heat of CO and HC conversion for the oxidation of the trapped soot.

3.3.3.3 CO₂ variation

The addition of CO₂ to the gas feed (Figure 3-19) has only a slight influence on the activity of catalytic soot oxidation. In contrast, the minimal decrease in T_{CO₂,max} may be ascribed to slight blocking of active Fe sites which are, in particular, responsible for the oxidation of CO as it is reported for α-Fe₂O₃ catalyst [27]. Carbon monoxide is always present in the catalytic soot oxidation. It originates from decomposition of oxygen surface complexes on the soot (see chapter 3.3.5) but may not be detected due to its oxidation on the catalyst (see chapter 3.3.1.3). Nevertheless, such small differences between the respective TPO profiles are in the range of experimental reproducibility (see Figure A-1). In addition, carbon conversion according to the Boudouard reaction (C + CO₂ → 2 CO, ΔG_r=+30 kJ/mol at 800 K [63]) can be excluded in the temperature range of the experiment.

3.3.3.4 H₂O variation

The experiments shown in Figure 3-20 exhibit promotional effects by adding water to the gas feed. The amount of water seems not to influence the TPO profiles, which is obvious from comparison of the CO₂ profile using 8.5 vol.% and 2 vol.% H₂O. The curve progression, i.e. peak volume fraction and temperature range of both experiments, is nearly identical. In the literature, several reasons are reported. Ahlström and Odenbrand [64] give two possibilities. The first possibility is a rapid reaction of water and carbon being accelerated by the removal of adsorbed hydrogen atoms by oxygen and the second possibility is an increase in BET surface area due to gasification of carbon by water:



This coincides with the findings presented (Figure 3-20 and Figure 3-21) and exhibited beneficial effects in the activity for both, the catalytic and non-catalytic oxidation of carbon. Neeft et al. [32] ascribe an enhancement in activity due to changes in the carbon surface. Although they see the occurrence of the water-gas-

shift reaction in the gas phase as rather unlikely, they observed an increase in the CO₂/CO ratio by adding water to the feed gas.

3.3.4 Temperature programmed reduction of α -Fe₂O₃ with soot

The studies presented here were performed in oxygen-free atmosphere and contribute to the understanding of the interaction between catalyst and soot. In this solid-solid reaction 10 mmol Fe₂O₃ and 5 mmol soot (assumed as carbon) theoretically provide total conversion of the soot under reduction of the iron oxide:



$$\Delta H_r \quad : +170 \text{ kJ/mol (T=298 K and p=1 bar)}$$

$$\Delta G_r \quad : +88 \text{ kJ/mol (T=298 K and p=1 bar)}$$

$$\Delta G_r \quad : -122 \text{ kJ/mol (T=1100 K and p=1 bar) [63]}$$

This reaction implies a continuous transfer of oxygen from the crystal lattice of the Fe₂O₃ to the carbon (Figure 3-22). The observed low-temperature CO_x formation corresponds to an amount of 1.73 mmol CO_x thus suggesting catalyst reduction according to Eq. (3-22) to be the major reaction. This route includes the theoretical production of 1.66 mmol CO₂ for the amount of Fe₂O₃ and carbon (5 mmol) used.



$$\Delta H_r \quad : +77 \text{ kJ/mol (T=298 K and p=1 bar)}$$

$$\Delta G_r \quad : -3 \text{ kJ/mol (T=298 K and p=1 bar)}$$

$$\Delta G_r \quad : -222 \text{ kJ/mol (T=1100 K and p=1 bar) [63]}$$

The high-temperature evolution of CO₂ and CO in Figure 3-22 indicates further reduction of the Fe₃O₄:



$$\Delta H_r \quad : +215 \text{ kJ/mol (T=298 K and p=1 bar)}$$

$$\Delta G_r \quad : +134 \text{ kJ/mol (T=298 K and p=1 bar)}$$

$$\Delta G_r \quad : -72 \text{ kJ/mol (T=1100 K and p=1 bar) [63]}$$



$$\Delta H_r \quad : +193 \text{ kJ/mol (T=298 K and p=1 bar)}$$

$$\Delta G_r \quad : +127 \text{ kJ/mol (T=298 K and p=1 bar)}$$

$$\Delta G_r \quad : -50 \text{ kJ/mol (T=1100 K and p=1 bar) [63]}$$

The Gibb's free enthalpy (ΔG_r) of the overall reaction equation (Eq. (3-21)) shows that the reaction necessitates high temperatures, especially for the reaction step leading to FeO (Eq. (3-23)). But the thermodynamic calculations of ΔG_r at 1100 K, which coincide with the temperature range of experimental CO_x formation (Figure 3-22), support the thermodynamical plausibility of the reaction equations presented. In addition, ΔG_r of -50 kJ/mol ($T=1100$ K) proves that CO formation according to Eq. (3-24) is also reasonable. In this respect CO production according to the Boudouard reaction ($\text{C} + \text{CO}_2 \rightarrow 2 \text{CO}$, $\Delta G_r=-22$ kJ/mol at 1100 K) is thermodynamically plausible. Moreover, the thermal decomposition of the Fe_2O_3 , which follows the reaction



reveals a free enthalpy of $\Delta G_r=+86$ kJ/mol at 1100 K and is therefore not considered. Referring to the high temperature CO_x formation in Figure 3-22 the amount of 3.17 mmol CO_x produced is close to a remaining theoretical quantity of 3.44 mmol carbon (derived from Eq. (3-22)). In addition, the XRD pattern (Figure 3-24, left) taken after the experiment shows the catalyst exclusively being in the wuestite phase (FeO). This substantiates total carbon conversion upon temperature programmed reduction on Fe_2O_3 with soot in tight contact. Furthermore, this implies maintenance of the contact between catalyst and soot even at high carbon conversion levels, despite changes in the crystalline structure of the iron oxide ($\text{Fe}_2\text{O}_3 \rightarrow \text{Fe}_3\text{O}_4 \rightarrow \text{FeO}$) and in the morphology of the soot. Similar observations were reported by Reichert. His HRTEM images prove contact of iron oxide and soot up to 90 % of conversion under oxygen-rich conditions [23].

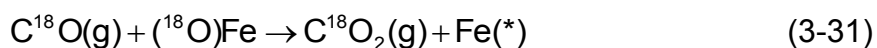
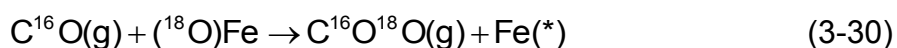
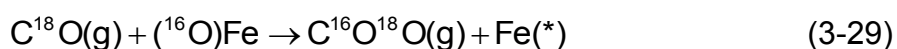
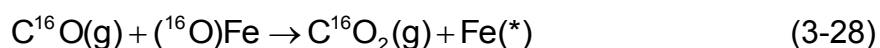
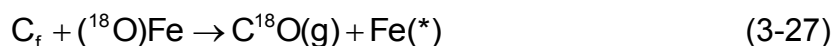
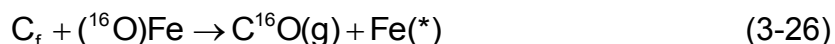
When using a loose contact mixture of Fe_2O_3 and soot (Figure 3-23) the CO_x profile shifts to higher temperatures including several shoulders. This may be attributed to different distances between the soot particles and the Fe_2O_3 resulting in different energy requirements needed to overcome this distance. This supports the assumption of soot migration as it was discussed for loose contact Fe_2O_3 /soot mixtures (see chapter 3.3.1.2). In addition, the XRD pattern (Figure 3-24, right), which reveals the Fe_2O_3 being reduced to Fe_3O_4 only, and the formed amount of CO_x (2.3 mmol) indicate incomplete soot conversion (46 %). This also suggests that the distance between Fe_2O_3 and soot in loose contact mode has a limiting influence on soot oxidation. To summarise, in loose contact mode the distance between catalyst

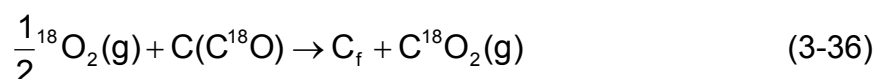
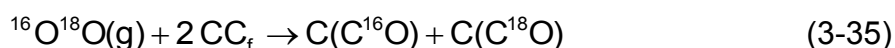
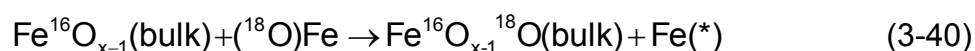
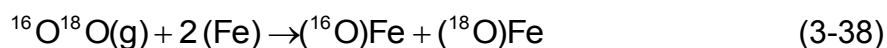
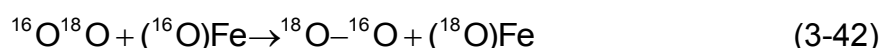
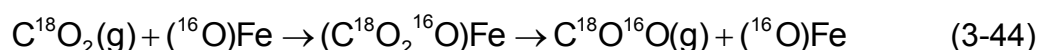
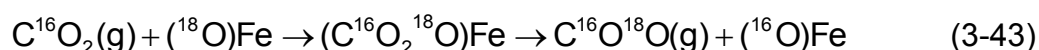
and soot is too large and becomes rate determining for the $\text{Fe}_2\text{O}_3/\text{C}$ reaction (Eq. (3-21)).

3.3.5 Isotopic studies with $^{18}\text{O}_2$

The isotopic TPO experiments shown in section 3.2.5 were carried out to aid the understanding of the mechanism of the soot oxidation on Fe_2O_3 catalysts. The use of $^{18}\text{O}_2$ enables the oxygen producing CO_2 to be identified. For example, the ^{18}O containing CO_2 is associated with gas phase oxygen, while ^{16}O containing CO_2 refers to oxygen from the catalyst. The variation of experimental conditions aims to elucidate the effect of contact mode, amount of catalyst and morphology of the catalyst. For interpretation of the product spectra recorded, the formation of the C^xO_2 species can be explained by using several reaction routes supposing catalytic and non-catalytic soot oxidation. However, these steps reflect overall processes and are no elementary reactions. Also, this is just a model to provide better understanding, based on reasonable pathways considered as the major routes. In the reaction scheme $(^x\text{O})\text{Fe}$ denotes oxygen adsorbed on an active Fe surface site (originated from dissociative adsorption), Fe^* implies a partially reduced Fe surface site, while C_f is an active carbon site of the soot and $\text{C}(\text{C}^x\text{O})$ represents an oxygen containing surface group of the soot formed in oxidation or initially present. The neighbouring carbon site can be activated by C^xO desorption. Terminal, saturated $\text{C}(\text{CH})$ groups of the soot are not included in the model since it has been shown that oxygen atoms, transferred from the catalyst, diffuse to the active C_f sites [23]. Furthermore, $\text{C}^x\text{O}(\text{g})$ was not found upon the isotopic TPO. The $\text{C}^x\text{O}(\text{g})$, included in the reaction scheme, is assumed to be oxidised to $\text{C}^x\text{O}_2(\text{g})$ due to the use of the Fe_2O_3 catalyst (Eqs. (3-23)-(3-26)), which was shown to exhibit high activity upon CO oxidation [27].

Catalytic CO_x formation



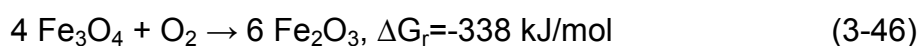
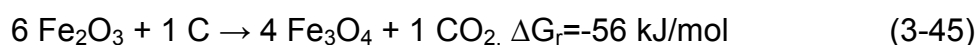
Non-catalytic CO_x formation**Regeneration of the catalyst by oxygen****Oxygen exchange between gas phase and catalyst oxygen****Oxygen exchange by surface carbonates**

On the basis of these suggested reaction steps, the formation of $C^{16}O_2$, $C^{16}O^{18}O$, $C^{18}O_2$ as well as ${}^{16}O^{18}O$ is described qualitatively. Furthermore, non-catalytic C^xO_2 production is not included, substantiated by studies of Sendt and Haynes [51]. They showed through DFT calculations that O_2 chemisorption on graphite rings exhibits low activation energies. Subsequent CO and CO_2 desorption, respectively, shows CO desorption as the major route.

Formation of $C^{16}O(g)$ and $C^{16}O_2(g)$

The catalytic formation of $C^{16}O_2(g)$ can be explained by different potential routes. $C^{16}O_2(g)$ is produced by reaction of $C^{16}O(g)$ and surface $({}^{16}O)Fe$ of the iron oxide

resulting in a partially reduced Fe site located on the catalyst surface (Eq. (3-28)); catalytic activity of Fe₂O₃ upon CO oxidation was already shown in previous studies [27]. For the formation of C¹⁶O(g) two mechanisms are considered. The first mechanism includes C¹⁶O(g) which originates from the soot due to thermal decomposition of ¹⁶O containing surface species (Eq. (3-32)). These surface species are either initially present on the soot surface or are formed via gas phase oxidation by ¹⁶O¹⁸O (Eq. (3-35)), which originates from oxygen exchange between gas phase and catalyst (Eq. (3-41) and Eq. (3-42)). The second mechanism includes C¹⁶O(g) which originates from interaction between catalyst and soot (Eq. (3-26)). TPO studies of the Fe₂O₃/soot mixtures imply a low as well as a high temperature regime of C¹⁶O₂(g) formation (e.g. Figure 3-26 and Figure 3-28). The C¹⁶O₂(g) formation at low-temperatures (200°C-310°C) could be explained by the pathway of Eq. (3-32) and Eq. (3-28), i.e. desorption of C¹⁶O(g) and subsequent oxidation on the catalyst; existence of oxygen containing surface species on soot was already confirmed, e.g. by Reichert et al. [23] and by Mul [35]. Our own studies (appendix, Figure E-3) exhibit desorption of CO (0.98 μmol/g) as well as CO₂ (0.92 μmol/g) from the C₃H₆ soot, corresponding to ca. 10 μmol oxygen for the used mass of 3.7 mg soot in the isotopic experiments under the assumption of complete desorption between 200°C to 300°C and involvement of the whole soot particle. This amount of oxygen may coincide with the integral quantity of the low-temperature C¹⁶O₂(g), which is ca. 4.5 μmol in the experiment with α-Fe₂O₃ and soot in tight contact (ratio 2:1, Figure 3-26). Furthermore, the temperature programmed reduction on Fe₂O₃ using soot as reducing agent (Figure 3-22, inlay) showed that Fe₂O₃ is able to release and transfer oxygen to a soot particle, even at temperatures of less than 250°C (even though in very small amounts, i.e. 0.8 μmol O₂). However, the presence of a reducing agent, i.e. the soot, is the driving force for transfer of oxygen from catalyst to soot. The results of the O₂-TPD of the α-Fe₂O₃ sample (Figure 5-4) offered no thermal release of oxygen. The calculation of the thermodynamics (T=500K, p=1bar) for Fe₂O₃ reduction by carbon and subsequent re-oxidation of Fe₃O₄ to be thermodynamically possible [63].



Moreover, strong oxygen pumping [28], i.e. ^{16}O transfer from catalyst to soot (Eq. (3-26) and (3-28)), has to be considered for the formation of $\text{C}^{16}\text{O}(\text{g})$ and $\text{C}^{16}\text{O}_2(\text{g})$ in the low-temperature range (200-300°C) of TPO as well.

The $\text{C}^{16}\text{O}_2(\text{g})$ formation at higher temperatures (>550°C) can mainly be ascribed to oxidation of $\text{C}^{16}\text{O}(\text{g})$ by ^{16}O present on the catalyst (Eq. (3-28)). At this, $(^{16}\text{O})\text{Fe}$ results from regeneration of reduced Fe^* surface sites via bulk ^{16}O (Eq. (3-39)). The origin of $\text{C}^{16}\text{O}(\text{g})$ is explained via direct interplay between soot and catalyst (Eq. (3-26)) or via oxidation of soot by $^{16}\text{O}^{18}\text{O}$ (Eq. (3-35)) and subsequent desorption of $\text{C}^{16}\text{O}(\text{g})$ (Eq. (3-32)), which may be seen as the favoured pathway. This is substantiated by traces of $^{16}\text{O}^{18}\text{O}$, $\text{C}^{16}\text{O}_2(\text{g})$ and $\text{C}^{16}\text{O}^{18}\text{O}(\text{g})$ (e.g. Figure 3-26); an increase in $^{16}\text{O}^{18}\text{O}$ volume fraction leads to a rise of the C^{16}O_2 signal and a simultaneous drop of the $\text{C}^{16}\text{O}^{18}\text{O}(\text{g})$ profile.

When using a molar Fe_2O_3 :soot ratio of 1:2 (Figure 3-30), the lower amount of formed $\text{C}^{16}\text{O}_2(\text{g})$ (30 μmol vs. 101 μmol for 2:1 ratio) and the peak volume fraction, respectively, can be explained by the lower initial volume fraction of available ^{16}O species due to the use of smaller amounts of catalyst.

The $\text{C}^{16}\text{O}_2(\text{g})$ formation in presence of nano-sized Fe_2O_3 (Figure 3-32) suggests effects of the morphology of the catalyst. Despite the same reaction conditions, as compared to the bulk $\alpha\text{-Fe}_2\text{O}_3$ sample (Figure 3-26), a completely different CO_2 profile is obtained. The occurrence of two $\text{C}^{16}\text{O}_2(\text{g})$ peaks in Figure 3-32 is ascribed to thermal instability of the sample. In chapter 4.2.4, we will see that the C^{16}O_2 high-temperature peak of the nano-sized Fe_2O_3 can be explained by structural changes in the catalyst. The low production of 30 μmol $\text{C}^{16}\text{O}_2(\text{g})$ is attributed to less contribution of bulk oxygen due the morphology of the catalyst, i.e. smaller primary particles ($d_p=15$ nm vs. $d_p(\text{bulk Fe}_2\text{O}_3)=70$ μm) and poorer crystalline structure (Table 5-4) as compared to the bulk $\alpha\text{-Fe}_2\text{O}_3$. PXRD analysis revealed a crystallinity of about 90 % consisting of 63 % $\gamma\text{-Fe}_2\text{O}_3$ and 27 % Fe_3O_4 , while the bulk Fe_2O_3 exhibited $\alpha\text{-Fe}_2\text{O}_3$ to be the only phase without any amorphous domains. Re-oxidation of partially reduced Fe surface sites, which is seen to be crucial for the catalytic activity of Fe_2O_3 , can be explained either via oxidation by $^{18}\text{O}_2(\text{g})$ and $^{16}\text{O}^{18}\text{O}(\text{g})$ (Eqs. (3-37) and (3-38)) or by bulk O transport and subsequent oxidation of the bulk (sequence along Eqs. ((3-39), (3-40) and (3-37)). The reaction step, which explains the oxygen supply from the bulk (Eq. (3-39)), can be considered as the predominant mechanism for the $\alpha\text{-Fe}_2\text{O}_3$ revealing a high crystalline order. This bulk Fe_2O_3 provides formation

of 101 $\mu\text{mol C}^{16}\text{O}_2(\text{g})$, whereas for the nano-sized Fe_2O_3 it is 30 μmol only. Furthermore, the re-oxidation rate of bulk oxygen seems to be lower compared to that of surface oxygen. This is indicated by the $\text{C}^{16}\text{O}_2(\text{g})$ peak which is located at the highest temperatures among all C^xO_2 species at all the isotopic experiments performed and by the degree of oxygen exchange. The degree of oxygen exchange of the $\alpha\text{-Fe}_2\text{O}_3$ is smaller compared to the nano-sized Fe_2O_3 (52 % vs. 60 %). This is ascribed to the bigger surface area (12 m^2/g vs. 74 m^2/g , see Table 5-4) and the lower crystallinity of the nano-sized material. Studies of Kingery [65] and Reddy [66] make a comparison between the mobility of inner crystalline oxygen and the diffusion rate of oxygen due to ^{18}O exchange between gas phase and $\alpha\text{-Fe}_2\text{O}_3$. At 600°C bulk oxygen transport is determined to be $2 \cdot 10^{-30} \text{ m}^2/\text{s}$ while oxygen diffusion due to gas phase exchange is calculated to be $4 \cdot 10^{-26} \text{ m}^2/\text{s}$. This shows that the re-oxidation by gas phase oxygen is favoured. However, Reddy identifies the area of validity for his calculations as being between 850°C-1077°C only. Nevertheless, at 950°C the rate of bulk O transport is $6 \cdot 10^{-20} \text{ m}^2/\text{s}$, while gas phase oxygen exchange is $3 \cdot 10^{-19} \text{ m}^2/\text{s}$. This indicates that both processes are almost in the same range of magnitude and that both pathways for re-oxidation (gas phase exchange, Eqs. (3-37) and (3-38), versus bulk oxygen transfer, Eqs. (3-39) and (3-40) are reasonable at high temperatures.

Formation of $\text{C}^{16}\text{O}^{18}\text{O}$

The formation of the cross product $\text{C}^{16}\text{O}^{18}\text{O}(\text{g})$ can be described by two routes. The first is via oxidation of $\text{C}^x\text{O}(\text{g})$ by $(^x\text{O})\text{Fe}$. The second route is via oxygen exchange between catalyst and $\text{C}^x\text{O}_2(\text{g})$ by surface carbonates, where $\text{C}^{16}\text{O}_2(\text{g})$ adsorbs in a first step on a $(^{18}\text{O})\text{Fe}$ sites and subsequently desorbs as $\text{C}^{16}\text{O}^{18}\text{O}(\text{g})$ under oxygen exchange with the catalyst (Eq.(3-43) and (3-44)). The first route implies two pathways; the oxidation of $\text{C}^{18}\text{O}(\text{g})$ by $(^{16}\text{O})\text{Fe}$, and the of $\text{C}^{16}\text{O}(\text{g})$ and $(^{18}\text{O})\text{Fe}$ (Eq. (3-29) and Eq. (3-30)). The first pathway requires $(^{16}\text{O})\text{Fe}$ surface sites, which are the pre-dominant surface species at the beginning of the TPO, while they are formed at higher temperatures by re-oxidation of reduced Fe sites, either by bulk-oxygen (Eq. (3-39)) or by gas-phase $^{16}\text{O}^{18}\text{O}(\text{g})$ (Eq. (3-38)). The gaseous educt $\text{C}^{18}\text{O}(\text{g})$ originates from catalytic oxidation of carbon (Eq. (3-27)) by $(^{18}\text{O})\text{Fe}$ or from direct oxidation of soot with $^{18}\text{O}_2$ as well as $^{16}\text{O}^{18}\text{O}(\text{g})$ (Eqs. (3-33), (3-34) and (3-35)). The second pathway, which is only relevant for the starting period of the TPO, requires $(^{18}\text{O})\text{Fe}$ surface sites originating from re-oxidation of partially reduced surface sites by $^{18}\text{O}_2$

(Eq. (3-37) and (3-38)) as well as presence of $C^{16}O(g)$. $C^{16}O(g)$ forms at the beginning of the TPO by catalytic oxidation of carbon (Eq. (3-26)) involving $(^{16}O)Fe$. However, the variation of the reaction conditions on isotopic TPO reveals no significant differences among the $C^{16}O^{18}O(g)$ traces. All the experiments show huge production of $C^{16}O^{18}O(g)$ in the same range (Table 3-8). Furthermore, the type of contact (137 μmol for tight contact vs. 144 μmol for loose contact) as well as the type of catalyst (133 μmol for the nano-sized Fe_2O_3 in tight contact) seems not to affect the formed quantity of the cross product. This indicates the same mechanism for the formation of $C^{16}O^{18}O(g)$, independent from the reaction conditions. The major part of the cross product formation may be attributed to the second route implying carbonate formation on the catalyst, i.e. oxygen adsorption of $C^{16}O_2(g)$ on $(^{18}O)Fe$ or $C^{18}O_2(g)$ on $(^{16}O)Fe$ and subsequent desorption of $C^{16}O^{18}O(g)$ and remaining $(^{16}O)Fe$ and $(^{18}O)Fe$, respectively (Eqs. (3-43) and (3-44)). The existence of such carbon complexes on the Fe_2O_3 surface was already shown in previous studies [27].

Formation of $C^{18}O_2$

The formation of $C^{18}O_2$ is associated with the reaction of $(^{18}O)Fe$ surface species with gas phase $C^{18}O(g)$ (Eq. (3-31)). The origin of these educts was already explained above (Eqs. (3-27), (3-33), (3-37) and (3-38)). When using a molar Fe_2O_3 :soot ratio of 1:2 $C^{18}O_2(g)$ forms as the main product as shown in Table 3-8 (150 μmol for a molar ratio of 1:2 vs. 69 μmol for 2:1, both tight contact). This can be attributed to the lower amount of ^{16}O being present in the catalyst, i.e. $Fe_2^{16}O_3$. Consequently, CO_2 formation along pathways, which include ^{16}O educts, decreases. Moreover, relative small amount of $C^{18}O_2(g)$ is also found in the TPO with the loose contact mixture of α - Fe_2O_3 :soot of 2:1 compared to the respective experiment with tight contact mixture (80 μmol vs. 69 μmol). However, the overall amount of exchanged ^{18}O , in reference to the HTPR results, is for both experiments similar (669 μmol vs. 667 μmol , see Table 3-7). The loose contact study exhibits more $^{16}O^{18}O$ compared to the tight contact TPO (422 μmol vs. 330 μmol), which indicates preferred oxygen exchange with the gas phase (Eq. (3-41) and (3-42)). This can be attributed to limited contact between catalyst and soot in case of the loose contact catalyst/soot mixture.

General aspects

i) The effect of the contact mode

From Figure 3-26 and Figure 3-28 it is obvious that loose contact causes a broadening of the CO₂ profile shifting up to 1000°C. Additionally, as already described above, C¹⁸O₂ production is favoured in the tight contact Fe₂O₃/mixture, whereas the formation of ¹⁶O¹⁸O is more prominent for loose contact mode (see Table 10 and 11). Both effects can be attributed to a limited number of contact points between catalyst and soot particle [67]. Overcoming the distance between catalyst and soot by migration of soot particles is assumed to have great influence on the reaction rate (for further discussion see chapter 3.2.1.2).

ii) The effect of a different catalyst modification

The effect of a different catalyst modification (i.e. crystallinity, surface area and primary particle diameter) is obvious by comparing the isotopic TPO using bulk and nano-sized Fe₂O₃ (Figure 3-26 and Figure 3-32). The nano-sized Fe₂O₃ shows the highest activity upon soot oxidation, apparent by a shift to lower temperatures of the CO₂ trace of about 100 K. Moreover, the overall quantity of C¹⁶O₂(g) formed is increased as referred to α-Fe₂O₃ (130 μmol vs. 101 μmol), while the amount of C¹⁸O₂(g) produced is decreased (43 μmol vs. 101 μmol). This can be ascribed to the high surface area (74 m²/g vs. 12 m²/g) of the nano-sized Fe₂O₃ which provides more ¹⁶O adsorbed on Fe surface sites.

iii) Variation of the amount of catalyst

The variation of the molar catalyst:soot ratio from 2 to 0.5 (Figure 3-26 and Figure 3-30) results in a different CO₂ spectrum, although the remaining reaction parameters are kept constant. Despite the fact that C¹⁶O₂ formation shows a similar peak temperature, the overall quantity is decreased for the TPO experiment with a molar ratio of Fe₂O₃:soot of 1:2 (101 μmol vs. 30 μmol) due to a smaller amount of ¹⁶O being present in the Fe₂O₃ used. Moreover, C¹⁶O¹⁸O(g) and C¹⁸O₂(g) are shifted to lower temperatures in the TPO with a smaller amount of catalyst. This aspect can be attributed to the lower heat capacity of the packed bed due to smaller amounts of catalyst. Since the mass of soot is kept constant, the reaction heat produced is distributed in a different volume (with different heat capacity) depending on the mass of catalyst used. This results in difference in the heat release in the packed bed. A detailed discussion of these effects was already presented in chapter 3.3.1.3.

iv) Oxygen exchange

The oxygen uptake of $^{18}\text{O}_2$ by the catalyst can be explained by Eqs. (3-37)-(3-42). The oxygen vacancies in the bulk of the Fe_2O_3 (Eq. (3-39)) are assumed to be filled by gas phase $^{18}\text{O}_2$. This uptake and oxygen exchange, respectively, is substantiated by the oxygen balance of the isotopic experiments including TPO and HTPR. To differentiate between ^{18}O , which contributes to gas phase oxygen exchange, and ^{18}O which participates in soot oxidation, Table 3-7 shows the exchanged overall quantity of ^{18}O derived from HTPR. The balance presented is based on the assumption that the total amount of exchanged ^{18}O is composed of a quantity, which is ascribed to oxygen substitution of gas phase oxygen ($^{18}\text{O}_2$, Eq. (3-41) and $^{16}\text{O}^{18}\text{O}$, Eq. (3-42)) and an amount, which is attributed to oxygen exchange due to carbon oxidation (Eq. (3-37) and Eq. (3-38)). These quantities suggest that bulk oxygen is participating in the soot oxidation. This contradicts the findings of Reichert [23]. He assumed that only the surface or sub-surface layer of the iron oxide is involved in the reaction. But, with the assumption of complete coverage of the Fe_2O_3 surface with spherical O atoms ($d=0.14$ nm [68]) a maximal amount of $31.3 \mu\text{mol O}$ is available for 96.3 mg Fe_2O_3 ($S_{\text{BET}}=12\text{m}^2/\text{g}$). A quantity of $259 \mu\text{mol } ^{16}\text{O}$ clearly indicates that the derived abundance of oxygen considerably exceeds this quantity thus substantiating the participation of bulk O in the catalytic soot oxidation.

Table 3-7: Balance and origin of exchanged ^{18}O .

Experiment	Total ^{18}O (derived from HTPR) μmol	Formed amount of $^{16}\text{O}^{18}\text{O}$ μmol	^{18}O in soot oxidation μmol
Bulk $\alpha\text{-Fe}_2\text{O}_3$ tight contact, 2:1	796	330	466
Bulk $\alpha\text{-Fe}_2\text{O}_3$ loose contact, 2:1	669	422	247
Bulk $\alpha\text{-Fe}_2\text{O}_3$ tight contact, 1:2	415	178	237
Nano-sized Fe_2O_3 tight contact, 2:1	927	513	414

Table 3-8: Formed amount of CO₂ and H₂O in the TPO and HTPR experiments with Fe₂O₃ catalysts.

Sample	C ¹⁶ O ₂ μmol	C ¹⁶ O ¹⁸ O μmol	C ¹⁸ O ₂ μmol	H ₂ ¹⁶ O μmol	H ₂ ¹⁸ O μmol
Bulk α-Fe ₂ O ₃ tight contact, 2:1	101	137	69	704	796
Bulk α-Fe ₂ O ₃ loose contact, 2:1	86	144	80	934	669
Bulk α-Fe ₂ O ₃ tight contact, 1:2	30	127	150	234	415
Nano-sized Fe ₂ O ₃ tight contact, 2:1	130	133	43	641	927

3.4 Summary and conclusion of the mechanistic studies

Based on the discussion presented above, the following conclusions have been drawn:

- Bulk oxygen is involved in catalytic soot oxidation on Fe₂O₃ and therefore the ratio of catalyst/soot affects the total amount of C¹⁶O₂ formed. The higher the proportion of Fe₂O₃ the higher the number of C¹⁶O₂.
- The catalyst morphology (i.e. crystallinity, surface area and particle diameter) affects the pathway for CO₂ formation because of a different quantity of (O)Fe present on the catalyst surface. Smaller particles and lower crystallinity seem to be beneficial for the performance of the Fe₂O₃.
- The local temperature in the catalyst/soot mixture depends on the amount of catalyst. This influences heat transfer and the reaction rate. Nevertheless, an optimum mass of catalyst is required.
- An insufficient amount of contact points between the catalyst and the soot decreases the activity upon catalytic soot oxidation.

Figure 3-36 shows a schematic illustration of a global reaction mechanism of the catalytic soot oxidation on Fe₂O₃. Oxygen is transferred from the catalyst surface to the soot by contact points. The resulting oxygen defect sites on the iron oxide surface may be refilled either by migration of (O)Fe sites and re-oxidation by gas phase oxygen, respectively, or by bulk oxygen. The oxygen deficiency in the bulk is balanced in a further step by migration of O atoms from the surface layer to the bulk

of the Fe_2O_3 catalyst. In this respect, the activity of the nano-sized Fe_2O_3 suggests O migration via (O)Fe sites to be the favoured route. To get a more detailed understanding of these processes future studies should focus on understanding the detailed mechanism for O transfer from the catalyst to the soot (e.g. spill-over) and measure the oxygen surface diffusion on the iron oxide.

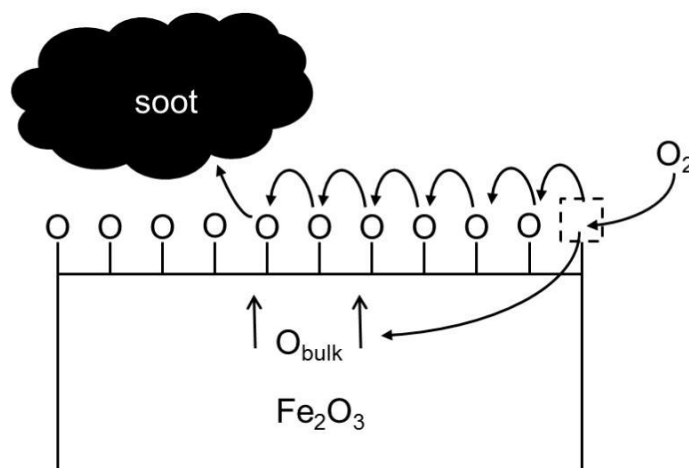


Figure 3-36: Schematic illustration of the mechanism of catalytic soot oxidation on Fe_2O_3 .

In summary, important findings for the development of advanced Fe_2O_3 catalysts may be formulated as follows:

- An advanced catalyst requires both crystalline and amorphous domains to assure bulk oxygen as well as surface oxygen transport which is required for re-oxidation of reduced Fe surface sites.
- Adequate oxygen uptake from the gas phase needs numerous active surface Fe sites, indicating that a catalyst with a high surface area and a high number of (O)Fe surface sites is required.
- To ensure sufficient contact points a nano-sized material in the same dimension as the soot particles (i.e. ca. 50 nm) is required.

4 Kinetic and fluid dynamic modelling of catalytic soot oxidation on Fe₂O₃ catalyst

This chapter covers the kinetic modelling of the catalytic soot oxidation and follows up the experimental results presented in chapter 3. The findings of the mechanistic studies form the basis for the kinetic and fluid dynamic description of the system. The foundation for the modelling is given by the presented TPO studies of Fe₂O₃/soot mixtures already presented in chapter 3.1.3. In the first step, unknown kinetic parameters are determined and validated by a 1-dimensional kinetic model. In the second step, the kinetic expression determined is coupled with fluid dynamics to obtain a 2-dimensional model, which is able to provide fundamental insights in the fluid dynamics of catalytic soot oxidation (i.e. heat distribution, CO₂ evolution, velocity field etc.). The setting-up of the 1-d model requires the development of a reactor model which can describe the experiment sufficiently, providing a suitable computation time for the determination of the unknown kinetic parameters. In further development processes, targeted catalyst design will support the development of efficient catalysts using knowledge of factors affecting the reaction rate of soot conversion, such as heat release, occurrence of hot-spots and fluid mechanics.

4.1 Development of a reactor model

The reactor model must implement two issues: (1) sufficient accuracy to mimic the experimental reality and (2) minimal computing time due to the least-square estimator used for the determination of unknown parameters. The approach to cover both issues is to set-up a 1-d model based on an ideal reactor (i.e. CSTR, PFR or tanks-in-series reactor) which allows the determination of the Bodenstein (Bo) number and the choice of a reactor model must be consistent with this Bo-number. The Bo number is defined as ratio of convectional mass transport and axial dispersion [69,70]:

$$Bo = \frac{u \cdot L}{D_{ax}} \quad (4-1)$$

u	: Flow rate	[m/s]
L	: Length of the reactor	[m]
D _{ax}	: Dispersion coefficient	[m ² /s]

A high Bo number ($Bo \gg 1$) indicates a flow dominated by convective transport, and can be described by a plug flow reactor (PFR). In contrast, a low Bo number ($Bo \ll 1$) has a diffusive dominated flow and is described by a continuously operated stirred tank reactor (CSTR). Bo numbers of ~ 1 can be well described by the tanks-in-series model. The number of tanks to be used can be calculated according to equation (4-2) [60,69]:

$$\frac{1}{N} = \frac{2}{Bo} + \frac{8}{Bo^2} \quad (4-2)$$

N : Number of CSTR's [/]

First of all, the Bo number for the reaction volume within the TPO experiments is determined. In the TPO studies, the catalyst/soot mixture is provided in the form of a packed bed in a glass tube as depicted in Figure 4-1 (left), i.e. the packed bed represents the location of the reaction.



Figure 4-1: Schematic illustration of the experimental set-up for determination of the Bo Number. Left: Reactor tube (length L) with packed bed (length x). Right: Empty reactor tube (length L-x).

The practical approach for the calculation of the Bo number requires knowledge of the retention time behaviour of the system examined. Therefore, a step experiment is performed. At time $t=0$ a tracer substance is dosed into the inflow of the reactor. This marked reaction mass displaces the non-marked mass and causes a gradual increase of the tracer concentration at the reactor outlet. The amount of tracer is quantified according equation (4-3):

$$\frac{dn}{dt} = F \cdot dc \quad (4-3)$$

n	: Amount of substance	[mol]
t	: Time	[s]
F	: Volume flow	[m ³ /s]
c:	: Concentration	[mol/m ³]

This enables the determination of the sum function on the basis of the step experiment [60,70]:

$$F(t) = \int_0^t E(t) \cdot dt = \frac{F}{\int_0^{c_0} F \cdot dc} \int_0^c dc = \frac{c(t)}{c_0} \quad (4-4)$$

The differentiation of the sum curve results in the probability curve $E(t)$:

$$E(t) = \frac{dF(t)}{dt} \quad (4-5)$$

This $E(t)$ curve is the basis for the calculation of the mean residence time \bar{t} and the variance σ^2 :

$$\bar{t} = \int_0^{\infty} t \cdot E(t) dt \quad (4-6)$$

$$\sigma^2 = \int_0^{\infty} t^2 \cdot E(t) dt - \bar{t}^2 \quad (4-7)$$

Finally, the Bo number is defined as follows [60,70]:

$$Bo = \frac{\bar{t}}{\sigma^2} = \frac{u \cdot L}{D_{ax}} \quad (4-8)$$

The experimental identification of the sum curve is done by dosing 7.5 vol.% CO₂ in 500 mL/min N₂ into the reactor. The outlet concentration is recorded dependent on the time. However, to differentiate between the retention time behaviour of the packed bed and the complete reactor, an approach presented by Aris is used. This states the additivity of means and variances of the $E(t)$ curves for small extents of dispersion [70]. The mean residence time \bar{t} and the variance of the tube reactor, including the packed, is determined (Figure 4-1, left) as well as \bar{t} and σ^2 of an empty tube reactor, shortened by the length x of the packed bed (Figure 4-1, right). This allows the identification of the Bo number of the packed bed:

$$\frac{\sigma_2^2 - \sigma_1^2}{(\bar{t}_2 - \bar{t}_1)} = \frac{\Delta\sigma^2}{(\Delta\bar{t})^2} = \frac{1}{2 \cdot Bo} \quad (4-9)$$

Figure 4-2 illustrates the input signal and the experimentally measured outlet concentration of the CO₂ tracer.

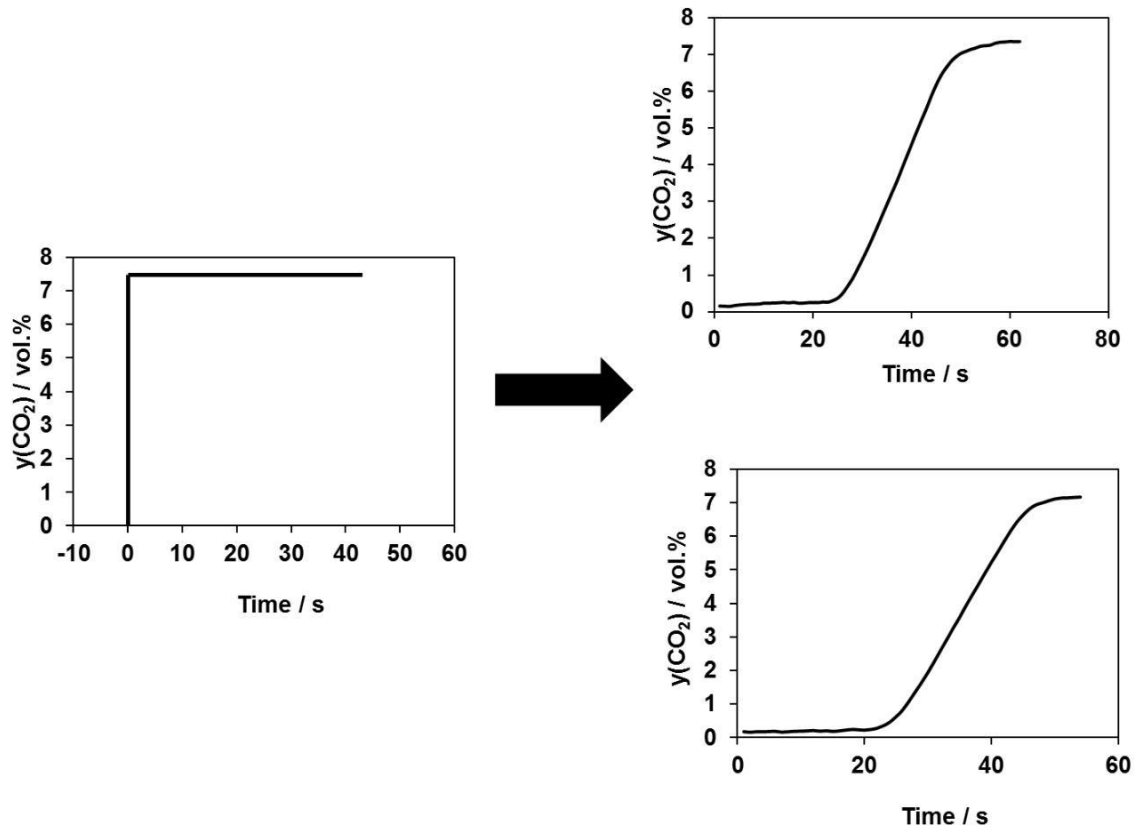


Figure 4-2: Step experiment: CO₂ signal at the reactor inlet (left) and CO₂ volume fraction at the outlet (right). The upper CO₂ curve corresponds to the measurements of the reactor with the packed bed (length L) and the lower CO₂ curve corresponds with the measurements of the empty reactor (length L-x). L=800 mm and x= 25mm.

A standardisation of the CO₂ output signals with the inlet concentration c_0 and a derivative with respect to time results in the probability function $E(t)$. This is depicted in a smoothed form in Figure 4-3 for the reactor with and without packed bed.

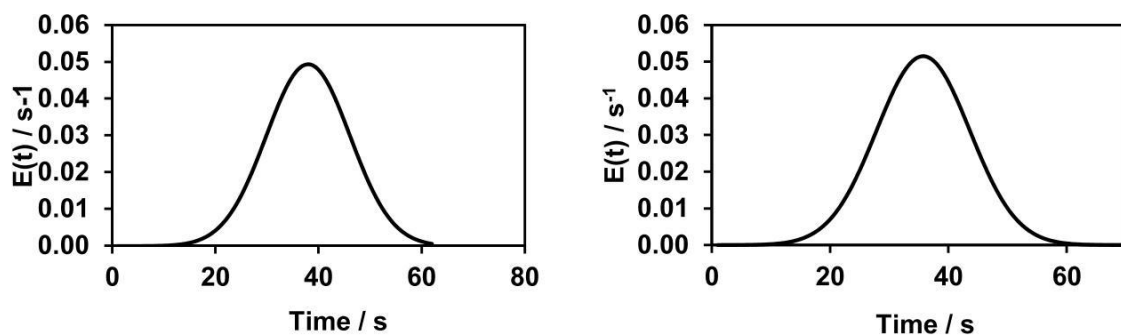


Figure 4-3: Smoothed $E(t)$ curve of the reactor with the packed bed (length L, left) and the empty reactor (length L-x, right).

On the basis of equations (4-6) and (4-7) the mean residence time for the reactor with the packed bed is calculated to $\bar{t} = 37.8$ s with $\sigma^2 = 68.2$ s². \bar{t} is quantified to 36.3 s and σ^2 to 40.9 s² for the shortened reactor without the packed bed. The Bo number of the reactor section including the packed bed can be determined according

to equation (4-9) resulting in a value of $Bo=0.41$ indicating CSTR behaviour. Nevertheless, the reactor model is based on several simplifications. The retention time behaviour is measured at isothermal conditions (room temperature) and change of the packed bed due to conversion of soot is not assumed, i.e. the soot proportion is negligible. In conclusion, the behaviour of the packed bed can be described in a simplified way by the CSTR model, providing the basis for the determination of unknown kinetic parameters.

4.2 Modelling of the chemical kinetics

The kinetic modelling is based on the expression presented in chapter 3.1.3:

$$r_{CO_2}(T, X) = A_{\infty} \cdot \exp\left(\frac{-E_A}{RT}\right) \cdot m_0 \cdot (1 - X(T)) \cdot \lambda \cdot S_0 \cdot \sqrt{1 + f \cdot X} \cdot c(O_2)^n \quad (4-10)$$

A_{∞}	: Pre-exponential factor	$[m^3/(\text{mol} \cdot \text{s})]$
E_A	: Activation energy	$[\text{J/mol}]$
λ	: Surface concentration of active sites	$[\text{mol}/m^2]$
X	: Soot conversion	$[/math>$
S_0	: Initial BET surface area ($X=0$)	$[m^2/g]$
$m(X)$: Mass after soot conversion X	$[g]$
$c(O_2)$: Oxygen concentration	$[\text{mol}/m^3]$
n_{O_2}	: Apparent reaction order of O_2	$[/math>$
f	: Semi-empiric structural factor of soot	$[/math>$

The mechanistic studies in chapter 3 indicated, in accordance with literature [23,32], an oxygen reaction order of $n=1$. Furthermore, the exothermic reaction and the packed bed have a significant effect on the reaction kinetics. To assure unified kinetics for variable reaction conditions the global reaction rate (Eq. (4-10)) is coupled with the mass and energy balance of the developed reactor model, which is schematically illustrated in Figure 4-4. Mass transfer limitations are neglected within the model in accordance to the calculation presented in chapter 3.2.1.4.

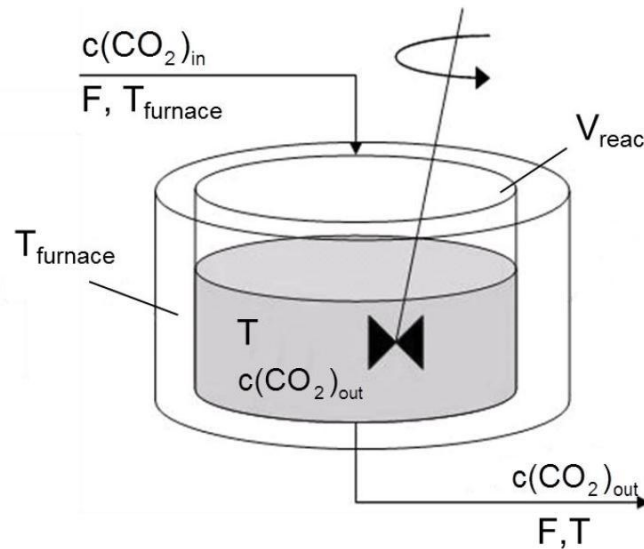


Figure 4-4: Schematic illustration of the CSTR model including the necessary values for energy and mass balance.

The mass balance (Eq.(4-11)) and the corresponding energy balance (Eq.(4-12)) are expressed as follows:

$$\frac{dc(\text{CO}_2)}{dt} = \frac{1}{\tau} (c(\text{CO}_2)_{\text{out}} - c(\text{CO}_2)_{\text{in}}) - \frac{r_{\text{CO}_2}}{V_r} \quad (4-11)$$

τ : Retention time [s]

V_r : Reactor volume [m^3]

$$m \cdot c_{p,\text{bed}} \cdot \frac{dT}{dt} = F \cdot c_{p,\text{gas}} \cdot (T_{\text{furnace}} - T) - r_{\text{CO}_2} \cdot \Delta H_{r,\text{soot}} - k \cdot A \cdot (T - T_{\text{furnace}}) \quad (4-12)$$

m : Reaction mass [g]

$c_{p,\text{bed}}$: Heat capacity of the reaction volume [$\text{J}/(\text{g}\cdot\text{K})$]

$c_{p,\text{gas}}$: Heat capacity of the gas flow [$\text{J}/(\text{m}^3\cdot\text{K})$]

$\Delta H_{r,\text{soot}}$: Reaction heat [J/mol]

k : Heat transfer coefficient [$\text{J}/(\text{m}^2\cdot\text{K})$]

A : Area for heat transfer [m^2]

The combination of these equations results in a system of two non-linear partial differential equations (pde), which are solved using Malab tool ode113 for the mass balance and ode45 for the energy balance [71,72]. These pde's are implemented in a self-developed program, whose structure is presented in Figure 4-5. The program represents a tanks-in-series model providing a broad field of application simply by adjusting the number of tanks m in accordance with the respective Bo number of the system to be described [69,70]. In the case of the CSTR model m is 1 and the

program calculates, in a pre-defined temperature range, steady-state conditions for each temperature step by solving Eqs. (4-10)-(4-12) for $t \rightarrow \infty$. The temperature dependent soot conversion is calculated according to Eq. (4-13).

$$X(T) = \frac{\sum_{T=T_0}^T n_{CO_2(T)}}{n_{0,soot}} \quad (4-13)$$

The amount of formed CO_2 , i.e. $n_{CO_2}(T)$, is determined in dependence of the dwell time of each temperature step:

$$n_{CO_2}(T) = \frac{r_{CO_2} \cdot (T(n) - T(n - 1))}{\beta} \quad (4-14)$$

After completion of the temperature loop $T_0 \dots T_n$ the program outputs an $(n \times m)$ array which is compared to experimental data by the least-square estimator `lsqcurvefit` of Matlab optimisation toolbox. This tool is based on non-linear regression and fits the calculated data to experimental data by changing the initial values of unknown parameters until a defined residue R^2 is accomplished according to Eq. (4-15).

$$RSS = \sum_{i=1}^N (y_i - F_i(x, b))^2 \rightarrow \min \quad (4-15)$$

RSS	: Residual sum of squares	$[F(x, b)^2]$
N	: Number of measured values	[/]
y_i	: Experimental value	[b]
$F_i(x, b)$: Simulated value	$[F(x, b)]$
b	: Parameter to be determined	[b]

The quality of the fit is quantified by the coefficient of determination which is calculated according (4-16) [73]:

$$R^2 = 1 - \frac{RSS}{\sum_{i=1}^N (y_i - \bar{y})^2} \quad (4-16)$$

Thereby, \bar{y} is the mean of the observed data:

$$\bar{y} = \frac{1}{N} \sum_{i=1}^N y_i \quad (4-17)$$

In addition to temperature and CO₂ concentration, time, conversion and temperature of the packed bed (outlet temperature of the reactor) are stored in an output file. The least-square estimator can be deactivated providing the possibility to predict CO₂ evolution for established kinetic parameters.

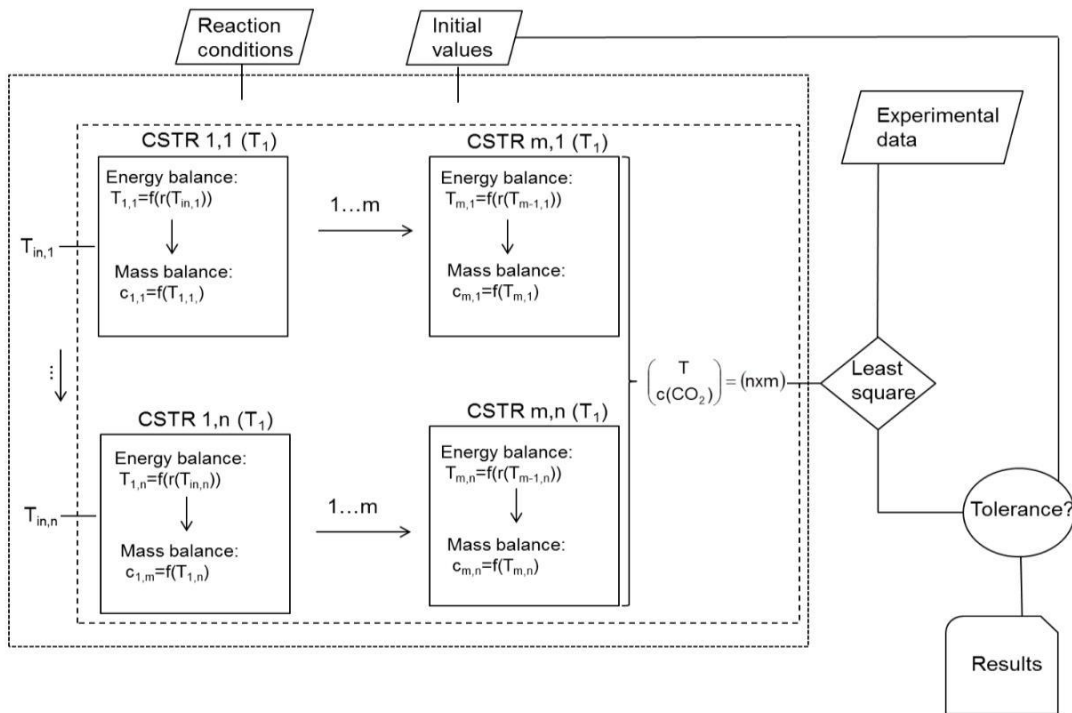


Figure 4-5: Flow chart of the program structure for the kinetic modelling and estimation of unknown kinetic parameters in a tanks-in-series reactor model.

4.2.1 Determination of unknown parameters

To minimise the number of free parameters in the fitting procedure, some parameters are taken from the literature as demonstrated in Table 4-1. For the kinetic modelling, the reactor volume is assumed to be equivalent to the dimensions of the packed bed, which gives a diameter of 0.01 m and a length of 0.025 m. Consequently, the parameters to be determined are the pre-exponential factor A_∞ , the activation energy E_A and the heat transfer coefficient k_0 , to cover the heat transfer in the energy balance. This balance is experimentally checked by temperature measurements in the middle of the packed bed, i.e. the outlet temperature of the CSTR in the modelling procedure. The experimental basis for the fitting procedure is given by the TPO experiment performed with a heating rate of 1.8 K/min and 10 vol.% O₂ in the gas feed using a mixture of 10 mmol Fe₂O₃ and 5 mmol home-made C₃H₆ soot in tight contact mode. This experiment is chosen because it exhibits moderate CO₂ evolution and heat production and therefore provides a suitable starting point for the modelling.

Table 4-1: Data for kinetic modelling of the catalytic soot oxidation.

Parameter	Symbol	Value	Source
Initial mass of soot	m_0	0.06 g	Chapter 2.4.1
Initial surface area of soot	S_0	90 m ² /g	[23]
Factor f	f	60	Chapter 3.1.3
Surface concentration	λ	8.7·10 ⁻⁶ mol/m ²	[23]
O ₂ concentration	$c(\text{O}_2)$	4.09 mol/m ³	Chapter 3.2.1.4
Reaction order O ₂	n	1	Chapter 3.2.3.1
Heating rate	β	0.03 K/sec	Chapter 3.2.1.4
Reactor volume	V_{reac}	1.96·10 ⁻⁶ m ³	Chapter 4.2.1
Volume flow (STP)	F	8.3·10 ⁻⁶ m ³ /s	Chapter 2.4.1
Heat capacity packed bed	$C_{p,\text{bed}}$	145 J/(mol·K)	[74]
Heat capacity fluid (600 K)	$C_{p,\text{fluid}}$	630 J/(m ³ ·K)	Appendix
Reaction enthalpy	ΔH_r	-400 kJ/mol	Table 3-2
Area for heat transfer	A	7.85·10 ⁻⁴ m ²	Chapter 4.2.1
Amount of catalyst	n_{cat}	5·10 ⁻³ mol	Chapter 2.4.1

Figure 4-6 and Figure 4-7 provide evidence that the calculated CO₂ volume fraction, soot conversion and temperature profile correspond well to the experimental results. The maximum difference of calculated and measured temperatures is below 5 K, whereas CO₂ volume fraction and soot conversion show certain divergence in the temperature range from 300-350°C. However, above 350°C the calculated and measured curve of the CO₂ volume fraction are in good agreement reflected by the correlation coefficient of 0.986. The determined kinetic parameters are demonstrated in Table 4-2.

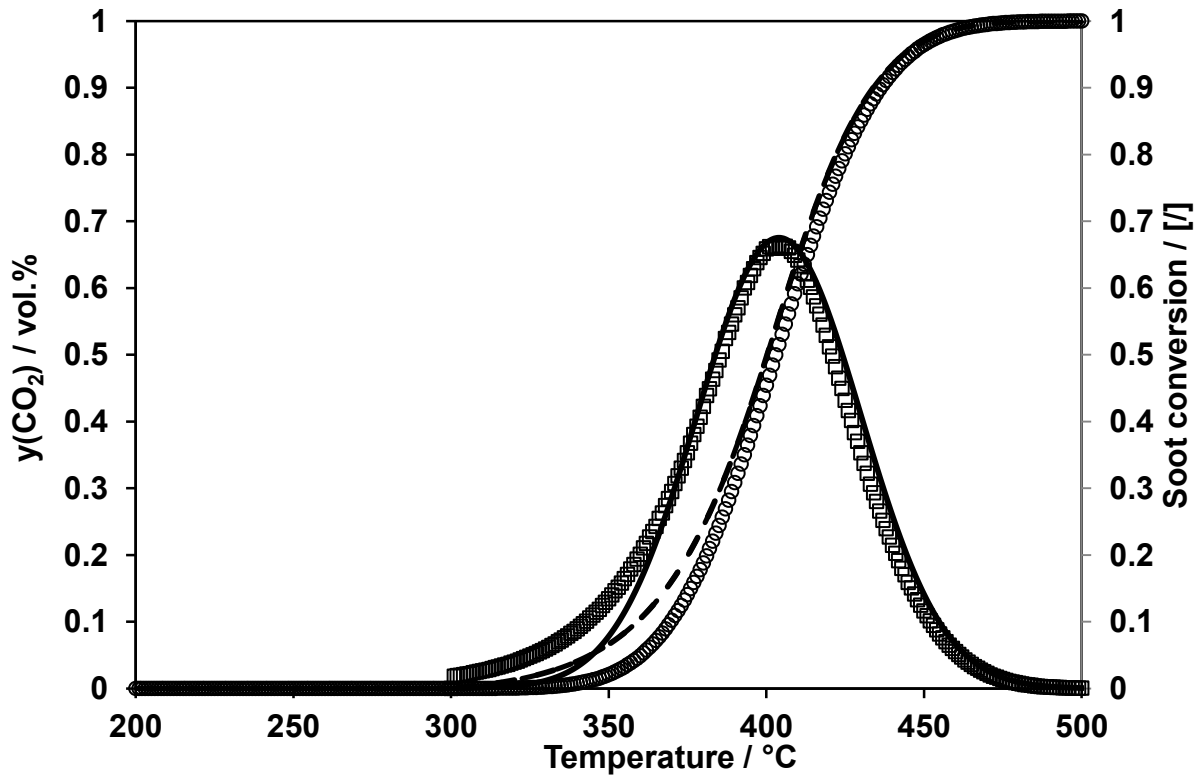


Figure 4-6: CO_2 formation (— exp., (\square) sim.) and conversion of soot (--- exp., (\circ) sim.). Conditions: $F=500$ ml/min (STP), $y(\text{O}_2)=10$ vol.%, N_2 balance, $\beta=1.8$ K/min, catalyst:soot ratio=10 mmol:5 mmol in tight contact mixture.

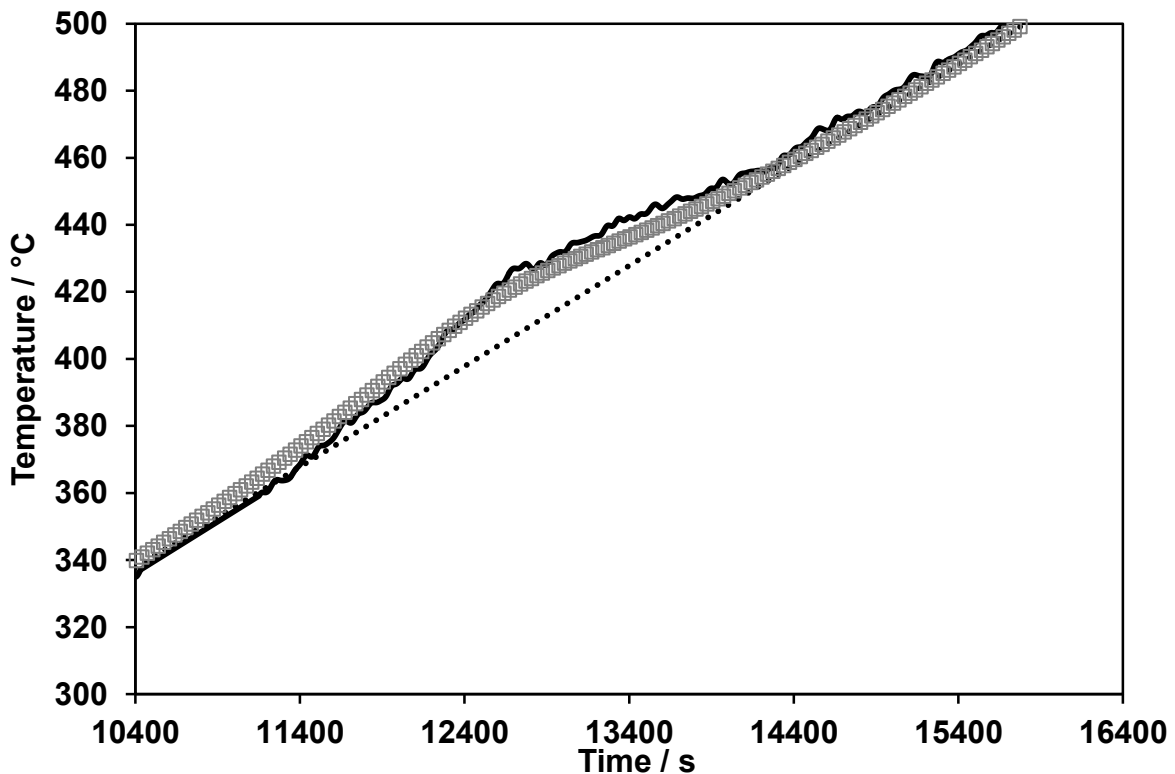


Figure 4-7: Temperature profile in the packed bed (—) and at the outlet of the CSTR (\square) in comparison to the inlet temperature (\cdots). Conditions: $F=500$ ml/min (STP), $y(\text{O}_2)=10$ vol.%, N_2 balance, $\beta=1.8$ K/min, catalyst:soot ratio=10 mmol:5 mmol in tight contact mixture.

Table 4-2: Determined kinetic parameters of the catalytic soot oxidation on α -Fe₂O₃. ($R^2=0.986$).

Parameter	Symbol	Value
Pre-exponential factor	A_∞	$1.58 \cdot 10^3 \text{ m}^3/(\text{mol} \cdot \text{s})$
Activation energy	E_A	73.4 kJ/mol
Heat transfer coefficient	k_0	121.35 W/(m ² ·K)

4.2.2 Validation of the kinetic model

For validation of the kinetic model, experiments with different reaction conditions are simulated. To cover a preferably broad extent of validity, heat transfer effects have to be considered in the model. In chapter 3.2.1.4 it was shown that the heating rate influences the formation of CO₂ significantly. A low heating ramp (1.8 K/min) resulted in a broad CO₂ signal and slight temperature increase in the catalyst/soot mixture, whereas a fast heating rate (>3.3 K/min) caused a sharp CO₂ signal and prominent heat production in the bed (see chapter 3.2.1.4). The heat transfer coefficient k_0 determined above has to be seen as a coefficient covering the heat transfer of the experiment using a slow heating rate and low heat formation exclusively. On that account, the heat transfer coefficient k_0 (Table 4-2, referring to $\beta_0=1.8 \text{ K/min}$) is modified by multiplying k_0 with the ratio of the respective heating rate β to be validated and β_0 . As a result, the heat transfer coefficient corresponding to β is obtained. It has to be stated that this is only an approximation which is not derived from physical principles.

$$k = \frac{k_0 \cdot \beta_0}{\beta} \quad (4-18)$$

The validations are carried out with the parameters presented in Table 4-1 and Table 4-2, whereas the special experimental conditions are considered in the model. Figure 4-8 shows the results of the simulation of a sharp CO₂ profile referring to a heating ramp of 3.3 K/min, 10 vol.% O₂ and a molar catalyst:soot ratio of 2 in tight contact mixture. The comparison with the experimental traces shows that the simulation is able to predict even such extreme curve progressions. This supports the reliability of the model. The difference in the height of the CO₂ signal is <3 % and the difference in peak location is smaller than 10 K. Furthermore, O₂ variation (7.5 vol%, $\beta=2 \text{ K/min}$) is depicted in Figure 4-9 revealing again good agreement of predicted and measured data; the maximum CO₂ volume fraction exhibits a difference of 0.05 vol.% (0.75 vol.% vs. 0.7 vol.%), while $T_{\text{CO}_2, \text{max}}$ shows a differential of 2 K only (418°C vs. 416°C).

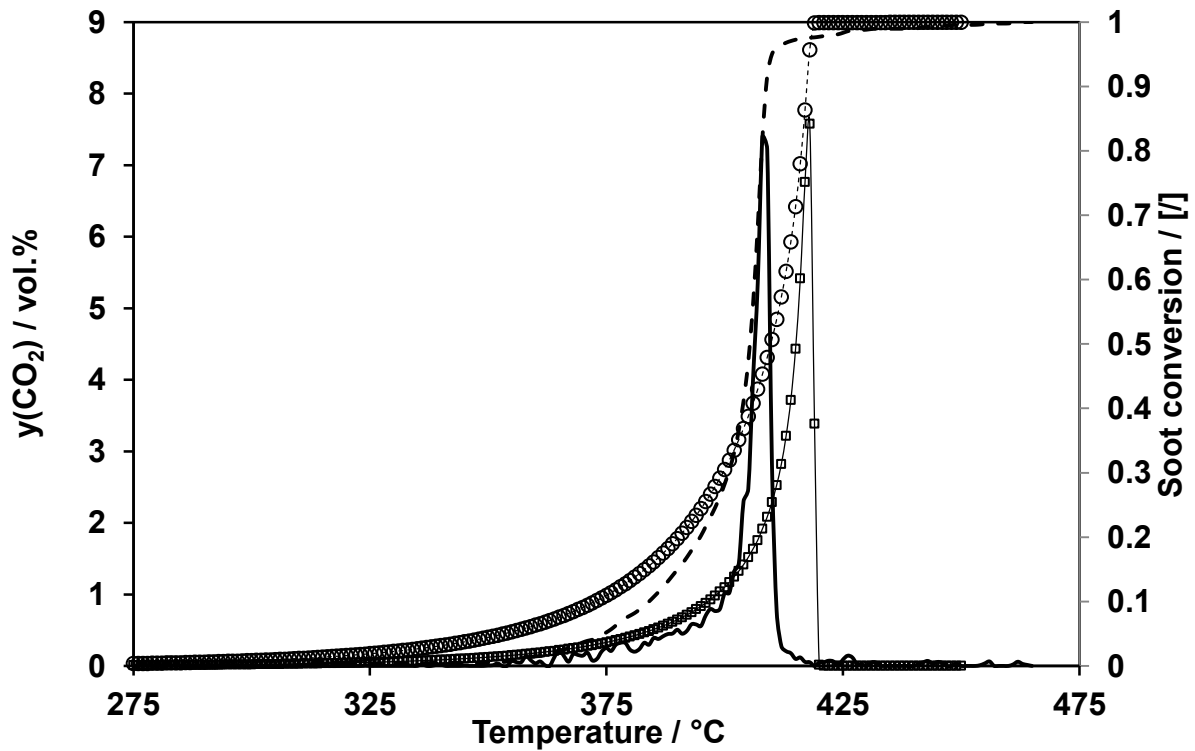


Figure 4-8: CO₂ formation ((—) exp., (□) sim.) and conversion of soot ((--), (○) sim.). Conditions: $F=500$ ml/min (STP), $y(\text{O}_2)=10$ vol.%, N_2 balance, $\beta=3.3$ K/min, catalyst:soot ratio=2.5 mmol:5 mmol in tight contact mixture.

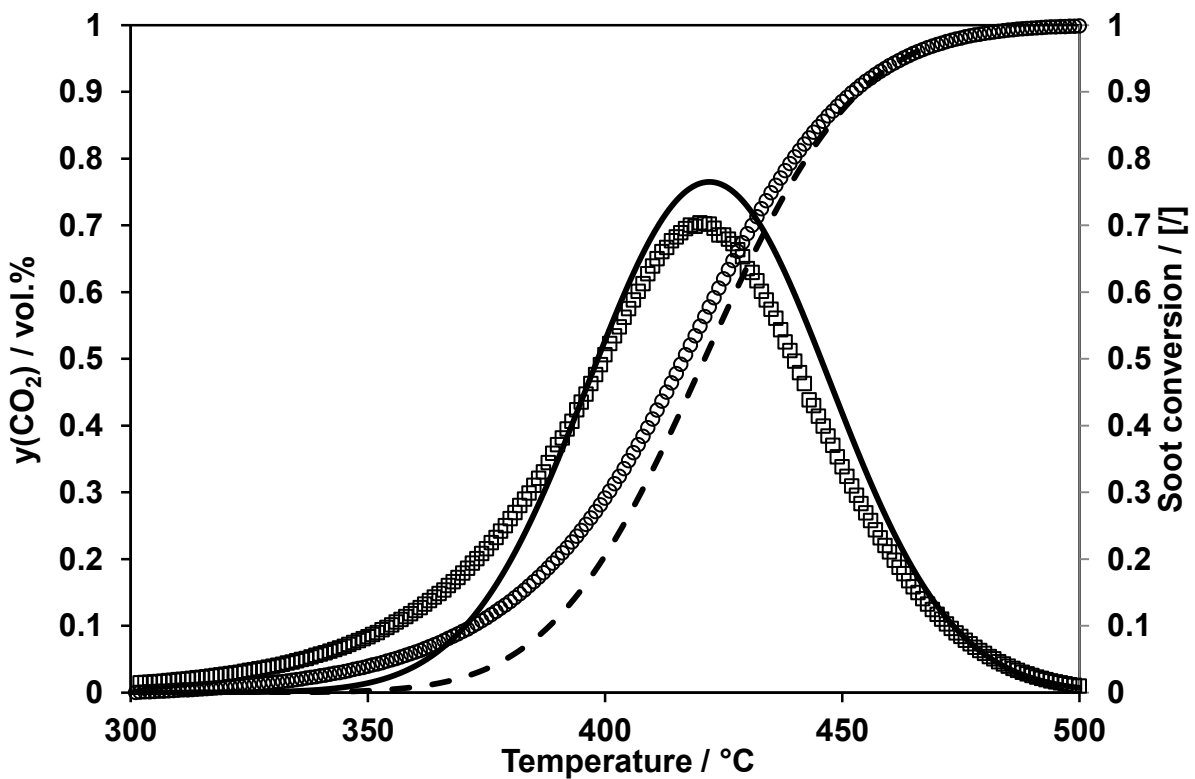


Figure 4-9: CO₂ formation ((—) exp., (□) sim.) and conversion of soot ((--), (○) sim.). Conditions: $F=500$ ml/min (STP), $y(\text{O}_2)=7.5$ vol.%, N_2 balance, $\beta=2$ K/min, catalyst:soot ratio=10 mmol:5 mmol in tight contact mixture.

4.2.3 Description of the effect of different contact modes on the kinetics of the catalytic soot oxidation

The TPO studies demonstrated in section 3.2.1.2 indicate special soot oxidation activity for different contact modes of catalyst and soot. Tight contact provides the highest activity, which is most likely due to the highest number of contact points [16,39]. To extend the area of validity of the model presented above, an expression for the description of different contact modes is necessary. Due to lack of literature describing a model covering loose as well as tight contact modes, a new expression has to be developed. The extension of the model should on the one hand cover the enhancement in catalytic performance by increasing the number of contact points, while on the other hand maintain the kinetic expression (see Eq. (4-10)). In mathematical terms, different contact modes can be implemented simply by pre-connecting an equation for the migration of soot particles (see Figure 4-10), similar to a serial connection of resistors.

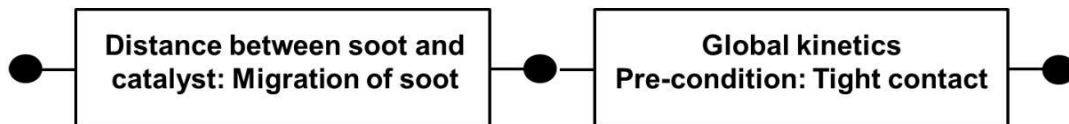


Figure 4-10: Serial connection of two expressions describing the migration and reaction of soot in catalytic oxidation thus enabling the description of different contact modes in the kinetic model.

This approach is additionally clarified in Figure 4-11 by presenting the validity of the control volume for the global kinetic expression (Eq. (4-10)). The left side of the figure indicates that the global kinetic approach covers all processes occurring on the interface between catalyst and soot, under precondition of intimate contact between Fe_2O_3 and soot. In the case of loose contact, preliminary “diffusion” of the soot particle into this control volume is necessary to maintain validity of equation (4-10).

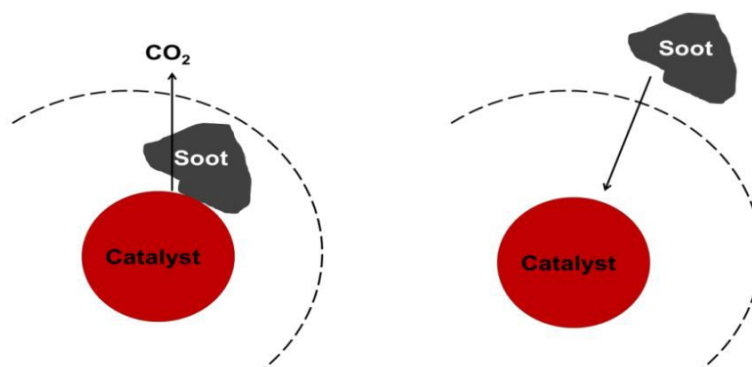


Figure 4-11: Schematic illustration for the approach for the kinetic description of loose contact Fe_2O_3 /soot mixtures. Left: Tight contact mode to be described by global kinetics. Right: Previous migration of soot particles in the control volume which is valid for the global kinetics is necessary for loose contact mixtures.

The assumption of soot migration is based on studies of Simonsen et al. [54], who showed by environmental TEM examinations of CeO₂/soot mixtures the migration of soot particles to the catalyst.

The implementation of loose contact mode in the model requires the introduction of an expression, which describes diffusion-analogical soot migration. Therefore, an equation similar to the process of surface diffusion [75] is introduced:

$$\frac{dm_{\text{soot}}}{dt} = -\frac{A}{V} \cdot D_i \cdot \frac{\partial m}{\partial x} \cdot \exp\left(\frac{-E_{\text{diff}}}{RT}\right) \quad (4-19)$$

m_{soot}	: Mass of migrated soot in time interval dt	[g]
A	: Exchange surface	[m ²]
V	: Control volume	[m ³]
D_i	: Diffusion coefficient	[m ² /s]
m	: Mass	[g]
x	: Distance	[m]
E_{diff}	: Activation energy for diffusion	[J/mol]

Combining A, V and D_i to a diffusion analogical coefficient D_a and linearizing the gradient leads to

$$\frac{dm_{\text{soot}}}{dt} = -D_a \cdot \exp\left(\frac{-E_{\text{diff}}}{RT}\right) \cdot \frac{(m_{\text{soot,cat}} - m_{\text{soot,0}})}{\Delta s} \quad (4-20)$$

D_a	: Diffusion analogical mass transfer coefficient	[m/s]
Δs	: Distance between soot and catalyst	[m]
$m_{\text{soot,cat}}$: Mass of soot in direct contact with the catalyst	[g]
$m_{\text{soot,0}}$: Initial mass of soot	[g]

The driving force for soot migration is given by the expression ($m_{\text{soot,cat}} - m_{\text{soot,0}}$) with $m_{\text{soot,cat}}$ representing the mass of soot, which is already in contact with the catalyst and where $m_{\text{soot,0}}$ is the ideal situation, meaning that the initial mass of used soot is in direct contact with the catalyst. In the model, $m_{\text{soot,cat}}$ is calculated via the sum of migrated mass of soot $m_{\text{soot,T}_i}$ within the temperature steps from T_0 to T_i :

$$m_{\text{soot,cat}} = \sum_{T=T_0}^{T_i} m_{\text{soot,T}_i} \quad (4-21)$$

The migrated mass of soot m_{soot,T_i} results from the integral mass of soot in the time interval t . In the computation procedure t refers to the holding time of one temperature step (see also Figure 4-5).

$$m_{\text{soot},T_i} = \int_0^t dt \cdot \left(-D_a \cdot \exp\left(\frac{-E_{\text{diff}}}{RT}\right) \cdot \frac{(m_{\text{soot},\text{cat}} - m_{\text{soot},0})}{\Delta s} \right) \quad (4-22)$$

$$t = \frac{(T_i - T_{i-1})}{\beta} \quad (4-23)$$

The mass transport of soot is implemented in the kinetic expression by the mass of soot in direct contact with the catalyst $m_{\text{soot},\text{cat}}$. This results in a modified equation for the formation rate of CO_2 (Eq. (4-24)). If the mass transfer of soot is slow, i.e. a big distance Δs between soot and catalyst, $m_{\text{soot},\text{cat}}$ is low. This indicates that soot migration is the rate determining step upon catalytic soot oxidation. In contrasting case, i.e. Δs is small, the chemical kinetics are rate determining.

$$r_{\text{CO}_2}(T, X) = A_\infty \cdot \exp\left(\frac{-E_A}{RT}\right) \cdot m_{\text{soot},\text{cat}} \cdot (1 - X(T)) \cdot \lambda \cdot S_0 \cdot \sqrt{1 + f \cdot X} \cdot c(\text{O}_2)^n \quad (4-24)$$

Equation (4-24) is inserted in the CSTR model and solved according the above described program structure (Figure 4-5) and parameters (Table 4-1). The distance between soot and catalyst was assumed to be $\Delta s = 1 \cdot 10^{-7}$ m (double size of a soot particle). Unknown parameters are the diffusion analogical mass transfer coefficient D_a , the activation energy E_{diff} and the heat transfer coefficient k , which can be distinguished from the value for tight contact mode on account of a different dimension of the packed bed and decreased heat conduction as a consequence of contact loss between catalyst and soot. These parameters are determined by least-square fitting with experimental data, shown in Figure 4-12. It is obvious that qualitative curve progression is revealed by the model. In particular, the loss in activity, indicated by the temperature shift of maximum CO_2 volume fraction, is reflected. Furthermore, the coefficient of determination is 0.977 indicating strong coherence between experiment and simulation. Nevertheless, the shoulder and the resulting height of the CO_2 signal is not expressed by the model, since the experimental curve progression can be attributed to non-catalytic oxidation of soot which is not covered by the model. The temperature profile in the fixed bed is illustrated in Figure 4-13 for experimental and simulated data, respectively. Both

graphs reveal no measurable temperature increase upon catalytic soot oxidation. Finally, the determined parameters are presented in Table 4-3. The heat transfer coefficient is only valid for the presented experiment. Further assumptions and constraints are presented in the discussion (section 4.4).

For validation, Δs is decreased to $1 \cdot 10^{-9}$ m, which is assumed to correspond to tight contact mode. The calculated CO_2 volume fraction and soot conversion (Figure 4-14) show good agreement with the experimental TPO (5 vol.% O_2 , tight contact mode). The difference in the height of the CO_2 signal is smaller 4 % while the discrepancy in peak location is 4 K, which only supports the validity of the presented approach as able to describe different contact modes. The heat transfer coefficient of this simulation is fitted to $40 \text{ W}/(\text{m}^2 \cdot \text{K})$ ($R^2=0.93$).

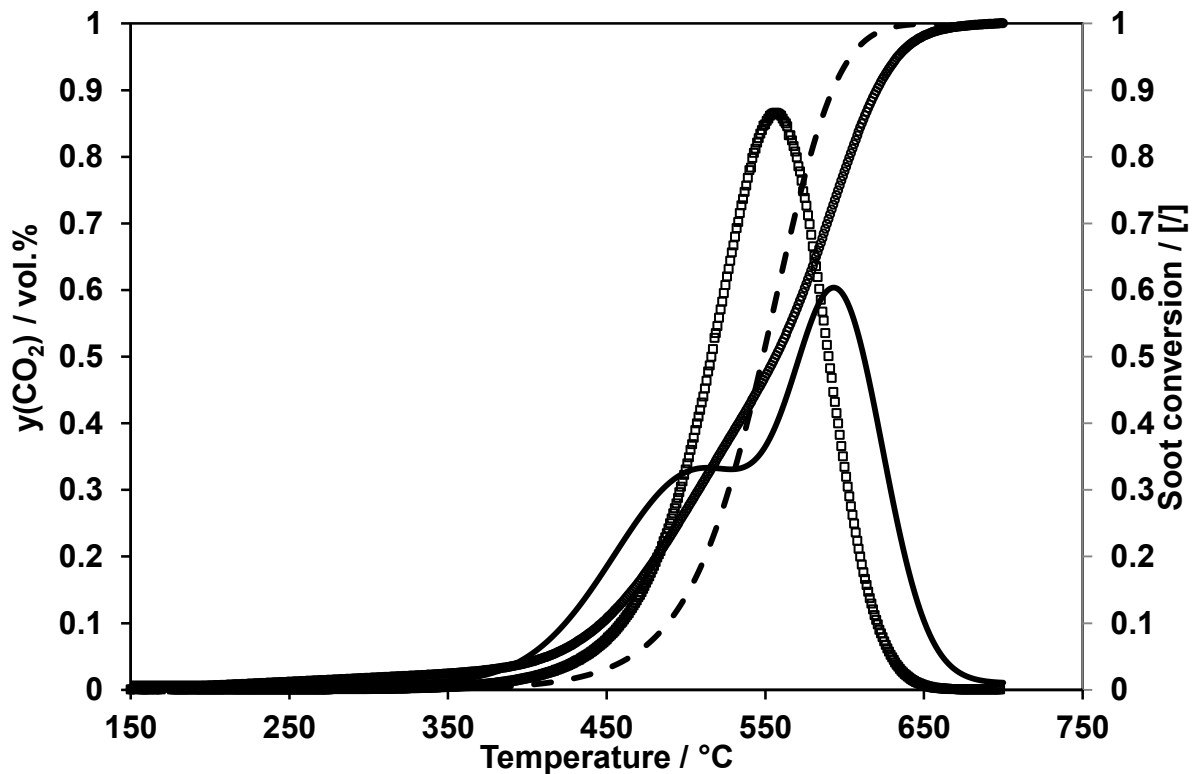


Figure 4-12: CO_2 formation ((—) exp., (\square) sim.) and conversion of soot ((--) exp., (\circ) sim.). Conditions: $F=500 \text{ ml}/\text{min}$ (STP), $y(\text{O}_2)=10 \text{ vol.}\%$, N_2 balance, $\beta=3.3 \text{ K}/\text{min}$, catalyst:soot ratio=10 mmol:5 mmol in loose contact mixture.

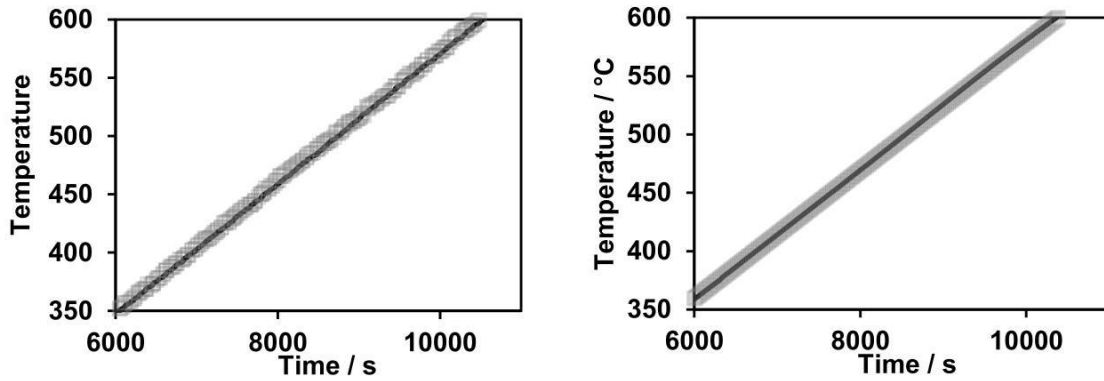


Figure 4-13: Left: Experimental temperature profile of in the middle of the packed bed (—) and the inlet of the reactor (\square). Right: Calculated outlet temperature of the CSTR (\square) in comparison to the inlet temperature (—). Conditions: $F=500$ ml/min (STP), $y(O_2)=10$ vol.%, N_2 balance, $\beta=3.3$ K/min, catalyst:soot ratio=10 mmol:5 mmol in loose contact mixture.

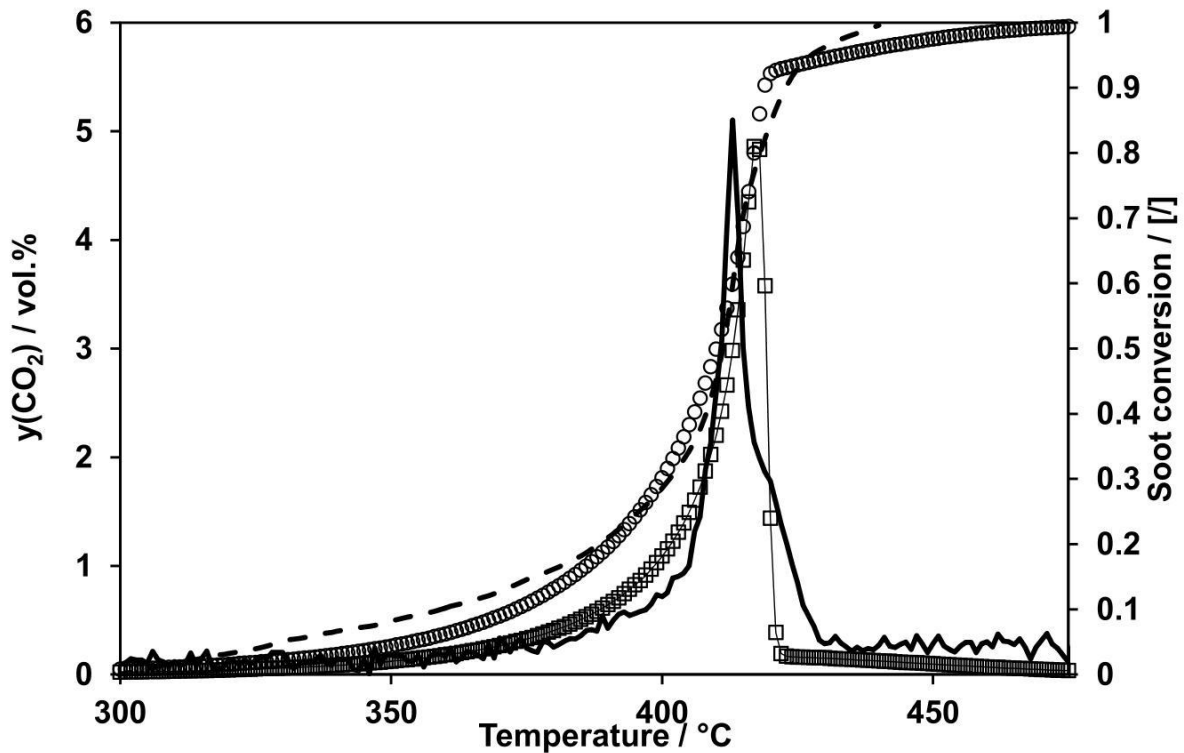


Figure 4-14: CO_2 formation ((—) exp., (\square) sim.) and conversion of soot ((--) exp., (\circ) sim.). Conditions: $F=500$ ml/min (STP), $y(O_2)=5$ vol.%, N_2 balance, $\beta=3.3$ K/min, catalyst:soot ratio=10 mmol:5 mmol in tight contact mixture.

Table 4-3: Determined parameters for the catalytic soot oxidation on $\alpha\text{-Fe}_2\text{O}_3$ and soot in loose contact mode. ($R^2=0.977$).

Parameter	Symbol	Value
Diffusion analogical mass transfer coefficient	D_a	$1e^{-11}$ m/s
Activation energy	E_{diff}	7.5 kJ/mol
Heat transfer coefficient	k	500 W/($m^2 \cdot K$)

4.3 Modelling of the fluid dynamics

For an advanced model and further insights into fluid dynamic issues upon catalytic soot oxidation, such as heat production, heat transfer and fluid mechanics a CFD (computational fluid dynamics) 2-d model has been developed. This comprises the setting-up of conservation equations for the performed TPO experiments and the implementation of the kinetics already determined. This approach provides deeper insights by revealing 2 dimensional information of the catalytic soot oxidation, i.e. temperature distribution, velocity field within the fixed bed and CO₂ profile inside the reactor.

4.3.1 Setting-up of conservation equation

The first step is the setting-up of the conservation equations of mass, heat and momentum transport. The momentum transport requires in this respect special attention. According to the experimental set-up of the TPO studies, the reactor geometry has to be split up into 3 control volumes located in the front (area 1, see Figure 4-15), inside (area 2) and behind the packed bed (area 3). Figure 4-15 illustrates attribution of the conservation equations to the respective control volume. In the later model, abutting areas are connected by boundary conditions.

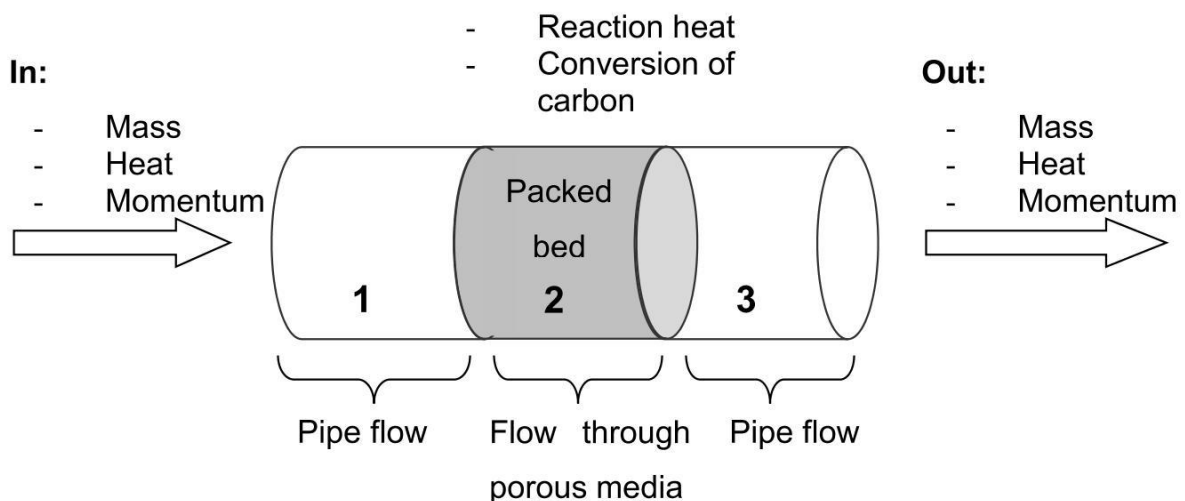


Figure 4-15: Scheme of the respective control volume and conservation equations used to describe the experimental setup.

To cover the transient behaviour of the system, i.e. the continuous temperature increase, the mathematical expressions imply non-stationarity. For an optimum of quality and expenditure of time a two-dimensional model is chosen.

The transient heat transfer is described by convection and conduction, whereas an additional source term for heat production has to be considered in the control volume of the packed bed:

$$\rho c_{p,pb} \frac{\partial T}{\partial t} = \dot{Q} - \nabla \cdot (\rho c_p u T - k \nabla T) \quad (4-25)$$

ρ	: Density of air	[kg/m ³]
c_p	: Heat capacity at constant pressure of air	[J/kg·K]
T	: Temperature	[K]
t	: Time	[s]
k	: Thermal conductivity	[W/(m·K)]
\dot{Q}	: Heat production	[W/m ³]
u	: Velocity field supplied by the momentum transport	[m/s]
∇	: Nabla Operator: First order spatial derivatives in x and y direction	[/]

In area 1 and 3 \dot{Q} is zero, while in area 2 the heat source is calculated according to

$$\dot{Q} = r_{CO_2} \cdot (-\Delta H). \quad (4-26)$$

r_{CO_2}	: Reaction rate of CO ₂ formation	[mol/s·m ³]
ΔH	: Reaction enthalpy	[J/mol]

Heat capacity, density, thermal conductivity (in area 1 and 3) as well as dynamic viscosity are calculated dependent on temperature. For simplicity, the gas was assumed to be air, which constitutes no significant error since the simulated gas feed consisted of 10 vol.% O₂ and 90 vol.% N₂ and is in close agreement with the composition of air, i.e. 21 vol.% O₂ and 79 vol.% N₂. The specific parameters adapted to the equations above are summarised in the appendix (see Appendix C and D). The determination of the thermal conductivity in the packed bed (control volume area 2) is done based upon the Brinkman equation, which is used to describe the flow through porous media. The Brinkman equation assumes that the streamed porous medium is a continuum showing physical properties of both, fluid and solid [76]. Thermal conductivity was determined accounting for Eq. (4-27).

$$k = (1 - \varepsilon_{\text{apparent}}) \cdot k_{\text{solid}} + \varepsilon_{\text{apparent}} \cdot k_{\text{gas}} \quad (4-27)$$

k_{solid}	: Thermal conductivity of $\alpha\text{-Fe}_2\text{O}_3$ [77]	[W/(m·K)]
--------------------	---	-----------

k_{gas}	: Thermal conductivity of air	[W/(m·K)]
$\epsilon_{\text{apparent}}$: Apparent porosity	[/]

The apparent porosity $\epsilon_{\text{apparent}}$ is determined by Eq. (4-28) to be 0.832; soot is neglected due to its small mass fraction. Finally, k results in 0.18 W/(m·K).

$$\epsilon_{\text{apparent}} = 1 - \frac{m_{\text{catalyst}}}{V_{\text{packed bed}} \rho_{\text{catalyst}}} \quad (4-28)$$

m_{catalyst}	: Mass of used catalyst.	[g]
$V_{\text{packed bed}}$: Volume of the packed bed.	[m ³]
ρ_{catalyst}	: Density of $\alpha\text{-Fe}_2\text{O}_3$.	[g/m ³]

Mass transfer is expressed by convection and diffusion, while the control volume of the packed bed requires an additional term to cover the reaction. The equation is a nonconservative formulation because the fluid is assumed to be incompressible:

$$\frac{\partial c_i}{\partial t} = r_{\text{CO}_2} - \mathbf{u} \cdot \nabla c_i - \nabla \cdot (-D_{\text{eff},i} \nabla c_i) \quad (4-29)$$

c_i	: Concentration of species i	[mol/m ³]
$D_{\text{eff},i}$: Effective diffusion coefficient of O_2 and CO_2 in N_2	[m ² /s]
r_{CO_2}	: Reaction rate (only in area 2)	[mol/m ³ ·s]
\mathbf{u}	: Velocity field supplied by the momentum transport	[m/s]

According to the Bosanquet equation, the effective diffusion coefficient $D_{\text{eff},i}$ combines molecular diffusion (mesopores and macropores) and Knudsen diffusion (micropores) [78]. In the model, diffusion of only two species is considered, i.e. diffusion of O_2 in N_2 and CO_2 in N_2 .

$$D_{\text{eff},i} = \frac{\epsilon}{\tau} \left(\frac{1}{D_{12}} + \frac{1}{D_k} \right)^{-1} \quad (4-30)$$

ϵ	: Porosity	[/]
τ	: Tortuosity	[/]
D_{12}	: Molecular diffusion coefficient (O_2 and CO_2 in N_2)	[m ² /s]
D_k	: Knudsen diffusion coefficient	[m ² /s]

The tortuosity takes into account the aberration of the pores from an ideal cylindrical geometry. Typically, a value between 2 and 4 is used as an approximation. The binary diffusion coefficient D_{12} is calculated based on the semi-empirical Fuller equation [79].

$$D_{12} = \frac{1.013 \cdot 10^{-7} \cdot T^{1.75} \cdot \left(\frac{1}{M_1} + \frac{1}{M_2} \right)^{\frac{1}{2}}}{p \left(v_1^{\frac{2}{3}} + v_2^{\frac{2}{3}} \right)^2} \quad (4-31)$$

v_i	: Diffusion volume of the respective molecules [80]	[m ³ /mol]
p	: Pressure	[bar]
M_i	: Molar mass of species i	[g/mol]

The Knudsen diffusion [81] occurs in pores with a smaller diameter as compared to the mean free path of the molecules. With the kinetic gas theory an expression for Knudsen diffusion is developed:

$$D_k = \frac{4}{6} \cdot d_{\text{pore}} \sqrt{\frac{2RT}{\Pi M_i}} \quad (4-32)$$

d_{pore}	: Pore diameter	[m]
-------------------	-----------------	-----

All the numerical values used for description of mass transport are listed in the appendix (see Appendix C and D).

The momentum transport in the control volumes of area 1 and area 2 exhibits pipe flow and is calculated on the basis of the Navier-Stokes equations:

$$\rho \frac{\partial \mathbf{u}}{\partial t} = \nabla [-p\mathbf{l} + \eta(\nabla \mathbf{u} + (\nabla \mathbf{u})^T)] - \rho(\mathbf{u} \cdot \Delta)\mathbf{u} \quad (4-33)$$

ρ	: Density of air	[kg/m ³]
η	: Dynamic viscosity of air	[Pa·s]
\mathbf{u}	: velocity field (2 dimensional)	[m/s]
\mathbf{l}	: Unit vector	[/]
Δ	: Laplace operator: Second order spatial derivatives in x and y direction	[/]

For a description of the momentum transport through the packed bed (area 2) the Brinkman equation is used [82]. This represents an extension of the Navier-Stokes equations and describes the flow in porous media when shear stresses in the fluid are of importance for momentum transport. The mathematical expression extends Darcy's law and includes a term that accounts for the viscous transport in the momentum balance. Pressure and flow velocity vector are considered to be independent variables.

$$\left(\frac{\rho}{\varepsilon}\right) \frac{\partial \mathbf{u}}{\partial t} = \nabla \cdot \left[-p\mathbf{I} + \left(\frac{1}{\varepsilon}\right) \left\{ \eta(\nabla \mathbf{u} + (\nabla \mathbf{u})^T) - \left(\frac{2\eta}{3}\right)(\nabla \cdot \mathbf{u})\mathbf{I} \right\} \right] - \left(\frac{\eta}{\kappa}\right) \mathbf{u} \quad (4-34)$$

κ : Permeability [m²]

The permeability depends on the properties of the fluid and the porous medium. An expression for the permeability is given by Brinkman [83].

$$\kappa = \frac{d_{\text{Pore}}^2}{18} \left(3 + \frac{4}{1-\varepsilon} - 3\sqrt{\frac{8}{1-\varepsilon} - 3} \right) \quad (4-35)$$

All numerical values used for the calculation of the velocity field are given in the appendix.

Final term for completion of the model is the reaction rate r_{CO_2} . In a first step, the assumptions presented for the conservation equation are verified by comparing the IR camera measurements from section 3.2.2 to the calculated surface temperature distribution. A formal kinetic expression for the reaction rate is used simply by fitting the experimental r_{CO_2} from the IR camera experiment with a Gaussian expression (Origin 8.1 software). The analytical equation depends only on the temperature:

$$r_{\text{CO}_2} = y_0 + (A(w \cdot \sqrt{\pi/2})) \cdot \exp(-2 \cdot ((T - T_0)/w)^2) \quad (4-36)$$

The result of the Gaussian fit (Figure 4-16) illustrates acceptable accordance with the experiment implying values for y_0 , A , T_0 and w , which are also listed in the appendix (see Table C-2).

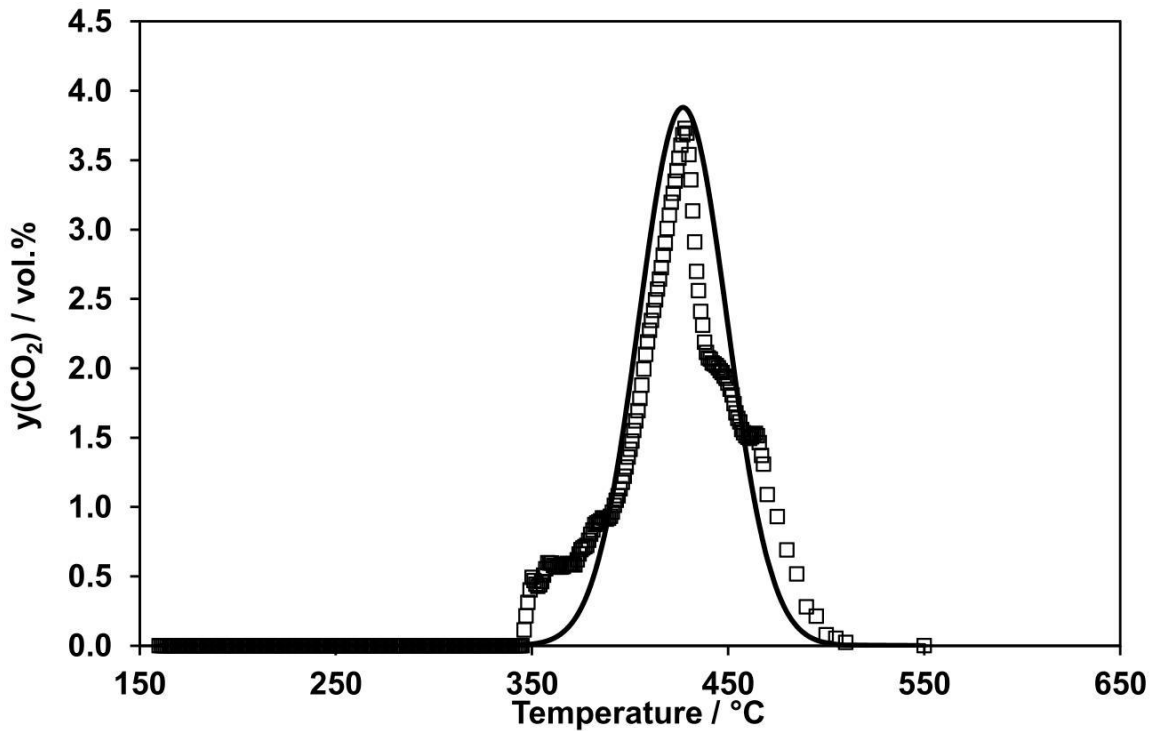


Figure 4-16: Experimental (\square) and fitted (—) data (Gaussian function) of CO_2 production in the TPO of the bulk $\alpha\text{-Fe}_2\text{O}_3$ /soot mixture performed in the special IR reactor. Conditions: $F=500$ ml/min (STP), $c(\text{O}_2)=10$ vol.%, N_2 balance, $\beta=8.64$ K/min, catalyst:soot ratio=10 mmol:5 mmol in tight contact mixture.

Finally, with all required equations and parameters available, the geometric dimensions of the reactor and the boundary conditions are formulated. The corresponding reactor design referring to the special reactor for IR camera measurements (see chapter 3.2.2) is depicted in Figure 4-17 (bottom), while dimensions and boundary conditions are given in Figure 4-17, Table 4-4 and Table 4-5.

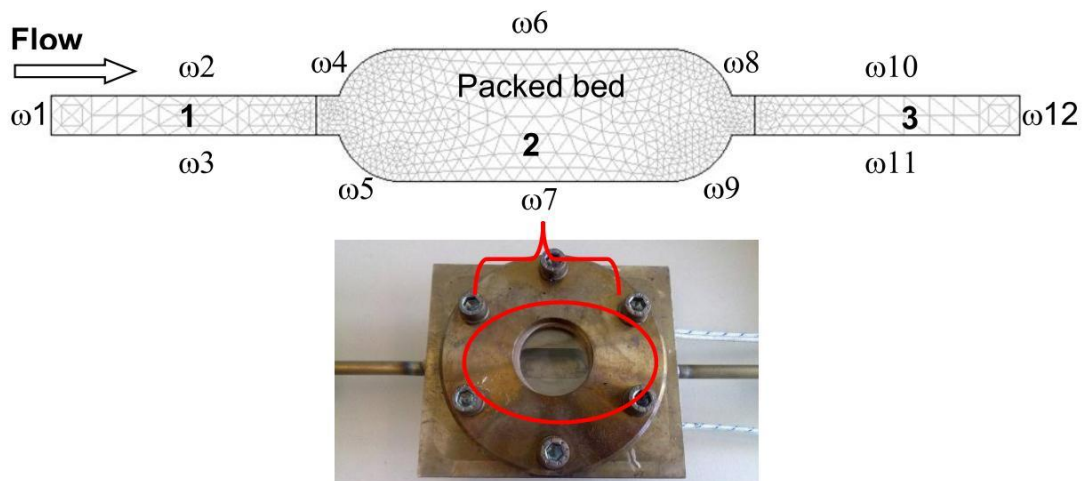


Figure 4-17: Computational domains and boundaries of the 2-d model (top) and picture of the IR reactor used (bottom). The mesh consists of 1192 elements.

Table 4-4: Dimensions of the simulated reactor geometry (see Figure 4-17).

Boundary	Length [m]
ω_1, ω_{12}	$3 \cdot 10^{-3}$
$\omega_2, \omega_3, \omega_{10}, \omega_{11}$	$3 \cdot 10^{-2}$
ω_6, ω_7	$2 \cdot 10^{-2}$
$\omega_4, \omega_5, \omega_8, \omega_9$	$6 \cdot 10^{-3}$

Table 4-5: Boundary conditions for the conservation equations

a) Heat Transport

Boundary	Boundary condition
ω_1, ω_{12}	$n \cdot (-k\nabla T) = 0$
$\omega_2, \omega_3, \omega_4, \omega_5, \omega_6, \omega_7, \omega_8, \omega_9, \omega_{10}, \omega_{11}$	$T = T_e^*$

b) Mass Transport

Boundary	Boundary condition
ω_1	$C_i = C_{i0}$
$\omega_2, \omega_3, \omega_4, \omega_5, \omega_6, \omega_7, \omega_8, \omega_9, \omega_{10}, \omega_{11}$	$n \cdot N = 0, N = -D\nabla c_i + c_i u$
ω_{12}	$n \cdot (-D\nabla c_i) = 0$

c) Momentum Transport

Boundary	Boundary condition
ω_1	$u = -u_0 \cdot n$
$\omega_2, \omega_3, \omega_4, \omega_5, \omega_6, \omega_7, \omega_8, \omega_9, \omega_{10}, \omega_{11}$	$u = 0$
ω_{12}	$\eta(\nabla u + (\nabla u)^T) \cdot n = 0, p = p_0$

^{*}) $T_e = \beta \cdot t$, with β = heating rate [K/s] and t = time [s].

The computation of the model was done by using the commercial software COMSOL Multiphysics (version 3.5a). The model is based on the parameters listed in the appendix (see Appendix C and D) and the experimental conditions referring to the IR camera experiments (3.2.2). In this method, the simulated and experimental results are contrasted in the temperature range, referring to the inlet, from 400 °C to 450 °C, where significant CO₂ evolution is observed. The comparison of the corresponding simulated and experimental results is given in Figure 4-18. The findings clearly show that the model describes the experiment acceptably. Heat production starts in the middle of the packed bed, both in the experiment and simulation. The increase in temperature is also reflected satisfactorily by the simulation. But, due to the use of

the Brinkman equation, the temperature distribution is more homogeneous when compared with the experiment. The hotspot, which occurs at the inlet temperature of 430°C, is not reflected by the model. Nevertheless, maximum differences between measured and simulated temperature are 20 K only. This proves that the assumptions implemented in the conservation equations and the boundary conditions taken are meaningful.

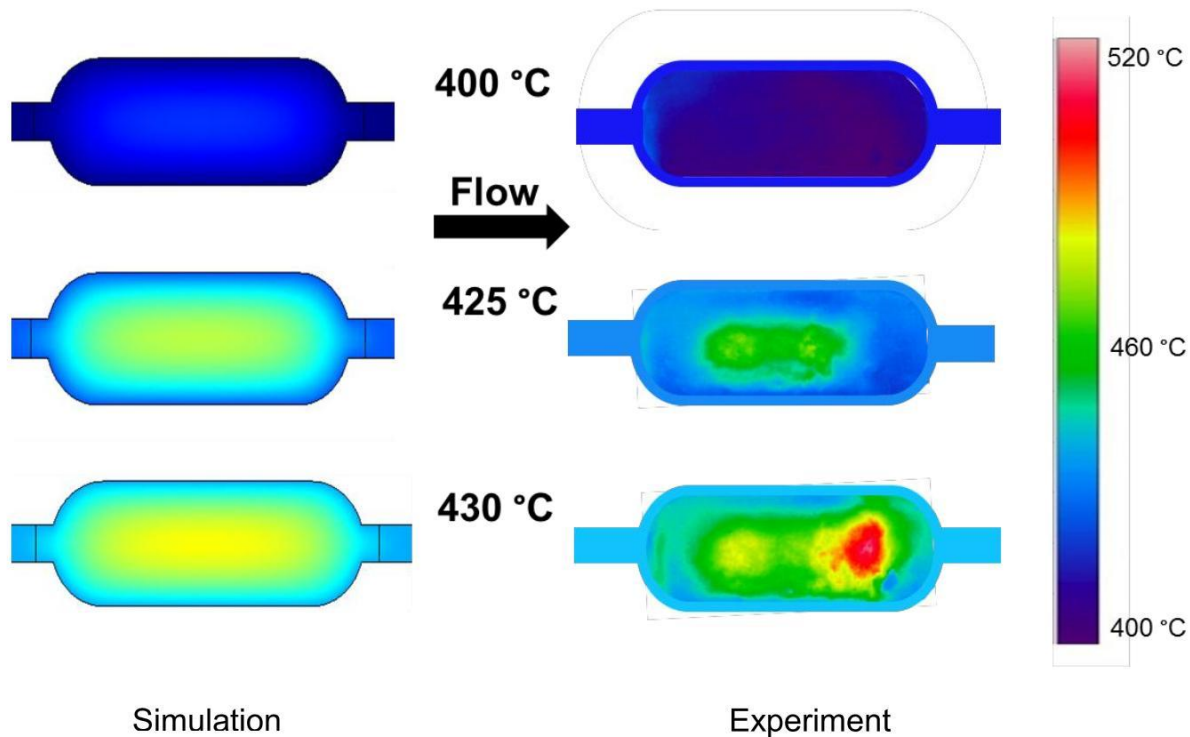


Figure 4-18: Three representative examples for temperature distribution of the packed bed during a TPO experiment. Left side: Modelling results, right side: IR measurements. Conditions: $F=500$ ml/min (STP), $y(\text{O}_2)=10$ vol.%, N_2 balance, $\beta=8.64$ K/min, catalyst:soot ratio=10 mmol:5 mmol in tight contact mixture.

4.3.2 Implementation of chemical kinetics

The next step to advance the model is to adapt the geometry to the standard tube reactor used for TPO experiments and the implementation of the above determined CSTR kinetics. In contrast to the reactor of the IR measurements, the tube reactor exhibits a constant diameter over the complete length (Figure 4-19). To describe soot oxidation in the packed bed (area 2), the following term is introduced:

$$\frac{\partial c_{\text{carbon}}}{\partial t} = \frac{-r_{\text{CO}_2}}{V_{\text{reac}}} \quad (4-37)$$

c_{carbon}	: Concentration of soot	[mol/m ³]
r_{CO_2}	: CO ₂ production rate	[mol/s]

The initial concentration of carbon is calculated to be 800 mol/m³. This refers to the initial molar amount of soot and geometry of the reactor. Equation (4-37) is added to the system of conservation equations demonstrated in the previous section. The dimensions and boundaries of the tube reactor model are depicted in Figure 4-19; dimensions and boundary conditions are listed in Table 4-6 and Table 4-7.

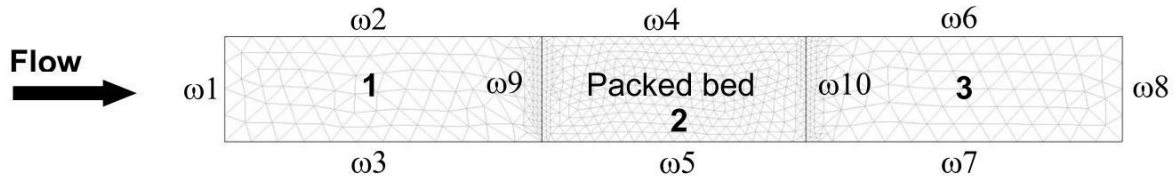


Figure 4-19: Computational domains and boundaries of the 2-d model. ω9 and ω10 are only valid for the equation of carbon oxidation. The mesh consists of 1129 elements.

Table 4-6: Dimensions of the simulated reactor geometry (see Figure 12).

Boundary	Length [m]
ω1, ω8	$10 \cdot 10^{-3}$
ω2, ω3, ω4, ω5, ω6, ω7	$2.5 \cdot 10^{-2}$

Table 4-7: Boundary conditions for the conservation equations

a) Heat Transport

Boundary	Boundary condition
ω1, ω8	$n \cdot (-k \nabla T) = 0$
ω2, ω3, ω4, ω5, ω6, ω7, ω8	$T = T_e^*)$

b) Mass Transport

Boundary	Boundary condition
ω1	$c_i = c_{i0}$
ω2, ω3, ω4, ω5, ω6, ω7	$n \cdot N = 0, N = -D \nabla c_i + c_i u$
ω8	$n \cdot (-D \nabla c_i) = 0$

c) Momentum Transport

Boundary	Boundary condition
ω1	$u = -u_0 \cdot n$
ω2, ω3, ω4, ω5, ω6, ω7	$u = 0$
ω8	$\eta (\nabla u + (\nabla u)^T) n = 0, p = p_0$

^{*)} $T_e = \beta \cdot t$, with β =heating rate [K/s] and t =time [s].

d) Carbon combustion

Boundary	Boundary condition
$\omega 1, \omega 2, \omega 3, \omega 6, \omega 7, \omega 8$	0
$\omega 4, \omega 5, \omega 9, \omega 10$	$n \cdot N = 0, N = -D \nabla c_{\text{carbon}}$

The kinetic expression for CO₂ formation is implemented according the equation described above (chapter 4.2), including the determined kinetic parameters A and E_A:

$$r_{\text{CO}_2} = A_{\infty} \cdot \exp\left(-\frac{E_A}{RT}\right) \cdot \lambda \cdot S_0 \cdot m(X) \cdot \sqrt{1 + 60 \cdot X} \cdot c(\text{O}_2) \quad (4-38)$$

The model is again solved by using COMSOL Multiphysics software in a range from 275°C to 600°C at a temperature increase of 1.8 K/min. CO₂ concentration and surface temperature (Figure 4-20) at three representative inlet temperatures of the reactor indicate simultaneous CO₂ formation and temperature rise in the packed bed of the PFR. Temperature increase is first observed in the middle of the packed bed and subsequently elliptically dispensed to the boundaries of the reactor. Further information is obtained by viewing CO₂, O₂ and carbon concentration, as well as the velocity field and the surface temperature (Figure 4-21) at the inlet temperature of 390°C, which is referred to the highest CO₂ concentration. A detailed analysis of the figure is presented in the discussion (chapter 4.4.1.3).

Finally, the CO₂ signal (Figure 4-22) derived from the last cell at the middle of the outlet of the reactor model is compared to the experimentally determined CO₂ volume fraction exhibiting acceptable accuracy indicated by a difference of 9 % in the CO₂ volume fraction and 11 K in T_{CO₂,max} only.

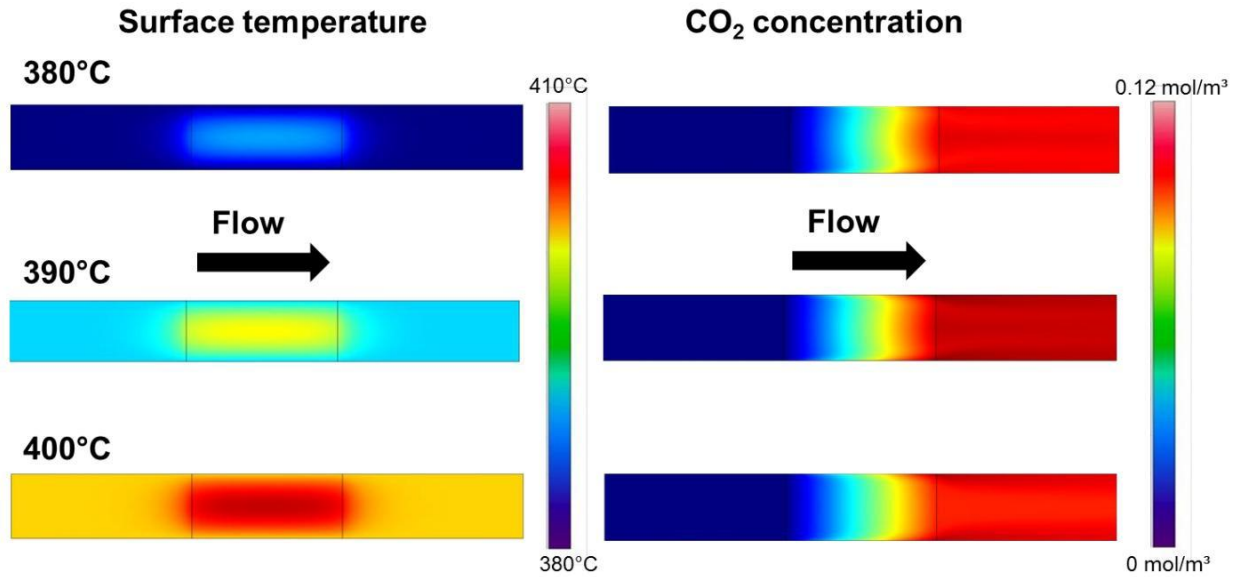


Figure 4-20: Simulated surface temperature (left) and CO₂ concentration (right) in catalytic soot oxidation on α -Fe₂O₃ at three representative inlet temperatures of the PFR. Conditions: F=500 ml/min (STP), $y(\text{O}_2)$ =5 vol.% O₂, N₂ balance, β =1.8 K/min, catalyst:soot ratio=10 mmol:5 mmol in tight contact mixture.

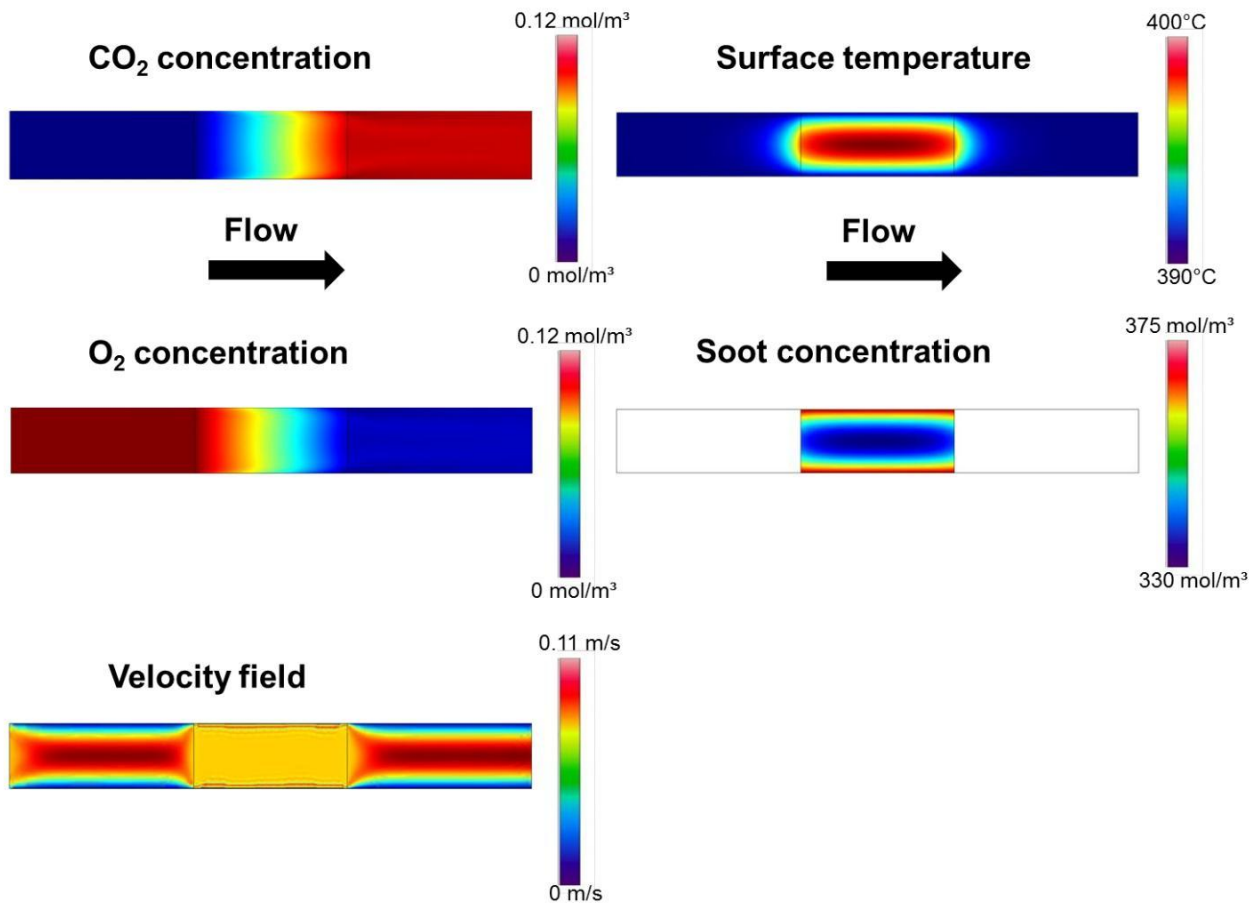


Figure 4-21: Simulated CO₂ concentration, surface temperature, O₂ and carbon concentration as well as velocity field in catalytic soot oxidation on α -Fe₂O₃ at an inlet temperature of 390°C of the PFR. Conditions: F=500 ml/min (STP), $y(\text{O}_2)$ 5 vol.%, N₂ balance, β =1.8 K/min, catalyst:soot ratio=10 mmol:5 mmol in tight contact mixture.

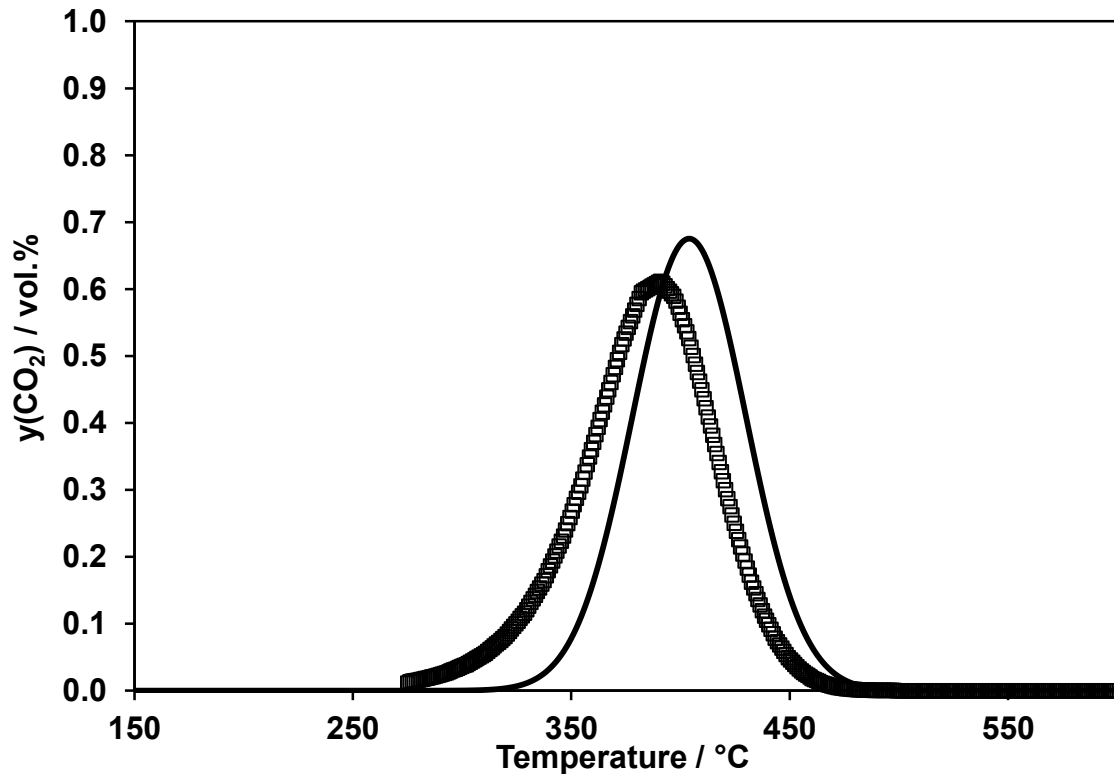


Figure 4-22: Comparison of experimental (—) and calculated (□) CO₂ volume fractions in catalytic soot oxidation on α -Fe₂O₃. Conditions: F=500 ml/min (STP), c(O₂) 10 vol.%, N₂ balance, β =1.8 K/min, catalyst:soot ratio=10 mmol:5 mmol in tight contact mixture.

4.4 Discussion

4.4.1.1 Reactor model

The approach presented for the determination of the Bo number is only valid for small extents of dispersion (<0.01). This is given by the overall Bo number of the complete reactor. But, due to the dispersion of the packed bed, the assumption of additivity of means and variances of the E(t) curves (Eq. (4-9)) might not be accurate [70]. Nevertheless, the intention of the calculation of the Bo number of the packed bed was to find a suitable reactor model. Therefore, a definite determination of Bo is not required. The calculated value of Bo=0.41 suggests backmixing in the packed bed justifying the CSTR model. Additionally, Carberry [83] demonstrated, under precondition of a low Re number, Pe_{ax} numbers for packed beds in a range between 0.03 and 1. The Pe_{ax} number is correlated with the Bo number by the particle diameter and the porosity of the packed bed [84,85]:

$$Pe_{ax} = \frac{u \cdot d_p}{\varepsilon \cdot D_{ax}} = Bo \cdot \frac{d_p}{L \cdot \varepsilon} \quad (4-39)$$

d_p : Particle diameter

[m]

L	: Length of the reactor	[m]
ϵ	: Porosity	[/]

Taking the experimental parameters of Carberry, i.e. a reactor length of 6" and a particle diameter of 6 mm, and assuming a porosity of 0.5 reveals a Bo number <1. This affirms the choice of the CSTR model for description of packed beds. Furthermore, the Re number [86] of the catalyst/soot mixture is calculated according to Eq. (4-40) as being 0.28. This supports the precondition of a small Re number for the approach of Carberry [83].

$$Re = \frac{\rho \cdot u_0 \cdot d_{p,Fe_2O_3}}{\eta \cdot (1 - \epsilon_{\text{apparent}})} \quad (4-40)$$

$\epsilon_{\text{apparent}}$: Apparent porosity (see chapter 4.3.1)	[/]
d_{p,Fe_2O_3}	: Particle diameter Fe_2O_3 (see Table C-1)	[m]
u	: Flow velocity in empty tube (see Table C-4)	[m/s]
η	: Dynamic viscosity of air (see Appendix D)	[Pa·s]
ρ	: Density of air (see Appendix D)	[kg/m ³]

4.4.1.2 Kinetic modelling

The kinetic modelling provides kinetic parameters to describe the reaction rate of the catalytic soot oxidation. As the model is based on a global reaction mechanism, an identification of the rate determining step (RDS) of the soot conversion is difficult. Nevertheless, a comparison between the activation energy obtained and the sub-steps of catalytic soot oxidation, i.e. oxygen adsorption, oxygen transfer, surface reaction and CO_2 desorption [23], aims to assess the RDS of the reaction. At catalytic soot oxidation, Stanmore [33] attributes a decrease of 60-95 kJ/mol in the activation energy, compared to the non-catalytic reaction, to an acceleration of oxygen adsorption on the soot surface due to presence of a catalyst. But, in accordance with Reichert [23], the isotopic studies (see chapter 3.2.5) revealed oxygen adsorption on the catalyst and subsequent oxygen transfer to the soot. Moreover, oxygen adsorption on the Fe_2O_3 catalyst is assumed to be non-activated [27] ($E_{A,ads}=0$ kJ/mol) and excluded as the RDS. Looking at the surface diffusion, Reichert shows, based on the studies of Becker, that the activation energy for oxygen diffusion upon catalytic soot oxidation is between 4 and 16 kJ/mol. This again indicates that it is not rate determining. In addition, a limitation due to product desorption can be excluded; the variation of the CO_2 volume fraction in the gas feed upon the mechanistic studies

presented (chapter 3.2.3.3) revealed no effect of CO_2 on the soot oxidation rate. This assumption is substantiated by Vronab [87] who assumed product desorption not to be rate determining at non-catalytic soot oxidation. Finally, the oxygen transfer from catalyst to soot has to be discussed. Unfortunately, due to lack of kinetic data a comparison between literature and obtained activation energy E_A cannot be drawn. Nevertheless, kinetic data of comparable reactions indicate that the oxygen transfer may be rate determining; Reddy [66] calculated the activation energy for oxygen exchange between Fe_2O_3 and the gas phase to be 405 kJ/mol. However, we must assume that the activation energy in presence of soot is considerably lower. As revealed by the mechanistic studies the O_2 -TPD of the $\alpha\text{-Fe}_2\text{O}_3$ sample (Figure 5-4) offered no thermal release of oxygen while the temperature programmed reduction on Fe_2O_3 using soot as reducing agent (Figure 3-22) showed that Fe_2O_3 is able to release and transfer oxygen to a soot particle even at low temperatures ($<250^\circ\text{C}$).

To compare the kinetic parameters obtained with literature, Table 4-8 summarises values of the activation energy of soot oxidation on different catalysts (type of catalyst, soot and contact mode), as well as the approach used for the determination of E_A . The presented values range between 65 and 201 kJ/mol indicating that the activation energy in this thesis ($E_A=73.4$ kJ/mol) is in the lower range of the values reported. This is ascribed to the determination method of the activation energy. The heat production of the reaction is not considered in the Arrhenius and modelling approaches presented (Table 4-8). Hence, the activation energies obtained result in very high values since the exothermal temperature increase is not included in these approaches. Furthermore, the values are only valid for a limited range of reaction conditions (i.e. mass of catalyst, mass of soot, heating rate, type of soot etc.) making it difficult to compare the kinetic parameters with each other. Also, a validation of the data is not presented by the authors, which questions the reliability of these activation energies.

Table 4-8: Values for the activation energy of catalytic soot oxidation derived from literature.

System	Method	E_A [kJ/mol]	Source
Fe ₂ O ₃ /self-made C ₃ H ₆ soot, tight contact	Global kinetic modelling	78	[18]
Fe ₂ O ₃ /Graphite		201	[88]
CeO ₂ /Diesel soot, loose contact	Redhead method [89]	159	[41]
Carbon Black/CeO ₂ , tight contact	E-TEM	133	[54]
Carbon Black/CeO ₂ , tight contact	Arrhenius plot [90]	65-90	[43]
Diesel soot/Cs ₄ V ₂ O ₇ , tight contact	Ozawa plot [91]	104	[44]
Diesel soot/K/CeO ₂ , tight contact	Arrhenius plot	73.9	[36]
Carbon Black/K/Cu/Cl, tight contact	Arrhenius plot	85-100	[92]
Flame soot/Pt/Al ₂ O ₃ -CoO _x -PbO _x	Redhead method	101	[93]

The modelling shows the heat transfer significantly affects the CO₂ formation. This is in accordance with the findings presented in chapter 3.2.1.4. Since the differential equations in the kinetic model for heat and mass transfer are solved for the time $t \rightarrow \infty$, implying stationary conditions, the initially determined heat transfer coefficient is valid for the corresponding experiment using a slow heating rate (i.e. 1.8 K/min) and low heat formation only. Hence, k has to be fitted for each TPO using different heating rates. The heat transfer coefficient is modified by multiplying k_0 with the ratio of the respective heating rate β to be validated and β_0 . As a result, the heat transfer coefficient k corresponding to β is obtained (Eq. (4-18)) thus extending the validity of the model. The validation of the experiment corresponding to a heating rate of 3.3 K/min, justifies the implementation of this expression by showing strong correlation between experiment and simulation. In addition, the heat transfer coefficient k has significant influence on the reaction rate and CO₂ profile. Changes < 1 % result in significantly different heat production and a CO₂ volume fraction. In further studies, the models area of validity should be checked for a broader range of oxygen volume fraction (e.g. <1 vol.% and >10 vol.%) as well as for different reaction conditions (e.g. heating rates >3.3 K/min).

An expression to cover loose contact mode between catalyst and soot by a global kinetic approach was presented in chapter 4.2.3. To verify the assumptions made and to obtain the foundations for the taken values (i.e. the diffusion analogical

coefficient, the activation energy and the distance between soot and catalyst) more experimental results are required from future studies. E-TEM studies as presented by Simonsen [54] might be a possibility to obtain deeper insights into processes occurring upon catalytic soot oxidation, e.g. by displaying and quantifying the processes on loose and tight contact Fe_2O_3 /soot mixtures under operando conditions.

4.4.1.3 Fluid dynamic modelling

Fluid dynamic modelling was carried out to obtain further insights into the physical and chemical processes upon catalytic soot oxidation. The one dimensional CSTR model (chapter 4.1) was only taken to determine the kinetic parameters, and is not able to describe the real reactor system in detail. The CFD model presented enables the description of TPO experiments in a satisfactory way. The transient examination and the use of the Brinkman equation result in higher accuracy of the model compared to the CSTR model. In particular, the transient heat transfer and the consideration of the heat conductivity of the packed bed by the Brinkman equation (Eq.(4-27)) overcomes the above mentioned problems concerning the heat transfer coefficient. The validity of the kinetic parameters, which were determined based on the CSTR model, is shown by the difference of $T_{\text{CO}_2, \text{max}}$ (Figure 4-22) between simulation and experiment. The coupling of the Brinkman equation and the kinetics, obtained on the basis of the CSTR model, exhibit a difference of 11 K in $T_{\text{CO}_2, \text{max}}$ only, which is within the reproducibility of the TPO experiments shown in the appendix (Figure A-1). The evolution and distribution of CO_2 (Figure 4-20) shows that behind the packed bed, the highest concentration is at the wall of the reactor. This can be explained by the simulated velocity field. The flow before and behind the packed bed is laminar and non-disturbed, which indicates a laminar boundary layer near the reactor walls. Inside the packed bed, the flow is influenced by the porous medium, which decreases the velocity field due to backmixing. The resulting velocity distribution corresponds well with the CO_2 concentration exhibiting high content in proximity to the wall behind the packed bed (area 3, Figure 4-15). This increased proportion is interpreted with the slow discharge of CO_2 nearby the reactor wall. The flow is non-disturbed on the longitudinal axis of the tube reactor and it offers the highest velocity. Close to the wall the velocity decreases as a consequence of friction (boundary condition $u=0$ m/s). This effect goes along with a small convective part of

the mass transport resulting in the accumulation of CO₂ in the boundary layers. Furthermore, the temperature rise in the packed bed reveals an increase of 10 K, and is in the same range compared to the experimentally determined temperature (Figure 4-7) under the given reaction conditions. The soot conversion is initiated in the middle of the packed bed and proceeds to the walls of the reactor, corresponding with the heat distribution of the packed bed. The high temperature in the middle of the packed bed may be attributed to the boundary current. The packed bed induces a high velocity in x-direction on the boundaries of the bed and a low velocity in the middle (Figure 4-21), which can be attributed to high backmixing due to the packed bed. This suggests low convective heat extraction in x-direction in the middle leading to accumulation of heat. The temperature in the middle exceeds the boundaries resulting in initiation of the reaction from the middle of the packed bed (Figure 4-20). The O₂ distribution shows sufficient oxygen, i.e. 1.7 mol/m³ (9 vol.%), is available, even at highest CO₂ formation under the given reaction conditions. To provide further insights, the model presented could be extended to a DPF system. For example, the description of two channels (i.e. one inlet and one outlet channel of the monolith) in the way that was shown by Knoth [94].

5 Evaluation of different iron oxide catalysts for soot oxidation

This chapter addresses the use of iron oxides catalysts for the oxidation of soot. The first section describes the requirements for soot oxidation catalysts, with a special focus on Fe_2O_3 . The second section examines seven different iron oxide catalysts which are physical-chemically characterised. Also NH_3 -TPD studies are extended by kinetic modelling of the NH_3 adsorption/desorption. Finally, the physical-chemical features are correlated with the catalytic performance of the respective samples to identify the determining properties for soot oxidation.

5.1 Requirements of an advanced catalyst for soot oxidation

For the use of catalysts in automotive exhausts, there are several technical requirements. Firstly, the coating of the wall-flow filter has to cause a low ignition temperature of the soot deposited. Secondly, thermal and hydrothermal stability must be assured due to high gas temperatures at full load conditions and uncontrolled soot burn-off. Thirdly, the catalytic material should consist of non-toxic components.

A series of materials, mainly transition metal oxides and rare earth metals, show catalytic activity for soot oxidation and have the ability to lower the ignition temperature of soot, respectively [38,54,95,96]. But considering that there is a rising demand for exhaust catalysts, it is impractical to use rare catalytic components, which will rise in cost as they become more scarce. Therefore, the development of catalysts with low or no noble metal content and with a preferably low rare earth fraction becomes more and more attractive. In this respect, iron based catalysts are reported to be effective for the oxidation of soot [23,28,34,40].

Due to the appearance of a multitude of different iron oxides [97] the process of catalyst development requires that iron oxides are pre-selected. This conforms to the requirements presented above. Among all the iron oxide compounds, Fe in a Fe^{3+} oxidation state represents the most stable modification. Such Fe_2O_3 species comprise ϵ -, γ - (Maghemite) and α - Fe_2O_3 (Hematite). While all modifications are stable below 300°C , the α -modification is thermodynamically favoured above 500°C [97,98]. Hence, Fe_2O_3 modifications are chosen to be the basis for the development of an advanced catalyst for soot oxidation.

5.2 Physical-chemical characterisation of different Fe₂O₃ catalysts

For physical-chemical characterisation, seven different iron oxides are used. This represents a broad basis for the detailed understanding of the crucial properties of soot oxidation. Thorough characterisation is carried out by using NH₃-TPD, O₂-TPD, HTPR, TEM, XRD and BET studies (see chapter 2). In doing so, the physical-chemical properties of the respective materials are elucidated to obtain information on the morphologies and phase composition of the samples. Subsequently, the determined features are coupled with the catalytic activity of the materials, derived from TPO experiments. The practical procedure covers experimental conditions following the mechanistic studies (chapter 3). This offers well defined results in the form of the temperature of maximum CO₂ concentration ($T_{CO_2,max}$), which is a degree for the catalytic activity. Formation of CO is not observed under these conditions. Moreover, the focus of this chapter is the correlation between catalytic activity and physical-chemical properties.

The following section presents the findings of the above mentioned analytical methods for the different Fe₂O₃ catalysts (see Table 5-1). Four commercial iron oxides were examined, two samples from Chempur company with different particle diameters and two samples from Lanxess company with different morphologies. Additionally, the experimental findings for two homemade Fe₂O₃ samples are presented. One of these samples is a α -Fe₂O₃, synthesised according to the PVA route [99] and the other is a γ -Fe₂O₃, which is also produced by a wet synthesis using a mixture of FeCl₂ and FeCl₃ precursors [19]. The last sample is the final result of the development process and it shows the highest activity for catalytic soot oxidation. It is synthesised by flame-spray pyrolysis (FSP). The synthesis of this advanced Fe₂O₃ material is presented in the following chapter. Afterwards, the respective experimental findings are demonstrated and discussed. Correlations and trends of all materials are shown in the last section of this chapter. The reasons for the high activity of the FSP sample are substantiated and discussed.

Table 5-1: Overview of the used Fe₂O₃ catalysts.

Sample	Manufacturer/Synthesis
Bulk α -Fe ₂ O ₃	PVA synthesis ex Fe(NO ₃) ₃ [99]
C10-20	Chempur Fe ₂ O ₃ , 10-20 nm primary particles
C7-10	Chempur Fe ₂ O ₃ , 7-10 nm primary particles
Bayoxide E 1.1	Lanxess company
Bayoxide E 2.1	Lanxess company
Bulk γ -Fe ₂ O ₃	Wet synthesis ex FeCl ₃ -FeCl ₂ precursor [19]
FSP Fe ₂ O ₃	Flame-spray pyrolysis ex Fe(NO ₃) ₃

5.2.1 Preparation of Flame-spray Fe₂O₃

The flame-spray synthesis (FSP) was chosen for the following reasons: its potential to produce metal oxide nanoparticles with a high number of active sites, thermal stability and the possibility to influence the product properties by changing a number of parameters in the synthesis procedure [100-102]. The principle of the FSP process is the atomisation of a liquid and combustible metal precursor, which is atomised and evaporated. This spray is ignited and requires a short residence time and high maximum process temperatures [103]. Particle formation is reported to proceed by following the steps of evaporation, reaction and nucleation [104].

The bench used for the FSP was exclusively developed and constructed for the synthesis of nano-sized catalysts useful for the oxidation of soot. Special focus was given to a high production rate (> 1 g/h) and the utilisation of on hand precursors. Many literature reports [101,103] concentrate on organic compounds only, implying minor availability and high costs. Therefore, the construction was designed to combust nitrate precursors, which are widely available, and provide high product rates. The general set-up of the bench (Figure 5-1) consists of four units: (1) the atomisation unit, (2) the combustion chamber, (3) the filtration system and (4) the exhaust gas unit.

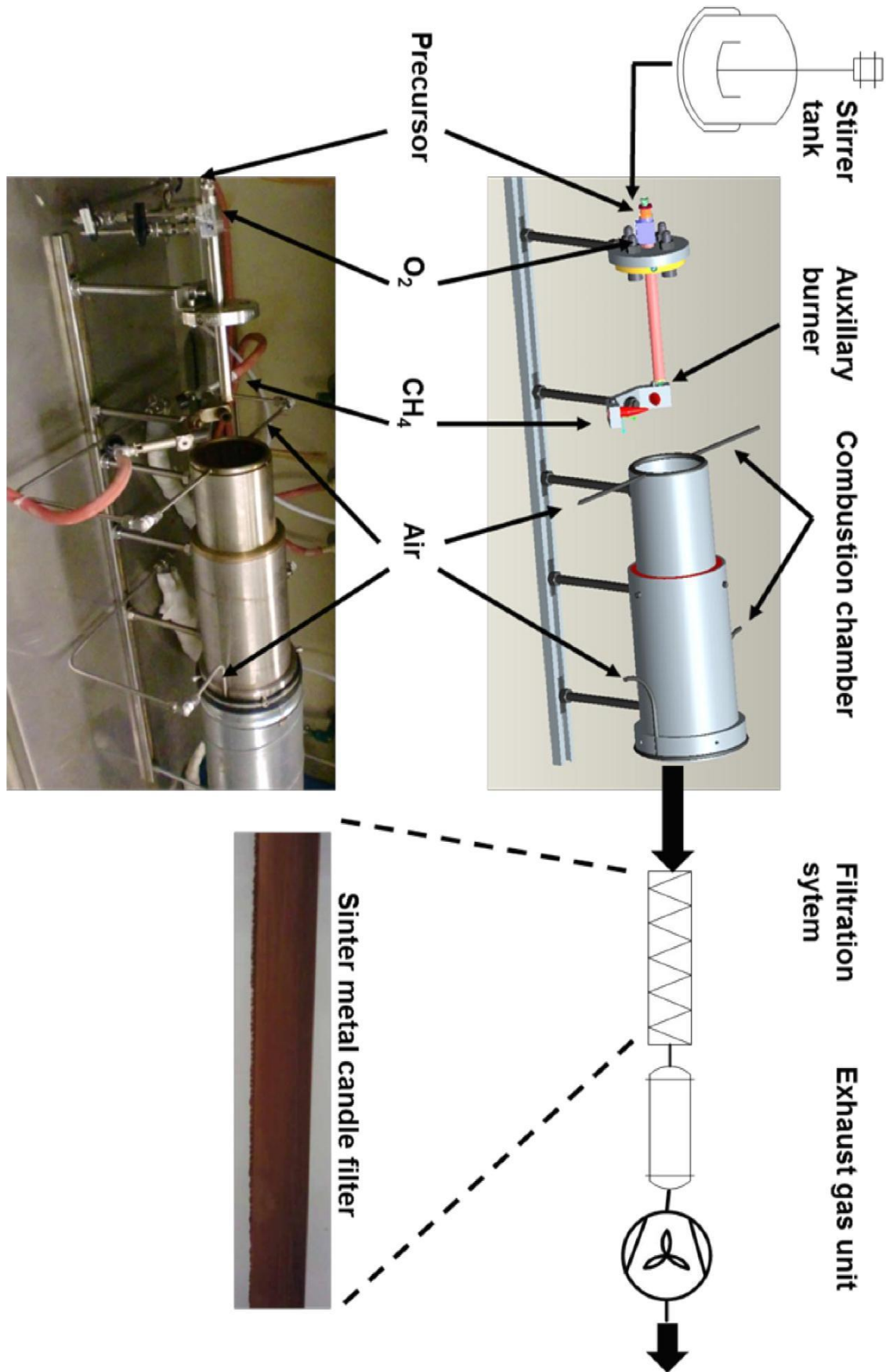


Figure 5-1: Flow-chart of the bench for the flame-spray synthesis. CAD drawing (top) and picture (bottom).

The atomisation unit (Figure 5-2) is a custom-made two-substance nozzle (Düsen-Schlick, Untersiemau/Coburg); the detailed characteristics are listed in the appendix (Table G-1). The injector system atomises the liquid precursor, which is provided by a stirrer tank and atomises the liquid by overpressure of an oxygen stream. This offers the advantage that a pump for atomisation is not required. This reduces the total number of components as well as the number of corrodible devices, which has to be considered due to the use of nitrate precursors. Furthermore, the nozzle facilitates the adjustment of the liquid flow by a needle valve and a change of the droplet size by variation of the oxygen pressure.

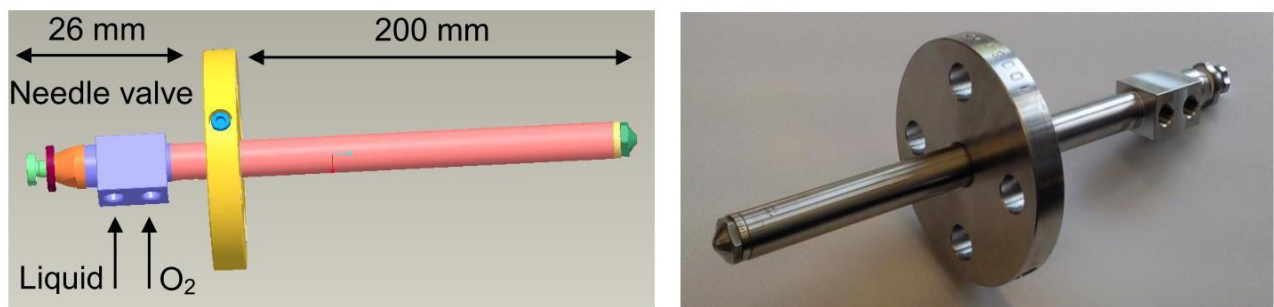


Figure 5-2: Two-substance nozzle for atomisation. CAD model (left) and picture of the custom-made nozzle (right). The CAD drawing is provided by Düsen-Schlick.

The atomised precursor solution is ignited by two Bunsen burners (CH_4 flame), which act also as an auxiliary burner. Afterwards, the flame is channelled into a tubular combustion chamber. To prevent agglomeration of the formed particles, the chamber is cooled by two bustle pipes at the beginning and at the end of the tube. This provides flow of cold air (quenched to -80°C by dry ice). The oxide particles are finally collected via a candle filter consisting of sinter metal with a length of 1200 mm and a diameter of 25 mm. The raw sheets of this filter are delivered by HJS (Menden) and modified to the required geometry. The particles are manually removed by a spatula from the filter as soon as a critical overpressure is achieved (flame backlash). To reduce the backpressure of the filter an aspirator is employed with an upstream heat exchanger, which quenches the gas flow to room temperature.

For stable working conditions the following parameters are found to be suitable. The precursor consists of an aqueous mixture of $\text{Fe}(\text{NO}_3)_3$ in volume ratio $\text{Fe}(\text{NO}_3)_3$ solution/propanol of 1:4. The concentration of the $\text{Fe}(\text{NO}_3)_3$ solution is 0.5 M. The other parameters are summarised in Table 5-2. Finally, the crop of Fe_2O_3 is quantified to be ca. 2-3 g/h.

Table 5-2: Operating parameters of the FSP bench.

Operating parameter	Value
Difference pressure of atomisation gas (O ₂)	$\Delta p=2$ bar
Throughput of liquid	Ca. 10 ml/min
Throughput of atomisation air (synthetic air)	Ca. 5 Nm ³ /h
Angle of spray cone	40°

5.2.2 Experimental results

5.2.2.1 Bulk α -Fe₂O₃

The NH₃-TPD curve of the bulk α -Fe₂O₃ catalyst demonstrates release of NH₃ within a range from 50°C to 360°C corresponding to an amount of $1.6 \cdot 10^{-6}$ mol/m² NH₃ desorbed. The deconvolution leads to $0.92 \cdot 10^{-6}$ mol/m² Brønsted bond and $0.68 \cdot 10^{-6}$ mol/m² Lewis bond ammonia (see chapter 2.4.2). The HTPR profile (Figure 5-3) includes a low-temperature maximum at 375°C, as well as a high-temperature maximum at 640°C with a shoulder at 560°C. This is in line with the reduction sequence Fe₂O₃→Fe₃O₄→FeO→Fe [26]. The area ratio of the high- to low-temperature peak was found to be 8.4. Additionally, the molar ratio of H₂ consumed to Fe used is 1.2. The O₂-TPD profile (Figure 5-4, right) exhibits no appreciable amount of thermally released O₂, even up to temperatures of more than 900°C. The phase analysis based upon XRD analysis (Figure 5-4, right) suggests α -Fe₂O₃ to be the only phase without any amorphous domains. Furthermore, TG analysis (Figure 5-5, left) reveals a relative mass loss of 0.6 %, whereas the DTA signal offers a broad curve progression without clear extremes indicating no phase changes. The BET study (Figure 5-5, right) quantifies the specific surface area to be 12 m²/g and suggests a total pore volume of 0.15 cm³/g. Such low values might be ascribed to the thermal aging procedure during the synthesis, i.e. aging for 5h at 600°C [24]. In combination with the TG/DTA findings these results indicate high-temperature stability of the bulk α -Fe₂O₃ making this sample very suitable for use as a reference material. Moreover, TEM images (Figure 5-6) illustrate particles ranging from 80 to 200 nm. Finally, TPO data show a clear catalytic effect of the bulk α -Fe₂O₃ as referred to a run without catalyst. In presence of α -Fe₂O₃ the maximum CO₂ volume fraction is at 408°C (Figure 5-7), whereas in the absence of catalyst it appears at ca. 570°C (Figure 3-3).

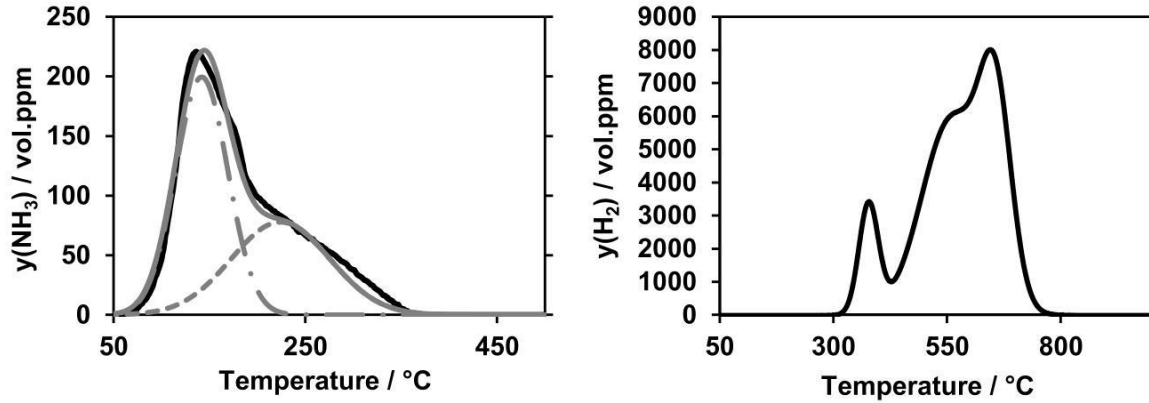


Figure 5-3: Bulk α - Fe_2O_3 . Left: Experimental data (—) and Gaussian fit (---) of the NH_3 -TPD spectrum. The dashed lines represent the deconvoluted spectrum, whereas (---) corresponds with the Brønsted bond NH_3 and (---) with the Lewis bond NH_3 . Conditions: $m_{\text{Fe}_2\text{O}_3}=2.57$ g, $F=500$ ml/min, $\beta=10$ K/min. Right: HTPR spectrum. Conditions: $m_{\text{Fe}_2\text{O}_3}=0.06$ g, $F=200$ ml/min, $\beta=15$ K/min.

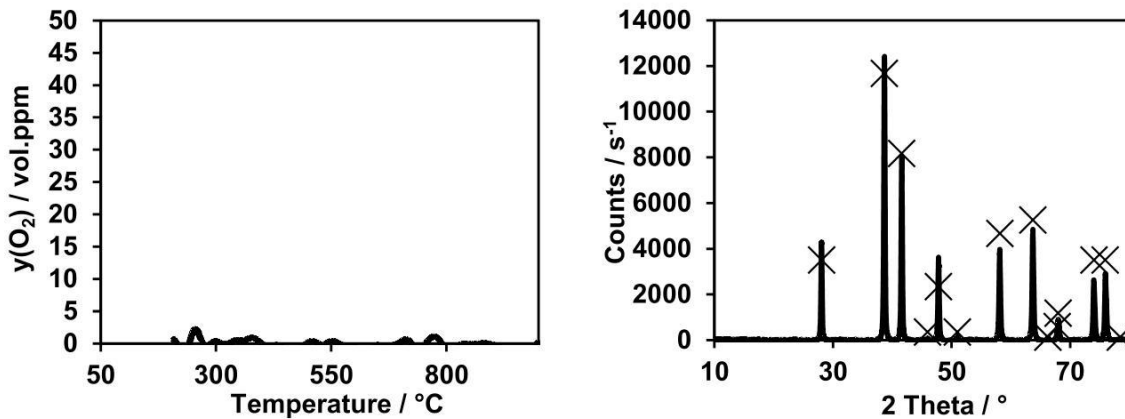


Figure 5-4: Bulk α - Fe_2O_3 . Left: O_2 -TPD spectrum. Conditions: $m_{\text{Fe}_2\text{O}_3}=5.06$ g, $F=500$ ml/min, $\beta=10$ K/min. Right: PXRD pattern. (X) corresponds to ideal hematite phase.

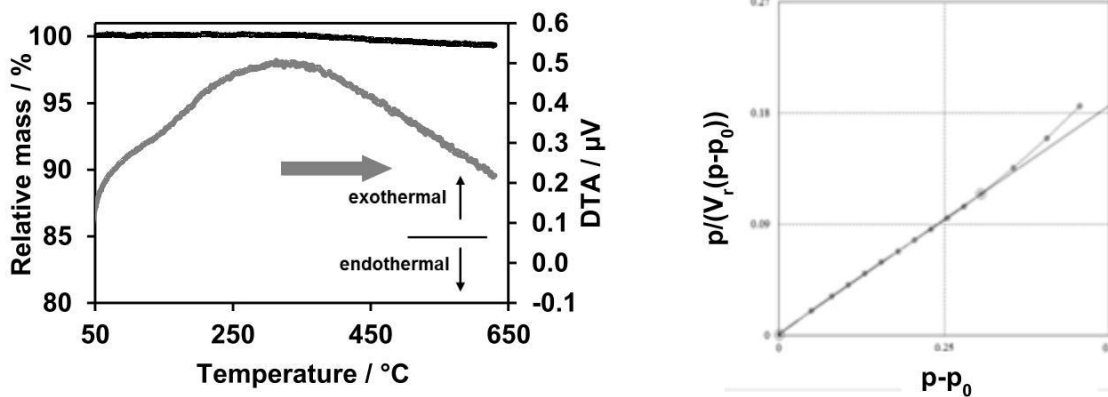


Figure 5-5: Bulk α - Fe_2O_3 . TG/DTA analysis. Conditions: $m_{\text{Fe}_2\text{O}_3}=0.053$ g, $F=500$ ml/min, $\beta=3.3$ K/min. Right: BET plot of N_2 physisorption.

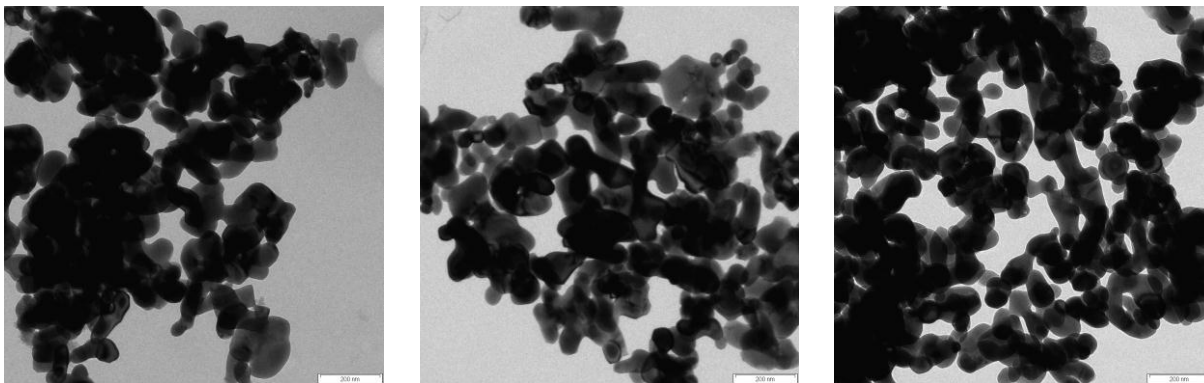


Figure 5-6: TEM images of Bulk α -Fe₂O₃.

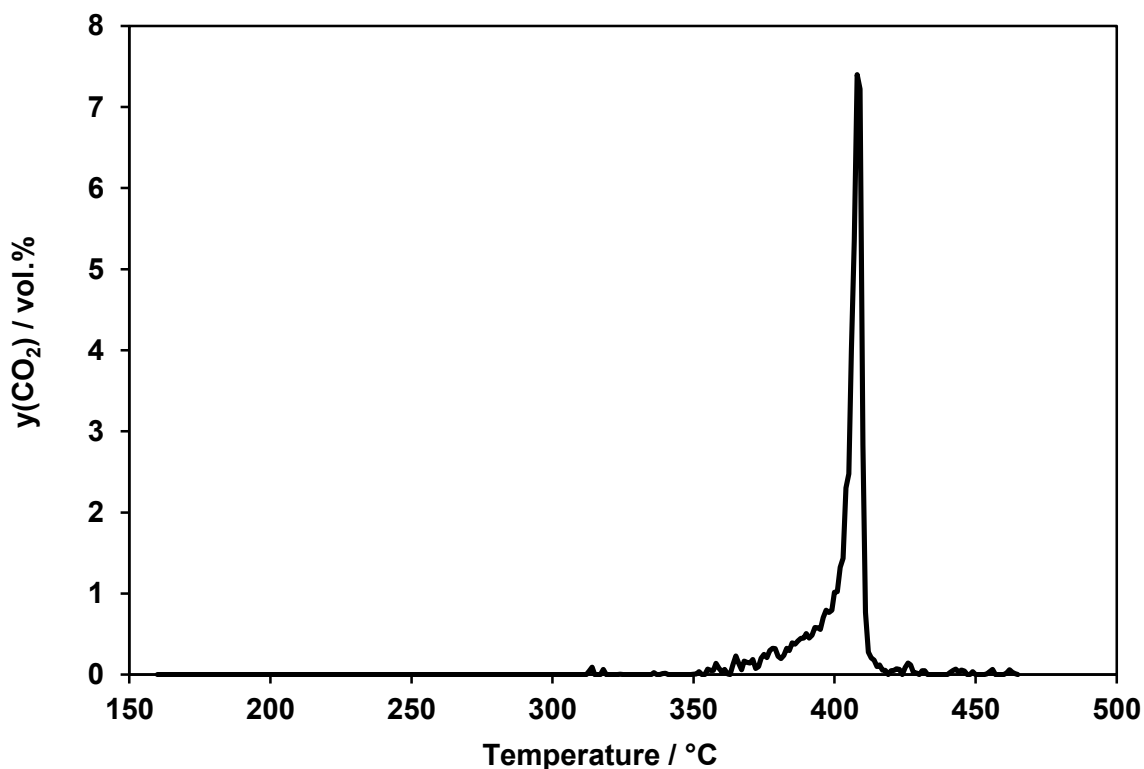


Figure 5-7: TPO pattern of Bulk α -Fe₂O₃. Conditions: 10 mmol catalyst and 5 mmol soot in tight contact mode, F=500 ml/min, 10 vol.% O₂ in N₂, β =3.3 K/min.

5.2.2.2 Chempur Fe₂O₃ 10-20 nm (C10-20)

The NH₃-TPD pattern of C10-20, shown in Figure 5-8, indicates a rather narrow desorption curve, which ranges from 50°C to 300°C and corresponds to $8.66 \cdot 10^{-7}$ mol/m² NH₃ desorbed. The deconvolution of the NH₃-TPD spectrum results in a dominating number of Brønsted acid sites ($8.38 \cdot 10^{-7}$ mol/m² vs. $0.28 \cdot 10^{-7}$ mol/m² for Lewis sites). The HTPR pattern (Figure 5-8, right) exhibits a low-temperature (peak at 344°C) and a high-temperature peak at 705°C with a shoulder at 585°C corresponding to the reduction cycle presented above. The area ratio of high- to low-temperature peak is 10.6, indicating the presence of reduced iron compounds. The

ratio of consumed H_2 to the used molar amount of Fe is 1.22. This suggests also the existence of Fe^{2+} species.

The O_2 -TPD profile (Figure 5-9) shows an oxygen release above $650^\circ C$ only. These oxygen species obviously play no major role in the catalytic soot oxidation occurring significantly below $400^\circ C$. Thus, the high-temperature oxygen release is rather associated with decomposition of the catalyst. The XRD analysis of the C10-20 (10-20nm) reveals a crystallinity of about 90 % consisting of 63 % γ - Fe_2O_3 and 27 % Fe_3O_4 . This agrees with the HTPR experiments. Additionally, the TG/DTA analysis (Figure 5-10) reveals 2 peaks and a mass loss of 1 % only. This loss is mainly due to the conversion of Fe_3O_4 (24.4 wt.% of the initial mass) to Fe_2O_3 under the given reaction conditions, which causes a mass increase of 0.84 wt.% in the case of that Fe_3O_4 fraction. This might also be in accordance with the DTA signal which increases continuously. The two peaks at $175^\circ C$ and $580^\circ C$ are attributed to desorption of water and hydroxide decomposition, respectively. The BET measurement, which is shown in Figure 5-10, results in an active surface area of $74\text{ m}^2/\text{g}$ and a pore volume of $0.26\text{ cm}^3/\text{g}$. Furthermore, the TEM studies (Figure 5-11) display primary particles diameters between 10 nm and 20 nm, as well as the formation of large agglomerates. Finally, the catalytic performance of the Chempur Fe_2O_3 C10-20 is presented in Figure 5-12, quantified by the temperature of maximum CO_2 volume fraction, which is $388^\circ C$ offering clearly better activity than bulk α - Fe_2O_3 ($T_{CO_2,max}=408^\circ C$).

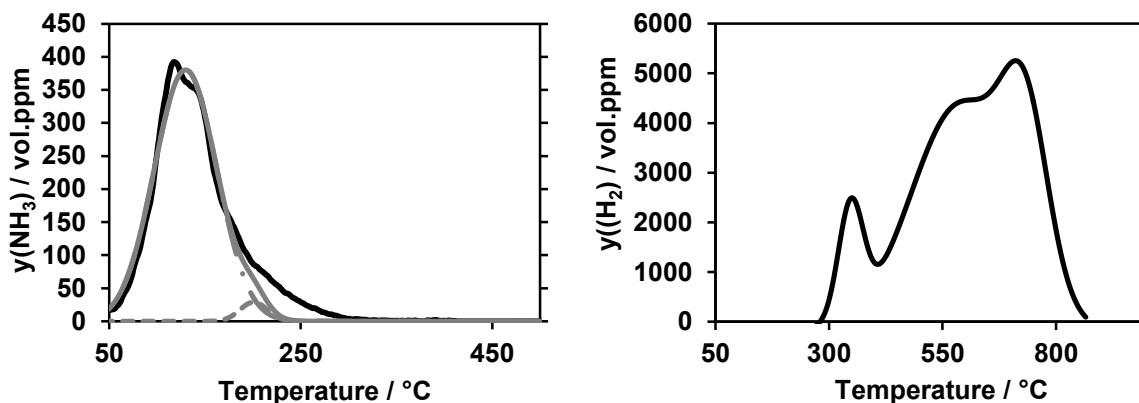


Figure 5-8: C10-20 sample. Left: Experimental data (—) and Gaussian fit (—) of the NH_3 -TPD spectrum. The dashed lines represent the deconvoluted spectrum, whereas (— · —) corresponds with the Brønsted bond NH_3 and (---) with the Lewis bond NH_3 . Conditions: $m_{Fe_2O_3}=1.02\text{g}$, $F=500\text{ ml/min}$, $\beta=10\text{ K/min}$. Right: HTPR spectrum, $m_{Fe_2O_3}=0.06\text{ g}$, $F=500\text{ ml/min}$, $\beta=10\text{ K/min}$.

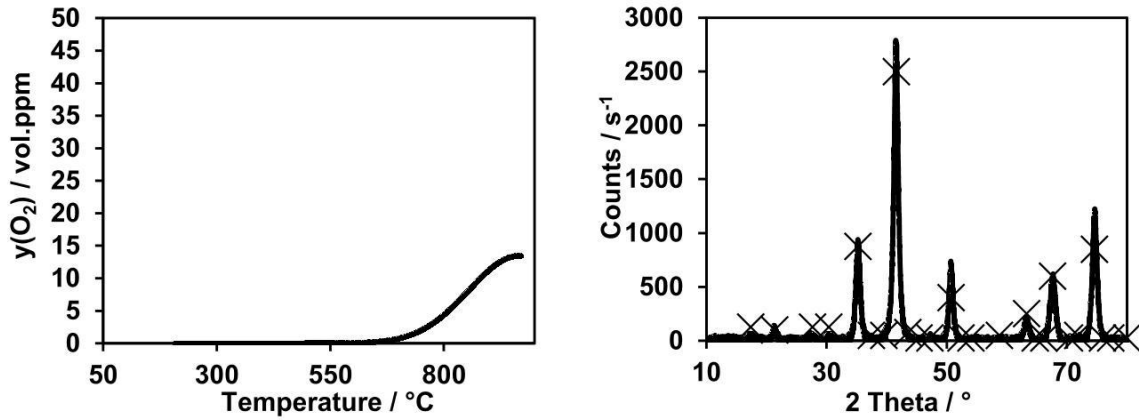


Figure 5-9: C10-20 sample. Left: O₂-TPD spectrum. Conditions: $m_{\text{Fe}_2\text{O}_3}=5.25$ g, $F=500$ ml/min, $\beta=10$ K/min. Right: PXRD pattern. (X) corresponds to ideal maghemite phase.

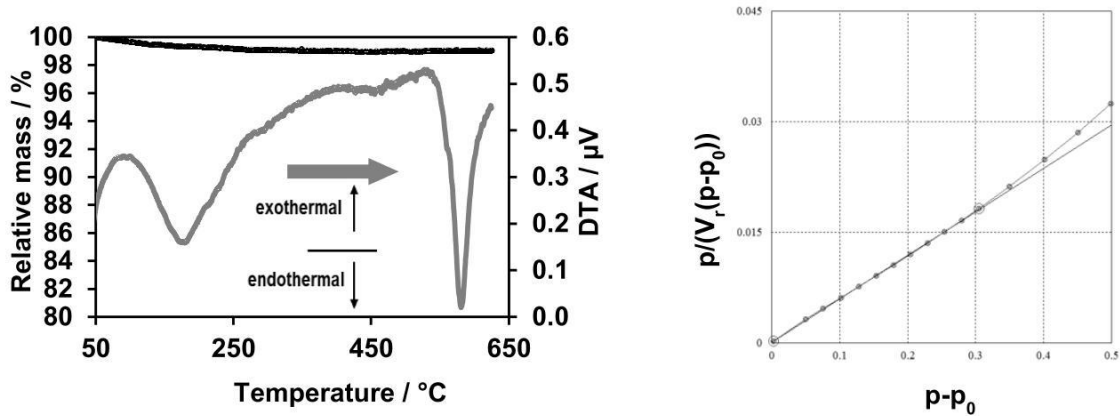


Figure 5-10: C10-20 sample. Left: TG/DTA analysis. Conditions $m_{\text{Fe}_2\text{O}_3}=0.070$ g, $F=500$ ml/min, $\beta=3.3$ K/min. Right: BET plot of N₂ physisorption.

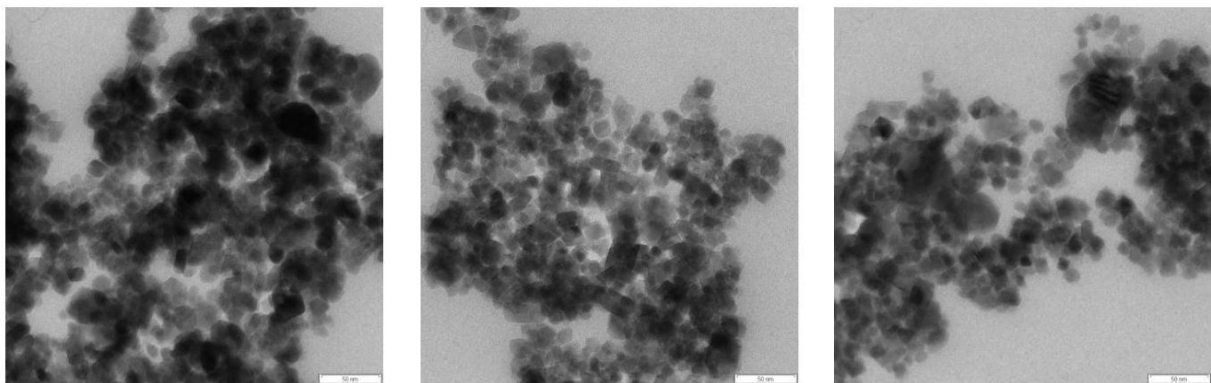


Figure 5-11: TEM images of C10-20 sample.

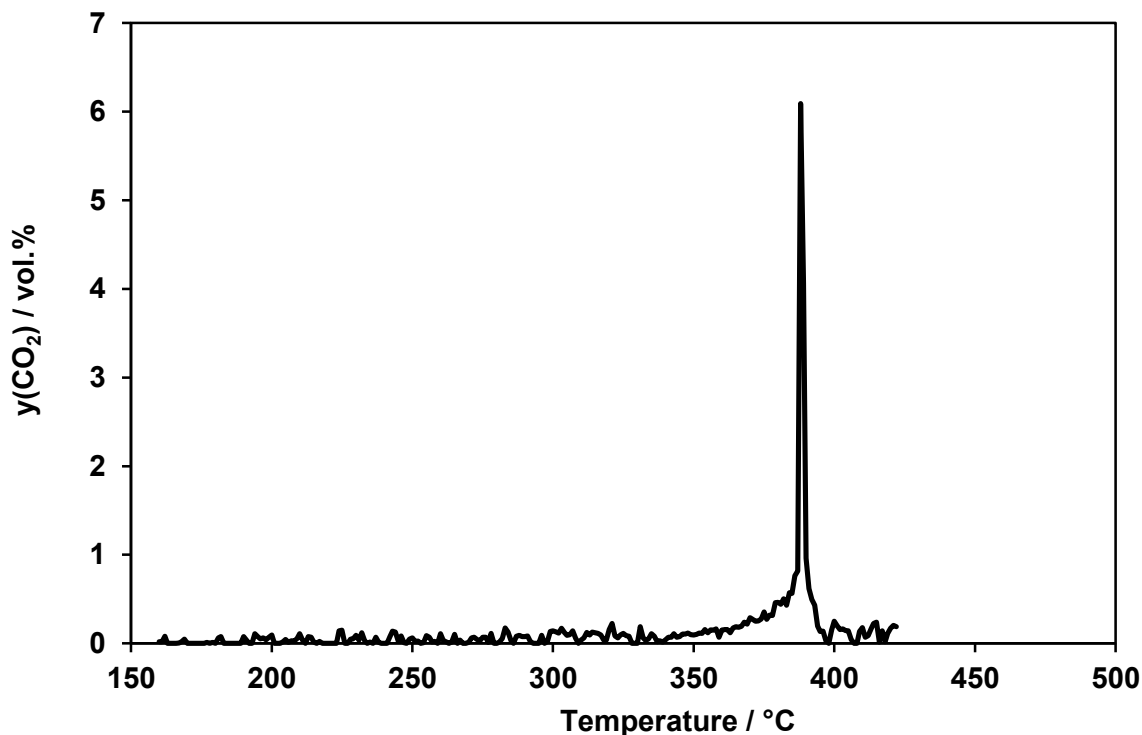


Figure 5-12: TPO pattern of C10-20 sample. Conditions: 10 mmol catalyst and 5 mmol soot in tight contact mode, $F=500$ ml/min, 10 vol.% O_2 in N_2 , $\beta=3.3$ K/min.

5.2.2.3 Chempur Fe_2O_3 7-10 nm (C7-10)

The NH_3 -TPD curve of the C7-10 sample shows desorption from 50°C to 250°C with a total NH_3 release of $4.12 \cdot 10^{-7}$ mol/m². A deconvolution of the desorption curve leads to $2.96 \cdot 10^{-7}$ mol/m² Brønsted and $1.16 \cdot 10^{-7}$ mol/m² Lewis bond NH_3 . The HTPR analysis (Figure 5-13) features two prominent H_2 consumption maxima, i.e. a low-temperature peak at 340°C and a high-temperature peak at 560°C including a small shoulder at 440°C showing an area ratio of 7.52. The proportion of consumed H_2 to used molar amount of Fe is 0.95. Both calculations suggest the existence of reduced iron compounds. The O_2 -TPD profile, shown in Figure 5-14, exhibit two clear, but weak signals at 575°C and at about 850°C. The latter refers to the decomposition of the material. The diffractogram of the C7-10 (Figure 5-14, right) reveals a proportion of crystalline domains of ca. 90 % with a fraction of 62 % γ - Fe_2O_3 and 38 % Fe_3O_4 . Nevertheless, the existence of other reduced iron oxide compounds, e.g. stoichiometric FeO, which might be derived from the HTPR studies, cannot be detected. The TG/DTA analysis (Figure 5-15, left) offers a mass loss of 1.1 %, whereas the DTA measurement reveals three extrema: (1) At 75°C the DTA signal shows a positive increase which may be attributed to oxidation of reduced surface compounds. (2) A negative DTA peak at 170°C as well as (3) at 565°C

indicating desorption of water. The latter may be attributed to hydroxide decomposition. The overall progression of the DTA signal shows a continuous rise, suggesting that the oxidation of reduced Fe is in line with the HTPR findings. BET measurement (Figure 5-15, right) results in a surface area of 91 m²/g and a pore volume of 0.28 cm³/g.

Moreover, TEM images of the sample are presented in Figure 5-16, which mainly illustrates particles with diameters between 7 nm and 10 nm. Finally, the catalytic activity of this sample was tested in a TPO experiment with soot (Figure 5-17) and can be named in form of the temperature for maximum CO₂ volume fraction which is 376°C indicating a temperature shift of 32 K compared to bulk α -Fe₂O₃ (T_{CO₂,max}=408°C).

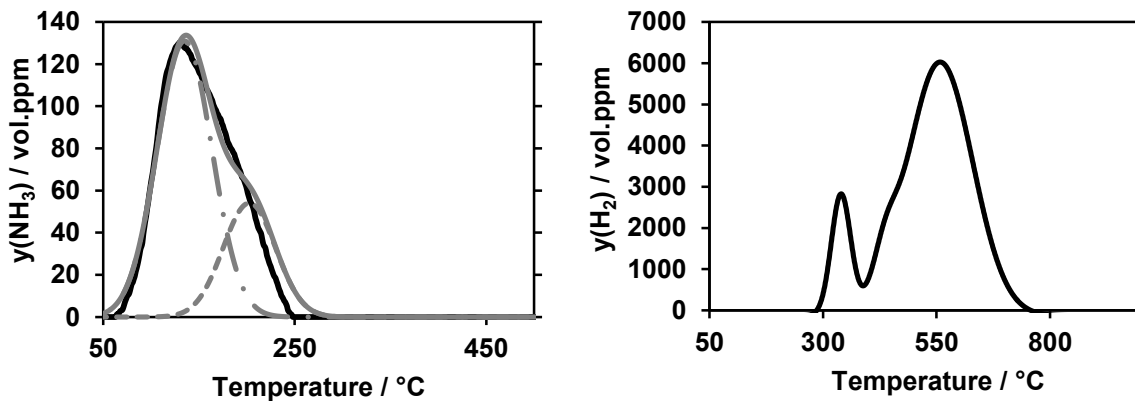


Figure 5-13: C7-10 sample. Left: Experimental data (—) and Gaussian fit (---) of the NH₃-TPD spectrum. The dashed lines represent the deconvoluted spectrum, whereas (— · —) corresponds with the Brønsted bond NH₃ and (---) with the Lewis bond NH₃. Conditions: m_{Fe₂O₃}=0.72 g, F=500 ml/min, β =10K/min. Right: HTPR spectrum. Conditions: m_{Fe₂O₃}=0.06 g, F=200 ml/min, β =15 K/min.

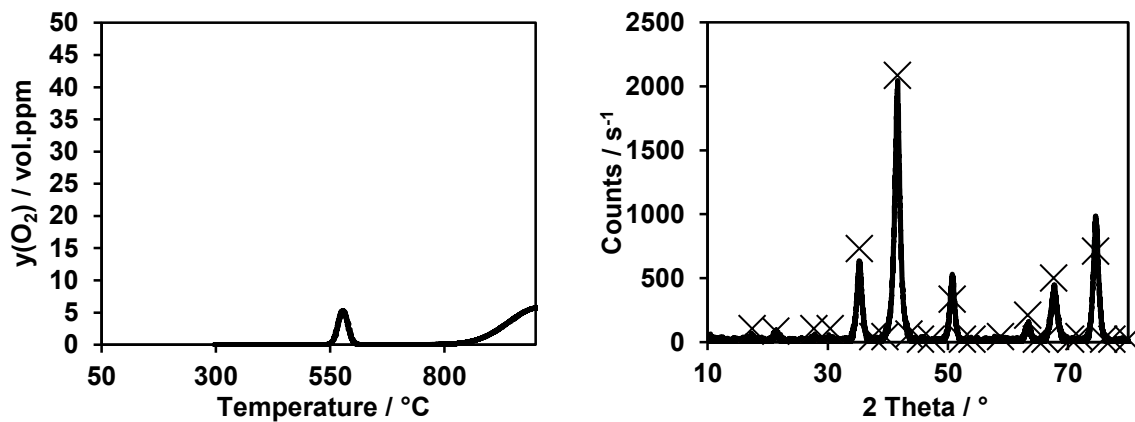


Figure 5-14: C7-10 sample. Left: O₂-TPD spectrum. Conditions: m_{Fe₂O₃}=2.56 g, F=500 ml/min, β =10 K/min. Right: PXRD pattern. (X) corresponds to ideal maghemite phase.

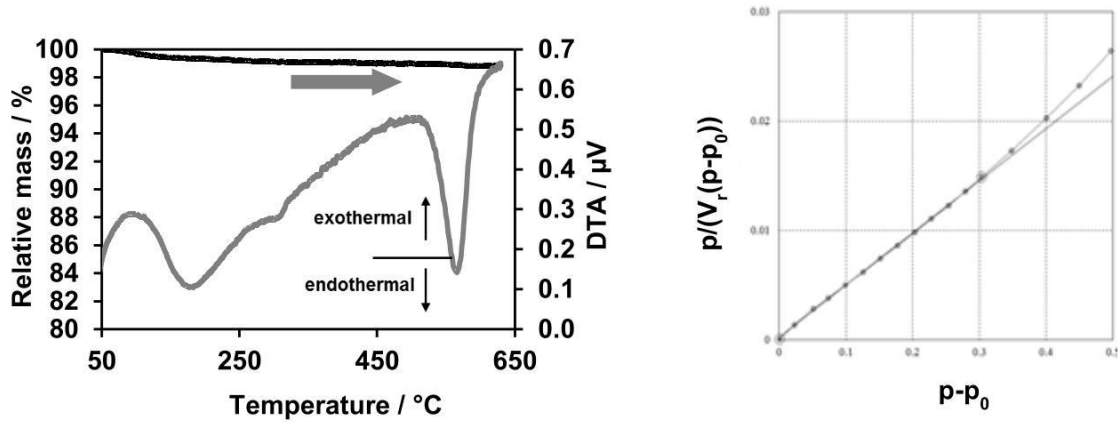


Figure 5-15: C7-10 sample. Left: TG/DTA analysis. Conditions: $m_{\text{Fe}_2\text{O}_3}=0.064$ g, $F=500$ ml/min, $\beta=3.3$ K/min. Right: BET plot of N_2 physisorption.

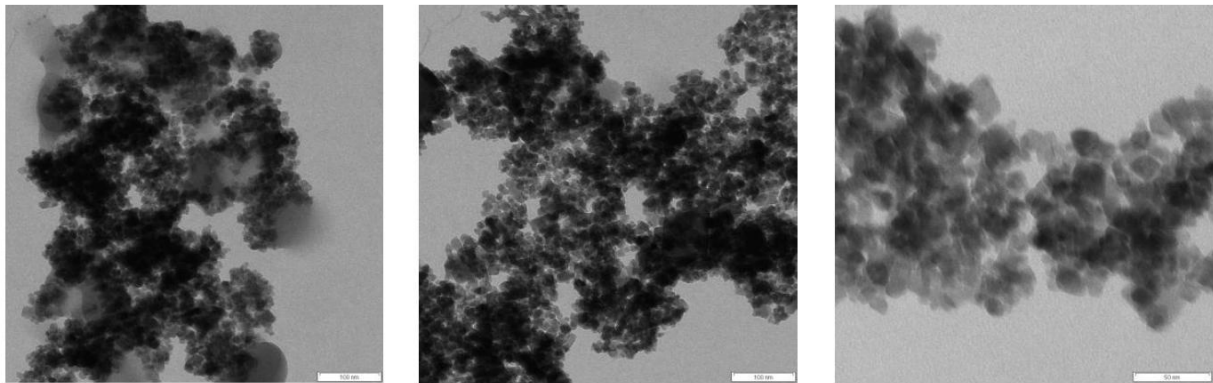


Figure 5-16: TEM images of C7-10 sample.

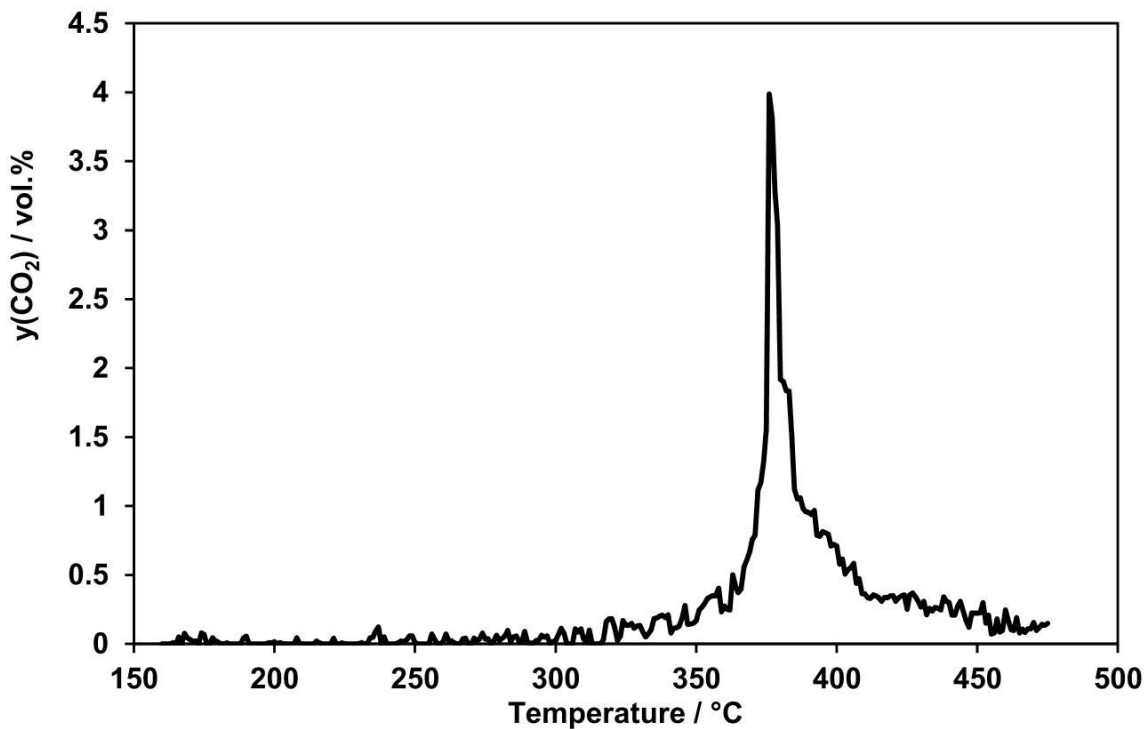


Figure 5-17: TPO pattern of C7-10 sample. Conditions: 10 mmol catalyst and 5 mmol soot in tight contact mode, $F=500$ ml/min, 10 vol.% O_2 in N_2 , $\beta=3.3$ K/min.

5.2.2.4 Lanxess Bayoxide E 1.1

The NH₃-TPD curve of the Lanxess Bayoxide E 1.1 (Figure 5-18) reveals ammonia desorption from 50°C to 340°C corresponding to an amount of $1.71 \cdot 10^{-6}$ mol/m² NH₃. The proportion of Brønsted and Lewis sites is quantified as $1.16 \cdot 10^{-6}$ mol/m² and to $0.55 \cdot 10^{-6}$ mol/m². The HTPR profile (Figure 5-18, right) exhibits a low-temperature H₂ signal ($T_{\text{peak}}=370^\circ\text{C}$) as well as a high-temperature range of H₂ consumption with a prominent maximum at 570°C and a shoulder at 710°C. This implies the reduction sequence $\text{Fe}_2\text{O}_3 \rightarrow \text{Fe}_3\text{O}_4 \rightarrow \text{FeO} \rightarrow \text{Fe}$. The molar ratio of consumed H₂ to Fe used is 1.32, indicating a predominant Fe³⁺ species. However, the area ratio of high- to low-temperature peak is 12 which suggests that Fe²⁺ compounds are present. But, in accordance with XRD and TEM studies, the broadening of the high-temperature peak might be ascribed to a broad particle size distribution. The literature reports [105] that an increase in particle size comes along with an increase in activation energy for the initial reduction sequence $\text{Fe}_2\text{O}_3 \rightarrow \text{Fe}_3\text{O}_4$. This causes an overlapping of the specific HTPR spectrum, since multiple processes proceed at the same temperature, i.e. small pre-reduced particles follow the sequence $\text{Fe}_3\text{O}_4 \rightarrow \text{FeO} \rightarrow \text{Fe}$, while bigger particles follow the sequence $\text{Fe}_2\text{O}_3 \rightarrow \text{Fe}_3\text{O}_4$.

The O₂-TPD (Figure 5-19, left) shows no clear release of oxygen below 850°C. The analysis of the x-ray diffractogram reveals a crystalline proportion of 86.4 % with a single phase ($\alpha\text{-Fe}_2\text{O}_3$). The TG/DTA study (Figure 5-20, left) shows a mass loss of 2.5 % and the DTA signal offers two low temperature extremes (70°C and 240°C) as well as continuous decrease of the signal, starting at 320°C. This might be ascribed to evaporation of water and decomposition of hydroxides. This decrease initiated at 320°C shows correlation with the O₂-TPD affirming the assumption of some kind of decomposition. Additionally, the BET surface area is 127 m²/g and the total pore volume is 0.54 cm³/g. The TEM images (Figure 5-21) of the sample display a multiplicity of particle shapes and sizes. The major part of the particles is spicular and shows a length from 50 nm to 100 nm at a diameter of 2-5 nm. Also, spherical particles are observed with diameters of more than 200 nm. Catalytic activity of the Bayoxide E 1.1 was tested by a TPO experiment, depicted in Figure 5-22 and revealing a temperature of maximum CO₂ volume fraction of 368°C which is 40 K below $T_{\text{CO}_2, \text{max}}$ of bulk $\alpha\text{-Fe}_2\text{O}_3$.

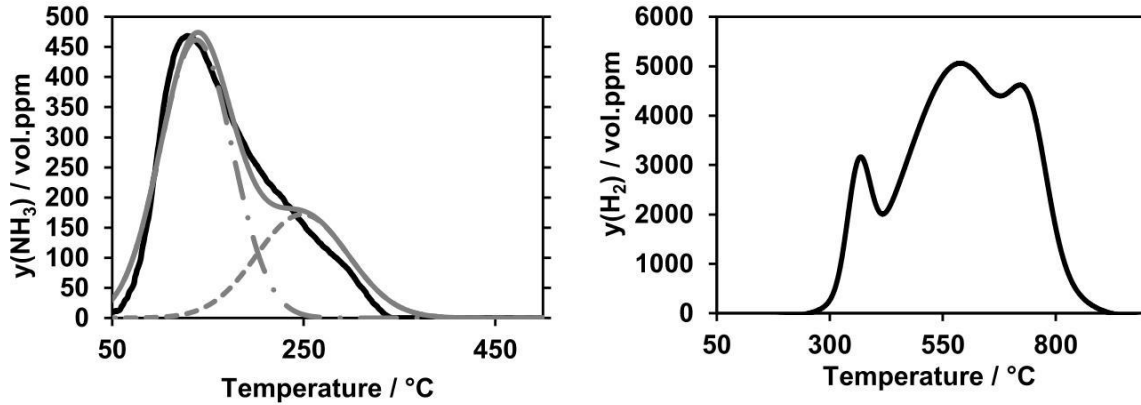


Figure 5-18: Bayoxide E 1.1. Left: Experimental data (—) and Gaussian fit (—) of the NH_3 -TPD spectrum. The dashed lines represent the deconvoluted spectrum, whereas (— · —) corresponds with the Brønsted bond NH_3 and (---) with the Lewis bond NH_3 . Conditions: $m_{\text{Fe}_2\text{O}_3}=0.61$ g, $F=500$ ml/min, $\beta=10$ K/min. Right: HTPR spectrum. Conditions: $m_{\text{Fe}_2\text{O}_3}=0.06$ g, $F=200$ ml/min, $\beta=15$ K/min.

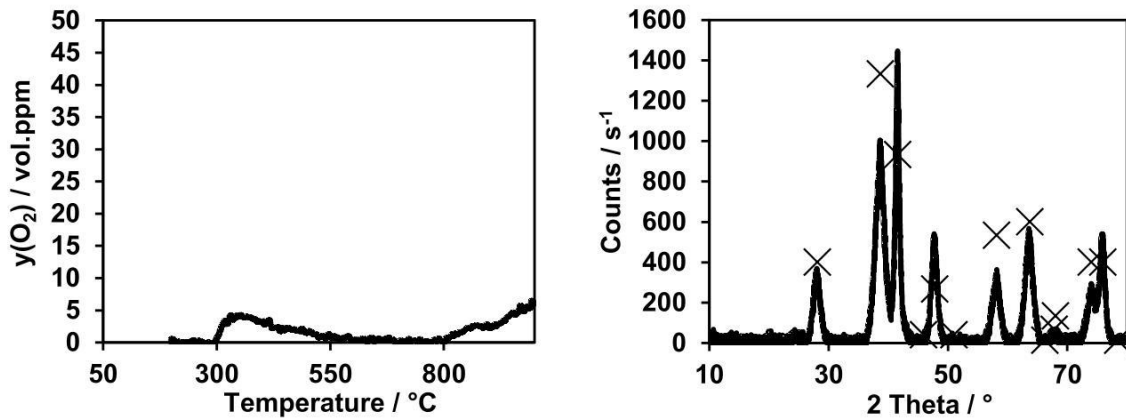


Figure 5-19: Bayoxide E 1.1. Left: O_2 -TPD spectrum. Conditions: $m_{\text{Fe}_2\text{O}_3}=4.8$ g, $F=500$ ml/min, $\beta=10$ K/min. Right: PXRD pattern. (X) corresponds to ideal hematite phase.

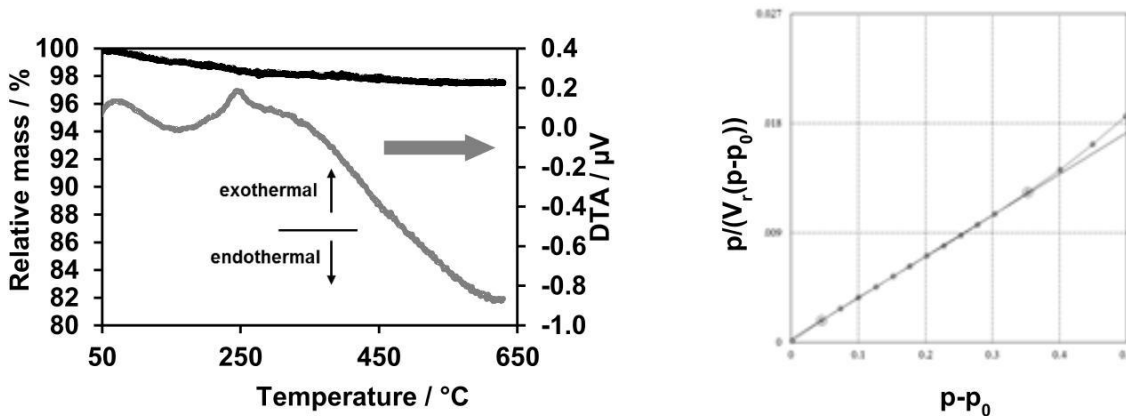


Figure 5-20: Bayoxide E 1.1. Left: TG/DTA analysis. Conditions: $m_{\text{Fe}_2\text{O}_3}=0.029$ g, $F=500$ ml/min, $\beta=3.3$ K/min. Right: BET plot of N_2 physisorption.

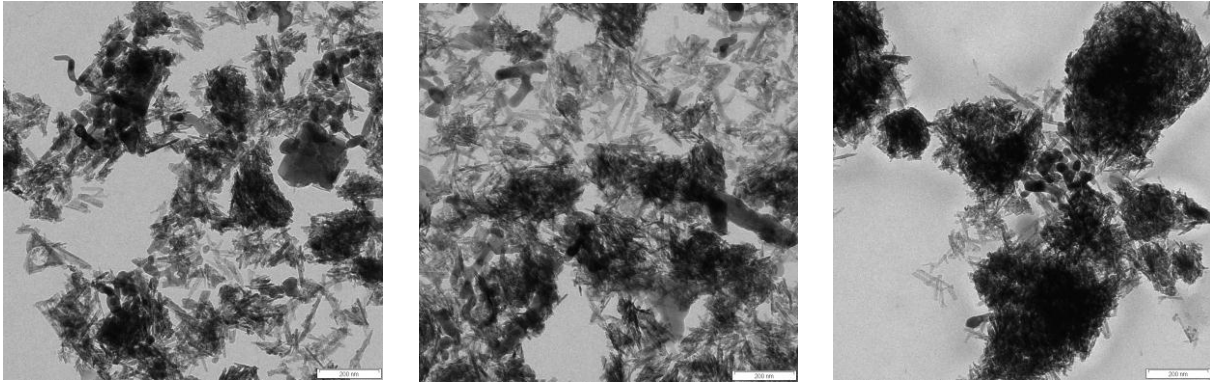


Figure 5-21: TEM images Bayoxide of E 1.1.

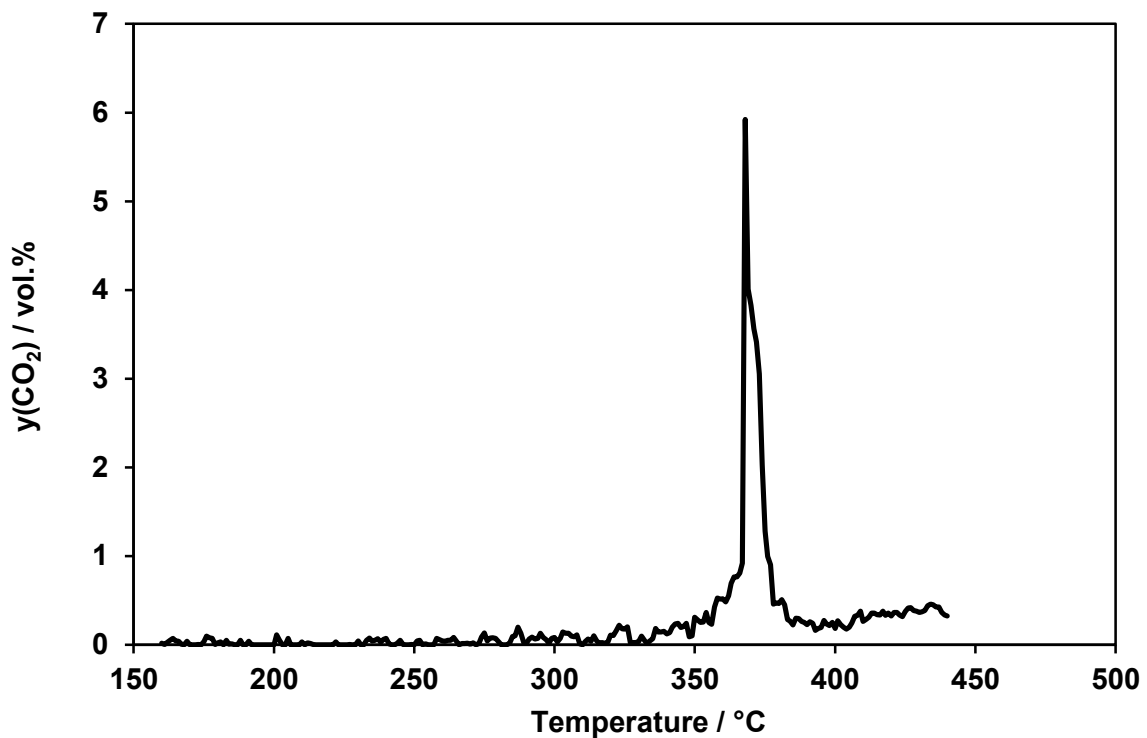


Figure 5-22: TPO pattern of Lanxess Bayoxide E 1.1. Conditions: 10 mmol catalyst and 5 mmol soot in tight contact mode, $F=500$ ml/min, 10 vol.% O_2 in N_2 , $\beta=3.3$ K/min.

5.2.2.5 Lanxess Bayoxide E 2.1

The ammonia TPD spectrum of the Bayoxide E 2.1 (Figure 5-23) indicates that an amount of $1.31 \cdot 10^{-6}$ mol/m² ammonia was desorbed. Deconvolution of the NH_3 -TPD reveals $6.7 \cdot 10^{-7}$ mol/m² Brønsted bond NH_3 and $6.4 \cdot 10^{-7}$ mol/m² Lewis bond NH_3 . The H_2 consumption during the HTPR experiment (Figure 5-23, right) exhibits several peaks. However, a classification is rather difficult. In accordance with the XRD results (Figure 5-19), which shows very poor reflexes, an absence of any crystalline structure is assumed. For this reason, a correlation of the HTPR curve corresponding to the reduction sequence $Fe_2O_3 \rightarrow Fe_3O_4 \rightarrow FeO \rightarrow Fe$ is not possible, which excludes the calculation of any area ratio. Nevertheless, the molar ratio of

consumed H_2 to used Fe is 1.162 indicating Fe^{3+} as major oxidation state. The O_2 -TPD (Figure 5-24) presents a massive oxygen release beginning at $720^\circ C$, can be ascribed to the decomposition of the sample. But, due to the high temperature, this process is irrelevant for catalytic soot oxidation. The TG analysis (Figure 5-25, left) offers a mass loss of 8.3 % and the DTA signal shows extremes at $80^\circ C$ and $550^\circ C$. The positive maximum at the beginning can be attributed to the oxidation of reduced surface compounds, whereas the negative peak can be ascribed to decomposition of the material, as supported by O_2 -TPD. The BET surface area is $230\text{ m}^2/\text{g}$ and the total pore volume quantifies $0.41\text{ cm}^3/\text{g}$. In addition, the TEM images (Figure 5-26) present very small particles without any visible long range order. Finally, Figure 5-27 reveals the catalytic activity of the Bayoxide E 2.1 indicated by a temperature of maximum CO_2 volume fraction of $414^\circ C$ which is 6 K higher compared to bulk $\alpha\text{-}Fe_2O_3$.

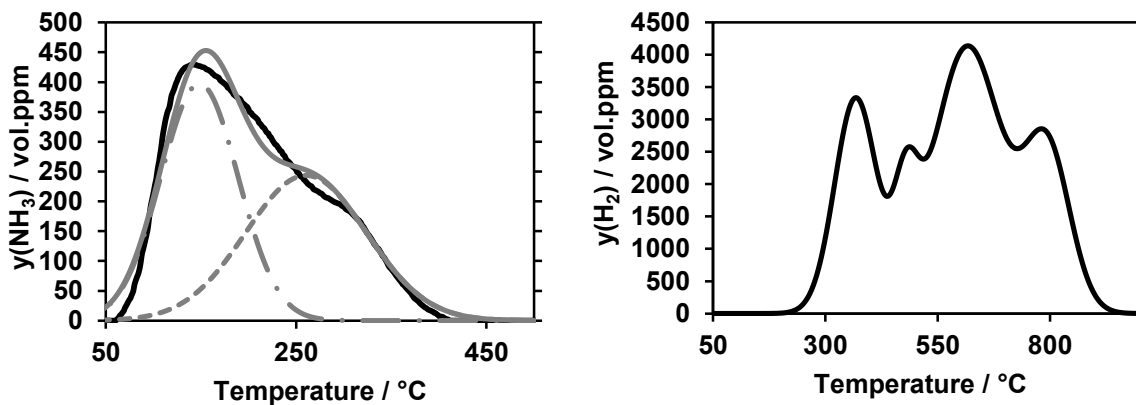


Figure 5-23: Left: Experimental data (—) and Gaussian fit (---) of the NH_3 -TPD spectrum. The dashed lines represent the deconvoluted spectrum, whereas (— · —) corresponds with the Brønsted bond NH_3 and (---) with the Lewis bond NH_3 . Conditions: $m_{Fe_2O_3}=0.54\text{ g}$, $F=500\text{ ml/min}$, $\beta=10\text{ K/min}$. Right: HTPR spectrum. Conditions: $m_{Fe_2O_3}=0.06\text{ g}$, $F=200\text{ ml/min}$, $\beta=15\text{ K/min}$.

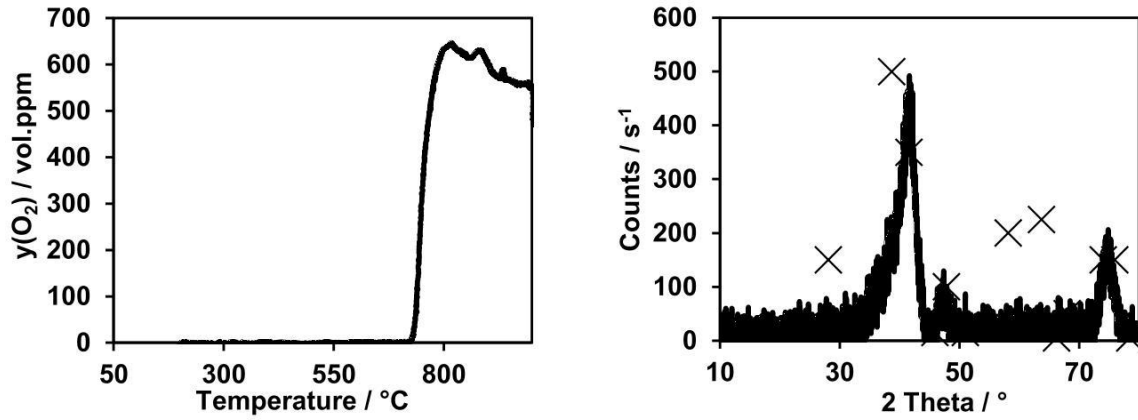


Figure 5-24: Bayoxide E 2.1. Left: O₂-TPD spectrum. Conditions: $m_{\text{Fe}_2\text{O}_3}=5.75$ g, $F=500$ ml/min, $\beta=10$ K/min. Right: PXRD pattern. (X) corresponds to ideal hematite phase.

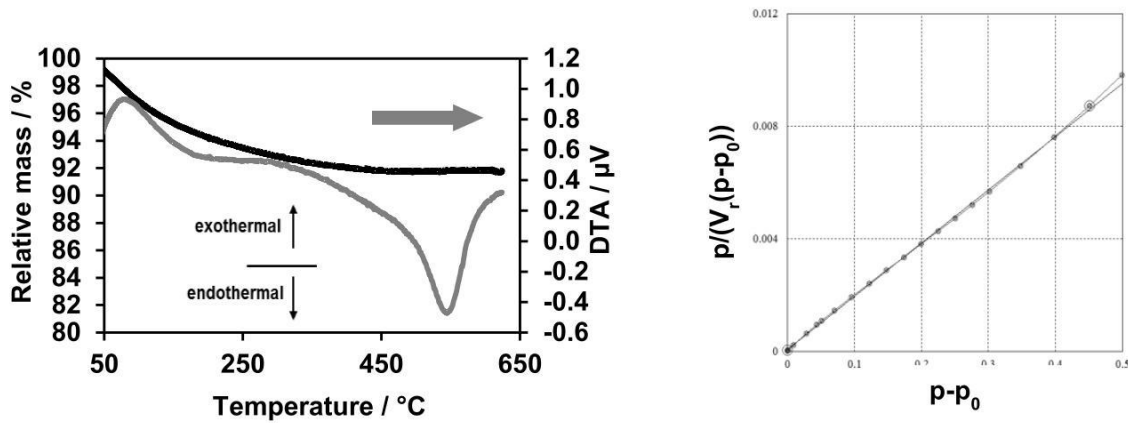


Figure 5-25: Bayoxide E 2.1. Left: TG/DTA analysis. Conditions: $m_{\text{Fe}_2\text{O}_3}=0.054$ g, $F=500$ ml/min, $\beta=3.3$ K/min. Right: BET plot of N₂ physisorption.

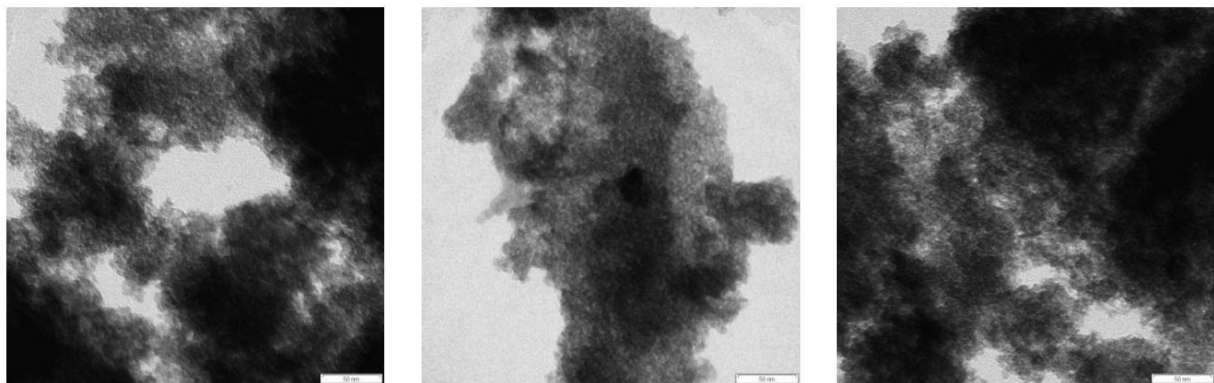


Figure 5-26: TEM images of Bayoxide E 2.1.

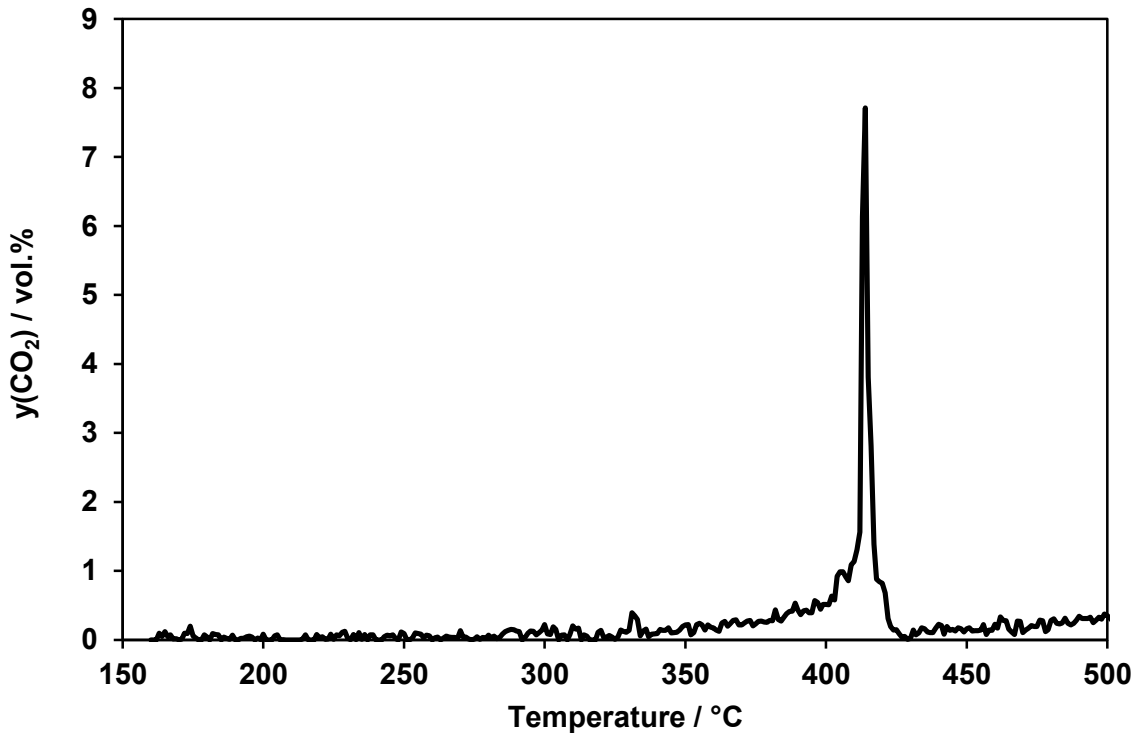


Figure 5-27: TPO pattern of Bayoxide E 2.1. Conditions: 10 mmol catalyst and 5 mmol soot in tight contact mode, $F=500$ ml/min, 10 vol.% O_2 in N_2 , $\beta=3.3$ K/min.

5.2.2.6 Bulk $\gamma\text{-Fe}_2\text{O}_3$

The NH_3 -TPD spectrum of the bulk $\gamma\text{-Fe}_2\text{O}_3$ sample (Figure 5-28) reveals NH_3 desorption from 50°C to 420°C including an amount of $1.59 \cdot 10^{-6}$ mol/m² NH_3 desorbed. The deconvolution of the spectrum results in $0.65 \cdot 10^{-6}$ mol/m² Brønsted bond and $0.94 \cdot 10^{-6}$ mol/m² Lewis bond NH_3 . The HTPR profile (Figure 5-28, right) exhibits a clear low-temperature signal at 412°C , as well as a high-temperature maximum at 680°C with a shoulder at 780°C . This can be attributed to the reduction cycle $Fe_2O_3 \rightarrow Fe_3O_4 \rightarrow FeO \rightarrow Fe$. The area ratio of high- to low-temperature peak is 8.15, indicating that Fe^{3+} is the predominant oxidation state. Also, the ratio of consumed H_2 to the molar amount of Fe used is 1.33. The O_2 -TPD signal (Figure 5-29, left) indicates no oxygen release, even at temperatures above 900°C . Moreover, the x-ray diffractogram of the $\gamma\text{-Fe}_2\text{O}_3$ sample (Figure 5-29, right) and the phase analysis, respectively, suggest a crystallinity of 80 % with a composition of 58 % Fe_3O_4 and 42 % $\gamma\text{-Fe}_2\text{O}_3$. But, in accordance to the HTPR findings, the proportion of $\gamma\text{-Fe}_2\text{O}_3$ should be almost 100 %. This discrepancy is explained by the use of the Co cathode and the resulting problems described in chapter 2.5. Additionally, TG/DTA exhibits a mass loss of 0.8 % and two prominent peaks in the DTA signal, i.e. at 205°C and at 565°C . The small mass loss indicates stable Fe_2O_3 composition

of the sample. The first peak of the DTA signal suggests evaporation of water. The second peak suggests a possible phase change from $\gamma\text{-Fe}_2\text{O}_3$ to $\alpha\text{-Fe}_2\text{O}_3$. The BET measurement (Figure 5-30, right) results in a specific surface area of $62\text{ m}^2/\text{g}$ and a total pore volume of $0.41\text{ cm}^3/\text{g}$. Furthermore, the TEM images (Figure 5-31) show particle diameters within a range from 10 nm to 100 nm. The catalytic performance of the $\gamma\text{-Fe}_2\text{O}_3$ material is presented in Figure 5-32, quantified by the temperature of maximum CO_2 volume fraction which is 381°C and 27 K below bulk $\alpha\text{-Fe}_2\text{O}_3$.

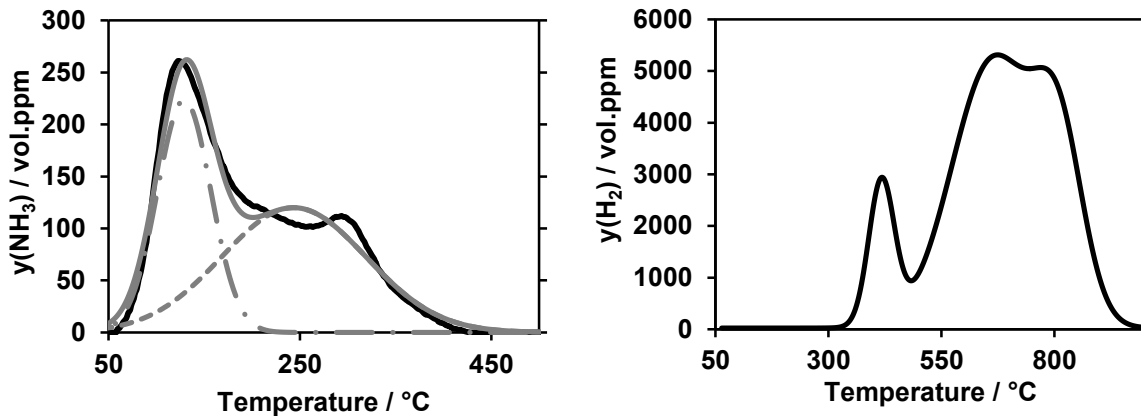


Figure 5-28: Bulk $\gamma\text{-Fe}_2\text{O}_3$. Left: Experimental data (—) and Gaussian fit (—) of the NH_3 -TPD spectrum. The dashed lines represent the deconvoluted spectrum, whereas (— · —) corresponds with the Brønsted bond NH_3 and (--) with the Lewis bond NH_3 . Conditions: $m_{\text{Fe}_2\text{O}_3}=0.8\text{ g}$, $F=500\text{ ml/min}$, $\beta=10\text{ K/min}$. Right: HTPR spectrum. Conditions $m_{\text{Fe}_2\text{O}_3}=0.06\text{ g}$, $F=200\text{ ml/min}$, $\beta=15\text{ K/min}$.

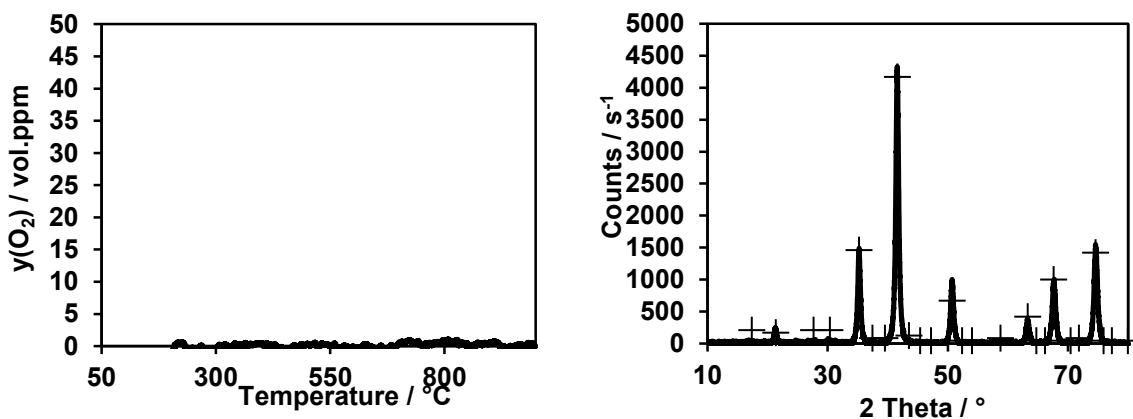


Figure 5-29: Bulk $\gamma\text{-Fe}_2\text{O}_3$. Left: O_2 -TPD spectrum. Conditions: $m_{\text{Fe}_2\text{O}_3}=4.25\text{ g}$, $F=500\text{ ml/min}$, $\beta=10\text{ K/min}$. Right: PXRD pattern. (X) corresponds to ideal maghemite phase.

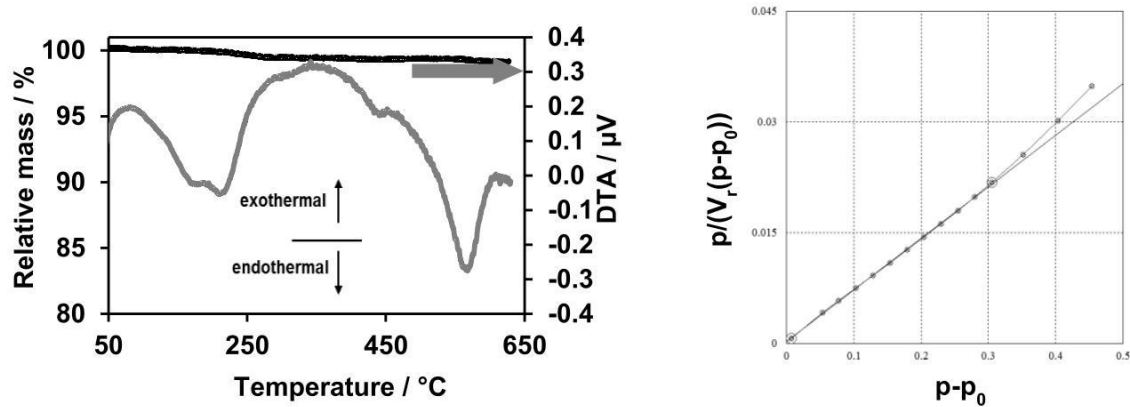


Figure 5-30: Bulk $\gamma\text{-Fe}_2\text{O}_3$. Left: TG/DTA analysis. Conditions: $m_{\text{Fe}_2\text{O}_3}=0.052$ g, $F=500$ ml/min, $\beta=3.3$ K/min. Right: BET plot of N_2 physisorption.

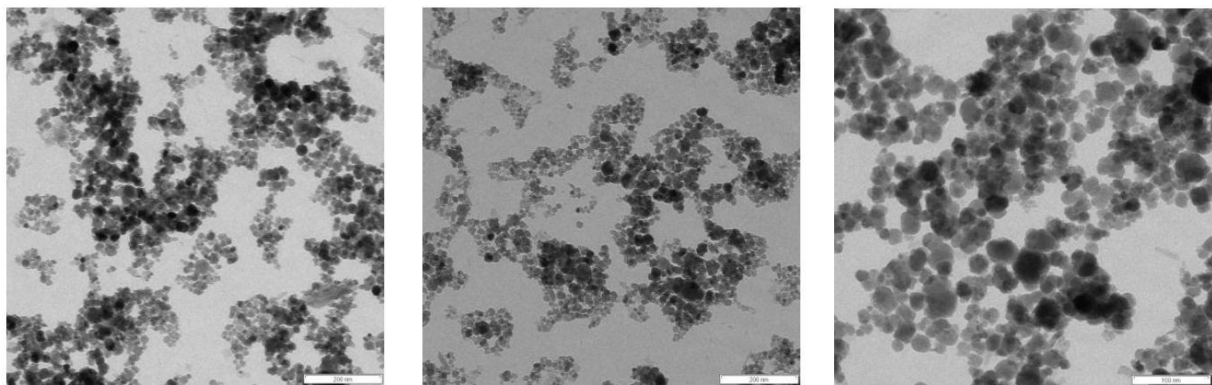


Figure 5-31: TEM images of Bulk $\gamma\text{-Fe}_2\text{O}_3$.

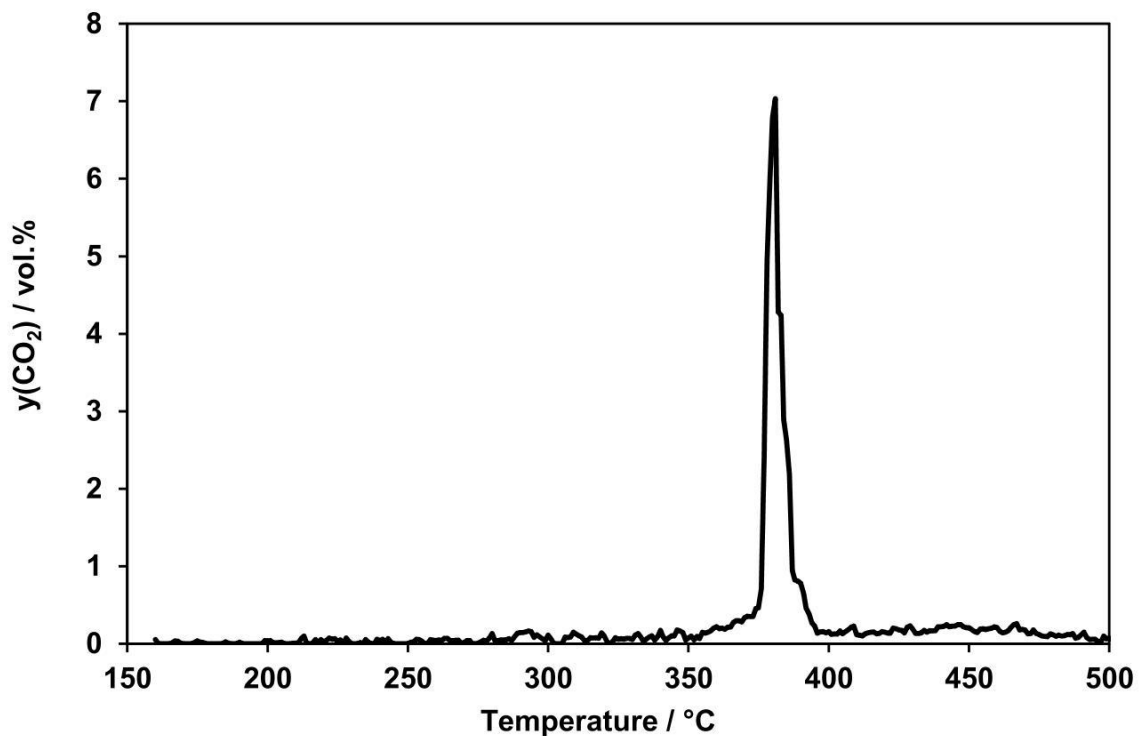


Figure 5-32: TPO pattern of Bulk $\gamma\text{-Fe}_2\text{O}_3$. Conditions: 10 mmol catalyst and 5 mmol soot in tight contact mode, $F=500$ ml/min, 10 vol.% O_2 in N_2 , $\beta=3.3$ K/min.

5.2.2.7 FSP-Fe₂O₃

The NH₃-TPD spectrum (Figure 5-33, left) of the FSP Fe₂O₃ sample reveals a broad desorption curve, which spans a temperature range from 50°C to 360°C. The total amount of desorbed ammonia is $2.72 \cdot 10^{-6}$ mol/m². Based on the deconvolution of TPD spectrum, the amount of Brønsted bond and Lewis bond NH₃ is quantified to $1.32 \cdot 10^{-6}$ mol/m² and $1.40 \cdot 10^{-6}$ mol/m², indicating a balanced ratio of Brønsted/Lewis sites. The HTPR profile (Figure 5-33, right) reveals both, a low- (360°C) and a high-temperature signal showing a shoulder at 550°C and peak H₂ consumption at 630°C. This can be associated with the reduction sequence Fe₂O₃ → Fe₃O₄ → FeO → Fe. The high- to low-temperature peak area ratio was found to be 8.7 suggesting Fe₂O₃ to be predominant. In addition, the total conversion of H₂ referred to the used molar amount of Fe results in a ratio of 1.13, suggesting the presence of reduced iron species. The O₂-TPD profile, shown in Figure 5-34, exhibits no appreciable amount of thermally released O₂, even at temperatures of more than 900°C. The phase analysis (Figure 5-34) suggests a crystalline fraction of 50 % with a proportion of 66 % α-Fe₂O₃, 19 % γ-Fe₂O₃ and 15 % Fe₃O₄. The separation of γ-Fe₂O₃ and Fe₃O₄ is difficult due to the use of the Co Cathode (see chapter 2.5). In addition to the HTPR results, which exhibits an area ratio of 8.6 of the temperature to high temperature peak and a H₂/Fe³⁺ ratio of 1.13, the existence of the Fe₃O₄ phase cannot be excluded. Furthermore, the TG/DTA analysis (Figure 5-35, left) reveals a mass loss of 4 % and 2 extrema in the DTA signal, at 230°C and 375°C, respectively as well as a continuous decrease above 500°C. The first peak can be attributed to evaporation of water, while the second peak can be ascribed to decomposition of hydroxides. The continuous decrease of the signal may be caused by phase changes. BET analysis (Figure 5-35, right) indicates a surface area of 32 m²/g and a total pore volume of 0.16 cm³/g. The TEM images in Figure 5-11 display the shape and size of the particles. Primary particles show a mean diameter of ca. 5 nm and form spherical agglomerates with a diameter of ca. 100 nm. The catalytic activity, derived from the TPO experiment (Figure 5-37), shows T_{CO₂,max} being 332°C and offers the best activity of all the iron oxides tested.

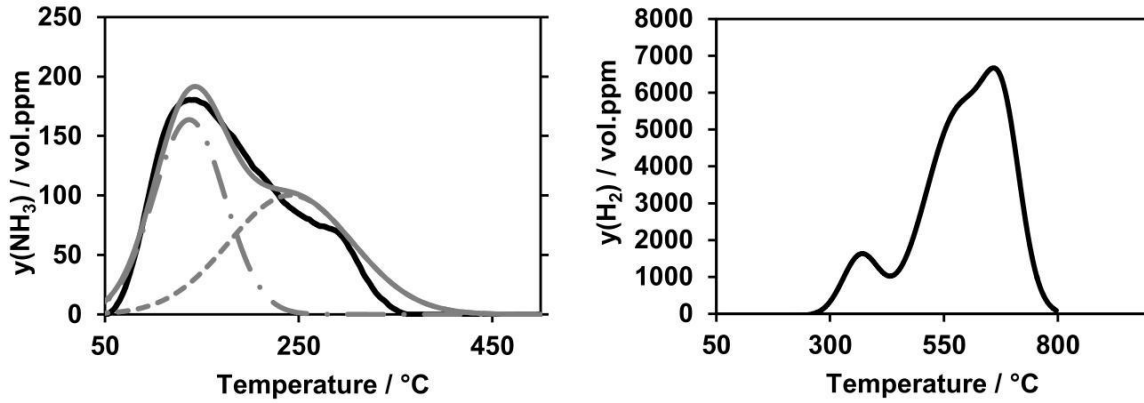


Figure 5-33: FSP Fe_2O_3 . Left Experimental data (—) and Gaussian fit (---) of the NH_3 -TPD spectrum. The dashed lines represent the deconvoluted spectrum, whereas (— · —) corresponds with the Brønsted bond NH_3 and (---) with the Lewis bond NH_3 . Conditions: $m_{\text{Fe}_2\text{O}_3}=0.78$ g, $F=500$ ml/min, $\beta=10\text{K/min}$. Right: HTPR spectrum. Conditions: $m_{\text{Fe}_2\text{O}_3}=0.06$ g, $F=200$ ml/min, $\beta=15$ K/min.

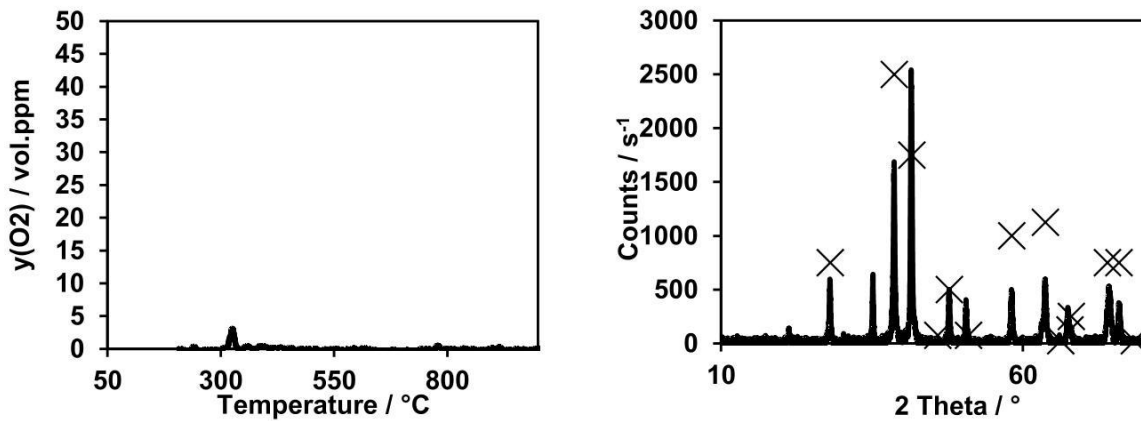


Figure 5-34: FSP Fe_2O_3 . Left: O_2 -TPD spectrum. Conditions: $m_{\text{Fe}_2\text{O}_3}=3.19$ g, $F=500$ ml/min, $\beta=10$ K/min. Right: PXRD pattern. (X) corresponds to ideal hematite phase.

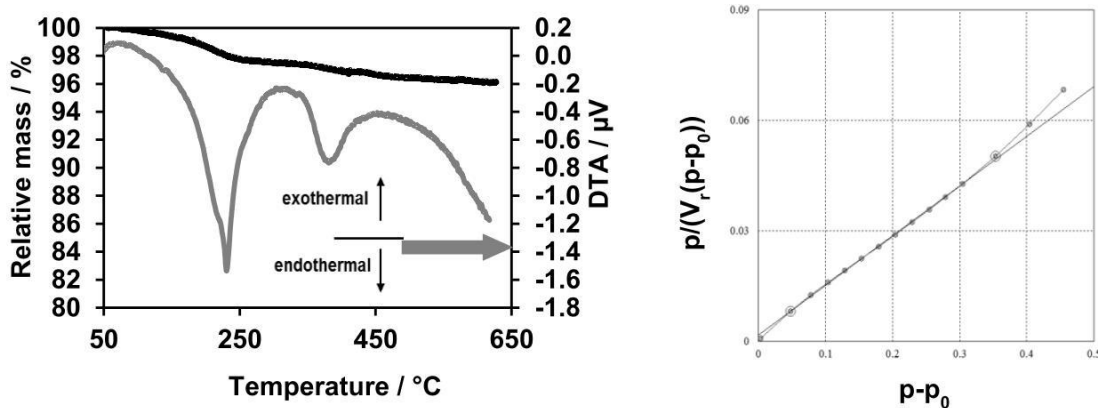


Figure 5-35: FSP Fe_2O_3 . Left: TG/DTA analysis. Conditions: $m_{\text{Fe}_2\text{O}_3}=0.025\text{g}$, $F=500\text{ml/min}$, $\beta=3.3\text{K/min}$. Right: BET plot of N_2 physisorption.

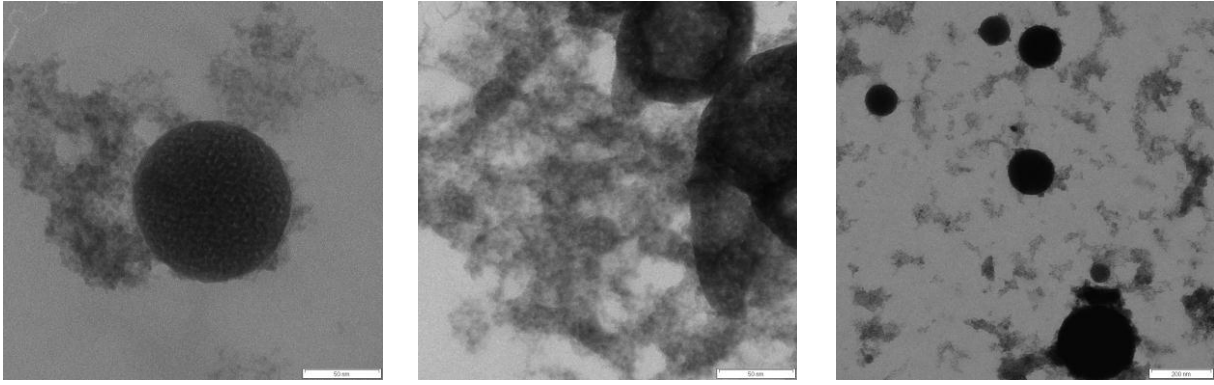


Figure 5-36: TEM images of the FSP Fe_2O_3 .

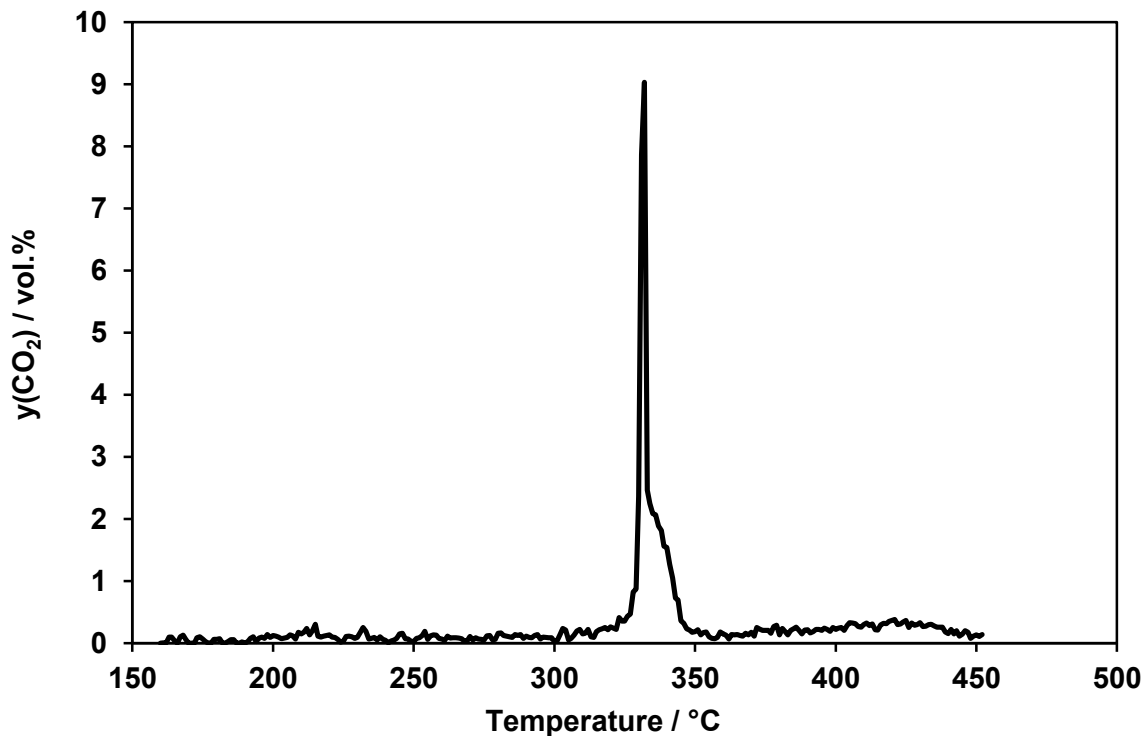


Figure 5-37: TPO pattern of FSP Fe_2O_3 ex ethanol precursor. Conditions: 10 mmol catalyst and 5 mmol soot in tight contact mode, $F=500$ ml/min, 10 vol.% O_2 in N_2 , $\beta=3.3$ K/min.

5.3 Kinetic modelling of the NH_3 adsorption and desorption

Based on the data derived from the NH_3 -TPD studies shown in the previous chapter, a kinetic model is introduced, which enables the determination of the relevant kinetic parameters of NH_3 adsorption and desorption. The parameters enfold surface coverage dependent activation energies and pre-exponential factors for adsorption and desorption. Furthermore, the adsorption and desorption of the molecular Lewis bond (NH_3) and Brønsted bond (NH_4^+) species are considered separately, which results in two sets of parameters. These kinetic parameters quantify the interaction between NH_3 and the respective iron oxide modifications and should contribute to the understanding of the catalytic performance by revealing further important

morphologic features required for an advanced catalyst. Finally, the determined parameters are validated by TPD experiments with different experimental conditions.

5.3.1 Fundamentals of the adsorption and desorption of NH₃

Due to the distinction between Lewis and Brønsted adsorption sites, two reaction steps are considered. Adsorption and desorption on Brønsted acid sites imply the interaction with surface hydroxide [24,105], where H⁺ stands for the acid OH groups:



For the adsorption and desorption on Lewis acid sites, assumed to be Fe³⁺ cations present on the catalyst surface, an interaction of the free electron pair of NH₃ is considered [105]:



The reaction rates of these elementary steps are described by Arrhenius-based rate expressions, which are as follows:

$$r_1 = A_1 \cdot \exp\left(-\frac{E_1}{RT}\right) \cdot c(\text{NH}_3) \cdot \Theta_{\text{H}^+} \quad (5-3)$$

$$r_2 = A_2 \cdot \exp\left(-\frac{E_2 - \alpha_2 \Theta_{\text{NH}_4^+}}{RT}\right) \cdot \Theta_{\text{NH}_4^+} \quad (5-4)$$

$$r_3 = A_3 \cdot \exp\left(-\frac{E_3}{RT}\right) \cdot c(\text{NH}_3) \cdot \Theta_{\text{Fe}^{3+}} \quad (5-5)$$

$$r_4 = A_4 \cdot \exp\left(-\frac{E_4 - \alpha_4 \Theta_{\text{NH}_3}}{RT}\right) \cdot \Theta_{\text{NH}_3} \quad (5-6)$$

A_i is the pre-exponential factor, E_i is the activation energy and $c(i)$ is the gas phase concentration of the respective species. $\Theta_{\text{Fe}^{3+}}$ and Θ_{H^+} represent free sites for NH₃ adsorption. Θ_{NH_3} and $\Theta_{\text{NH}_4^+}$ represent the coverage by NH₃ and NH₄⁺. The mean field approximation in the kinetic model considers the different types of NH₃ and NH₄⁺ surface species to be equivalent and disregards the shoulders in the desorption spectra. This rather rough assumption is generally used as an effective standard method for designing catalytic converters and describing interactions of NH₃ and other probe molecules with metal and metal oxide surfaces [24,105].

For desorption of NH_3 , a linear decrease in activation energy with rising coverage is assumed due to repulsion of adsorbed species [106]. For this reason, the factors α_2 and α_4 are introduced. $E_i(0)$ is the activation energy at zero coverage. $\Theta_{\text{Fe}^{3+}}$ represents the free sites for NH_3 adsorption, while $\Theta_{\text{NH}_4^+}$ and Θ_{NH_3} represent the coverage by NH_4^+ and NH_3 and are defined as follows:

$$\Theta_i = \frac{N(i)}{\Gamma_i A_{\text{act}}} \quad (5-7)$$

$N(i)$: Remaining quantity of adsorbed amount of species i	[mol]
Γ_i	: Surface concentration of free site	[mol/m ²]
A_{act}	: Absolute active surface area (derived from BET)	[m ²]

The kinetic modelling of the TPD profile is based on the mass balance of gaseous and adsorbed NH_3 species, described in Eqs (5-8)-(5-10).

$$F \cdot c(\text{NH}_3)_{,\text{out}} = F \cdot c(\text{NH}_3)_{,\text{in}} - A_{\text{act}}r_1 + A_{\text{act}}r_2 - A_{\text{act}}r_3 + A_{\text{act}}r_4 \quad (5-8)$$

$$A_{\text{act}}\Gamma_{\text{NH}_4^+}\beta \frac{d\Theta_{\text{NH}_4^+}}{dT} = A_{\text{act}}r_1 - A_{\text{act}}r_2 \quad (5-9)$$

$$A_{\text{act}}\Gamma_{\text{NH}_4^+}\beta \frac{d\Theta_{\text{NH}_3}}{dT} = A_{\text{act}}r_3 - A_{\text{act}}r_4 \quad (5-10)$$

In accordance with Hinrichsen et al. [24,107], the employed tube reactor is described by the model of a CSTR, i.e. the differential term of the former is neglected by assuming stationary conditions. This approach is reported to be a fair approximation in the numerical modelling of TPD patterns and is widely accepted [67]. The mass balances result in a system of one algebraic and two non-linear-differential equations. The surface coverage is calculated using Matlab tool ode15s, while free parameters are estimated with lsqcurvefit. The reliability of the estimated parameters is assessed with the 95 % confidence interval calculated by the Matlab function nlparci.

To reduce the number of free parameters within the fitting procedure, the pre-exponential factors of adsorption are calculated using Eq. (5-11), which is derived from the kinetic gas theory.

$$A_i = \frac{N_A RT}{(2\pi^2 i RT)^{1/2}} a_m \Gamma_i S^0 \quad (5-11)$$

N_A	: Avogadro number	[/]
-------	-------------------	-----

a_m	: Place requirement	[m]
S_0	: Sticking coefficient	[/]

Due to the lack of sticking coefficients on iron oxides in literature, the sticking coefficient of NH_3 on (110) surface of iron ($S^0=0.10$) is used for the calculation of the pre-exponential factor A_i of NH_3 on Lewis as well as on Brønsted sites for all Fe_2O_3 samples. This is in fair agreement with literature [105]. The required space a_m of one NH_3 molecule is calculated to be $2 \cdot 10^{-20} \text{ m}^2$, based on the cross section area of an ammonia molecule with a diameter of 1.6 \AA . The surface concentration of $\Gamma_{\text{NH}_4^+}$ and Γ_{NH_3} is calculated on the basis of the desorbed amount of Lewis and Brønsted bond NH_3 , derived from the deconvoluted TPD spectrum:

$$\Gamma_i = \frac{N_{\text{complete}}(i)}{A_{\text{act}}} \quad (5-12)$$

with

$$N_{\text{complete}}(i) = \left(\frac{1}{V_m} F \frac{1}{\beta} \int y(\text{NH}_3) dt \right) \quad (5-13)$$

V_m	: Molar volume at STP	[m ³ /mol]
F	: Volume flow	[m ³ /s]
β	: Heating rate	[K/s]
$y(\text{NH}_3)$: Volume fraction	[/]

The model assumes complete surface coverage ($\Theta_0=1$) at the beginning of every TPD. Furthermore, the activation energy for adsorption is neglected ($E_2=E_4=0$), which agrees with the findings for related solid-gas systems, particularly for NH_3 [105]. The results of the respective Fe_2O_3 materials are demonstrated in the following section.

5.3.2 Results of the kinetic modelling

The results of the calculations are presented in Figure 5-38 to Figure 5-44 showing that the TPD curves are satisfactorily reproduced by the kinetic model and the parameters implemented. The figures on the left show the calculated and experimental NH_3 -TPD spectra, related to an exposure temperature of 50°C . For model validation, experiments with a saturation temperature of 150°C were performed. The results are shown in the figures on the right, revealing good agreement between calculation and experiment. The kinetic parameters determined for each Fe_2O_3 sample are listed in Table 5-3. As mentioned in section 5.2, the

intention of modelling NH_3 -TPD was to check possible correlations between the ammonia adsorption/desorption and the catalytic activity of the samples for use in soot oxidation. However, the analysis of the data derived from the modelling, reveal that the kinetic parameters obtained for the NH_3 adsorption/desorption on the Brønsted and Lewis sites are very similar for all samples investigated. Clear trends, which might be ascribed to the morphology or composition of the sample, are not observed. Differences in the NH_3 -TPD spectra such as intensity and proportion of the peaks, are fully ascribable to the different surface areas and specific proportion of Lewis to Brønsted acid sites, which are both implemented in the model. Interaction between ammonia and iron oxide occurs only in surface and sub-surface layers of the catalyst without any bulk contribution.

The activation energy of the Brønsted bond NH_3 species ranges from 100 kJ/mol to 112 kJ/mol, the pre-exponential factors for Brønsted bond desorption vary between $1 \cdot 10^{10}$ mol/s·m² and $9 \cdot 10^{10}$ mol/s·m² and the α_2 -factor lies between 3 and 22 kJ/mol. The kinetic parameters for Lewis bond NH_3 vary for E_4 between 120 kJ/mol and 133 kJ/mol, for A_4 between $9 \cdot 10^8$ mol/s·m² and $5.5 \cdot 10^{10}$ mol/s·m² and for α_4 between 3 and 22 kJ/mol. A comparison with other materials reveals that kinetic parameters of Fe/HBEA zeolites [105], used for selective catalytic reduction (SCR), are within the same range, whereas the pre-exponential factor A_2 ($A_2=5.5 \cdot 10^{11}$ mol/s·m²) and the activation energy E_4 ($E_4=140$ kJ/mol) are slightly higher than the parameters of the pure iron oxides. A higher pre-exponential factor could be attributed to the acidic zeolite support of the Fe/HBEA and the higher activation energy E_4 indicates a stronger bonding between Fe and NH_3 , which is beneficial for SCR at high temperatures.

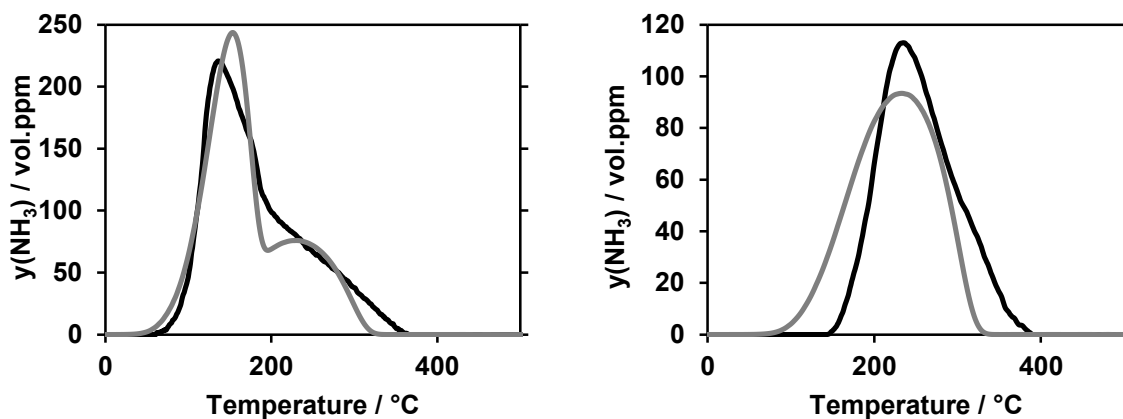


Figure 5-38: Bulk $\alpha\text{-Fe}_2\text{O}_3$. Experimental (—) and calculated (---) NH_3 -TPD pattern obtained for saturation at 50°C (left) and 150°C (right).

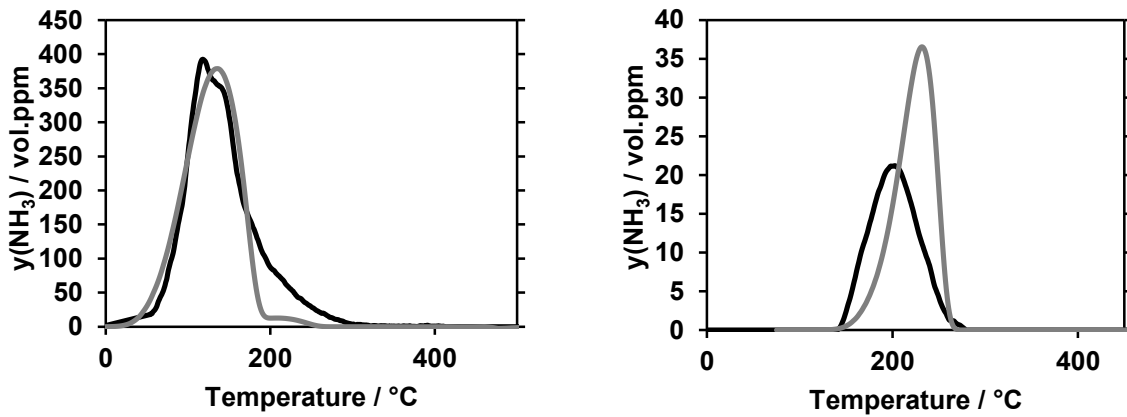


Figure 5-39: C10-20. Experimental (—) and calculated (---) NH₃-TPD pattern obtained for saturation at 50°C (left) and 150°C (right).

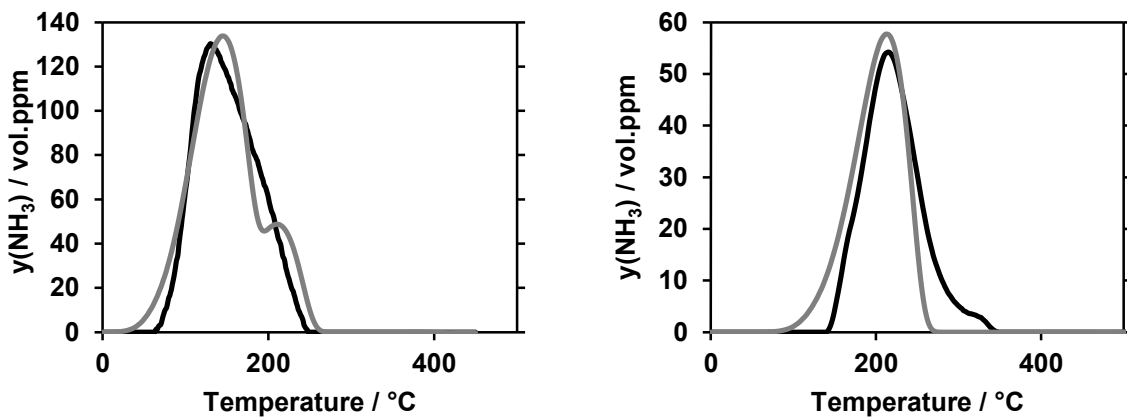


Figure 5-40: C7-10. Experimental (—) and calculated (---) NH₃-TPD pattern obtained for saturation at 50°C (left) and 150°C (right).

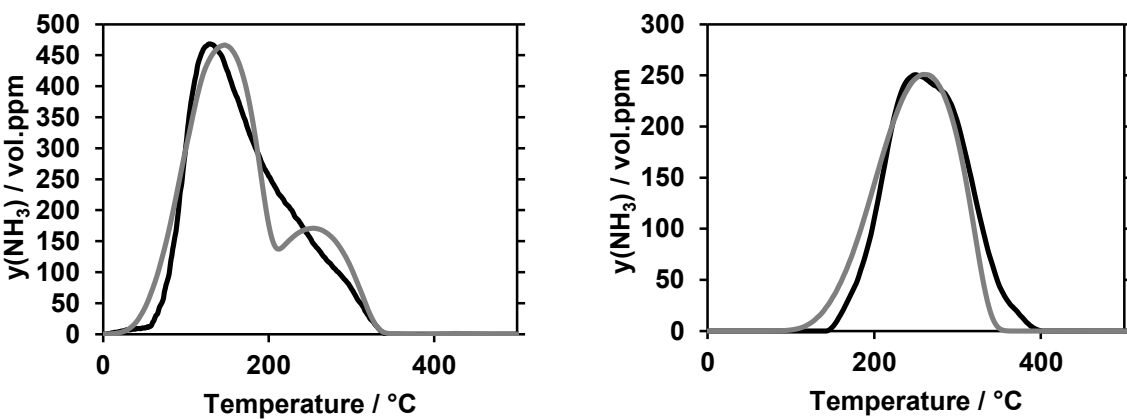


Figure 5-41: Bayoxide E 1.1. Experimental (—) and calculated (---) NH₃-TPD pattern obtained for saturation at 50°C (left) and 150°C (right).

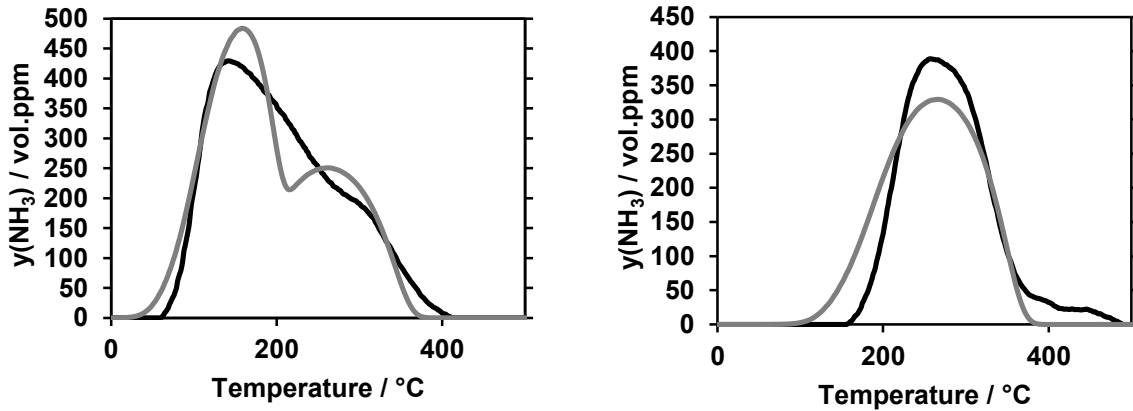


Figure 5-42: Bayoxide E 2.1. Experimental (—) and calculated (---) NH₃-TPD pattern obtained for saturation at 50°C (left) and 150°C (right).

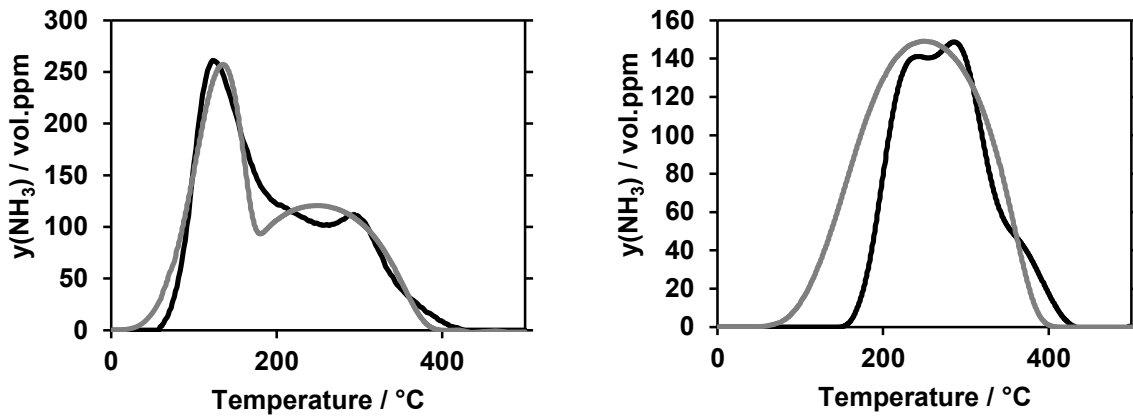


Figure 5-43: Bulk γ -Fe₂O₃. Experimental (—) and calculated (---) NH₃-TPD pattern obtained for saturation at 50°C (left) and 150°C (right).

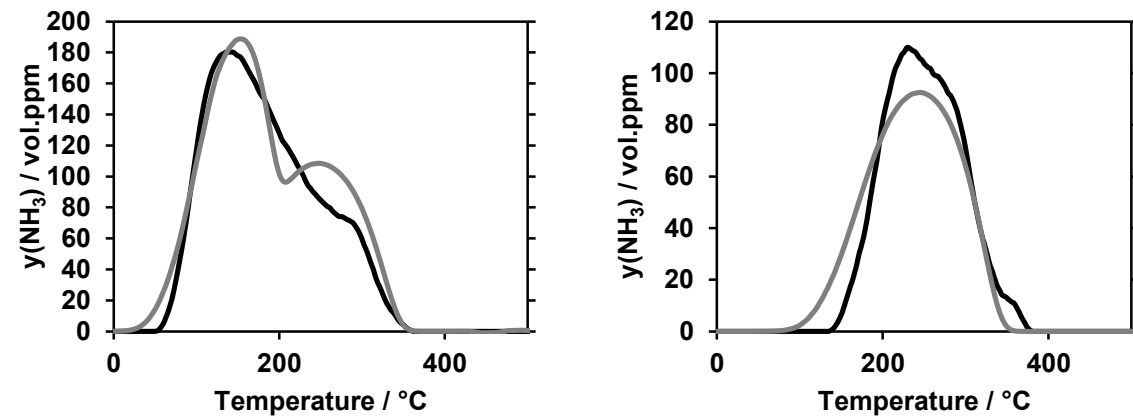


Figure 5-44: FSP Fe₂O₃. Experimental (—) and calculated (---) NH₃-TPD pattern obtained for saturation at 50°C (left) and 150°C (right).

Table 5-3: Kinetic parameters for ammonia desorption/adsorption on Fe₂O₃ modifications.

Fe ₂ O ₃ sample	Parameter	Value	Tolerance	Unit	Reference
FSP Fe ₂ O ₃ ex Ethanol	A ₁ , A ₃	0.30		m/s	Calculated
	E ₁ , E ₃	0		kJ/mol	
	A ₂	1.0·10 ¹⁰	4.3·10 ⁻²	mol/s·m ²	Fit
	E ₂	105	1.3·10 ⁻⁵	kJ/mol	Fit
	α ₂	10	1.1·10 ⁻⁶	kJ/mol	Fit
	A ₄	1.0·10 ⁹	3.8·10 ¹	mol/s·m ²	Fit
	E ₄	128	1.9·10 ⁻²	kJ/mol	Fit
	α ₄	18	1.9·10 ⁻²	kJ/mol	Fit
Chempur Fe ₂ O ₃ (10-20nm)	A ₁ , A ₃	0.3		m/s	Calculated
	E ₁ , E ₃	0		kJ/mol	
	A ₂	4.4·10 ¹⁰	2.8·10 ⁻²	mol/s·m ²	Fit
	E ₂	104	8.8·10 ⁻⁷	kJ/mol	Fit
	α ₂	7	1.1·10 ⁻⁷	kJ/mol	Fit
	A ₄	1.0·10 ⁹	9.2	mol/s·m ²	Fit
	E ₄	120	5.5·10 ⁻⁵	kJ/mol	Fit
	α ₄	5.2	4.6·10 ⁻⁶	kJ/mol	Fit
Chempur Fe ₂ O ₃ (7-10nm)	A ₁ , A ₃	0.3		m/s	Calculated
	E ₁ , E ₃	0		kJ/mol	
	A ₂	1.5·10 ¹⁰	5.7·10 ⁻²	mol/s·m ²	Fit
	E ₂	105	9.7·10 ⁻⁷	kJ/mol	Fit
	α ₂	5.7	3.2·10 ⁻⁸	kJ/mol	Fit
	A ₄	5.5·10 ¹⁰	1.71	mol/s·m ²	Fit
	E ₄	121	1.4·10 ⁻⁵	kJ/mol	Fit
	α ₄	3	4.1·10 ⁻⁷	kJ/mol	Fit
Lanxess Bayoxide E 1.1	A ₁ , A ₃	0.3		m/s	Calculated
	E ₁ , E ₃	0		kJ/mol	
	A ₂	3.0·e ¹⁰	0.15	mol/s·m ²	Fit
	E ₂	106	1.5·10 ⁻⁶	kJ/mol	Fit
	α ₂	10.9	5.8·10 ⁻⁷	kJ/mol	Fit
	A ₄	4.0·10 ⁹	9.1	mol/s·m ²	Fit
	E ₄	130	1.6·10 ⁻⁴	kJ/mol	Fit
	α ₄	12	3.5·10 ⁻⁶	kJ/mol	Fit

Fe_2O_3 sample	Parameter	Value	Tolerance	Unit	Reference
Lanxess Bayoxide E 2.1	A_1, A_3	0.30		m/s	Calculated
	E_1, E_3	0		kJ/mol	
	A_2	$8.0 \cdot 10^{10}$	$1.23 \cdot 10^{-1}$	mol/s·m ²	Fit
	E_2	112	$3.1 \cdot 10^{-6}$	kJ/mol	Fit
	α_2	14	$3.1 \cdot 10^{-7}$	kJ/mol	Fit
	A_4	$3.0 \cdot 10^9$	7.9	mol/s·m ²	Fit
	E_4	133	$5.7 \cdot 10^{-4}$	kJ/mol	Fit
	α_4	19	$2.6 \cdot 10^{-4}$	kJ/mol	Fit
$\alpha\text{-Fe}_2\text{O}_3$	A_1, A_3	0.3		m/s	Calculated
	E_1, E_3	0		kJ/mol	
	A_2	$9.0 \cdot 10^{10}$	$4.2 \cdot 10^{-2}$	mol/s·m ²	Fit
	E_2	110	$1.8 \cdot 10^{-7}$	kJ/mol	Fit
	α_2	2	$1 \cdot 10^{-8}$	kJ/mol	Fit
	A_4	$9.0 \cdot 10^8$	$1.0 \cdot 10^1$	mol/s·m ²	Fit
	E_4	123	$2.1 \cdot 10^{-4}$	kJ/mol	Fit
	α_4	15	$4.9 \cdot 10^{-5}$	kJ/mol	Fit
$\gamma\text{-Fe}_2\text{O}_3$	A_1, A_3	0.3		m/s	Calculated
	E_1, E_3	0		kJ/mol	
	A_2	$5.0 \cdot 10^{10}$	$8.0 \cdot 10^{-2}$	mol/s·m ²	Fit
	E_2	100	$1.6 \cdot 10^{-5}$	kJ/mol	Fit
	α_2	4	$3.8 \cdot 10^{-8}$	kJ/mol	Fit
	A_4	$1.0 \cdot 10^8$	$2.1 \cdot 10^1$	mol/s·m ²	Fit
	E_4	116	$2.0 \cdot 10^{-4}$	kJ/mol	Fit
	α_4	22	$6.5 \cdot 10^{-5}$	kJ/mol	Fit

5.4 Coupling of physical-chemical properties and the catalytic performance of different Fe₂O₃ materials

This section discusses the trends, connections and correlations between catalytic activity and physical-chemical properties of the different iron oxide catalysts. The data obtained from the characterisation studies are summarised in Table 5-4. The results show a correlation between Lewis acid sites and catalytic performance for soot oxidation, e.g. the FSP Fe₂O₃ sample reveals highest specific number of Lewis acid sites ($n(\text{NH}_3)_{\text{Lewis}} = 1.40 \cdot 10^{-6} \text{ mol/m}^2$) and best catalytic activity ($T_{\text{CO}_2, \text{max}} = 332^\circ\text{C}$). In contrast, the number of Brønsted sites seems to have no influence. Table 5-4 demonstrates connection between crystallinity and activity. While both high and low crystalline proportion offer poor activity, a mean crystallinity exhibits high catalytic performance. This is supported by the α -Fe₂O₃, which features $T_{\text{CO}_2, \text{max}}$ at 408°C and a crystallinity of 100 % as well as by the Bayoxide E 2.1, which has the lowest crystallinity and poorest catalytic activity shown by $T_{\text{CO}_2, \text{max}}$ at 414°C . In contrast, the FSP Fe₂O₃ exhibits a crystalline proportion of 50 % and has the best activity, i.e. $T_{\text{CO}_2, \text{max}} = 332^\circ\text{C}$. To illustrate these correlations, Figure 5-45 depicts the dependency of $T_{\text{CO}_2, \text{max}}$ on the number of Lewis acid sites, as well as on crystalline proportion. Hence, a balance of both features seems to have good effect on the catalytic activity.

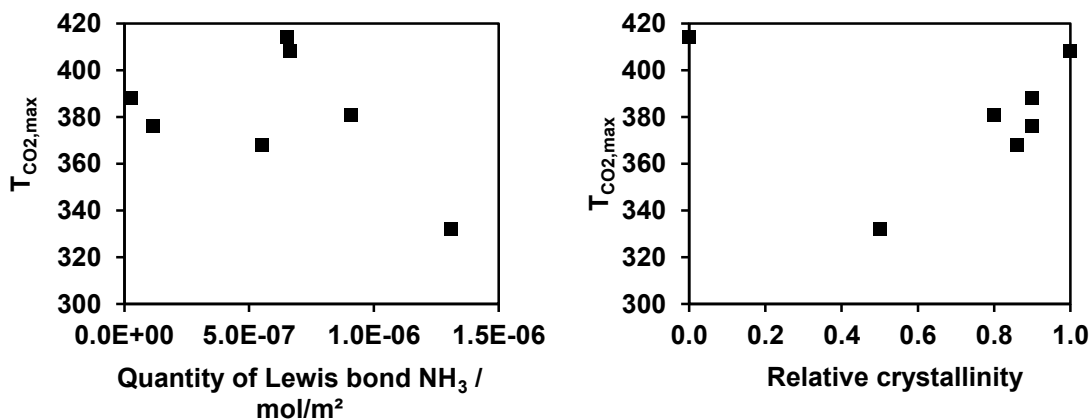


Figure 5-45: $T_{\text{CO}_2, \text{max}}$ in dependency on amount of Lewis acid sites (left) and crystallinity (right).

No conclusions can be obtained from the N₂-physisorption studies, neither from the active surface area, nor from the total pore volume. Both high and low values do not affect the catalytic performance. Also, the particle size, deduced from TEM, exhibits no correlation between particle size and activity. Referring to particle diameter and BET, the most active sample, i.e. FSP Fe₂O₃, shows moderate values in comparison

to the other materials. Furthermore, no conclusions can be drawn from the HTPR studies. Neither the location of the low-temperature peak nor the derived ratios, i.e. high- to low-temperature peak and consumed H_2 to used Fe, can be correlated with the catalytic activity.

The relationship between Lewis acid sites, crystalline proportion and catalytic activity is illustrated in Figure 5-46. The contour plot clarifies the trend of this correlation. The best catalytic activity is provided for moderate crystallinity (ca. 50 %) and a large number of specific Lewis acid sites (illustrated by blue areas), whereas a moderate quantity of specific Lewis bond NH_3 and high (ca. 100 %) or low (ca. 0 %) crystallinity reveals poor activity, indicated by red areas.

From a mechanistic point of view, these findings strongly support the findings presented in chapter 3.4. The importance of Lewis acid sites can be ascribed to their capability to act as contact points in catalytic soot oxidation by transferring atomic oxygen from the catalyst surface to the soot, subsequently resulting in surface oxygen defect sites [23]. In this respect, the kinetic modelling of the NH_3 -TPD also revealed the same activity for the Lewis acid sites for all iron oxides, which was indicated by related kinetic parameters for adsorption and desorption on Lewis acid sites. This excludes any influence from the bulk of the iron oxides on the catalytically active surface. Nevertheless, the mechanistic studies with $^{18}O_2$ (chapter 3.2.5) showed that these surface defect sites are refilled from both, bulk and migrating surface oxygen atoms. Crystalline domains of the catalyst provide bulk oxygen transport, whereas amorphous domains advance migration of surface oxygen atoms by promoting oxygen uptake from the gas phase. The derived correlation between Lewis sites and crystallinity clearly coincides with the mechanistic studies and accounts for the high activity of the FSP Fe_2O_3 .

In summary, the studies presented reveal features of iron oxide catalysts which improve their catalytic activity. However, focus should additionally be given to the stability of the materials, which is a problematic issue. The TG/DTA studies exhibited a high mass loss for samples with low crystallinity. Therefore, the development of future materials requires special consideration in respect to thermal stability. A possible strategy to fulfil these requirements would be the implementation of dopants (e.g. Ce, Zr, Pr) which act as stabilisers for the crystalline structure and also act as sinter barriers.

Finally, two explanatory notes should be given concerning the correlations above. First, the given interpretations rather suggest trends in the behaviour of different iron oxides. For complete interpretation, the number of samples is not sufficient. Second, phase and mass changes in the TG/DSC signal, which occur below the ignition temperature of the TPO, may cause a deviation of the correlation between properties and activity.

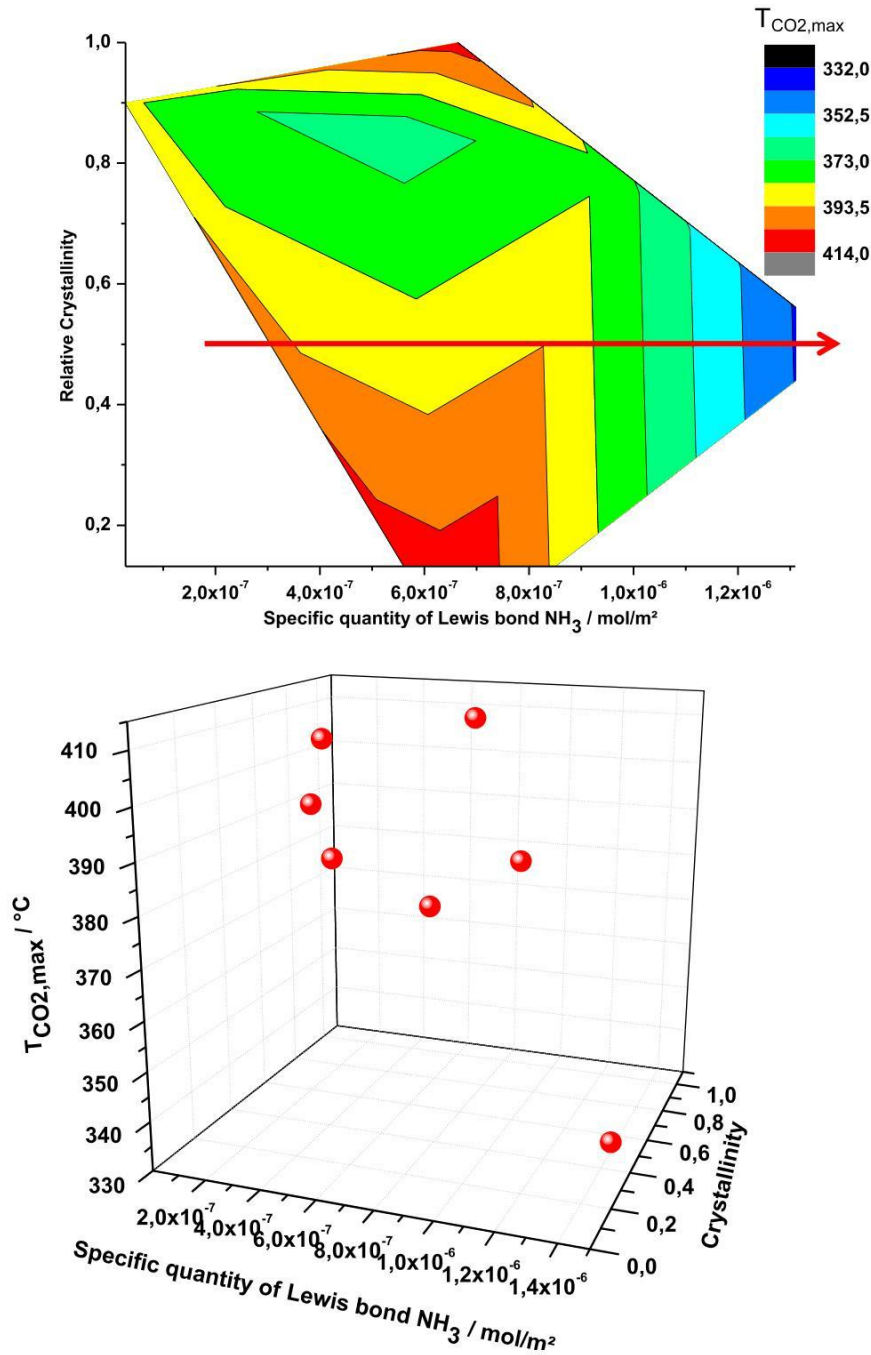


Figure 5-46: Contour plot (top) and graphical display (below) of the correlation between T_{CO₂,max}, quantity of specific Lewis bond NH₃ and crystallinity.

Table 5-4: Physical-chemical properties of the Fe₂O₃ samples.

Analysis	α -Fe ₂ O ₃	C 10-20	C 7-10	Bayoxide E 1.1	Bayoxide E 2.1	γ -Fe ₂ O ₃	FSP Fe ₂ O ₃
TPO [°C]	408	388	376	368	414	381	332
Crystallinity [%]	100	90	90	86	0	80	50
S _{BET} [m ² /g]	12	74	90	127	230	62	32
V _{pore} [cm ³ /g]	0.15	0.26	0.28	0.54	0.41	0.41	0.16
n(NH _{3,complete}) [mol/m ²]	1.6·10 ⁻⁶	8.7·10 ⁻⁷	4.1·10 ⁻⁷	1.7·10 ⁻⁶	1.3·10 ⁻⁶	1.6·10 ⁻⁶	2.7·10 ⁻⁶
n(NH _{3,Bronsted}) [mol/m ²]	0.9·10 ⁻⁶	8.4·10 ⁻⁷	3.0·10 ⁻⁶	1.2·10 ⁻⁶	6.7·10 ⁻⁷	0.7·10 ⁻⁶	1.3·10 ⁻⁶
n(NH _{3,Lewis}) mol/m ²	0.7·10 ⁻⁶	0.3·10 ⁻⁷	1.2·10 ⁻⁷	0.6·10 ⁻⁶	6.4·10 ⁻⁷	0.9·10 ⁻⁶	1.4·10 ⁻⁶
d _{particle} [nm]	80-200	10-20	7-10	5x50 (specula)	1-5	10-100	5 (primary)-100 (agglomerates)

6 Coating and testing of laboratory diesel particulate filters

The final chapter addresses the testing and coating of diesel particulate filters (DPF) on laboratory scale (300 cpsi, 1"x2"). The strategy of the coating procedure is to transfer the encouraging results of the FSP powder material to a more realistic filter scale. Furthermore, coating and synthesis are combined to one process step thus reducing workflow and assuring reproducibility.

The experimental work within this chapter covers the production of Fe_2O_3 filters with different loadings. Subsequently, these DPF (CDPF) are evaluated. In addition, the axial coating thickness and the backpressure of three Fe_2O_3 -coated DPFs are examined.

6.1 Modification of the flame-spray pyrolysis bench

For direct coating of the mini filters within the flame-spray synthesis, a new filter device was constructed. The general set-up of the modified bench is shown in Figure 6-1. Apart from the different filter device used, the bench remains the same as presented in Figure 5-1. The original candle filter is changed using a special tool to adjust the mini DPF. This novel filter device has a different backpressure compared to the standard candle filter. A stable operating point required new experimental parameters. These are as follows:

- Difference pressure of oxygen (atomisation gas): 1 bar.
- Throughput of oxygen: 1 Nm^3/h .
- Throughput of liquid: ca. 5-10 ml/min.
- Throughput of synthetic air (bustle pipes): 2.5 Nm^3/h .
- Angle of the spray cone: 40°.
- Concentration of precursor solution: 0.5 M.
- Volume ratio $\text{Fe}/\text{Mn}(\text{NO}_3)_3$ solution/propanol: 1:4.

An advantage of this coating strategy is the simple adjustment of catalyst loadings, achieved by variation of the deposition time. Furthermore, the deposition of the catalytic particles on the filter is beneficial due the transport of these particles by gas flow. They are positioned in the same locations on the filter, where the soot is deposited as well. The coated DPF were thermally pre-treated (30 min at 500°C under atmosphere) to remove adsorbed NO_x from the synthesis procedure.

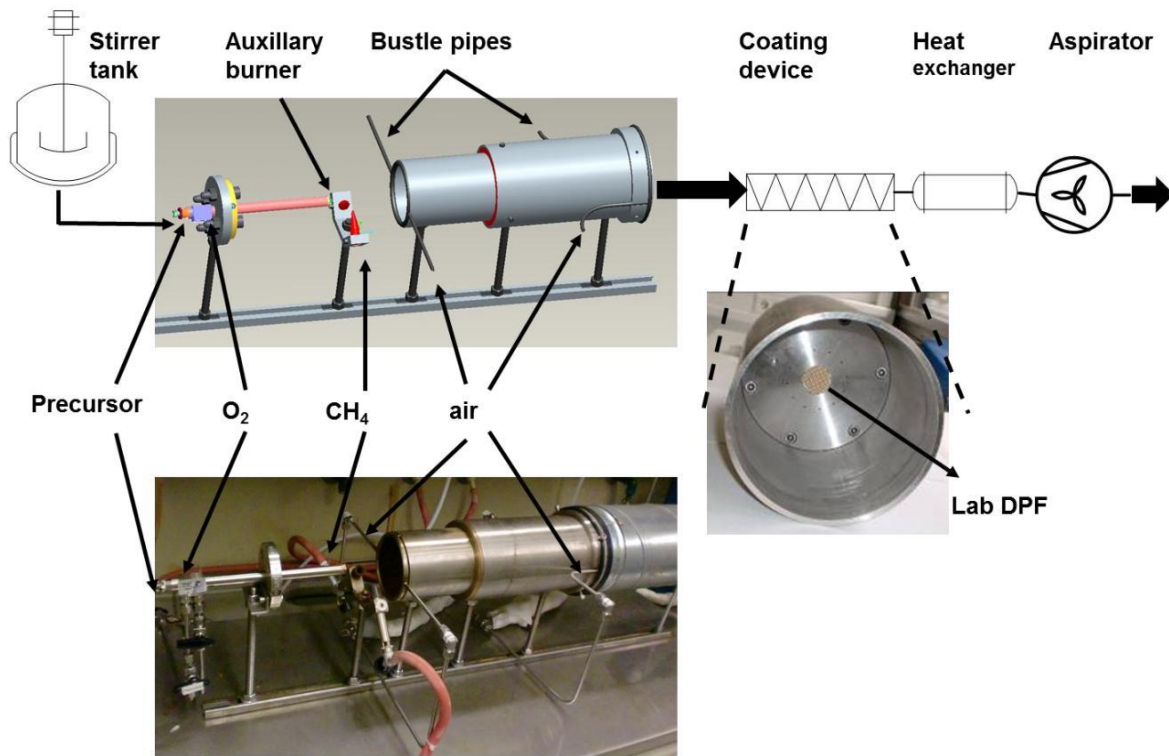


Figure 6-1: Flow-chart of the flame-spray with setup for coating of lab DPFs. CAD drawing (top) and picture (bottom).

6.2 TPO studies of the coated laboratory filters

Three DPF were coated on the modified FSP bench (Figure 6-1), giving 28 g/l, 50 g/l and 93 g/l Fe_2O_3 loading. For the realisation of activity measurements, the filters had to be loaded with soot, which was established on a special device (Figure 6-2) in a C_3H_6 diffusion burner [49,50]. The time for soot deposition was ca. 10 min resulting in soot loadings between 0.5 g and 1.0 g, strongly depending on the backpressure of the DPF's used.

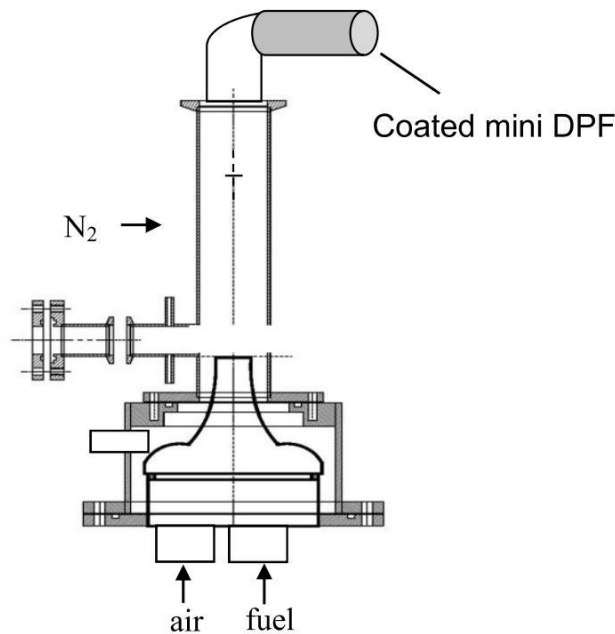


Figure 6-2: Scheme of the soot deposition on the coated filter in diffusion C₃H₆ burner [68].

The catalytic performance of the samples was tested in TPO experiments with a total gas flow of 6500 ml/min with 10 vol.% O₂, 2 vol.% H₂O and N₂ balance resulting in a space velocity of 15600 h⁻¹ (STP). The filters were fixed in a special quartz glass reactor (i.d. 1") and the temperature was linearly increased at 3.3 K/min.

6.2.1 DPF coated by Fe₂O₃

Figure 6-3 illustrates the CO₂ traces of a mini filter with a Fe₂O₃ loading of 28 g/l using a TPO run in comparison to a bare DPF. The Fe₂O₃ coated filter shows no low-temperature maximum, whereas a high-temperature signal of the Fe₂O₃ sample shows the same progression as referred to the bare DPF. This indicates that there is no catalytic benefit. Nevertheless, CO formation was not detected during the experiment, suggesting that CO oxidation occurs on the Fe₂O₃ components of the filter. The TPO results at a load of 50 g/l Fe₂O₃ (Figure 6-4) give a small CO₂ peak at 273°C, indicating certain catalytic activity within this temperature range. The major part of soot oxidation occurs above 500°C and is very similar to the non-catalytic reaction. Again, CO could not be detected. Finally, similar effects are observed for a loading of 93 g Fe₂O₃/l. But, in comparison to the sample with 50 g/L the area ratio of the low-temperature peak and high-temperature peak is higher. However, due to high backpressure the sample offers only 0.47 g/l soot loading (compared to 0.67 g/l). More detailed examinations concerning backpressure and activity are presented in section 6.3.

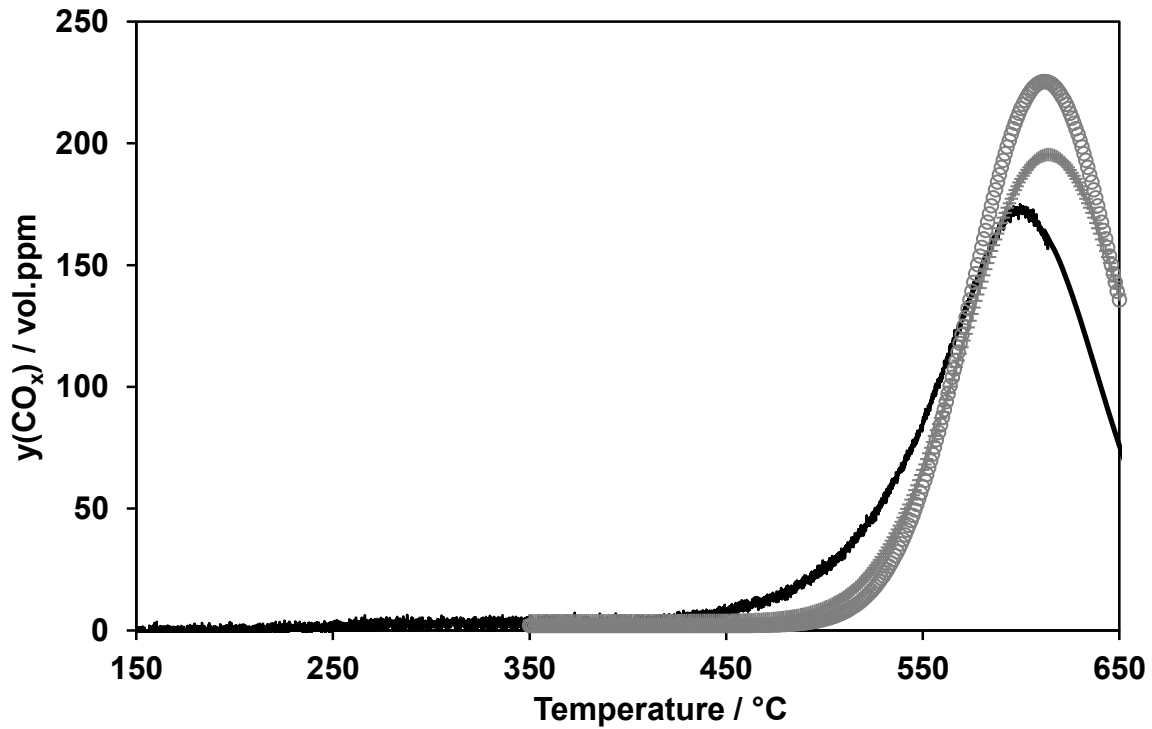


Figure 6-3: TPO profile (—) of coated lab DPF with 28 g/l Fe_2O_3 loading and an initial soot loading of 0.67 g/l. (○) and (+) correspond with the CO_2 and CO signal of a bare DPF with initial soot loading of 1.72 g/l. Conditions: 6500 mL/min N_2 with 10 vol.% O_2 and 2 vol.% H_2O , $\beta=3.3$ K/min, S.V.=15'600 h^{-1} (STP).

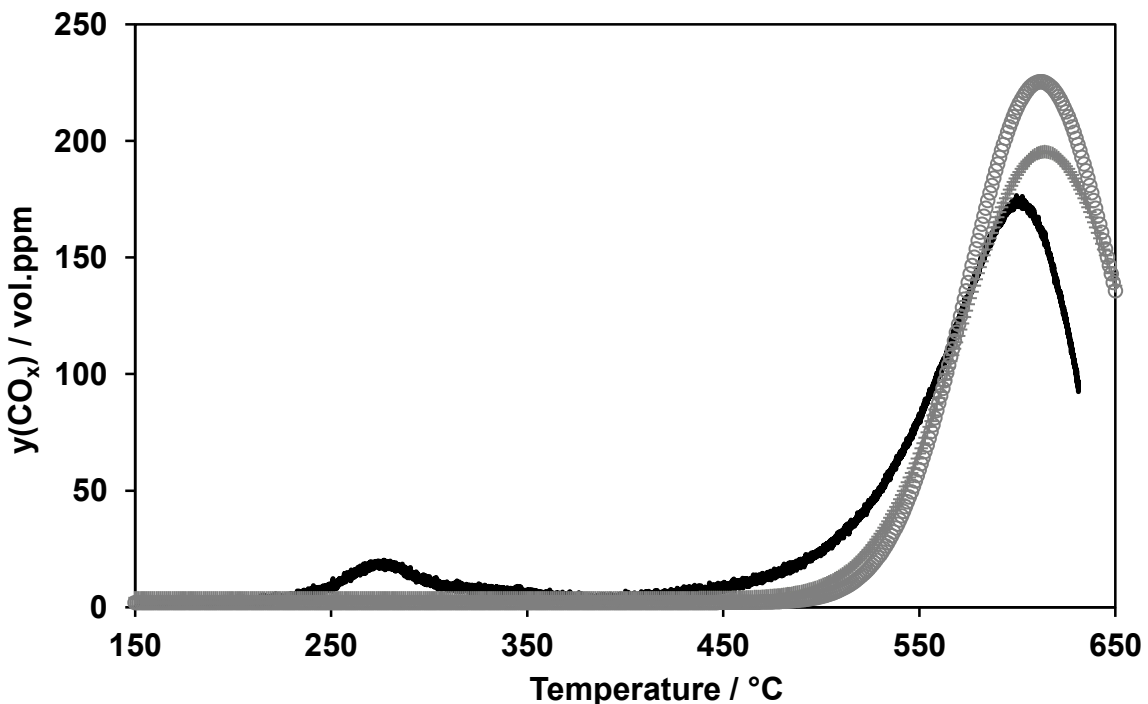


Figure 6-4: TPO profile (—) of coated lab DPF with 50 g/l Fe_2O_3 loading and an initial soot loading of 0.67 g/l. (○) and (+) correspond with the CO_2 and CO signal of a bare DPF with initial soot loading of 1.72 g/l. Conditions: 6500 mL/min N_2 with 10 vol.% O_2 and 2 vol.% H_2O , $\beta=3.3$ K/min, S.V.=15'600 h^{-1} (STP).

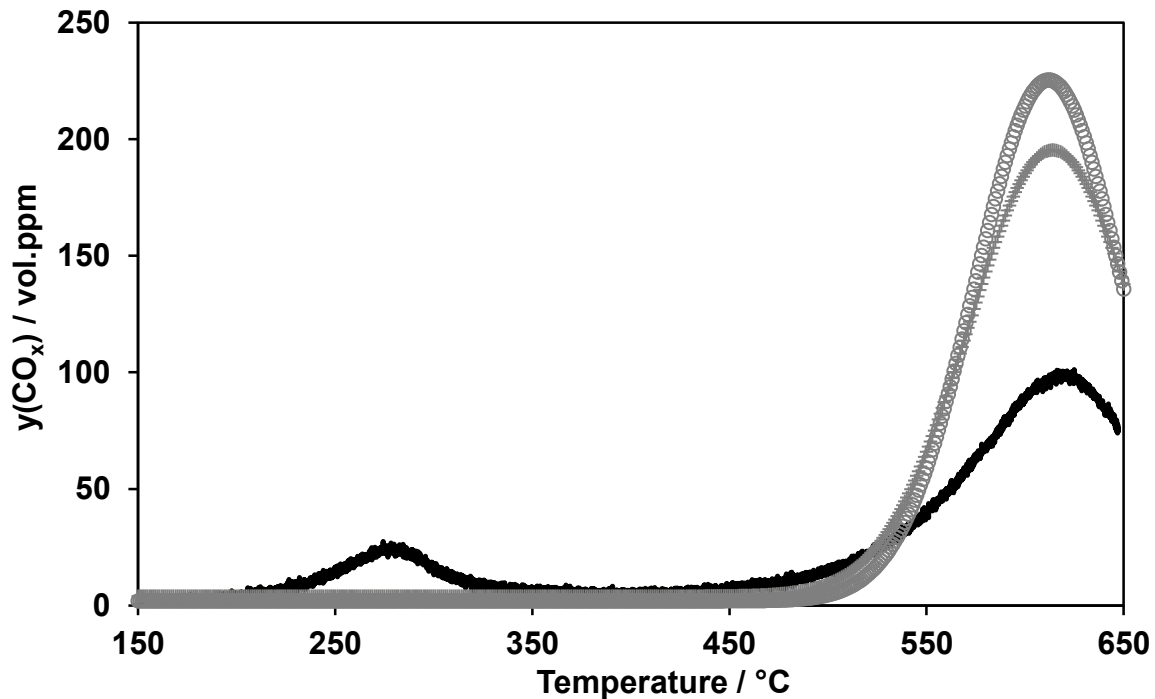


Figure 6-5: TPO profile (—) of coated lab DPF with 93 g/l Fe_2O_3 loading and an initial soot loading of 0.47 g/l. (○) and (+) correspond with the CO_2 and CO signal of a bare DPF with initial soot loading of 1.72 g/l. Conditions: 6500 mL/min N_2 with 10 vol.% O_2 and 2 vol.% H_2O , $\beta=3.3$ K/min, S.V.=15'600 h^{-1} (STP).

6.3 Characterisation of the coated laboratory filters

In order to draw assumptions about the coating quality and the effects of different loadings on the backpressure performance, studies were made to elucidate the impact of these items.

6.3.1 Backpressure vs. loading

The measurements for the elucidation of the backpressure performance were made with the Fe_2O_3 coated filters (28 g/l, 50 g/l and 93 g/l loading), while the pressure drop was measured at a flow of 80 l/min corresponding to a S.V. of 192000 h^{-1} (STP). Figure 6-6 presents the results dependent on the Fe_2O_3 loading. In addition, the catalytic activity of the respective samples is also correlated with the loading. To obtain comparable values for the activity, the area ratio between the integral amount of low-temperature and high-temperature peaks of the TPO patterns (Figure 6-3, Figure 6-4 and Figure 6-5) is calculated. Figure 6-6 reveals that increasing the Fe_2O_3 loading increases both the backpressure and the catalytic activity. However, a backpressure of 150 mbar is not acceptable, meaning that a loading of 50 g/l Fe_2O_3 offers both good catalytic performance and acceptable filter backpressure.

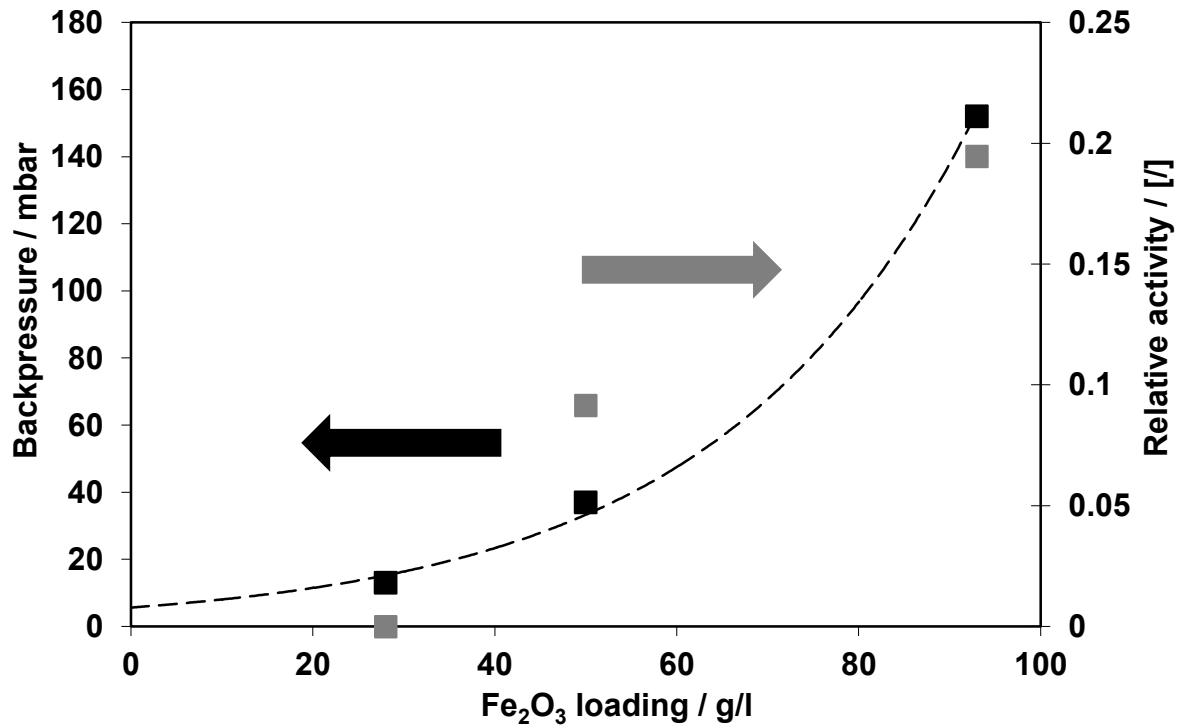


Figure 6-6: Activity and backpressure vs. Fe₂O₃ loading. (--) is a guide for the eyes. Relative activity is derived from the area ratio of low-temperature peak to high-temperature peak of the TPO profiles.

6.3.2 Axial coating thickness

The axial coating thickness of the above presented Fe₂O₃ coated filters was illustrated by light microscopic pictures of the cross section of 1 honeycomb. These pictures were taken in different axial sections of the DPF. The DPF was chipped with a special ceramic saw. The images were taken in top view with a light microscope from Hund-Wetzlar equipped with a Tucsen Techmon digital camera and x15-x45 magnification.

Figure 6-7 shows the images from three axial slices of the 28 g/l sample. We can see that the front and middle section of the filter exhibit a constant thickness at the walls of the honeycomb, whereas blurring can be ascribed to perspective problems caused by an inexact cutting edge. In contrast, the picture of the last section, which is located at the outlet of the filter, shows very little Fe₂O₃ deposits on the filter walls.

The mini filter with 50 g/l loading (Figure 6-8) reveals an increase of the Fe₂O₃ deposits from first slice to fourth slice (in flow direction), whereas the last slice shows again very small deposits on the wall.

Finally, Figure 6-9 displays the Fe₂O₃ deposits in the case of the 93 g/l Fe₂O₃ loading. It is obvious, that such a high loading results in a blocking of the channels by the iron oxide deposits, as is shown in the 3rd, 4th and 5th picture. Moreover, it should

be stated that this blocking of the honeycomb is also a result of the cutting procedure, which dispenses with the Fe_2O_3 deposits by every move of saw blade. In particular, this becomes apparent for the filter wall which is covered completely with Fe_2O_3 particles.

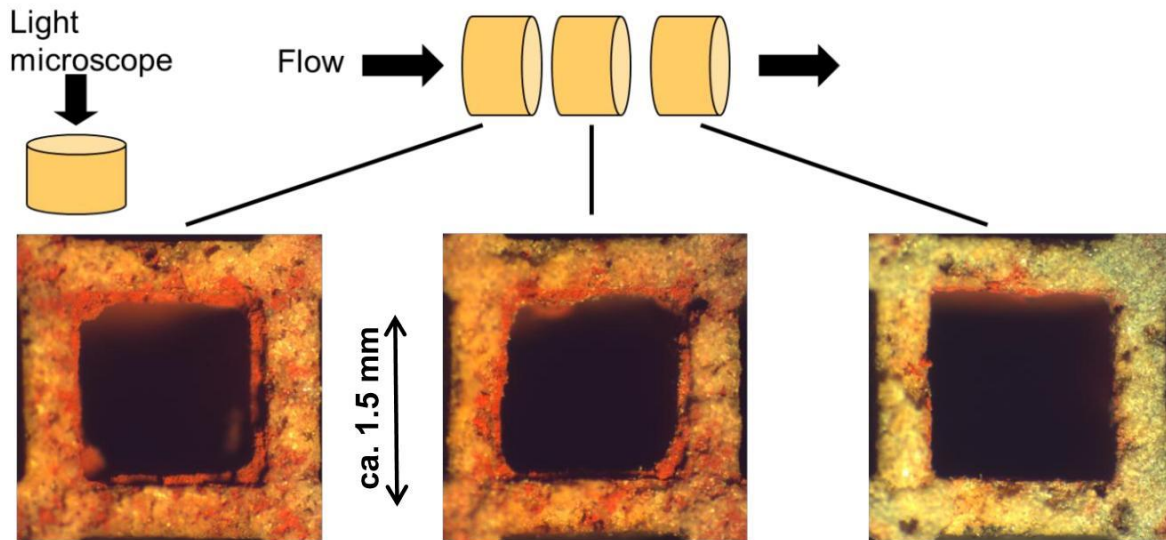


Figure 6-7: Light microscopic pictures of axial cross sections of the lab DPF with 28 g/l Fe_2O_3 coating. Each image section displays 1 honeycomb which is located in the mean of the filter.

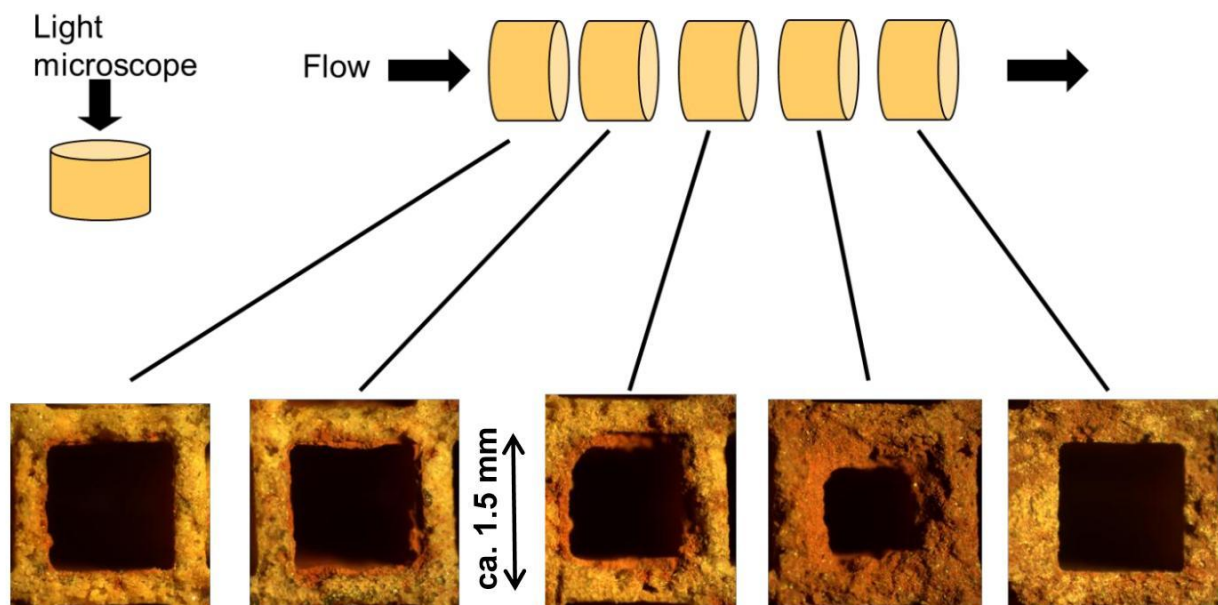


Figure 6-8: Light microscopic pictures of axial cross sections of the lab DPF with 50 g/l Fe_2O_3 coating. Each image section displays 1 honeycomb which is located in the mean of the filter.

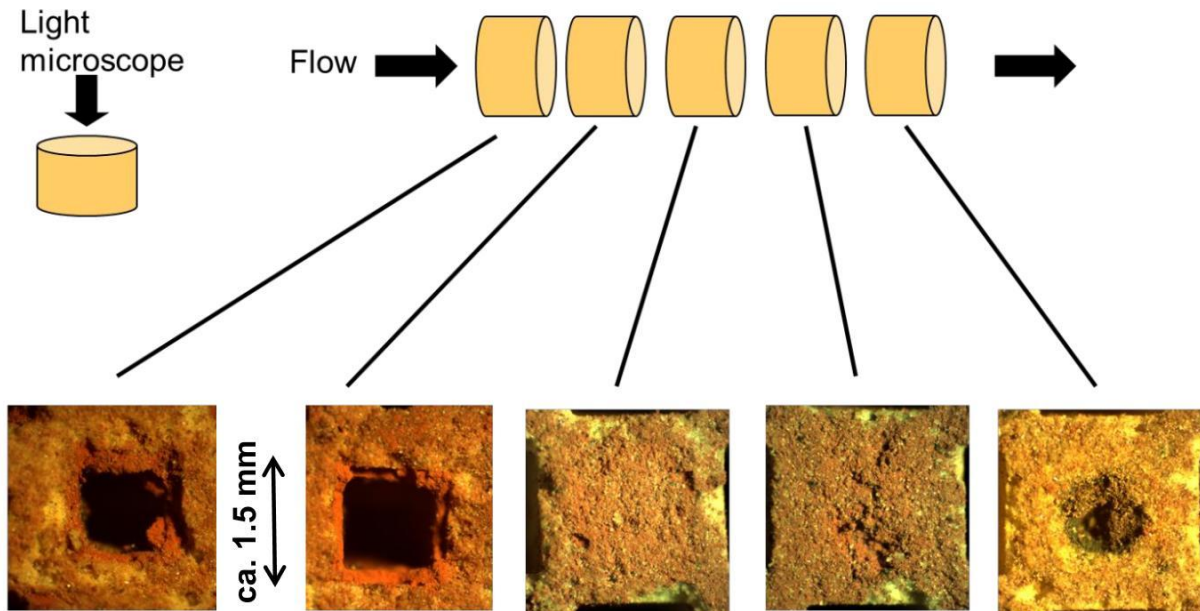


Figure 6-9: Light microscopic pictures of axial cross sections of the lab DPF with 93 g/l Fe_2O_3 coating. Each image section displays 1 honeycomb which is located in the mean of the filter.

6.4 Discussion

The experiments described in this chapter illuminate three crucial points in the coating of DPF, i.e. activity, backpressure and coating quality.

Figure 6-3 to Figure 6-5 show that a certain amount of Fe_2O_3 loading is necessary to see catalytic effects in soot oxidation. Even a high catalyst loading (93 g/l) suggest the majority of the deposited soot is oxidised by non-catalytic processes. The reasons for this can be attributed to contact loss between the catalytic coating and the soot [16,53]. Approaches to overcome this issue suggest the use of mobile catalysts with a low melting point [37]. These catalysts provide advanced contact by so-called wetting of the soot surface. Nevertheless, these materials contain alkaline and earth alkaline components resulting in elution due to the high water content in diesel exhaust. Another possibility to allow oxygen release in non-mobile catalysts, as shown for the case of CeO_2 materials [36]. In the case of Fe_2O_3 materials this might be attained by influencing the crystalline structure, e.g. by the implementation of dopants like Ce, Pr etc. (see also conclusions in chapter 7).

The issue of backpressure can be attributed to the total mass of the catalytic loading and to the density of the coating. For an improvement in the backpressure behaviour of the filter, a catalyst that offers catalytic soot oxidation at a low level of catalytic filter loading must be found.

Finally, the quality of the coating process may be enhanced by further investigations on the flame-spray bench. Alternative coating procedures, e.g. depositing the catalyst

by a binding agent, may be taken into account. This might also affect the backpressure of the filter.

7 Conclusions and outlook

This work demonstrates the knowledge-based development of a Fe_2O_3 based catalyst for the oxidation of soot. Fundamental examinations covering the elucidation of the reaction mechanism, kinetic and fluid-dynamic modelling as well as physical-chemical analyses have enabled us to determine the properties and parameters which are beneficial for soot oxidation using Fe_2O_3 catalysts. Based on these findings, an advanced catalyst has been synthesised showing high catalytic activity for soot oxidation. In addition, the production of this material by flame-spray synthesis has allowed the transfer from powder experiments to realistic DPF systems by catalytically coating filters at laboratory scale.

Further activities addressing the development of Fe_2O_3 based catalysts should focus on two issues: the thermal stability of the material and the improvement in catalyst/soot contact.

Regarding the thermal stability of the catalyst, thorough studies focussing on thermal and hydrothermal aging of the material would be required. The possible application in exhaust aftertreatment in diesel cars requires a resistance against high exhaust temperatures and uncontrolled soot burn-off which may occur under full load conditions [5]. Hence, the catalyst must sustain its morphology and therefore the active surface area, crystalline structure and surface acidity (i.e. number of Lewis sites). A possible strategy to fulfil these requirements would be the implementation of dopants (e.g. Ce, Zr, Pr) which act as stabilisers for the crystalline structure and also act as sinter barriers.

In order to improve the contact between catalyst and soot, two routes can be considered: (1) An optimisation of the flame-spray pyrolysis may increase the number of contact point between catalytic coating of the DPF and soot deposited. (2) A more easy oxygen release of the catalyst may overcome the problems shown by the experiments using loose contact catalyst/soot mixtures. Such an approach must aim to influence the crystalline structure e.g. by the generation of lattice defects and amorphous domains, again suggesting the implementation of dopants [108].

8 Literature

- [1] C. Bliefert, Umweltchemie, VCH Verlag, Weinheim, 1995.
- [2] Umweltbundesamt, Nationale Emissionsübersicht, 2008, www.uba.de.
- [3] J.P.A. Neeft, M. Makkee, J.A. Moulijn, Fuel Processing Technology 47 (1996) 1.
- [4] S. Kureti, Catalytic purification of automotive exhaust, Universität Karlsruhe (TH), 2008.
- [5] C. Brinkmeier, F. Opferkuch, U. Tuttlies, V. Schmeißer, J. Bernnat, G. Eigenberger, Chemie Ingenieur Technik 9 (2005) 1333.
- [6] E. Rotter, Entwicklung der internationalen Automobilmärkte, www.innovations-report.de.
- [7] S. Kureti, Angewandte heterogene Katalyse: Vom etablierten Drei-Wege-Katalysator zu neuen Konzepten der Abgasreinigung bei Kraftfahrzeugen, Universität Karlsruhe (TH), 2007.
- [8] W. Weisweiler, Chemie Ingenieur Technik 72 (2000) 441.
- [9] P. Kässner, W. Grünert, H. Papp, Chemiesche Technik 48 (1996) 77.
- [10] P. Balle, B. Geiger, S. Kureti, Applied Catalysis B: Environmental 85 (2009) 109.
- [11] B.A.A.L.v. Setten, M. Makkee, J.A. Moulijn, Catalysis Reviews 43 (2001) 489.
- [12] A. Mayer, U. Matter, G. Scheidegger, J. Czerwinski, M. Wyser, D. Kieser, J. Weidhofer, SAE Technical Paper Series 1999-01-0116.
- [13] J.S. Howitt, M.R. Montierth, SAE Technical Paper Series 810114 (1981).
- [14] A. Setiabudi, M. Makkee, J.A. Moulijn, Applied Catalysis B: Environmental 50 (2004) 185.
- [15] O. Salvat, P. Marez, G. Belot, SAE Technical Paper Series 2000-01-0473.
- [16] B.A.A.L.v. Setten, J.M. Schouten, M. Makkee, J.A. Moulijn, Applied Catalysis B: Environmental 28 (2000) 253.
- [17] B.W.L. Southward, S. Basso, SAE Technical Paper Series 1 (2009) 239.
- [18] D. Reichert, T. Finke, N. Atanassova, H. Bockhorn, S. Kureti, Applied Catalysis B: Environmental 84 (2008) 803.
- [19] U. Schwertmann, R.M. Cornell, Iron oxides in the laboratory, Weinheim, Wiley-VCH, 1991.

- [20] J.W. Niemantsverdriet, Spectroscopy in catalysis, Weinheim, Wiley-VCH, 2007.
- [21] S. Brunauer, P.H. Emmett, E. Teller, Journal of the American Chemical Society 60 (1938) 309.
- [22] T. Finke, Untersuchung der spezifischen Wechselwirkungen von organischen Prozessmaterialien mit den Oberflächen keramischer Pulver am Beispiel von Zirkoniumdioxid, Universität Karlsruhe (TH), 2008.
- [23] D. Reichert, Untersuchungen zur Reaktion von Stickstoffoxiden und Sauerstoff am Katalysator α -Fe₂O₃, Karlsruhe, Universität Karlsruhe (TH), 2008.
- [24] T. Finke, M. Gernsbeck, U. Eisele, C. Vincent, M. Hartmann, S. Kureti, H. Bockhorn, Thermochimica Acta 473 (2008) 32.
- [25] R. Schoch, Untersuchungen zur Oberflächenstruktur von Eisenoxid, Seminar thesis, Karlsruhe Institute of Technology, 2010.
- [26] E.E. Unmuth, L.H. Schwartz, J.B. Butt, Journal of Catalysis 61 (1980) 242.
- [27] S. Wagloehner, D. Reichert, D. Leon-Sorzano, P. Balle, B. Geiger, S. Kureti, Journal of Catalysis 260 (2008) 305.
- [28] D. Reichert, H. Bockhorn, S. Kureti, Applied Catalysis B: Environmental 80 (2008) 248.
- [29] H.M. Rietveld, Acta Crystallographica 22 (1967) 151.
- [30] T. Schröder, Katalysierte Zersetzung von NO am Perowskit LaNiO₃, Karlsruhe, Universität Karlsruhe (TH), 2006.
- [31] J.A. Moulijn, F. Kapteijn, Carbon 33 (1995) 1155.
- [32] J.P.A. Neeft, T.X. Nijhuis, E. Smakman, M. Makkee, J.A. Moulijn, Fuel 76 (1997) 1129.
- [33] B.R. Stanmore, J.F. Brilhac, P. Gilot, Carbon 39 (2001) 2247.
- [34] G. Mul, F. Kapteijn, C. Doornkamp, J.A. Moulijn, Journal of Catalysis 179 (1998) 258.
- [35] G. Mul, J.P.A. Neeft, F. Kapteijn, J.A. Moulijn, Carbon 36 (1997) 1269.
- [36] M.S. Gross, M.A. Ulla, C.A. Querini, Applied Catalysis A: General 360 (2009) 81.
- [37] V. Serra, G. Saracco, C. Badini, V. Specchia, Applied Catalysis B: Environmental 11 (1997) 329.
- [38] E. Aneggi, C.d. Leitenburg, G. Dolcetti, A. Trovarelli, Catalysis Today 114 (2006) 40.

-
- [39] J.P.A. Neeft, O.P.v. Pruisen, M. Makkee, J.A. Moulijn, *Applied Catalysis B: Environmental* 12 (1997) 21.
- [40] Z. Zhang, D. Han, S. Wei, Y. Zhang, *Journal of Catalysis* 276 (2010) 16.
- [41] B. Dernaika, D. Uner, *Applied Catalysis B: Environmental* 40 (2003) 219.
- [42] A. Yezerets, N.W. Currier, H.A. Eadler, SAE Technical Paper Series 2003-01-0833.
- [43] M.N. Bokova, C. Decarne, E. Abi-Aad, A.N. Pryakhin, V.V. Lunin, A. Aboukais, *Thermochimica Acta* 428 (2005) 165.
- [44] D. Fino, N. Russo, C. Badini, G. Saracco, V. Specchia, *AIChE Journal* 49 (2003) 2173.
- [45] R.H. Hurt, B.S. Haynes, *Proceedings of the Combustion Institute* 30 (2005) 2161.
- [46] S.K. Bhatia, D.D. Perlmutter, *AIChE Journal* 26 (1980) 379.
- [47] S.K. Bhatia, D.D. Perlmutter, *AIChE Journal* 27 (1981) 247.
- [48] S. Ahmed, M.H. Back, *Carbon* 23 (1985) 513.
- [49] P. Balle, H. Bockhorn, B. Geiger, N. Jan, S. Kureti, D. Reichert, T. Schröder, *Chemical Engineering and Processing* 45 (2006) 1065.
- [50] D. Reichert, Diplomarbeit, Universität Karlsruhe (TH), 2003.
- [51] K. Sendt, B.S. Haynes, *Journal of Physical Chemistry* 111 (2007) 5465.
- [52] N. Nejar, M. Makkee, M.J. Illan-Gomez, *Applied Catalysis B: Environmental* 75 (2007) 29.
- [53] J.P.A. Neeft, O.P.v. Pruisen, M. Makkee, J.A. Moulijn, *Applied Catalysis B: Environmental* 12 (1997) 21.
- [54] S.B. Simonsen, S. Dahl, E. Johnson, S. Helveg, *Journal of Catalysis* 255 (2008) 1.
- [55] J.v. Doorn, J. Varloud, P. Mériaudeau, V. Perrichon, *Applied Catalysis B: Environmental* 1 (1992) 117.
- [56] P. Barthe, H. Chacrosset, J.M. Guet, *Fuel* 65 (1986) 1330.
- [57] J.P.A. Neeft, F. Hoornaert, M. Makkee, J.A. Moulijn, *Thermochimica Acta* 287 (1996) 261.
- [58] VDI, *VDI-Wärmeatlas*, Springer, Berlin, 2006.
- [59] D.E. Mears, *Industrial and Engineering Chemistry Process Design and Development* 10 (1971) 541.

- [60] M. Baerns, H. Hofmann, A. Renken, *Chemische Reaktionstechnik*, Georg Thieme Verlag Stuttgart, 1987.
- [61] H. Bockhorn, *Grundlagen der Verbrennungstechnik I*, Universität Karlsruhe (TH), 2006.
- [62] H. Randall, R. Doepper, A. Renken, *Industrial and Engineering Chemistry Research* 36 (1997) 2996.
- [63] NIST-JANAF Thermochemical Tables, 2011, <http://kinetics.nist.gov/janaf>.
- [64] A.F. Ahlström, C.U.I. Odenbrand, *Carbon* 27 (1989) 475.
- [65] W.D. Kingery, D.C. Hill, R.P. Nelson, *Journal of the American Ceramic Society* 43 (1960) 473.
- [66] K.P.R. Reddy, A.R. Cooper, *Journal of the American Ceramic Society* 66 (1983) 664.
- [67] D. Reichert, H. Bockhorn, S. Kureti, *Applied Catalysis B: Environmental* 80 (2008) 248.
- [68] T. Klos, *Eindimensionale-Multikomponenten-Raman-Streuung zur Messung charakteristischer Turbulenzeigenschaften*, VDI-Reihe 8, Fortschr.-Ber. Nr. 692(1998).
- [69] H. Bockhorn, *Chemische Technik1: Einführung in die chemische Reaktionstechnik*, Universität Karlsruhe (TH), 1998.
- [70] O. Levenspiel, *Chemical reaction engineering*, Jon Wiley & sons, 1999.
- [71] A. Angermann, M. Beuschel, M. Rau, U. Wohlfahrt, *Matlab-Simulink-Stateflow*, Oldenbourg-Verlag München Wien, 2005.
- [72] A. Biran, M. Breiner, *Matlab 5 für Ingenieure*, Addison-Wesley-Verlag, 1999.
- [73] P.P. Eckstein, *Repetitorium Statistik*, Wiesbaden, Gabler, 2006.
- [74] C.L. Snow, C.R. Lee, Q. Shi, J. Boerio-Goates, B.F. Woodfield, *Journal of chemical thermodynamics* 42 (2010) 1142.
- [75] G. Ertl, *Handbook of heterogeneous catalysis*, Weinheim, Wiley-VCH, 2008.
- [76] A.E. Scheidegger, *The physics of flow through porous media*, Toronto, University of Toronto, 1973.
- [77] J. Koenigsberger, J. Weiss, *Annalen der Physik* 4 (1911).
- [78] C.H. Bosanquet, *British TA Report BR-507*, (1944).
- [79] E.N. Fuller, P.D. Schettler, J.C. Giddings, *Industrial and Engineering Chemistry* 58 (1966) 18.
- [80] E.M. Schlunder, *Heat exchanger design handbook*, VDI-Verlag, 1987.

-
- [81] M. Knudsen, *Annalen der Physik* 333 (1909) 75.
- [82] A.E. Scheidegger, *The physics of flow through porous media*, University of Toronto Press, 1974.
- [83] J.J. Carberry, R.H. Bretton, *AIChE Journal* 4 (1958) 367.
- [84] E. Fitzer, W. Fritz, *Technische Chemie*, Springer-Verlag, Berlin, 1982.
- [85] S. Kureti, *Reaktionstechnik*, TU Bergakademie Freiberg, 2011.
- [86] M. Rhodes, *Introduction to particle technology*, Wiley, Chichester, 2008.
- [87] R. Vonarb, A. Hachimi, E. Jean, D. Bianchi, *Energy & Fuels* 9 (2005) 35.
- [88] E.A. Heintz, W.E. Parker, *Carbon* 4 (1966) 473.
- [89] P.A. Redhead, *Vacuum* 12 (1962) 203.
- [90] P. Atkins, J.D. Paula, *Atkins' Physical Chemistry*, Oxford University Press, 2006.
- [91] T. Ozawa, *Journal of Thermal Analysis and Calorimetry* 2 (1970) 301.
- [92] P. Ciambelli, P. Parrella, S. Vaccaro, *Studies in Surface Science and Catalysis* 71 (1991) 323.
- [93] D. Uner, M.K. Demikrol, B. Dernaika, *Applied Catalysis B: Environmental* 61 (2005) 334.
- [94] J.F. Knoth, A. Drochner, H. Vogel, J. Gieshoff, M. Kögel, M. Pfeiffer, M. Votsmeier, *Catalysis Today* 105 (2005) 598.
- [95] J. Oi-Uchisawa, A. Obuchi, Z. Zhao, S. Kushiyama, *Applied Catalysis B: Environmental* 18 (1998) 183.
- [96] J. Oi-Uchisawa, S. Wang, T. Nanba, A. Ohi, A. Obuchi, *Applied Catalysis B: Environmental* 44 (2003) 207.
- [97] R.M. Cornell, U. Schwertmann, *The iron oxides*, Wiley-VCH Weinheim, 2003.
- [98] A.F. Hollemann, E. Wiberg, N. Wiberg, *Lehrbuch der Anorganischen Chemie*, Walter de Gruyter, Berlin, 2007.
- [99] S.K. Saha, P. Pramanik, *Nanostructured Materials* 8 (1997) 29.
- [100] L. Mädler, H.K. Kammler, R. Mueller, S.E. Pratsinis, *Aerosol science* 33 (2002) 369.
- [101] S.E. Pratsinis, *Journal of Aerosol Science* 27 (1996) S153.
- [102] K. Wegner, S.E. Pratsinis, *Powder Technology* 150 (2005) 117.
- [103] R. Strobel, A. Baiker, S.E. Pratsinis, *Advanced Powder Technology* 17 (2006) 457.
- [104] L. Mädler, *KONA Powder and Particle* 22 (2004) 107.

- [105] D. Klukowski, P. Balle, S. Wagloehner, S. Kureti, B. Kimmerle, A. Baiker, J.-D. Grunwaldt, *Applied Catalysis B: Environmental* 93 (2009) 185.
- [106] M. Weiss, G. Ertl, F. Nitschké, *Applications of Surface Science* 2 (1979) 614.
- [107] O. Hinrichsen, F. Rosowski, M. Muhler, G. Ertl, *Studies in Surface Science and Catalysis* 109 (1997) 389.
- [108] A. Trovarelli, *Catalysis Reviews* 38 (1996) 439.

Student contributions

- 1 F. Mück, Untersuchungen zur katalytischen Rußoxidation an α -Fe₂O₃, Seminar thesis, Karlsruhe Institute of Technology, 2010.
- 2 J. Bär, Elementarkinetische Modellierung der Desorption von NH₃ an verschiedenen Eisenoxid-Modellkatalysatoren, Seminar thesis, Karlsruhe Institute of Technology, 2010.
- 3 E. Ogel, Untersuchungen zu Aktivität und Morphologie von Eisenoxid basierten Katalysatoren bei der Rußoxidation, Seminar thesis, Karlsruhe Institute of Technology, 2011.
- 4 G. Cevasoglu, Untersuchung des Einflusses verschiedener Reaktionsparameter auf die katalysierte und nicht-katalysierte Rußoxidation, Seminar thesis, Karlsruhe Institute of Technology, 2011.

9 Appendix

A Accuracies of measurements

To aid the reproducibility and show the accuracy of the measurements, the results of three TPO experiments, which were done by using identical experimental conditions are presented in Figure A-1. The temperature of maximum CO₂ volume fraction ranges between 398°C and 416°C. Moreover, the CO₂ peak volume fraction differs between 7.4 vol% and 10.9 vol%. This shows that reproducibility is a crucial point for catalytic soot oxidation. Due to the influence of heat transfer in the packed bed and the oxygen sensitivity of the reaction rate repeatable experiments were major challenges. To avoid such differences hands-on experience in the preparation procedure (e.g. placement and powder density of the catalyst/soot mixture) is necessary.

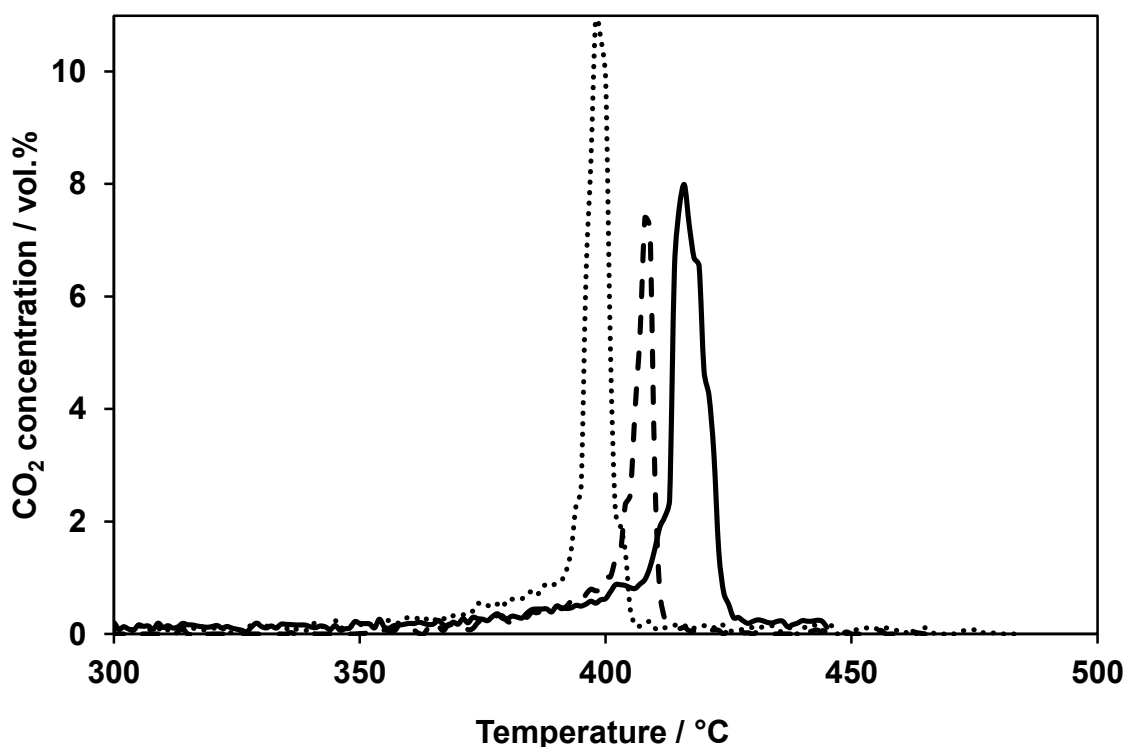


Figure A-1: CO₂ profiles of three TPO runs using the same reaction conditions. Conditions: F=500 ml/min (STP), 10 vol.% O₂, N₂ balance, catalyst:soot ratio=10 mmol:5 mmol, tight contact mixture.

B Calculation of mass transfer limitations

B.1 Film diffusion

Outer mass transfer limitations can be estimated according to the Mears criterion [59] by taking the ratio of convective mass transport and mass transport due to chemical reaction:

$$\frac{r_{\text{eff}} \cdot d_p}{2 \cdot k_i \cdot c_{i,g}} < 0.15 \quad (\text{B-1})$$

r_{eff}	: Effective reaction rate	[mol/(m ³ ·s)]
d_p	: Particle diameter	[m]
k_i	: Mass transfer coefficient of species i	[m/s]
$c_{i,g}$: Concentration of species i in gas phase	[mol/m ³]

The effective reaction rate is derived from TPO (Figure 3-9) being 7.92 mol/(m³·s), referring to a 10 vol.% CO₂ at 400°C for the experiment using a heating rate of 10 K/min. The mass transfer coefficient is determined on the basis of the Sh-number considering the marginal case of minimal Sh_{min} (for Re≈0) number being 2 for a overflowed spherical particle [58]:

$$\text{Sh}_{\text{min}} = 2 = \frac{k_i \cdot d_p}{D_i} \quad (\text{B-2})$$

D_i	: Diffusion coefficient of species i	[m ² /s]
-------	--------------------------------------	---------------------

Since the diffusion coefficients of O₂, CO and CO₂ species are within the same range ($D_{\text{O}_2}=8.65 \cdot 10^{-5}$ m²/s, $D_{\text{CO}_2}=6.84 \cdot 10^{-5}$ m²/s and $D_{\text{CO}}=8.27 \cdot 10^{-5}$ m²/s, determined according Eq. (4-31) for T=400°C) an unambiguous differentiation among these species is not possible. The further estimation of a possible mass transfer limitation is done by taking a value of $D_i=6 \cdot 10^{-5}$ m²/s which is considered as worst case. The mass transfer coefficient results in 2400 m/s corresponding to a diameter of $5 \cdot 10^{-8}$ m of the soot particles. Finally, the Mears criterion offers a value of $2 \cdot 10^{-11}$ clearly showing no limitations due to film diffusion.

B.2 Pore diffusion

Inner mass transfer limitation for first order reactions can be estimated on the basis of the Weisz-Prater module [60]:

$$\Psi = L_c^2 \cdot \frac{r_{\text{eff}}}{D_{\text{eff}} \cdot C_{i,g}} > 1 \quad (\text{B-3})$$

L_c	: Characteristic length	[m]
D_{eff}	: Effective diffusion coefficient	[m/s]

For spherical particles, L_c corresponds to the particle diameter, while the surface concentration conforms to the gas phase concentration for negligible film diffusion. The effective diffusion coefficient D_{eff} is calculated according to Eq. (4-30) being $1.22 \cdot 10^{-5}$ m²/s referring to Table C-1 and $D_f = 6 \cdot 10^{-5}$ m/s (see above). The Weisz-Prater module reveals a value of $4 \cdot 10^{-10}$ being clearly smaller than 1, thus suggesting no limitations by pore diffusion.

C Numerical values for CFD

Table C-1: Properties of Fe₂O₃ and the packed bed

Parameter	Denotation	Value
ε	Porosity of Fe ₂ O ₃	0.509
k	Permeability	$2 \cdot 10^{-11}$ m ²
d_{pore}	Pore diameter	$1 \cdot 10^{-5}$ m
k	Thermal conductivity	0.14 W/(m·K)
$k_{\text{Fe}_2\text{O}_3}$	Thermal conductivity Fe ₂ O ₃	0.8365 W/(m·K)
$\varepsilon_{\text{apparent}}$	Apparent porosity	0.832
τ	Tortuosity of Fe ₂ O ₃	2
$d_{p,\text{Fe}_2\text{O}_3}$	Particle diameter of Fe ₂ O ₃	$70 \cdot 10^{-6}$ m

Table C-2: Parameters for the Gaussian fit of the CO₂ reaction rate

Parameter	Value
y_0	0
A	89.5
w	45
T_0	427

Table C-3: Parameters for the kinetic expression of the CO₂ reaction rate

Parameter	Denotation	Value
λ	Surface concentration	$8.7 \cdot 10^{-6} \text{ mol/m}^2$
S_0	Initial BET area	91 m ² /g
f	Factor	60
ΔH	Reaction enthalpy	400 kJ/mol
n_{O_2}	Reaction order O ₂	1

Table C-4: Initial values of the model (for tube reactor design)

Parameter	Denotation	Value
u	Velocity x-direction	0.074 m/s
v	Velocity y-direction	0 m/s
p	Pressure=constant	$1 \cdot 10^5 \text{ Pa}$
$c(O_2)$	Concentration O ₂	4.09 mol/m ³
$c(CO_2)$	Concentration CO ₂	0 mol/m ³
$c(\text{carbon})$	Concentration soot	800 l/m ³

D Physical Parameters for CFD

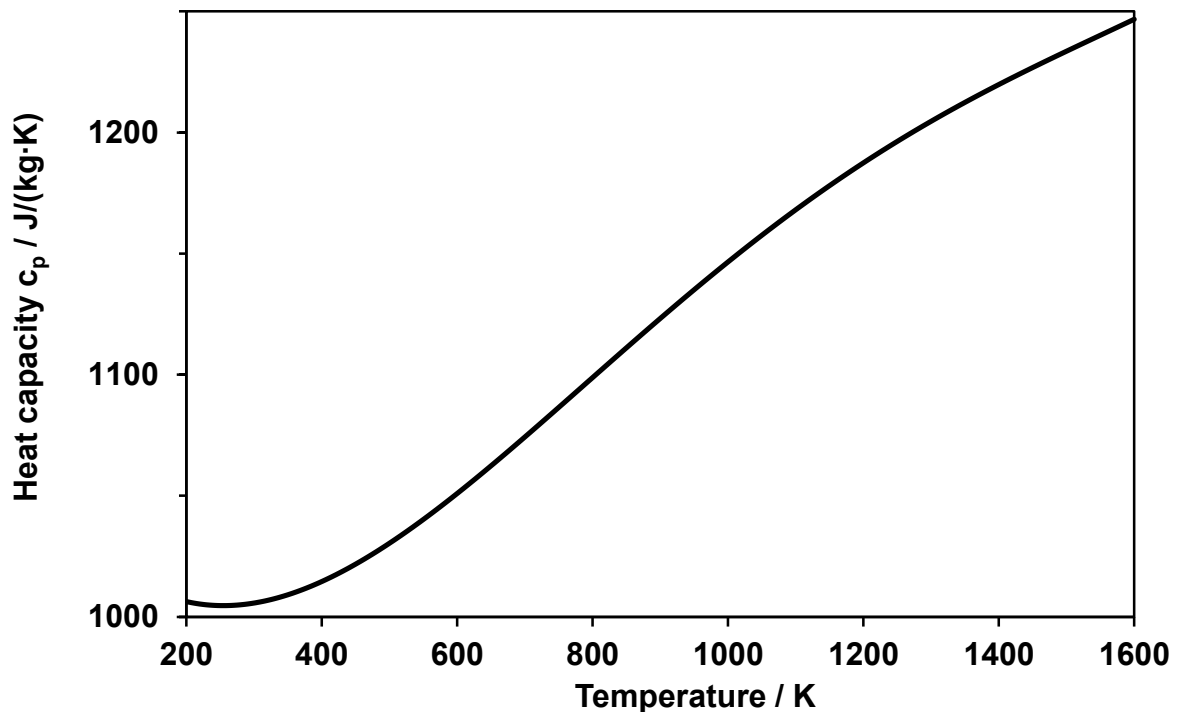


Figure D-1: Heat capacity of air dependent on temperature. Data is obtained from COMSOL database.

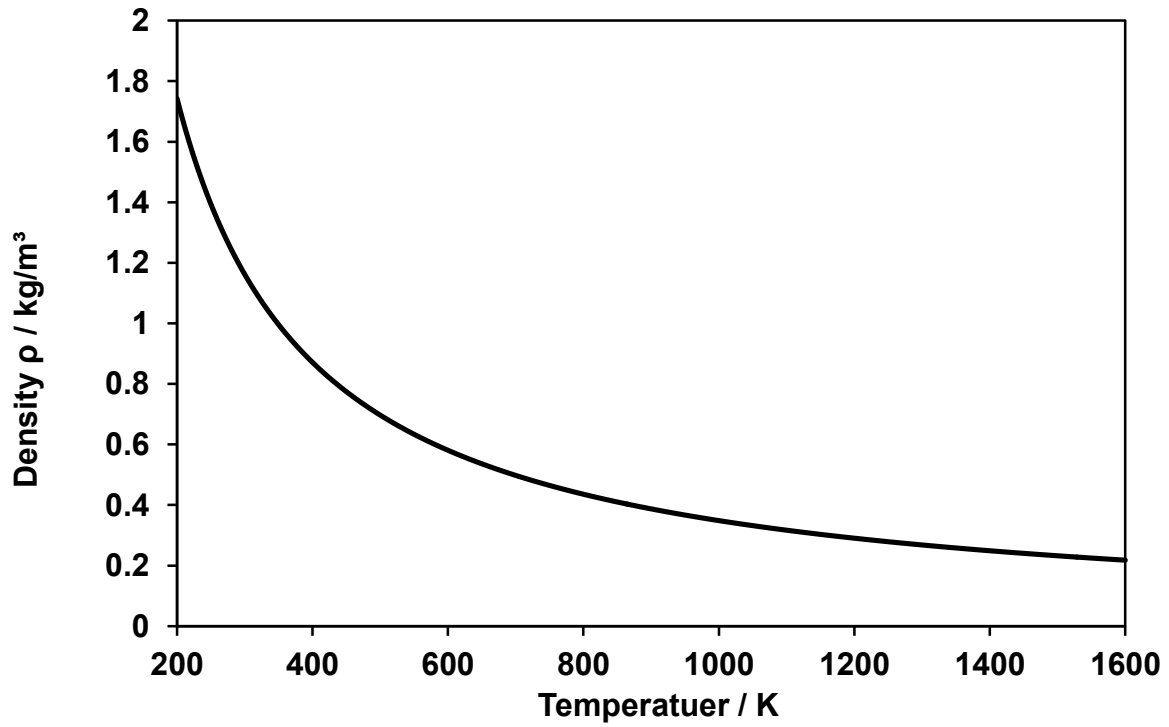


Figure D-2: Density of air in dependent on temperature. Data is obtained from COMSOL database.

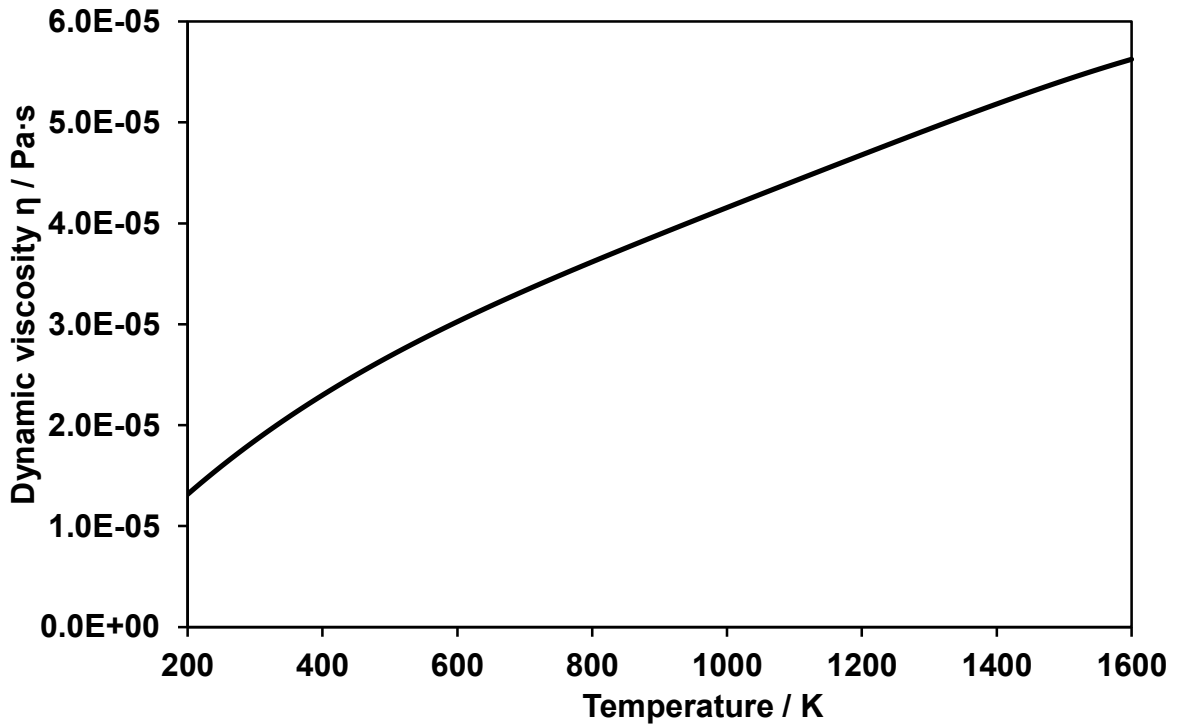


Figure D-3: Dynamic viscosity of air in dependent on temperature. Data is obtained from COMSOL database.

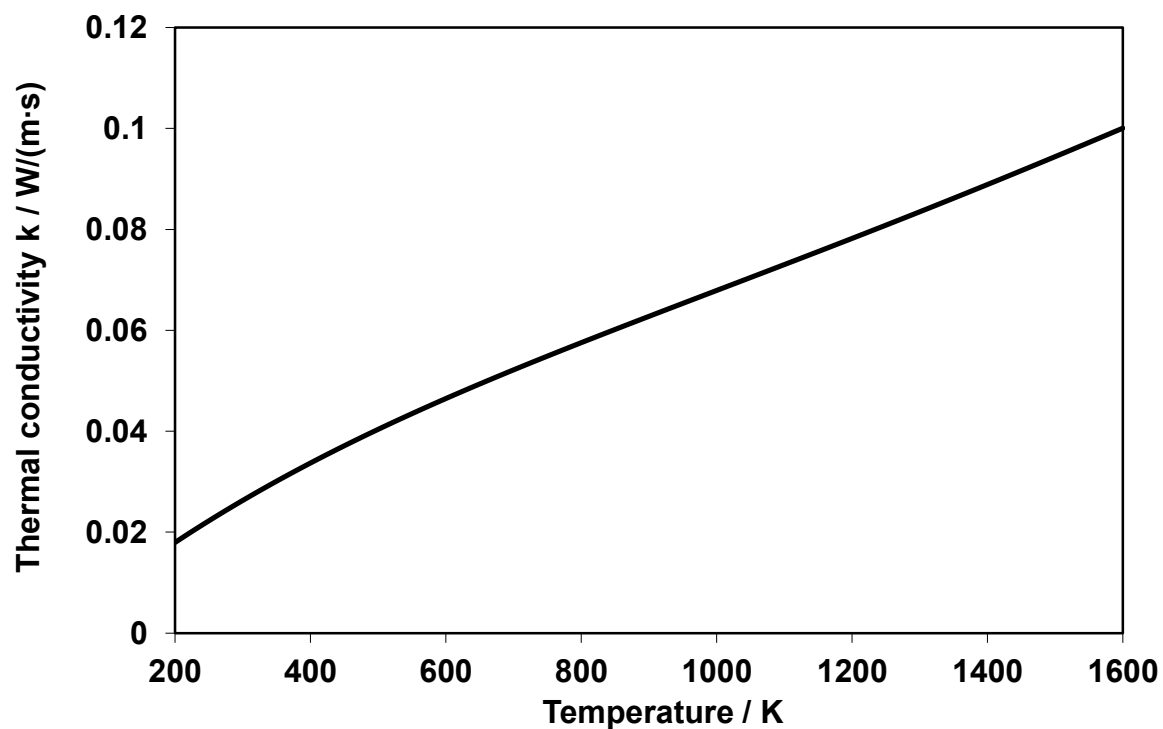


Figure D-4: Thermal conductivity of air in dependent on temperature. Data is obtained from COMSOL database.

E TPD studies of different types of soot

Table E-1: Formed amount of CO_x upon the TPD studies using different types of soot.

Sample	n _{co} [mmol/g]	n _{co2} [mmol/g]	n _{cox} [mmol/g]
Spezial Schwarz 6	2.9	3.6	5.5
PrintexU	1.2	1.4	2.6
Home-made C ₃ H ₆	1	0.9	1.9
PrintexL	0.7	2.4	3.1

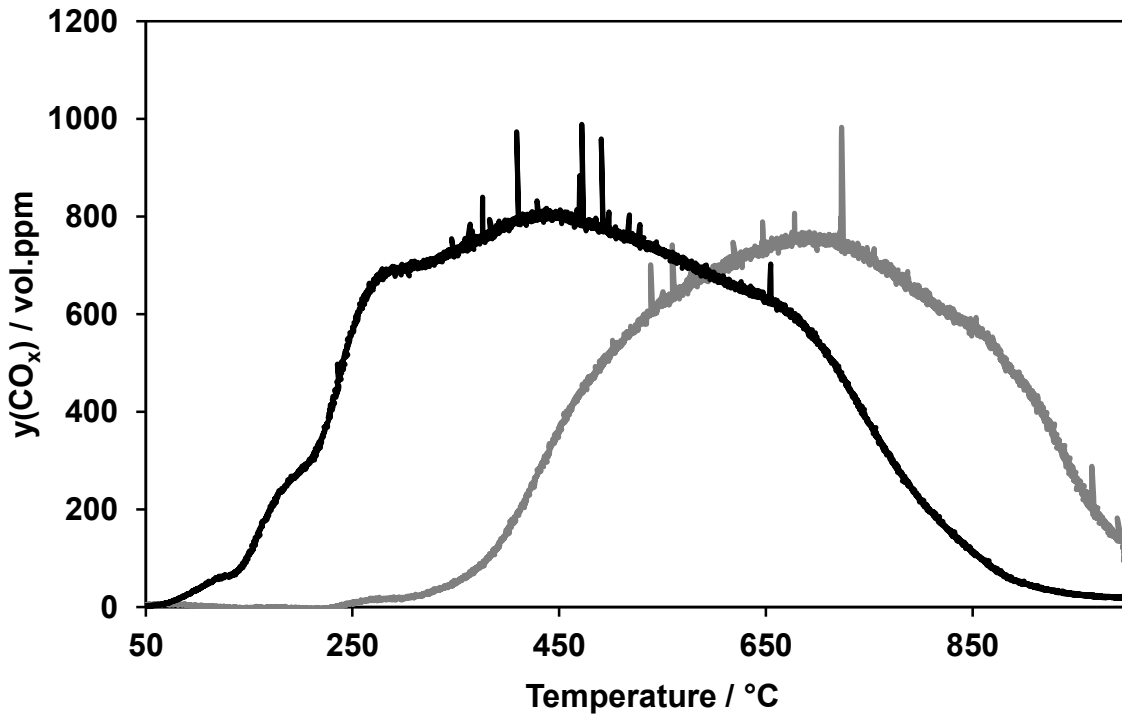


Figure E-1: CO₂ (—) and CO (···) profile of TPD of Spezial Schwarz 6 soot. Conditions: 120 mg soot, F=500 mL/min N₂, β =20 K/min.

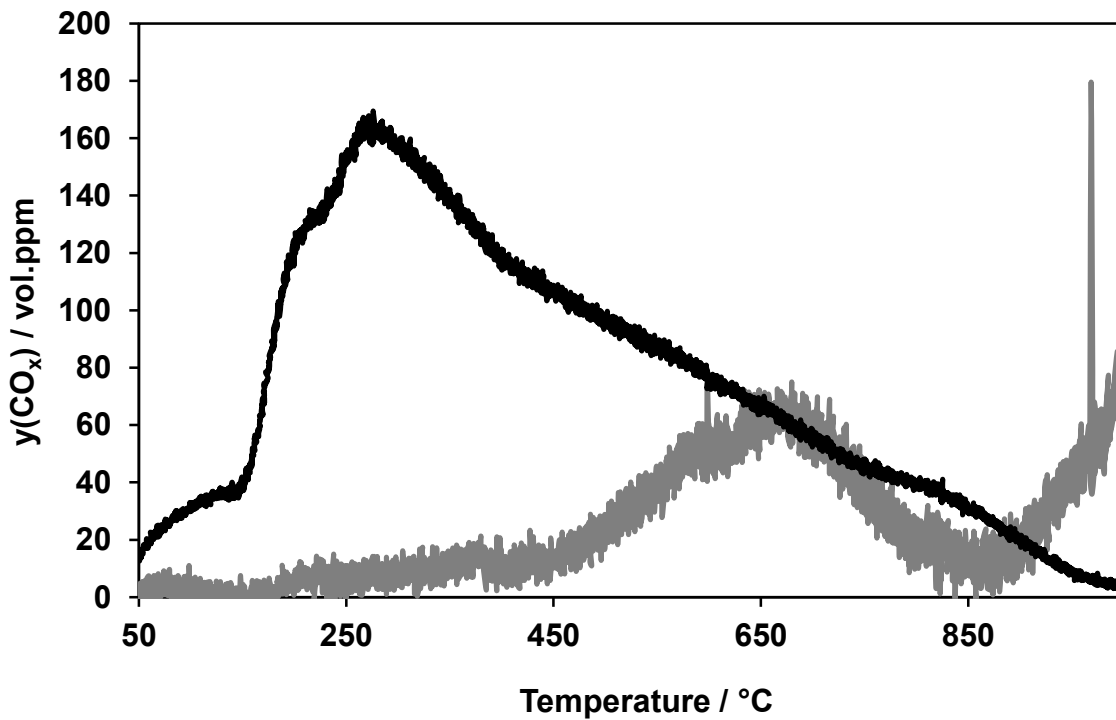


Figure E-2: CO₂ (—) and CO (···) profile of TPD of PrintexL soot. Conditions: 120 mg soot, F=500 mL/min N₂, β =20 K/min.

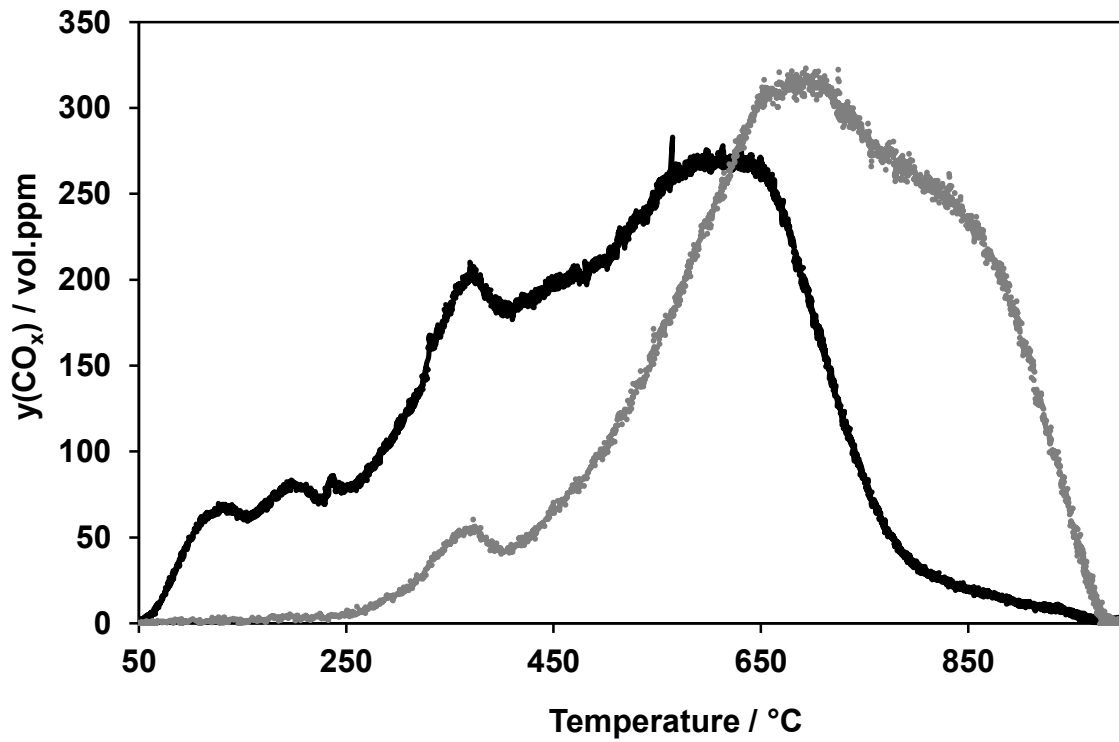


Figure E-3: CO₂ (—) and CO (···) profile of TPD of home-made C₃H₆ soot. Conditions: 120 mg soot, F=500 mL/min N₂, β=20 K/min.

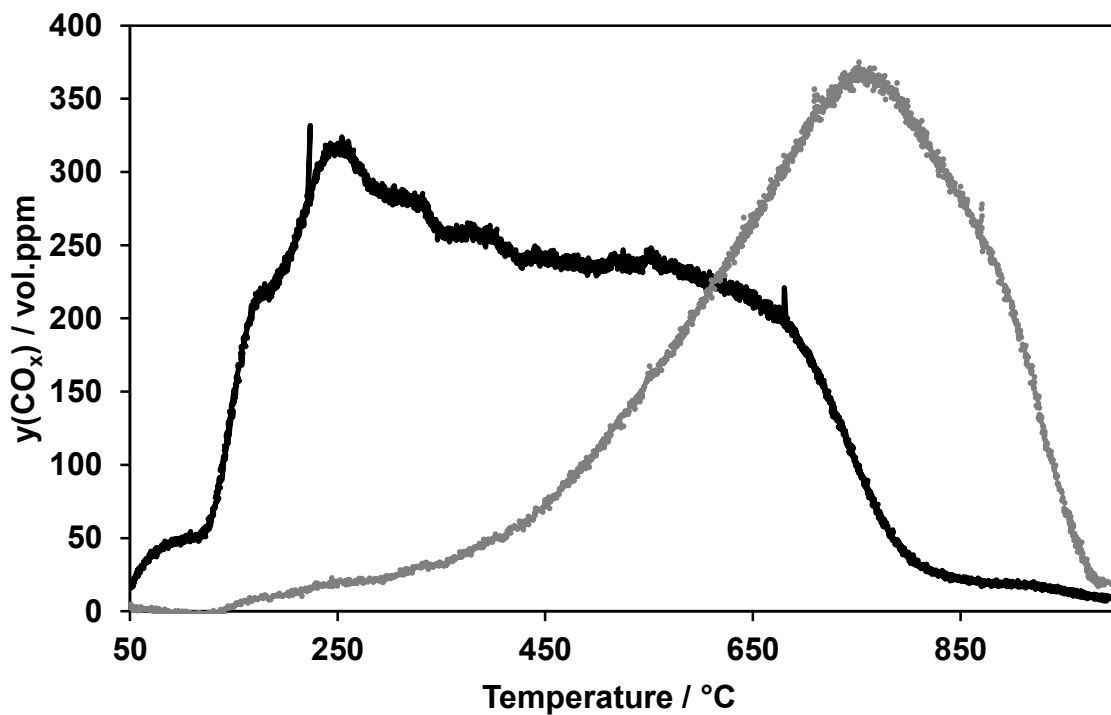


Figure E-4: CO₂ (—) and CO (···) profile of TPD of PrintexU soot. Conditions: 120 mg soot, F=500 mL/min N₂, β=20 K/min.

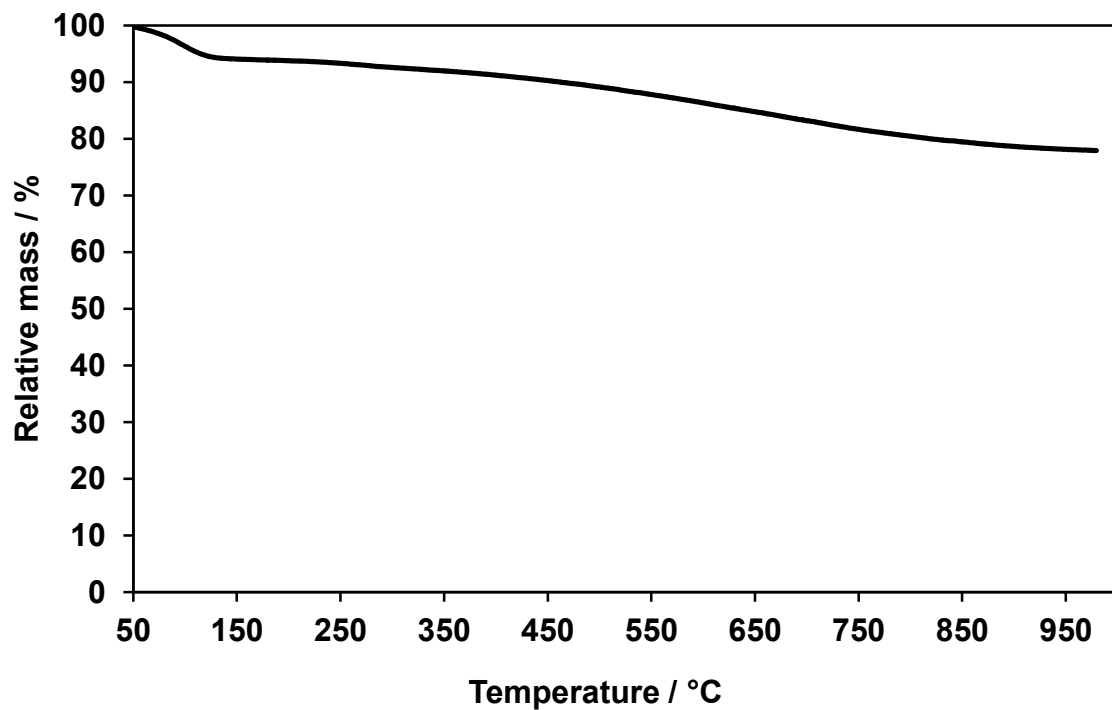
F Thermogravimetric analysis of different types of soot

Figure F-1: TG analysis of Aktiv Schwarz 6 soot. Conditions: $F=3$ l/min N_2 , $\beta=10$ K/min.

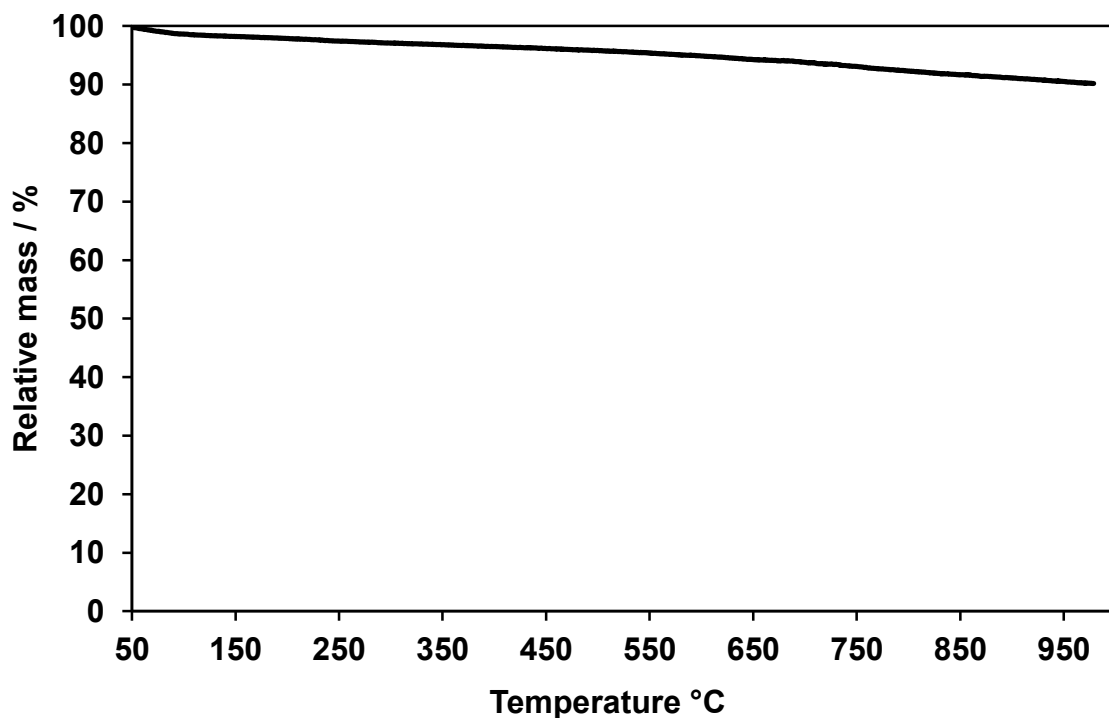


Figure F-2: TG analysis of PrintexU soot. Conditions: $F=3$ l/min N_2 , $\beta=10$ K/min.

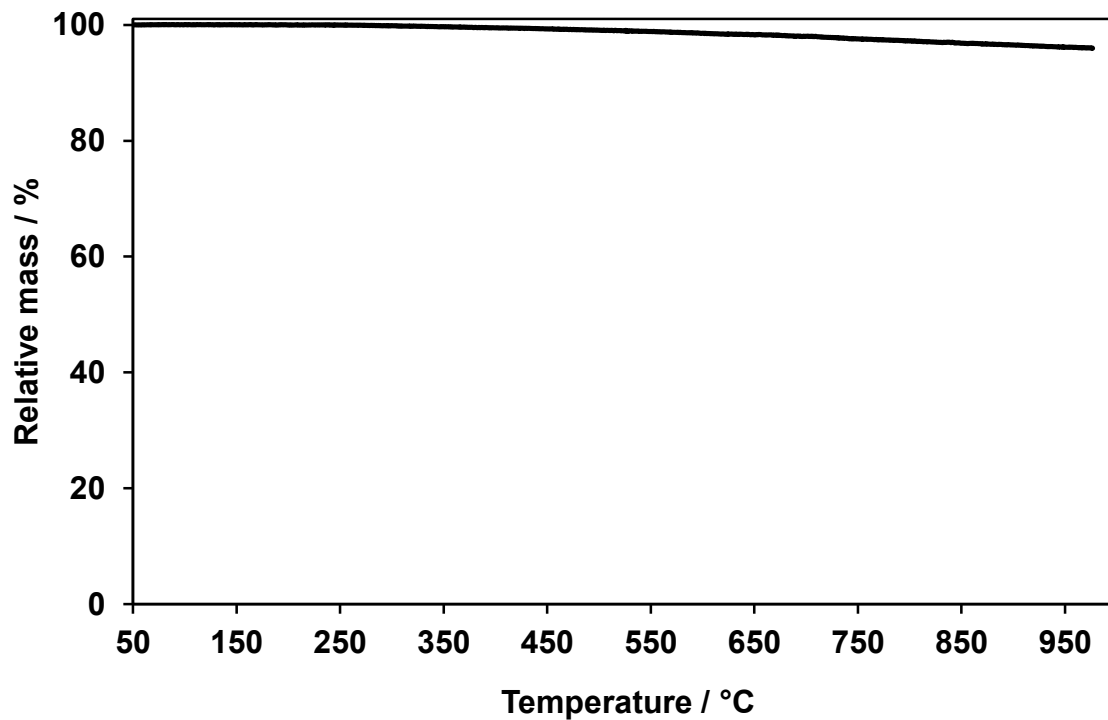


Figure F-3: TG analysis of home-made C₃H₆ soot. Conditions: F=3 l/min N₂, β =10 K/min.

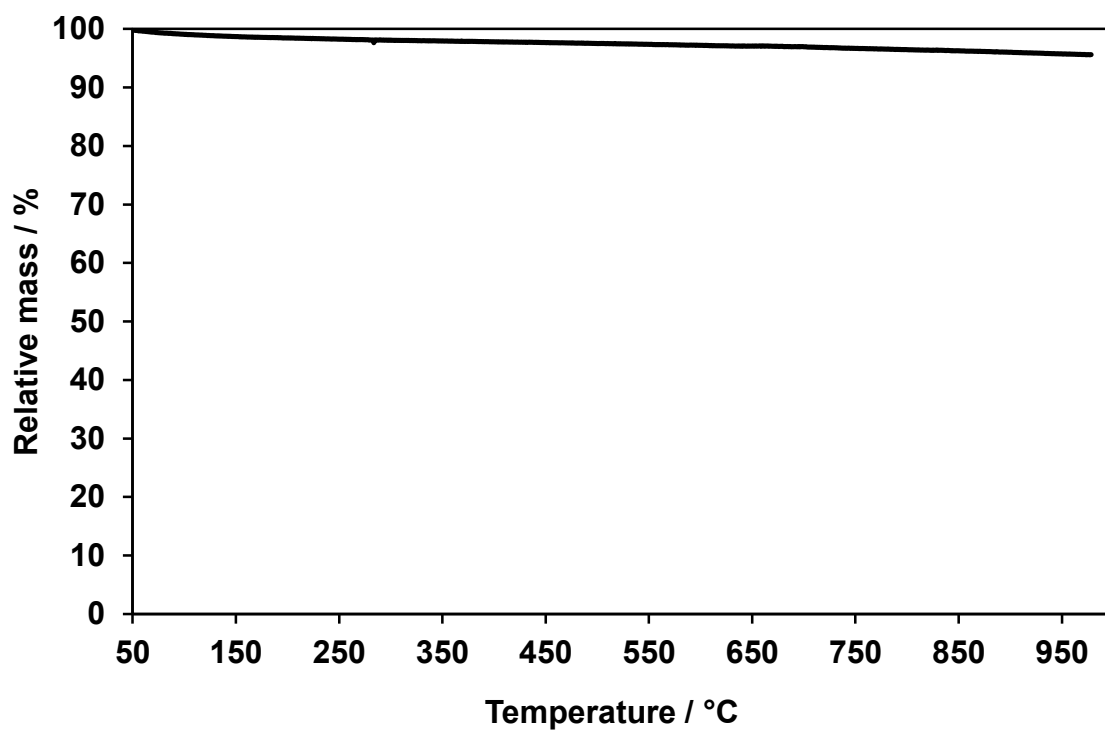


Figure F-4: TG analysis of PrintexL soot. Conditions: F=3 l/min N₂, β =10 K/min.

G Properties of the atomisation nozzle of the FSP bench

Table G-1: Operating ranges and characteristics of the atomisation nozzle

Operating parameter	Value
Difference pressure of atomisation gas	$\Delta p=0.1-4.0$ bar
Throughput of liquid	0.05-0.30 l/min
Throughput of atomisation air	0.35-4.00 Nm ³ /h
Diameter of nozzle outlet	0.5 mm
Material	V4A
Droplet size	15 μ m referring to 5 l/h water and 7.4 Nm ³ /h air at 5 bar
Atomization cone	10°-40°

H Glossary of abbreviations and symbols

Table H-1: Glossary of abbreviations

Abbreviation	Denotation
BET	Brunauer, Emmet and Teller
CAD	Computation aided design
CDPF	catalytically coated diesel particulate filter
CFD	Computational fluid dynamics
CIMS	Chemical ionisation mass spectrometer
CRT	Continuous regenerating trap
CSTR	Continuously operated stirred tank reactor
DOC	Diesel oxidation catalyst
DPF	Diesel particulate filter
DTA	Differential thermal analysis
FBC	Fuel borne catalyst
FSP	Flame-spray pyrolysis
FTIR	Fourier transformed infrared spectroscopy
HTPR	Temperature programmed reduction by H ₂
IR	Infrared spectroscopy
MS	Mass spectrometer
NDIR	Non-dispersive infrared spectroscopy
NMVOC	non-methane volatile organic carbons
pde	Partial differential equation
PFR	Plug flow reactor

PM	Particulate matter
ppm	Parts per million
PVA	Polyvinyl alcohol
R&D	Research and development
RSS	Residual sum of squares
SCR	Selective catalytic reduction
STP	Standard temperature and pressure
$T_{CO_2,max}$	Temperature of maximum CO ₂ concentration
TEM	Transmission electron microscope
TG	Thermogravimetry
TPD	Temperature programmed desorption
TPO	Temperature programmed oxidation
TPR	Temperature programmed reduction
TWC	Three way catalyst
XRD	X-ray diffraction

Table H-2: Glossary of symbols

Symbol	Denotation	Unit
A	Preexponential factor	m ³ /(mol·s)
A	Area	m ²
a _m	Place requirement	m
Bo	Bodenstein number	[/]
c	Concentration	mol/m ³
c _p	Heat capacity	J/(g·K)
d	Diameter	m
D ₁₂	Molecular diffusion coefficient	m ² /s
D _{ax}	Dispersion coefficient	m ² /s
D _{eff}	Effective diffusion coefficient	m ² /s
D _k	Knudsen diffusion coefficient	m ² /s
D _a	Diffusion analogical coefficient	m/s
E(T)	Probability curve	1/s
E _A	Activation energy	J/mol
E _{diff}	Activation energy for diffusion	J/mol
f	Factor	[/]

F	Volume flow	m ³ /s
F(T)	Sum curve	[/]
k	Rate constant	m ³ /(mol·s)
k	Thermal conductivity	W/(m·K)
k _i	Mass transfer coefficient	m/s
k _s	Heat transfer coefficient	W/(m ² ·K)
L	Length	m
m	Mass	g
M _i	Molar mass	g/mol
n	Molar amount	mol
n	Reaction order	[/]
N	Number of CSTRs	[/]
N _A	Avogadro number	[/]
p	Pressure	bar
\dot{Q}	Heat production	W/m ³
r	Reaction rate	mol/s
R	Molar gas constant	J/(mol·K)
R ²	Coefficient of determination	[/]
S	Specific BET surface area	m ² /g
S(X)	Absolute surface area	m ²
S ⁰	Sticking coefficient	[/]
T	Temperature	°C
T ⁰	Temperature at STP	K
t	Time	s
u	Velocity	m/s
X	Conversion	[/]
y	Function value	[/]
y(i)	Volume fraction of species i	[vol.%]
λ	Surface concentration	mol/m ²
α	Factor for coverage dependent activation energy	J/mol
β	Heating rate	K/s
Γ	Surface concentration	mol/m ²
Δ	Difference	[/]
ΔG _r	Gibb's free reaction enthalpy	kJ/mol

ΔH_f^0	Formation enthalpy	kJ/mol
ΔH_r	Reaction enthalpy	kJ/mol
ε	Porosity	[/]
η	Dynamic viscosity	Pa·s
κ	Permeability	m ²
ρ	Density	g/m ³
σ^2	Variance	[/]
Ψ	Weisz-Prater module	[/]
ω	Boundary definition	[/]
Θ	Surface coverage	[/]
τ	Retention time	s
τ	Tortuosity	[/]
Δ	Laplace operator	[/]
∇	Nabla operator	[/]

Diesel particulate filters (DPF) represent a state-of-the-art technology for the removal of soot from diesel exhaust. However, the continuous regeneration of these filter systems remains a considerable challenge, as the trapped soot causes backpressure effects potentially decreasing the engine efficiency. While the so-called continuous regenerating trap (CRT) technique using nitrogen dioxide is already established for heavy duty vehicles, the catalytic soot oxidation by oxygen is considered to be a promising procedure for passenger cars, ships and work machines. Therefore, the present work addresses the rational development of a highly active iron oxide based catalyst for soot oxidation. The approach of this development process comprises three fundamental research methods, namely mechanistic and kinetic experiments, kinetic and fluid dynamic modelling and structure-activity relations of different types of iron oxides. A combination of this enables the synthesis of an advanced catalytic material, which is transferred to a real DPF system and tested under real diesel exhaust conditions.



ISBN 978-3-86553-405-7

